



HAL
open science

Chemistry and physical properties of normal valence and hypervalent polar chalcogenides

Stefan Maier

► **To cite this version:**

Stefan Maier. Chemistry and physical properties of normal valence and hypervalent polar chalcogenides. Other. Normandie Université, 2017. English. NNT : 2017NORMC247 . tel-01717571

HAL Id: tel-01717571

<https://theses.hal.science/tel-01717571>

Submitted on 26 Feb 2018

HAL is a multi-disciplinary open access archive for the deposit and dissemination of scientific research documents, whether they are published or not. The documents may come from teaching and research institutions in France or abroad, or from public or private research centers.

L'archive ouverte pluridisciplinaire **HAL**, est destinée au dépôt et à la diffusion de documents scientifiques de niveau recherche, publiés ou non, émanant des établissements d'enseignement et de recherche français ou étrangers, des laboratoires publics ou privés.



Normandie Université

THESE

Pour obtenir le diplôme de doctorant

Spécialité CHIMIE

Préparée au sein de l'ENSICAEN et de l'UNICAEN

Chemistry and physical properties of normal valence and hypervalent polar chalcogenides

Présentée et soutenue par
Stefan MAIER

Thèse soutenue publiquement le 12.12.2017
devant le jury composé de

M. Anthony POWELL	Professeur à l'Université de Reading, Angleterre	Rapporteur
M. Stéphane CORDIER	Directeur de Recherche CNRS à l'Université de Rennes	Rapporteur
Mme. Houria KABBOUR	Chargée de recherche CNRS à l'Ecole Nationale Supérieure de Chimie de Lille	Examineur
M. Olivier PEREZ	Directeur de recherche CNRS à l'ENSICAEN	Examineur
M. David BERTHEBAUD	Chargé de recherche CNRS à l'ENSICAEN	Examineur
M. Franck GASCOIN	Maître de conférences, HDR à l'Université de Caen	Directeur de thèse

Thèse dirigée par Franck GASCOIN, laboratoire CRISMAT



UNIVERSITÉ
CAEN
NORMANDIE

 **ENSICAEN**
ÉCOLE PUBLIQUE D'INGÉNIEURS
CENTRE DE RECHERCHE



*The meeting ground of the
sciences is here and now, in new
materials with novel properties.*

*One is unlikely to make such
materials and understand them if
one is wearing pure chemical or
physical blinders*

Roald Hoffmann

Introduction

Ces travaux de thèse portent sur l'étude des propriétés chimiques et physiques de chalcogénures polaires (CPs) à valence normale ou hypervalents. Ces composés appartiennent à la famille des intermétalliques polaires, et s'inscrivent donc dans le champ d'étude de la chimie des intermétalliques. Le but premier de cette étude est la synthèse de nouveaux composés de structure cristalline complexe, afin d'étudier la relation entre la structure cristalline, la nature des liaisons chimiques et les propriétés physiques, déterminées par des mesures expérimentales et des analyses théoriques. Les CPs ont été choisis comme matériaux d'étude car ils se situent à la frontière entre les matériaux métalliques et non-métalliques. Pour ces matériaux (les CPs), les propriétés chimiques sont gouvernées par l'interaction entre les différents types de liaisons – covalente, métallique et ionique – ouvrant la voie à l'étude des liens entre structure cristalline et liaisons chimiques. La recherche de matériaux à structure complexe permet de cibler de potentiels matériaux thermoélectriques prometteurs, puisque la complexité structurale est souvent liée à une faible conductivité thermique, qui est une propriété clé des thermoélectriques. Les matériaux thermoélectriques transforment la chaleur en électricité, et sont donc au cœur des enjeux économiques et environnementaux actuels. La découverte de thermoélectriques à bon rendement appartenant à la famille des chalcogénures, tels que PbTe, Bi₂Te₃, CsBi₄Te₆ et le composé superionique Cu_{2-x}Se ont orienté les recherches vers l'exploration de composés chalcogénures de type Cu- et Pn- (Pn = Sn, Bi), et ont motivé l'étude de matériaux voisins, comme BaBiTe₃ (Chapitre V). Une des possibilités pour induire des structures complexes est d'obtenir un transfert de charge du cation (Ba, Se) vers une structure anionique, créant ainsi des réseaux covalents anioniques complexes sous forme de chaînes ou de couches, qui sont à l'origine de propriétés physiques intéressantes. Une paire d'électrons libres et stéréoactifs peut également augmenter la complexité de la structure, via une distorsion des polyèdres de coordination, ce qui justifie l'étude de matériaux contenant des éléments de type Pn comme Bi ou Sb. L'analyse des propriétés physiques ainsi que l'étude de la structure cristalline et des liaisons chimiques de chalcogénures polaires de structure complexe, certains connus et d'autres découverts au cours de ce travail de thèse, ont résulté en des découvertes prometteuses.

Présentation du programme scientifique

Ce manuscrit de thèse est organisé en six chapitres qui se regroupent dans deux parties principales : les chalcogénures Cu-(I)- et Pn- de valence normale d'une part, et hypervalents d'autre part. Le chapitre I est une courte introduction à la chimie des intermétalliques et des chalcogénures polaires, qui permet de discuter de la compétition existant entre les liaisons covalentes et ioniques présentes dans tous les composés CPs. Les liaisons de type hypervalentes ou en résonance y sont ensuite traitées, en remontant à la chimie moléculaire qui a développé ces concepts. Enfin, une courte présentation des applications fondées sur les composés chalcogénures ayant inspiré cette étude est donnée.

Le chapitre II propose une classification des CPs ternaires et quaternaires, basée sur deux paramètres : le nombre quantique principal moyen \bar{n} et la différence d'électronégativité entre le cation et le réseau anionique. Cette classification s'appelle « Extended Mooser Pearson plots » car elle s'appuie sur le travail de Mooser et Pearson (1959), qui ont été les premiers à fournir une classification pour les composés de valence normale A_iX_j ($i, j = 1, 2, 3$). Les « Extended Mooser Pearson Plots » permettent de quantifier le degré de polarité des CPs et peuvent se révéler utiles pour la compréhension des changements structuraux lors d'échanges d'ions, et de manière plus spécifique pour le ciblage de certains types de structures. Le chapitre III donne les paramètres expérimentaux, de calcul et de modélisation.

Le chapitre IV expose les résultats des structures cristallines, des types de liaison chimique et des propriétés physiques de CPs de valence normale découverts durant cette thèse. Pour tous les composés présentés dans ce chapitre, la liaison chimique peut être décrite comme une liaison $2c-2e$ classique respectant la règle de l'octet. Dans une première sous-partie, les structures cristallines de quatre nouveaux composés cuivre-(I)-sélénides $A_{0.5}CuZrSe_3$ et $ACuYSe_3$ ($A = Sr, Ba$), appartenant à la famille dite « 1113 », sont étudiées. Elles sont ensuite mises en relation avec les rayons ioniques, afin de comprendre l'influence de ces derniers sur les types de structures et les différentes symétries obtenus. Dans une seconde sous-partie, deux nouveaux CPs contenant d'une paire d'électrons libres, $Ba_2FePnSe_5$ ($Pn = Sb, Bi$), sont étudiés, avec une discussion portant sur leur structure cristalline et les distorsions induites par les paires d'électrons libres de Sb et Bi. La structure électronique, la résistivité électrique ainsi que la conductivité thermique de ces composés sont également analysées pour les deux composés.

Une rapide transformation de phase de l'état cristallin à l'état amorphe lors d'une exposition aux radiations a été mise en évidence pour les deux composés. Ces résultats ainsi que leur origine, possiblement liée à une structure de liaisons en résonance, sont également discutés, et sont suivis d'une conclusion sur les anomalies observées dans la conductivité thermique et les constantes diélectriques à la température de Néel.

Le chapitre V traite des CPs pour lesquels les types de liaisons classiques, comme la liaison *deux électrons-deux-centres* et la règle de l'octet, ne sont pas suffisants pour comprendre la structure cristalline. Pour ces composés, des modèles de liaisons hypervalentes et le concept de résonance sont nécessaires pour une description précise du système. Tout d'abord, l'étude se penche sur le composé $\text{Ba}_4\text{Cu}_8\text{Se}_{13}$, un nouveau sélénure de cuivre-(I), qui est aussi le premier composé hypervalent découvert dans le système ternaire Ba/Cu/Se. Les procédés utilisés pour déterminer la structure cristalline, ainsi que la structure cristalline et le type de liaisons dans ce composé sont discutés. Cela inclut l'analyse des liaisons Se-Se et Cu-Cu, et les réflexions quant à l'appartenance de $\text{Ba}_4\text{Cu}_8\text{Se}_{13}$ aux composés à « clusters ». Cette partie est suivie par une discussion sur le nano-maclage, les modulations de structure et les effets de structure réelle, qui doivent être pris en compte et compliquent l'analyse du composé. La structure cristalline moyenne est ensuite confirmée par microscopie électronique à transmission, et comparée à la structure locale. Cette sous partie se conclut par une discussion sur les propriétés de transport du composé à basse température. Dans un second temps, les composés $\text{BaBiTe}_{3-x}\text{Se}_x$ ($x = 0, 0.05, 0.1$ et 3) sont étudiés. Pour BaBiTe_3 , aucun état d'oxydation de l'élément Te ne peut être clairement identifié, à cause de l'existence d'un réseau étendu de liaisons hypervalentes Te-Te. Les liaisons présentes dans ce composé sont repensées grâce à des calculs *ab-initio* fondés sur la théorie de la fonctionnelle de la densité (DFT). Ensuite, la structure électronique est discutée en incluant toutes les contributions orbitales à la structure de bandes, puis est mise en relation avec les propriétés optiques du composé, et de ses variantes où Se substitue Te. Les propriétés thermoélectriques des composés $\text{BaBiTe}_{3-x}\text{Se}_x$ ($x = 0, 0.05$ and 0.1) sont analysées et discutées en détail, avec une attention particulière portée à la question de l'impact des défauts natifs et de la structure cristalline et électronique complexe de $\text{BaBiTe}_{3-x}\text{Se}_x$ ($x = 0, 0.05$ and 0.1) sur les propriétés thermoélectriques. Le chapitre VI est un résumé et une conclusion des principaux résultats de cette étude. Enfin, des perspectives d'étude sont suggérées.

Conclusion

La multiplicité de phases intermétalliques connues pourrait laisser penser qu'il ne reste plus rien à découvrir dans ce domaine. Cependant, l'exemple de la famille « 1113 » présenté ici prouve le contraire. Malgré les 160 composés de cette famille déjà connus, un troisième sous-groupe ($A_{0.5}^{+2}M^{+1}M'^{+4}(Q^{2-})_3$) inconnu jusqu'à lors (cf. chapitre IV) ouvre la voie à de nouvelles expériences, en utilisant des éléments différents. Le lien établi ici entre le type de structure et les symétries des composés « 1113 » d'une part et le rapport des rayons des atomes A et M' d'autre part ouvre également la voie à un nouveau domaine d'études. Par exemple, l'utilisation du rapport $r(A^{2+})/r(M'^{3+/4+})$ comme unique variable pourrait permettre de cibler de manière spécifique un type de structure et de symétrie précis. Les *Extended Mooser Pearson plots* présenté dans le deuxième chapitre sont une autre voie permettant d'améliorer la prédiction de formation d'intermétalliques polaires d'une certaine structure.

$Ba_2FePnSe_5$ avec $Pn = Sb, Bi$ sont deux semiconducteurs très prometteurs, au regard de leurs propriétés physiques. La transformation de phase rapide entre l'état cristallin initial et un état amorphe par exposition à une pulsation laser (Chapitre IV) est fascinante. La question qui se pose ensuite concerne leur potentielle utilisation comme matériaux à changement de phase (PCMs). La suite de l'étude sera donc de faire grandir des couches minces de ces composés et d'étudier leurs propriétés de changement de phase. Cette partie sera faite en collaboration avec l'université de Singapour de Technologie et Design (SUTD). Une autre question qui reste ouverte concerne l'origine des anomalies observées dans les mesures de conductivité thermique et de constante diélectrique à la température de Néel. Afin de répondre à cette question, une première étape consiste à résoudre la structure cristalline et magnétique au-dessus et en-dessous de T_N .

La présence des motifs Cu_4Se_9 et la coexistence de Se_2^{2-} et de Se_3^{4-} linéaires et hypervalents sont probablement les découvertes les plus étonnantes de ce travail (Chapitre V). On peut alors se demander s'il existe d'autres composés contenant des motifs Cu_4Se_9 avec des atomes de Cu planaires, et également de potentielles liaisons Cu-Cu? Ce composé pourrait-il permettre d'améliorer la compréhension du domaine à l'interface de la chimie du solide classique et de la chimie des clusters ou de la chimie moléculaire?

Le composé BaBiTe₃ est également très intéressant, avec son réseau Te-Te hypervalent complexe à appréhender (Chapitre V). Cependant des analyses théoriques (COHP et ELF) suggèrent que le réseau peut très certainement être décrit comme une combinaison linéaire de groupes (Te¹⁻)₂ entrecroisés et de chaînes infinies de Te_n. Dans BaBiTe₃, les défauts natifs et les effets de bandes multiples jouent un rôle dans les propriétés thermoélectriques de transport. Ces résultats incitent à étudier à l'avenir plus en détail les intermétalliques polaires, avec une attention particulière portée aux propriétés thermoelectriques des composés à structure de bande complexe. L'étude présentée ici permet également d'insister sur l'importance et la puissance du concept de liaisons en résonance, qui aide à comprendre les liaisons chimiques dans les intermétalliques polaires hypervalents. Ceci a été vérifié à la fois pour les unités moléculaires comme Se₃⁴⁻ et pour les réseaux étendus Q-Q comme celui du composé BaBiTe₃.

Les mesures des propriétés physiques et l'étude des structures cristallines et de la nature des liaisons pour des chalcogénures polaires de structure complexe, connus ou découverts pendant cette thèse, a permis d'accéder à des résultats intéressants et inattendus. La richesse de cette famille de matériaux, tant sur le plan de la chimie que sur celui des propriétés physiques, est remarquable et extrêmement prometteur, et l'exploration plus poussée de la chimie et des propriétés physiques de composés de la branche des chalcogénures polaires réserve encore certainement de belles découvertes.

Abstract

This thesis has its focus on the chemistry and physical properties of normal valence and hypervalent polar chalcogenides (PCs). The motivation for this study lies in the synthesis of new compounds with complex crystal structures. It aims at understanding the relationship between crystal structure, chemical bonding and physical properties through experimental and theoretical analyses. PCs are of special interest since they are at the interface between metals and nonmetals. The chemistry at this interface is governed by the interplay between covalent, metallic and ionic bonding, which makes it interesting and challenging to understand the relationship between crystal structure and chemical bonding. The main reason for aiming at structural complexity is to target new materials with low thermal conductivities – a key requirement for efficient thermoelectric materials. Thermoelectrics are capable of converting waste heat into electricity, which is of considerable economic and environmental interest. Previous discoveries of efficient, chalcogenide-based thermoelectrics such as PbTe, Bi₂Te₃, CsBi₄Te₆ and superionic Cu_{2-x}Se motivated the exploratory search for new Cu- and Pn-chalcogenides (Pn = Sb, Bi) and to study related materials such as BaBiTe₃ (*cf.* Chapter V). One route towards complex crystal structures is to use a charge transfer from cations such as Sr or Ba to an anionic framework in order to create complex anionic, covalent networks (e.g. channels or layers) which can lead towards interesting physical properties. Stereoactive lone pairs can increase structural complexity through distortions of the coordination polyhedra, which is one reason for studying systems containing Pn atoms such as Sb and Bi. Probing the physical properties and studying the crystal structure and chemical bonding of both, new and known polar chalcogenides with complex crystal structures resulted in interesting new discoveries, i.e. new compounds and crystal structures as well as unexpected physical properties. The thesis is separated in normal valence compounds, which can be entirely described by classical two-center two-electron (*2c-2e*) bonds (i.e. where the electrons are fully localized) and those, which contain hypervalent bonds and networks in which the electrons are partially delocalized. It contains four main parts: the study of 1) A_{0.5}CuZrSe₃ and ACuYSe₃ (A = Sr, Ba) belonging to a family of compounds known as the “1113 family”, 2) Ba₂FePnSe₅ (Pn = Sb, Bi), 3) Ba₄Cu₈Se₁₃ and 4) BaBiTe_{3-x}Se_x (x = 0, 0.05, 1 and 3).

Acknowledgement

First of all I want to express my sincere gratitude to Franck Gascoin and David Berthebaud for the opportunity to work at the CRISMAT laboratory, for their constant support and advice and for all the great opportunities (conferences, collaborations etc...) they opened up for me during my PhD. Thanks to you I got to travel to many different places, try lobster for the first time and meet many great people who inspired me both personally and scientifically. It was a pleasure working with both of you!

I am also sincerely thankful to all members of my Jury for taking the time to critically evaluate my thesis.

I am also especially grateful to Olivier Perez, Sylvie Hebert and Denis Pelloquin for all their support during my thesis. I learned many many things from you – thank you!

A special “thank you” also goes to Prof. Jeffrey Snyder and Prof. Svilen Bobev for two excellent opportunities to work in their laboratories during my PhD. Your support and advice helped me tremendously over the past three years.

Thanks also to Geoffroy Hautier, Houria Kabbour, Michael Gaultois, Robert Simpson and Prof. Mercouri Kanatzidis for their support and advice. You all taught me many things and helped me reach a deeper understanding during my thesis.

Special thanks to all the PhD students and postdocs at the CRISMAT lab, the LCS lab and in Jeffs and Svilens lab who supported me so kindly and with whom I had great times - especially: Robin, Nami, Chantal, Tristan, Clarisse, Rodolphe, Alexandre, Fabien, Bruno, Clement, Saneyuki, Matthias, Shash, Riley, Stephen, Thomas, Jai, Julien, Guodong, Anh, Sam, Umut, Max, Dilla (and all those I might have forgotton).

I also thank Fabien Veillon, Stéphanie Gascoin, Jérôme Lecourt, Sophie Dufourd and everyone else at the CRISMAT lab who supported me over the past three years.

Special thanks to all my friends outside the lab who constantly support (and surprise) me – especially: Korbinian, Michael, Brad, Fanny, Ced, Maëlle, Julian, Juliana, Marine, Fabian, Maximilian, Fritz, Felix, Julius, Nadja, Jens.

A big “thank you” also goes to my family who always supports me no matter what I’m doing and where I’m going.

And last but not least I want to sincerely thank Lola for all her support, inspiration and for making me discover France. THANK YOU!

List of figures

FIG. I.1 PERIODIC TABLE OF THE ELEMENTS	22
FIG. I.2 BONDING SCHEME ILLUSTRATING 2C-2E BONDING AND HYPERVALENT 3C-4E BONDING	25
FIG. II.1 EXTENDED MOOSER-PEARSON PLOT FOR TERNARY AND QUATERNARY POLAR CHALCOGENIDES.....	35
FIG. II.2 EXTENDED MOOSER-PEARSON PLOT FOR TERNARY AND QUATERNARY POLAR CHALCOGENIDES - DETAILS	36
FIG. II.3 EXTENDED MOOSER-PEARSON PLOT FOR TERNARY AND QUATERNARY POLAR CHALCOGENIDES - DETAILS	37
FIG. III.1 PRINCIPLE OF MECHANICAL ALLOYING WHEN USING A PLANETARY MICRO MILL.....	41
FIG. III.2 SCHEMATIC PRINCIPLE OF THE SPARK PLASMA SINTERING METHOD	44
FIG. IV.1 PERSPECTIVE VIEW OF THE FIVE AMM'Q ₃ STRUCTURE TYPES FORMING LAYERED STRUCTURES.....	64
FIG. IV.2 PERSPECTIVE VIEW OF THE TWO AMM'Q ₃ STRUCTURE TYPES FORMING CHANNEL STRUCTURES	64
FIG. IV.3 CRYSTAL STRUCTURE OF A _{0.5} CuZrSe ₃ (A = SR, BA)	72
FIG. IV.4 CRYSTAL STRUCTURE OF A _{0.5} CuZrSe ₃ - DETAILS	72
FIG. IV.5 CRYSTAL STRUCTURE OF A _{0.5} CuZrSe ₃ - DETAILS	73
FIG. IV.6 SrCuYSe ₃ CRYSTAL STRUCTURE WITH COORDINATION ENVIRONMENTS OF SR AND BA.....	74
FIG. IV.7 CHANGES IN THE LATTICE PARAMETERS AND UNIT CELL VOLUME DEPENDING ON TRANSITION METAL AND CATION	75
FIG. IV.8 DIFFERENCES IN THE A ²⁺ ••• A ²⁺ INTERATOMIC DISTANCES BETWEEN BA _{0.5} CuZrSe ₃ AND ACuYSe ₃	76
FIG. IV.9 DIFFERENCES IN THE INTRALAYER TRANSITION METAL DISTANCES BETWEEN BA _{0.5} CuZrSe ₃ AND ACuYSe ₃	76
FIG. IV.10 RATIO BETWEEN THE CATION AND TRANSITION METAL/LANTHANUM IONIC RADII R(A ²⁺)/R(M ^{3+/4+})	78
FIG. IV.11 A•••Se (A = SR, BA), CU•••Se AND M'•••Se (M = ZR, Y) DISTANCE RANGES.	79
FIG. IV.12 CRYSTAL STRUCTURE OF BA ₂ FeSbSe ₅	86
FIG. IV.13 DISTORTED COORDINATION ENVIRONMENT OF PN = Sb AND Bi IN BA ₂ FePNSe ₅ (PN=Sb,Bi).....	87
FIG. IV.14 RIETVELD REFINEMENTS OF BA ₂ FePNSe ₅ DIFFRACTION PATTERNS	88
FIG. IV.15 ANTIFERROMAGNETIC CONFIGURATION USED FOR ALL SPIN-POLARIZED CALCULATIONS.	90
FIG. IV.16 BAND STRUCTURES (GGA) OF BA ₂ FePNSe ₅	91
FIG. IV.17 BAND STRUCTURES (GGA+U) OF BA ₂ FePNSe ₅	92
FIG. IV.18 PDOS (GGA) OF BA ₂ FePNSe ₅	94
FIG. IV.19 PDOS (GGA+U) OF BA ₂ FePNSe ₅	95
FIG. IV.20 ELECTRICAL RESISTIVITIES OF BA ₂ FePNSe ₅	96
FIG. IV.21 HIGH-TEMPERATURE THERMAL CONDUCTIVITIES OF BA ₂ FePNSe ₅	97
FIG. IV.22 LOW- AND HIGH-TEMPERATURE THERMAL CONDUCTIVITIES OF BA ₂ FeBiSe ₅	98
FIG. IV.23 LOW- AND HIGH-TEMPERATURE THERMAL CONDUCTIVITIES OF BA ₂ FeSbSe ₅	99
FIG. IV.24 SEM IMAGES AND PICTURE OF A SAMPLE WITH AN AMORPHOUS LAYER.	100
FIG. IV.25 ROOM TEMPERATURE XRD PATTERNS OF BA ₂ FeSbSe ₅ ILLUSTRATING SURFACE AMORPHIZATION	100
FIG. IV.26 HIGH-TEMPERATURE PXRD PATTERNS FOR BA ₂ FeSbSe ₅	101
FIG. IV.27 HRTEM IMAGE OF A BA ₂ FeSbSe ₅ CRYSTALLITE	102
FIG. IV.28 HRTEM IMAGES AND SAED PATTERNS OF A BA ₂ FeSbSe ₅ CRYSTALLITE.....	103
FIG. IV.29 THERMAL CONDUCTIVITY OF BA ₂ FeBiSe ₅ AT ROOM TEMPERATURE AS A FUNCTION OF LASER PULSES.....	104
FIG. IV.30 ROOM TEMPERATURE PXRD PATTERNS OF BA ₂ FeBiSe ₅ (SURFACE AFTER 0 AND 170 LASER PULSES).	105
FIG. IV.31 RESONANT BONDING SCHEME.	107
FIG. IV.32 MAGNETIC SUSCEPTIBILITY, DIELECTRIC PERMITTIVITY AND THERMAL CONDUCTIVITY OF BA ₂ FeSbSe ₅	110
FIG. IV.33 DIELECTRIC PERMITTIVITY (DIFFERENT FREQUENCIES) AND LOSSES OF BA ₂ FeSbSe ₅	111
FIG. IV.34 CAPACITANCE OF BA ₂ FeSbSe ₅ AS A FUNCTION OF MAGNETIC FIELD.....	112
FIG. V.1 (h0l)* AND (h1l)* PLANES OF BA ₄ Cu ₅ Se ₁₃ AND SCHEMATIC ILLUSTRATION OF THE STRUCTURAL MODEL.....	120

FIG. V.2 AVERAGE CRYSTAL STRUCTURE OF $\text{Ba}_4\text{Cu}_8\text{Se}_{13}$ OBTAINED FROM SINGLE CRYSTAL X-RAY DIFFRACTION.....	126
FIG. V.3 Cu_4Se_9 AND Se_3^{4-} UNITS IN $\text{Ba}_4\text{Cu}_8\text{Se}_{13}$, SEM IMAGE OF A SINGLE CRYSTAL AND COMPOSITIONAL MAPS	126
FIG. V.4 Cu_4Se_9 CLUSTER WITH A SLIGHTLY DISTORTED D_{4d} SYMMETRY.....	127
FIG. V.5 HAADF IMAGE + FOURIER TRANSFORM OF POLYCRYSTALLINE $\text{Ba}_4\text{Cu}_8\text{Se}_{13}$ TAKEN IN THE ZONE AXIS $[110]$	129
FIG. V.6 ENLARGEMENT OF A PART OF THE HAADF IMAGE SHOWN IN FIG.V.5 ILLUSTRATING NANOTWINNING.....	130
FIG. V.7 ENLARGEMENT OF LAYER 1 SHOWN IN FIG.V.6 ILLUSTRATING NANOTWINNING	131
FIG. V.8 $[110]$ PROJECTION OF THE $\text{Ba}_4\text{Cu}_8\text{Se}_{13}$ STRUCTURE ILLUSTRATING NANOTWINNING	132
FIG. V.9 BA1 AND BA2 ENVIRONMENTS IN THE $\text{Ba}_4\text{Cu}_8\text{Se}_{13}$ CRYSTAL STRUCTURE	133
FIG. V.10 CONFIRMATION OF THE STRUCTURAL MODEL OF $\text{Ba}_4\text{Cu}_8\text{Se}_{13}$ BY TRANSMISSION ELECTRON MICROSCOPY.....	135
FIG. V.11 ATOMIC PAIR DISTRIBUTION FUNCTION OF $\text{Ba}_4\text{Cu}_8\text{Se}_{13}$	136
FIG. V.12 LeBAIL REFINEMENT OF AN EXPERIMENTAL PXRD PATTERN RECORDED AFTER SINTERING $\text{Ba}_4\text{Cu}_8\text{Se}_{13}$	138
FIG. V.13 DSC SCAN, ELECTRICAL RESISTIVITY, THERMAL CONDUCTIVITY AND SEEBECK COEFFICIENT OF $\text{Ba}_4\text{Cu}_8\text{Se}_{13}$	140
FIG. V.14 CRYSTAL STRUCTURE OF BaBiTe_3	144
FIG. V.15 PREVIOUS AND NEW $\text{Te}\cdots\text{Te}$ BONDING SITUATIONS IN BaBiTe_3	145
FIG. V.16 RIETVELD REFINEMENTS OF EXPERIMENTAL DIFFRACTION PATTERNS OF $\text{BaBiTe}_{3-x}\text{Se}_x$ ($x=0,0.05$ AND 0.1).....	147
FIG. V.17 ILLUSTRATION OF PREFERENTIAL SITE SUBSTITUTION IN $\text{BaBiTe}_{2.9}\text{Se}_{0.1}$	147
FIG. V.18 EXPERIMENTAL EDS SPECTRA OF $\text{BaBiTe}_{3-x}\text{Se}_x$ ($x=0,0.05$ AND 0.1).....	148
FIG. V.19 ELECTRONIC STRUCTURE OF BaBiTe_3	150
FIG. V.20 COHP CURVES OF BaBiTe_3 CONTAINING BI-TE AND TE-TE INTERACTIONS + MO DIAGRAM OF BaBiTe_3	151
FIG. V.21 COHP CURVES SHOWING ALL BA-TE INTERACTIONS	153
FIG. V.22 OPTICAL BAND GAPS AND ABSORPTION SPECTRA (EXPERIMENTAL) + TAUC ANALYSIS.....	154
FIG. V.23 EXPLANANATION FOR THE TWO OPTICAL TRANSITIONS IN $\text{BaBiTe}_{3-x}\text{Se}_x$ ($x=0,0.05$ AND 0.1)..	155
FIG. V.24 ILLUSTRATION OF BAND CONVERGENCE IN $\text{BaBiTe}_{2.95}\text{Se}_{0.05}$	156
FIG. V.25 THERMOELECTRIC PROPERTIES OF $\text{BaBiTe}_{3-x}\text{Se}_x$ ($x = 0, 0.05, 0.1$).....	157
FIG. V.26 ILLUSTRATION OF MULTIBAND EFFECTS IN $\text{BaBiTe}_{3-x}\text{Se}_x$ ($x = 0, 0.05$)	160
FIG. V.27 FORMATION ENERGIES OF INTRINSIC DEFECTS IN BaBiTe_3	163
FIG. V.28 FORMATION ENERGIES OF EXTRINSIC DEFECTS IN BaBiTe_3	165

List of tables

TABLE I.1 EXAMPLES OF <i>Zintl</i> PHASES AND POLAR CHALCOGENIDES	23
TABLE II.1 OVERVIEW OVER ALL POLAR CHALCOGENIDES REPRESENTED IN FIG.II.1-3	38
TABLE III.1 SYNTHESIS CONDITIONS OF ALL POLYCRYSTALLINE SAMPLES MADE BY MECHANICAL ALLOYING.....	42
TABLE III.2 STARTING MATERIALS FOR ALL SYNTHESSES INCLUDING MECHANICAL ALLOYING AND SINGLE CRYSTAL GROWTH	43
TABLE III.3 EXPERIMENTAL AND THEORETICAL DENSITIES OF ALL SAMPLES	45
TABLE III.4 SYSTEMATIC ABSENCES FOR THE SPACE GROUPS <i>Pnma</i> AND <i>Cmcm</i>	47
TABLE IV.1 STRUCTURAL DETAILS OF THE AMM' Q_3 STRUCTURE TYPES FORMING LAYERED CRYSTAL STRUCTURES.....	66
TABLE IV.2 STRUCTURAL DETAILS OF THE $BAAGERS_3$ AND $BACULAS_3$ STRUCTURE TYPES FORMING CHANNEL STRUCTURES. ...	67
TABLE IV.3 GENERAL CRYSTALLOGRAPHIC INFORMATION FOR $A_{0.5}CuZrSe_3$ AND $ACuYSe_3$ ($A = Sr, Ba$).....	69
TABLE IV.4 ISOTROPIC DISPLACEMENT AND POSITIONAL PARAMETERS OF $A_{0.5}CuZrSe_3$ AND $ACuYSe_3$ ($A = Sr, Ba$).....	70
TABLE IV.5 SELECTED INTERATOMIC DISTANCES IN $A_{0.5}CuZrSe_3$ AND $ACuYSe_3$ ($A = Sr, Ba$).....	71
TABLE IV.6 CRYSTALLOGRAPHIC DATA FOR $BA_2FePnSe_5$ ($Pn = Sb, Bi$).	84
TABLE IV.7 THERMAL DISPLACEMENT AND POSITIONAL PARAMETERS FOR $BA_2FePnSe_5$ ($Pn = Sb, Bi$).....	85
TABLE IV.8 RIETVELD REFINEMENT RESULTS FOR $BA_2FePnSe_5$ ($Pn = Sb, Bi$).....	89
TABLE V.1 GENERAL CRYSTALLOGRAPHIC INFORMATION OF THE STRUCTURE SOLUTION OF $BA_4Cu_8Se_{13}$	122
TABLE V.2 EQUIVALENT ISOTROPIC DISPLACEMENT FACTORS AND POSITIONAL PARAMETERS OF $BA_4Cu_8Se_{13}$	123
TABLE V.3 SELECTED INTERATOMIC DISTANCES AND ANGLES IN $BA_4Cu_8Se_{13}$	124
TABLE V.4 THERMAL DISPLACEMENT PARAMETERS AND DIFFERENCES IN ATOMIC POSITIONS (LOCAL VS AVERAGE STRUCTURE)	136
TABLE V.5 LE BAIL REFINEMENT RESULTS OF AN EXPERIMENTAL PXRD PATTERN OF $BA_4Cu_8Se_{13}$	138
TABLE V.6 RIETVELD X-RAY REFINEMENT RESULTS FOR $BABiTe_{3-x}Se_x$ ($x = 0, 0.05, 0.1$).....	148
TABLE V.7 EXPERIMENTAL COMPOSITIONS OF $BABiTe_{3-x}Se_x$ ($x = 0, 0.05, 0.1$).....	149
TABLE V.8 SPEED OF SOUND DATA, DEBYE TEMPERATURE AND FREQUENCIES OF $BABiTe_3$ AND $BABiSe_3$	159

Table of contents

I. Introduction.....	19
1. Polar chalcogenides – between covalent and ionic bonding.....	21
2. Classical vs. hypervalent bonding	24
3. The concept of resonant bonding in solids	26
4. Polychalcogenides	27
5. Chalcogenides and their applications.....	28
II. A classification of normal valence polar chalcogenides	31
1. Introduction.....	33
2. Extended Mooser-Pearson plots for ternary and quaternary polar chalcogenides	33
III. Experimental and computational details	39
1. Mechanical alloying (ball milling).....	41
2. Spark Plasma Sintering	43
3. Single crystal growth	45
4. Single crystal structure determination	46
5. Powder X-ray diffraction (PXR).....	47
6. Electron microscopy and energy dispersive X-ray spectroscopy	48
7. Thermoelectric characterization.....	49
8. Magnetic measurements	50
9. Dielectric measurements.....	50
10. X-ray Pair Distribution Function (XPDF) analysis	51
11. Differential scanning calorimetry	52
12. Optical absorption measurements	52
13. Speed of sound measurements	53
14. Modelling high-temperature thermoelectric transport data	54
15. Electronic structure and defect calculations	56
16. Calculating the optical absorption coefficient	57

IV. Normal valence Cu-(I)- and Pn-chalcogenides with Pn = Sb, Bi	59
1. Overview.....	61
2. Polar chalcogenides with classical two-center two-electron ($2c-2e$) bonds.....	62
2.1 $A_{0.5}CuZrSe_3$ and $ACuYSe_3$ (A = Sr, Ba) – four new quaternary copper-(I)-selenides	62
2.1.1 Introduction	63
2.1.2 Results and Discussion	68
2.1.2.1 Crystal structures obtained by single crystal X-ray diffraction	68
2.1.2.2 Influence of the $r(A^{2+})/r(M^{3+/4+})$ ratio on the structure type and symmetry ..	77
2.1.3 Conclusion.....	80
3. Polar chalcogenides with stereoactive lone pairs and potential resonant bonding	81
3.1 $Ba_2FePnSe_5$ (Pn = Sb, Bi).....	81
3.1.1 Introduction	81
3.1.2 Results and Discussion	83
3.1.2.1 Crystal structure	83
3.1.2.2 Electronic structure and electrical resistivity	90
3.1.2.3 Thermal conductivity	97
3.1.2.4 Irradiation induced phase changes between crystalline and amorphous $Ba_2FePnSe_5$ (Pn = Sb, Bi)	99
3.1.2.5 Potential resonant bonding in $Ba_2FePnSe_5$ (Pn = Sb, Bi)	106
3.1.2.6 $Ba_2FeSbSe_5$: striction driven changes in the dielectric permittivity?.....	108
3.1.3 Conclusion.....	112

V. Hypervalent Cu-(I)- and Pn-chalcogenides with Pn = Sb, Bi – from fully localised to partially delocalised electrons	115
1. Overview.....	117
2. Polar chalcogenides with hypervalent three-center four-electron (<i>3c-4e</i>) bonds.....	118
2.1 Ba ₄ Cu ₈ Se ₁₃ – a new ternary copper-(I)-selenide.....	118
2.1.1 Introduction	118
2.1.2 Results and Discussion	119
2.1.2.1 Average crystal structure obtained by single crystal X-ray diffraction	119
2.1.2.2 Nanotwinning, structural modulation and real structure effects	128
2.1.2.3 Confirmation of the structural model by transmission electron microscopy	134
2.1.2.4 Local crystal structure	135
2.1.2.5 Transport properties	137
2.1.3 Conclusion.....	140
3. Polar chalcogenides with an extended hypervalent network	142
3.1 BaBiTe _{3-x} Se _x (x = 0, 0.05, 0.1 and 3).....	142
3.1.1 Introduction	142
3.1.2 Results and Discussion	144
3.1.2.1 Crystal structure and hypervalent Te-Te bonding.....	144
3.1.2.2 Preferential site substitution of Se on the Te ₄ and Te ₅ sites.....	146
3.1.2.3 Optical properties, electronic structure and its orbital contributions	149
3.1.2.4 Band convergence and an explanation for the two optical transitions.....	154
3.1.2.5 Thermoelectric properties	157
3.1.2.6 Multiband effects in the thermoelectric transport properties	160
3.1.2.7 Defect chemistry	162
3.1.3 Conclusion.....	165
VI. Conclusion and Outlook	167
VII. Bibliography.....	171
VIII. Publications	185

I. Introduction

1. Polar chalcogenides – between covalent and ionic bonding

This thesis has its focus on the chemistry and physical properties of polar chalcogenides (PCs), which belong to the group of polar intermetallics and hence to the field of intermetallic chemistry. There is a clear distinction between geometric and electronic compounds within the field of intermetallic chemistry. The former are described using geometric considerations, i.e. the closed packing of spheres (e.g. hexagonal closed packing (hcp) and cubic closed packing (fcc)), which is mainly governed by the size of the atoms. Examples are *Laves phases* (e.g. MgZn₂, MgCu₂, MgNi₂), *Frank-Kasper phases*^[1] and *Nowotny phases*^[2,3] (e.g. Mn₁₁Si₁₉^[4]). The crystal structure of electronic compounds such as the *Hume-Rothery phases* (e.g. β-Brass, γ-Brass and ε-phases) on the other hand is mainly determined by electronic factors such as the valence electron concentration.^[5] It was long believed that all intermetallic compounds are solely based on the classical concept of metallic bonding and that no stoichiometric compounds exist within intermetallic phases.^[6-8] Eduard Zintl and his research stood in clear contrast with these beliefs since for him ionic and covalent bonding clearly played a role in some intermetallics and he introduced chemical valences into the field of intermetallic chemistry.^[9,10] The so-called *Zintl phases* are a subgroup within the group of polar intermetallics and some PCs can also be interpreted as *Zintl phases*. The most classical *Zintl phase* is NaTl, where one electron is transferred from Na to Tl (i.e. Na⁺Tl⁻) resulting in a diamond-type substructure formed by Tl. This is known as the concept of pseudo-elements introduced by Klemm, which resulted in an extension of the *Zintl concept* to the *Zintl-Klemm concept*.^[11] Fig. I.1 shows a schematic periodic table, which illustrates the elements used in the *Zintl Chemistry* (purple) and those, which were used in this study and are part of the *Zintl Chemistry* (blue). All elements in black are elements, which do not fall into the field of intermetallic chemistry or which are neither part of the *Zintl Chemistry* nor this thesis. Table I.1 contains examples of *Zintl phases* and of polar chalcogenides, which are relevant for this thesis.

H										He	
Li	Be					B	C	N	O	F	Ne
Na	Mg					Al	Si	P	S	Cl	Ar
K	Ca	TM				Ga	Ge	As	Se	Br	Kr
Rb	Sr					In	Sn	Sb	Te	I	Xe
Cs	Ba	L				Tl	Pb	Bi	Po	At	Rn
Fr	Ra	A									

- Zintl chemistry
- Zintl chemistry + elements used in this thesis
- elements, which fall clearly outside of intermetallic chemistry or which are neither part of this thesis nor of the Zintl chemistry

Fig. I.1 Schematic periodic table showing elements used in the Zintl chemistry and in this thesis as well as elements, which are neither part of the Zintl chemistry nor this thesis.

Polar chalcogenides are at the interface between metals and nonmetals. Nowadays it is known, that the chemistry at this interface is governed by the interplay between covalent, metallic and ionic bonding, which makes it interesting and challenging to understand the relationship between crystal structure and chemical bonding. The extent of electron localization, i.e. the polarity of an intermetallic compound and hence the type of chemical bonding can be influenced by the electronegativity difference between the elements or between the electropositive and electronegative subunits of the crystal structure. Polar chalcogenides fall into a category of compounds, where covalent and ionic bonding can be present in the same compound. Mooser and Pearson were the first to classify the crystal structures of normal valence AB compounds, which have both covalent and ionic character.^[12] So far, there is no such classification for ternary or quaternary PCs since their crystal structures are far more complex than those of normal valence AB compounds and the term “polar chalcogenides” has only recently been introduced.^[13] Within the frame of this thesis, PCs can be understood as compounds containing a cation from group 1, 2 or 13 and an anionic framework, which contains chalcogen atoms such as S, Se and Te.

Table I.1Examples of *Zintl* phases and polar chalcogenides

<i>Zintl</i> phases	Polar chalcogenides
Li ₃ Bi	Ba _{0.5} CuZrSe ₃
Na ₃ As	BaCuYSe ₃
LiAl	Sr _{0.5} CuZrSe ₃
LiTl	SrCuYSe ₃
LiAlSi	SrCuLuSe ₃
NaAlSi	SrCuGdSe ₃
BaGe ₂ As ₂	SrCuPrSe ₃
KSnSb	SrCuCeSe ₃
CaGe	SrCuLaSe ₃
AlB ₂	Ba ₂ FeSbSe ₅
CaIn ₂	Ba ₂ FeBiSe ₅
Ni ₂ In	Ba ₂ FeSbS ₅
LiGaGe	Ba ₂ FeBiS ₅
CaAl ₂ Si ₂	Ba ₂ GaSbTe ₅
CaAl ₄	Ba ₂ GaBiTe ₅
Ba ₄ Al ₅	Ba ₂ GaSbSe ₅
Ba ₃ Al ₅	Ba ₂ GaBiSe ₅
CaAl ₂	Ba ₂ InSbTe ₅
BaCu ₅ Al ₈	Ba _{0.5} Cr ₅ Se ₈
LaAl ₃	TlV ₅ Se ₈
TmAl ₃	TlCr ₅ Se ₈
NaTl	TlTi ₅ Se ₈
BaCuAs	TlV ₅ S ₈
KZnP	KCr ₅ S ₈
LiZnSb	RbCr ₅ S ₈
LiZnBi	CsCr ₅ S ₈
LiGaGe	Ba _{0.5} Cr ₅ S ₈
SrZnSi	InTi ₅ S ₈
CaCuBi	InCr ₅ S ₈
SrIn ₂	RbCr ₅ Se ₈
GdCuSn	CsCr ₅ Se ₈
GdCuPb	TlCr ₅ Te ₈

In chapter II, a more thorough and general classification of ternary and quaternary PCs is discussed. It is based on their average principal quantum number of the valence shell of the atoms (which is a measure of their metallicity) and the electronegativity difference (ΔEN) between the cation and the anionic framework, i.e. the polarity of a polar chalcogenide. The polarity of PCs is what results in a charge transfer from the cation to the anionic framework. This charge transfer is characteristic for all PCs and the fact that the cation usually plays no significant role in their covalent structure makes the chemistry of polar chalcogenides related to the *Zintl* chemistry^[14], i.e. the same electron counting rules can be applied to some PCs (e.g. $Ba_4Cu_8Se_{13}$ and all compounds in chapter IV). However, none of the compounds presented in chapter IV and V are *Zintl phases* in the original sense. The original *Zintl* concept is based on a complete charge transfer between an electropositive group 1 or 2 metal (A) and an electronegative main group metal (X). The *Zintl* border was originally defined between group 13 and 14 elements and at first *Zintl phases* did not contain any transition metal or rare-earth elements.^[15] The charge transfer between A and X results in a noble gas configuration of both and a closed shell configuration. As a consequence, *Zintl phases* are charge balanced semiconductors and diamagnetic. Nesper proposed that *Zintl* compounds show the characteristics of normal valence compounds, i.e. they are line compounds, all X-X bonds are two-center two-electron ($2c-2e$) bonds, the octet rule is fulfilled for A and X, the 8-N rule can be applied, they are charge balanced and diamagnetic. Throughout this thesis, a variety of new and known polar chalcogenides are presented, where covalent and ionic bonding coexists and where it is debatable of whether or not these compounds belong to the *Zintl* family. The thesis is separated in normal valence compounds, which can be entirely described by classical two-center two-electron ($2c-2e$) bonds (i.e. where the electrons are fully localized) and those, which contain hypervalent bonds and networks in which the electrons are partially delocalized.

2. Classical vs. hypervalent bonding

Normal valence compounds are compounds where the covalent part of the structure can be fully described by classical two-center two-electron ($2c-2e$) bonds without violating the octet rule. This is not the case for the compounds presented in chapter V, where crystal structure, chemical bonding and physical properties of $Ba_4Cu_8Se_{13}$ and $BaBiTe_3$ (including Se substituted variants) are discussed.

These compounds contain Q-Q (Q = Se, Te) bonds or networks - both classical and hypervalent, i.e. the octet rule is violated if only $2c-2e$ bonds are used to describe the chemical bonding in those compounds. The concept of hypervalent bonding was first introduced by Musher in 1969^[16] for molecules and ions formed by group 15-18 elements in order to describe any valences higher than their lowest, stable one (i.e. 3, 2, 1 and 0, respectively). Musher's description involved doubly-occupied lone-pair orbitals, which form hypervalent bonds allowing the description of molecules violating the octet rule (e.g. PCl_5) by using classical $2c-2e$ bonds and the concept of octet expansion (i.e. more than 4 pairs of electrons in the Lewis formula). However, the debate on how to rationalize bonding in these molecules goes way back to Lewis^[17] and Langmuir^[18] and the question of whether the octet rule or the $2c-2e$ bond should be used to describe hypervalent species since both criteria cannot be fulfilled at the same time. If the former is used rigorously, then hypervalent bonds have to be assumed to be ionic rather than covalent. Hence, it has to be kept in mind that for hypervalent polar chalcogenides there is already a competition between ionic and covalent bonding within the hypervalent bonds. Before Musher introduced the term "hypervalent", there were already studies (e.g. those by Hach et al.^[19] and Pimentel et al.^[20]), where the 3-center 4-electron ($3c-4e$) bond model was used to describe the bonding in the I_3^- and I_5^- molecules, which also violate the octet rule if described only by classical $2c-2e$ bonds. Fig. I.2 illustrates the difference between classical $2c-2e$ and hypervalent $3c-4e$ bonding as well as the chemical bonding in the I_3^- and I_5^- molecules.

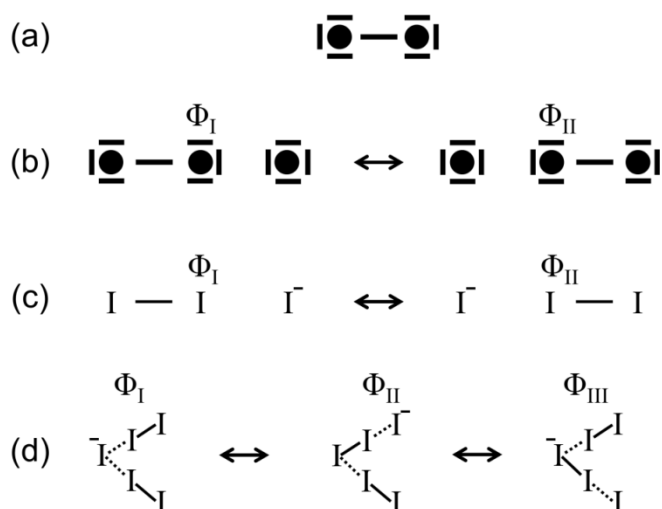


Fig. I.2 a) classical $2c-2e$ bonding scheme, b) hypervalent $3c-4e$ bonding scheme, c) chemical bonding in the I_3^- molecule and d) chemical bonding in the I_5^- molecule; Φ_I , Φ_{II} and Φ_{III} correspond to the resonating structures.

The *3c-4e* model is based on the concept of resonance between different energetically degenerate molecular structures. In the next section, a short introduction to the concept of resonance and resonant bonding in solids is given. The *3c-4e* bond model considers both, the covalent and ionic character of the hypervalent bonds and it is by now accepted as a valid hypervalent bond model, which is in accord with the octet rule. Other descriptions such as the two-center one-electron bond model proposed by Sudge^[21] were not accepted mainly because of the simultaneous development of quantitative MO calculations, which mostly confirmed the *3c-4e* bond model proposed by Rundle and Pimentel. Later on, Papoian and Hoffmann extended the concept of hypervalent bonding to solids focusing on electron-rich intermetallic compounds in order to rationalize nonclassical geometries such as linear chains and square nets in various Sb phases.^[22] The authors developed counting rules for these nonclassical phases, which are based on the *Zintl-Klemm* electron counting concept, which helps rationalizing hypervalent intermetallic compounds, where a complete charge transfer between the cation and the anionic framework can be assumed. In chapter V the *Zintl-Klemm* concept and hypervalent bond models (based on the concept of resonance) are used to rationalize the crystal structure of Ba₄Cu₈Se₁₃ and BaBiTe₃.

3. The concept of resonant bonding in solids

The concept of resonant bonding goes back to Heisenberg, who introduced resonance into the field of quantum mechanics, where any structure of a system is described in form of a wave function Ψ .^[23] If there are several structures (Φ_I , Φ_{II} , Φ_{III} etc.) in resonance with each other, as it is the case in the I_3^- and I_5^- molecules, the structure can be described as a linear combination of these resonating structures according to (I.1), where α , β or c_i are obtained by minimizing the energy of the system. For the I_3^- and I_5^- molecules, a graphical representation of I.1 is shown in Fig. I.2. α , β or c_i are weighting factors representing the contribution of each resonating structure to Ψ .

$$\psi = \alpha\phi_I + \beta\phi_{II} + \dots = \sum_{i=1}^n c_i\phi_i \quad (\text{I.1})$$

The driving force of resonant bonding is that the binding energy of the resonant system is larger compared to each resonating structure.

In molecular chemistry the concept of resonance turned out to be extremely useful to describe the resonance of a molecule among several valence-bond structures^[8], especially if hypervalent molecules want to be described without violating the octet (*cf.* section *Classical vs. hypervalent bonding* and especially Fig. I.2 c) and d). In 1973, Lucovsky and White extended the concept of resonant bonding to solids in order to explain differences between the properties of amorphous and crystalline solids with special focus on group VI elements and IV-VI semiconductors (e.g. PbTe, one of the most efficient thermoelectric materials).^[24] In 2008 and 2016 the concept was picked up by Shportko et al. and Lee et al. who suggested that resonant bonding is the underlying phase change mechanism in phase change materials (PCMs) and the origin of the low lattice thermal conductivity of rocksalt-type IV-VI semiconductors.^[25,26] Hence, there is renewed interest in resonant bonding in solids and it might help understanding physical properties such as phase-change or thermoelectric properties. In chapter *V* the concept of resonance is used to rationalize the crystal structure of BaBiTe₃ and Ba₄Cu₈Se₁₃ and in chapter *IV* a possible resonant bonding situation in Ba₂FePnSe₅ (Pn = Sb, Bi) is discussed as the potential origin for their phase change properties.

4. Polychalcogenides

Chapter *V* has its focus on compounds with Q-Q (Q = Se, Te) bonds resulting in both molecular units (e.g. Se₃⁴⁻ in Ba₄Cu₈Se₁₃) and extended chalcogen networks (e.g. in BaBiTe₃). All compounds discussed in chapter *V* belong to the family of polychalcogenides, i.e. compounds containing Q-Q bonds. The structural diversity within this family and the number of different polyanionic fragments is striking.^[27-30] Examples are Se_n⁴⁻ (n = 3-5), Se_n²⁻ (n = 9-11) and Se₁₆⁴⁻ for the selenides and Te_n²⁻ (n = 2-6, 8, 12, 13), Te₅⁴⁻, Te₇⁴⁻ and Te₆³⁻ for the tellurides. One can distinguish between molecular Q-Q and extended Q-Q fragments (“polymer-like”). One factor determining the size of the fragment is the number of electrons transferred to the chalcogen atom, i.e. small, molecular fragments are rather electron-rich. In tellurides infinite three-, two-, and one-dimensional anionic networks as well as isolated anions were discovered, while selenides tend to form rather molecular units than extended Se-Se networks. One reason for this trend is that tellurides are capable of forming intermolecular interactions (secondary bonding, i.e. closed shell interactions of p-block elements with lone pairs), which are stabilized by electrostatic and covalent contributions.^[31] Such interactions are apparently absent in selenides and sulfides.^[28]

The chemistry of polychalcogenides, especially within the anionic part of their crystal structure is determined by the polarity and the charge transfer (*Zintl-Klemm* concept) between cation and anionic network.

5. Chalcogenides and their applications

Why study the chemistry and physical properties of polar chalcogenides? Chalcogenide-based materials (in amorphous, crystalline or nanocrystalline form) show a variety of interesting physical properties (e.g. semiconducting behavior or phase change properties, i.e. rapid changes between the amorphous and crystalline phase upon external radiation accompanied by a severe change in optical properties and resistivity). Such physical properties led to a number of valuable technological applications. Here only a brief overview over some chalcogenide applications is given with special focus on PCMs and thermoelectrics (i.e. materials to convert waste heat into electricity). In chapter *III*, *IV* and *V* more details concerning PCMs and thermoelectrics are given. Chalcogenide-based applications range from optical fibers, electrochemical sensing, imaging and detection, photovoltaics and infrared detectors to thermoelectric applications and data storage devices such as non-volatile electronic memories (Phase Change Random Access Memory = PCRAM).^[32] Many oxides are multiferroics, which are promising candidates for developing microelectronics and spintronics. The most established phase change material is $\text{Ge}_2\text{Sb}_2\text{Te}_5$, which belongs to a class of materials called GST, i.e. compounds belonging to the ternary system Ge-Sb-Te.^[33-35] Data storage applications (where PCMs are used) and thermoelectric applications both require materials with low thermal conductivities. This is one of the reasons why Oeckler et al. proposed that PCMs are promising thermoelectrics.^[36] Subsequent research efforts showed that GST-based materials are indeed promising thermoelectric materials.^[37-38] Hence, the search for new thermoelectric materials with low thermal conductivities (the original goal of this thesis) can result in the discovery of new potential PCMs (demonstrated in chapter *IV*) and vice versa. The efficiency of a thermoelectric material is defined by the thermoelectric figure of merit zT , where S , ρ , κ and T correspond to the Seebeck coefficient, electrical resistivity, thermal conductivity and temperature.

$$zT = \frac{S^2}{\rho\kappa} T \quad (\text{I.2})$$

Industrial applications of thermoelectric materials can be considered for $zT > 1$ if only the efficiency of a single material is taken into account. The two most prominent examples of successful chalcogenide-based thermoelectrics are PbTe and Bi₂Te₃.^[39-42] Recent studies on GST based materials revealed that some of them also show remarkable zT s. Examples are GST containing skutterudite and cobalt germanide precipitates with zT s of 1.4 and 2 at 450 °C.^[38,43] A very promising polar chalcogenide with a high thermoelectric efficiency is CsBi₄Te₆ ($zT_{\text{max}} \sim 0.8$ at 225 K).^[44] The discovery of CsBi₄Te₆ and its promising thermoelectric properties is one of the motivations to look for new polar *Pn*-chalcogenides (*Pn* = Sb, Bi) as potential thermoelectrics and to study similar materials such as BaBiTe₃ (*cf.* chapter V). Another promising class of thermoelectric materials are copper chalcogenides such as Cu_{2-x}Se ($zT \sim 1.5$ at 1000 K), where highly disordered copper ions result in a liquid-like mobility of the ions.^[45] The recent interest in superionic thermoelectrics such as Cu_{2-x}Se motivated the exploratory search for new copper chalcogenides (*cf.* chapter IV and V).

Many of the above mentioned physical properties are inherently connected to the crystal structure and in the case of materials with low thermal conductivities to structural complexity. The main focus of this thesis is on the study of new and known polar chalcogenides with complex crystal structures aiming at understanding their crystal structures, chemical bonding and physical properties. One route towards complex crystal structures is to use the previously described charge transfer from cations such as Sr or Ba to an anionic framework in order to create complex anionic, covalent networks (e.g. channels or layers) which can lead towards interesting physical properties such as low thermal conductivities. Stereoactive lone pairs can increase the structural complexity through distortions of the coordination polyhedra, which motivated the study of systems containing *Pn* atoms such as Sb and Bi. Probing the physical properties and studying the crystal structure and chemical bonding of both, new and known polar chalcogenides with complex crystal structures may then result in interesting new discoveries, i.e. new crystal structures and unexpected physical properties.

II. A classification of normal valence polar chalcogenides

1. Introduction

Up to now there is no classification of ternary or quaternary polar chalcogenides, which helps understanding and predicting their crystal structures and to get an idea of the flexibility of a certain crystal structure towards ion exchange. In this chapter such a classification is discussed for normal valence polar chalcogenides. It allows to quantify the polarity and metallicity of ternary and quaternary chalcogenides and to compare them to those of ionic compounds such as NaCl and CsCl. The classification presented in this chapter can also be applied to normal valence *Zintl* compounds with isolated cations and a covalent anionic network, which makes it a powerful tool to create 2D maps of different structure types reflecting their polarity, metallicity and their flexibility towards ion exchange and it may help to rationally access certain structure types.

2. Extended Mooser-Pearson plots for ternary and quaternary polar chalcogenides

The classification of normal valence polar chalcogenides, which is presented here, is based on the work of Mooser and Pearson from 1959.^[12] Their pioneering work allows a classification of the crystal structures of normal valence A_iX_j ($i, j = 1, 2, 3$) compounds and it is based on two parameters: the average principal quantum number \bar{n} and the electronegativity difference between the cation and the anion (Δx). The former is defined according to (II.1) and it is a measure for how directional chemical bonds are.^[46]

$$\bar{n} = \frac{\sum c_i n_i}{\sum c_i} \quad (\text{II.1})$$

n_i and c_i correspond to the principal quantum number of the valence electrons and the number of atoms per formula unit of the atom type i . The larger \bar{n} the less directional the bonds are, i.e. an increase in \bar{n} signifies an increase in metallicity. Mooser and Pearson defined Δx as the difference between the anion and cation electronegativities defined by Gordy and Thomas in 1956.^[47]

$$\Delta x = |x_{anion} - x_{cation}| \quad (\text{II.2})$$

Here, a new parameter ΔEN is defined (*cf.* II.3), which corresponds to the difference between the average electronegativity of the anionic network and the electronegativity of a cation, which has no covalent bonds to the anionic network

$$\Delta EN = |\bar{x}_{anionic\ network} - x_{cation}| \quad (II.3)$$

$\bar{x}_{anionic\ network}$ is defined as:

$$\bar{x}_{anionic\ network} = \frac{\sum c_i x_i}{\sum c_i} \quad (II.4)$$

x_i and c_i correspond to the electronegativity of each element in the anionic network and the number of atoms (in the anionic network) per formula unit of the atom type i . The former were taken from the work of Gordy and Thomas^[47] in order to make the results comparable to those obtained by Mooser and Pearson. $Ba_2FeBiSe_5$ for example has an average principal quantum number of $(2 \times 6 + 4 + 6 + 5 \times 4) / 9 = 4.67$ and its anionic framework has an average electronegativity of $(1.8 + 1.8 + 5 \times 2.4) / 7 = 2.23$. From these values one can calculate a ΔEN of $2.23 - 0.9 = 1.33$. All results of the “extended Mooser-Pearson plots are summarized in Fig. II.1-3. The main focus lies on structure types, which are relevant for this thesis and on those, where many compounds crystallize in the same or similar structure types. This thesis contains four studies involving compounds belonging to the “1113” family (e.g. $KCuZrSe_3$) and the “2115” family (e.g. $Ba_2FeSbSe_5$), as well as $Ba_4Cu_8Se_{13}$ and $BaBiTe_3$ and its Se substituted variants. Details can be found within the corresponding chapters IV and V. However, extended Mooser-Pearson plots can only be used for normal valence compounds, where the oxidation state of the elements is well defined since the electronegativity of each element depends on its oxidation state.^[47] This is why Fig. II.1-3 only contain compounds belonging to the 1113 and 2115 families since for $Ba_4Cu_8Se_{13}$ and $BaBiTe_3$ no definitive formal oxidation state can be assigned to Se and Te. Fig. II.1-3 also include compounds belonging to the pseudo-hollandite family or “158” family. Examples of compounds belonging to this family are TlV_5Se_8 , $TlTi_5Se_8$ and $TlCr_5Se_8$.^[48] The reason for including compounds of this family is that it contains many compounds with different cations crystallizing in the same or similar structure types, i.e. it is a good example where extended Mooser-Pearson plots can be used to deduce trends in polarity and metallicity with respect to the type of cation and chalcogen atom.

Table II.1 contains all compounds represented in Fig. II-3 with their corresponding values for \bar{n} and ΔEN . Fig. II.1 shows a general comparison of polar chalcogenides with group 13 cations such as Tl and In, polar chalcogenides containing alkaline or alkaline-earth cations and purely ionic compounds such as CsCl and NaCl.

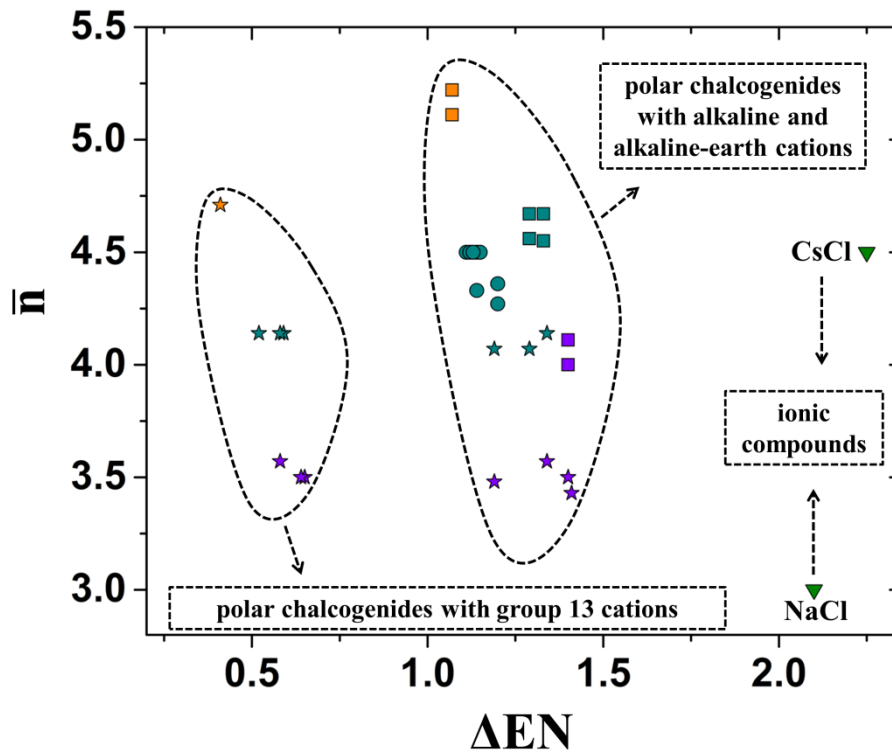


Fig. II.1 Extended Mooser-Pearson plot for ternary and quaternary polar chalcogenides belonging to the 158 (e.g. TlV_5Se_8), 1113 (e.g. $KCuZrSe_3$) and 2115 (e.g. $Ba_2FeSbSe_5$) family and for the purely ionic compounds CsCl and NaCl; asterisks: 158 compounds, squares: 2115 compounds, circles: 1113 compounds; purple: sulfides, blue: selenides, yellow: tellurides. This plot shows the effect of the cation on the polarity and the effect of the chalcogen atom on the metallicity of polar chalcogenides and it allow the comparison of PCs to purely ionic compounds such as CsCl and NaCl.

Fig. II.1 shows that polar chalcogenides are less ionic (or polar) than CsCl and NaCl and that the polarity strongly depends on the cation in the structure. The polarity decreases logically from polar chalcogenides with alkaline and alkaline-earth cations to those with group 13 cations. ΔEN can also be interpreted as a measure for the charge transfer from the cation to the anionic network and it reflects the extent of charge localization. Hence, “normal” chalcogenides (i.e. those containing only elements of similar electronegativity) will appear close to $\Delta EN = 0$. Fig. II.2 gives a more detailed picture of the information contained in extended Mooser-Pearson plots.

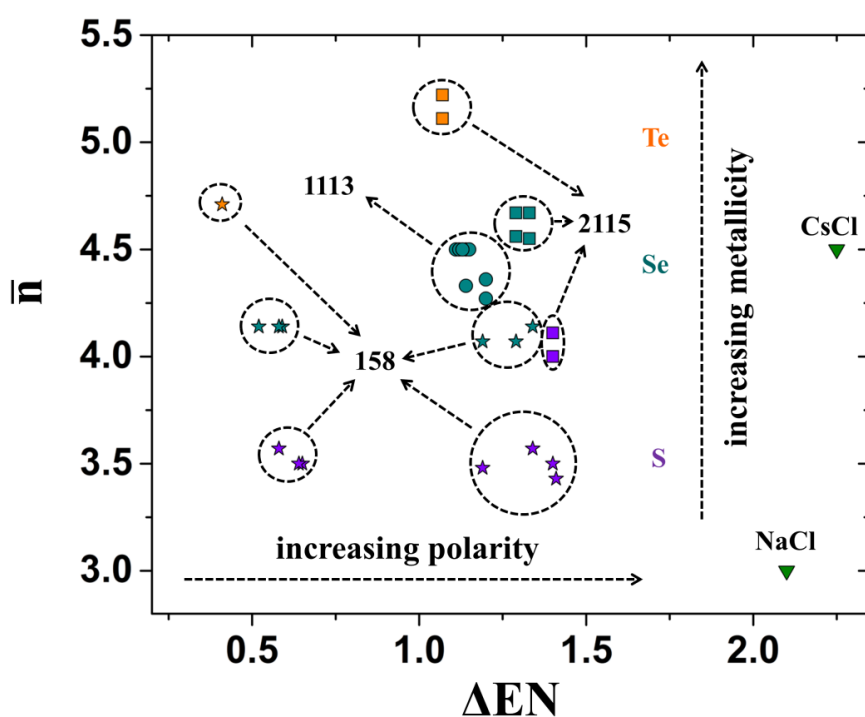


Fig. II.2 Extended Mooser-Pearson plot for ternary and quaternary polar chalcogenides belonging to the 158 (e.g. TlV_5Se_8), 1113 (e.g. KCuZrSe_3) and 2115 (e.g. $\text{Ba}_2\text{FeSbSe}_5$) family and for the purely ionic compounds CsCl and NaCl; asterisks: 158 compounds, squares: 2115 compounds, circles: 1113 compounds; purple: sulfides, blue: selenides, yellow: tellurides. This plot shows that the 158 family is very flexible towards ion exchange and that compounds with the same chalcogen atom and cation fall in the same region of the Mooser-Pearson plot.

Extended Mooser-Pearson plots not only reflect trends in polarity depending on the cation, but also trends in metallicity depending on the chalcogen atom (S, Se and Te). Logically, the metallicity increases going from the sulfides to the tellurides within the same family of compounds. The broader the data points are scattered within one structure type the more flexible a structure is towards ion exchange, i.e. the higher are the chances to obtain the same structure type if changing the cation and/or the chalcogen atom. The 158 family for example is highly flexible and compounds with a large variety of different cations (e.g. Tl, In, Ba, Sr, K, Rb, Cs) and chalcogen atoms (S, Se and Te) can be obtained. Fig. II.3 gives a more detailed picture of the effect of the cation on the polarity of compounds belonging to the 158 family. It shows that extended Mooser-Pearson plots can also resolve more subtle changes in the polarity, e. g. when changing the cation from Tl to In or from Ba to K, Rb and Cs. Extended Mooser-Pearson plots are not only applicable to polar chalcogenides, but to any compound with ionic bonding between the cation and a covalent, anionic framework and they might be helpful for understanding structural changes upon ion exchange and to specifically

target certain structure types. It is also imaginable to correlate these plots to the band gap since it depends on the polarity (i.e. ΔEN). Such a correlation could help to systematically find narrow band gap semiconductors, which are ideal for thermoelectric applications or insulators with gaps in the visible energy spectrum needed for optical applications. Even targeting materials with a more or less specific band gap could be possible, which could enable “application maps” by plotting e.g. ΔEN vs. type of application or band gap (sorted by the required band gap). Such plots could be valuable in form of a database comparable to e.g. The Materials Project.^[49]

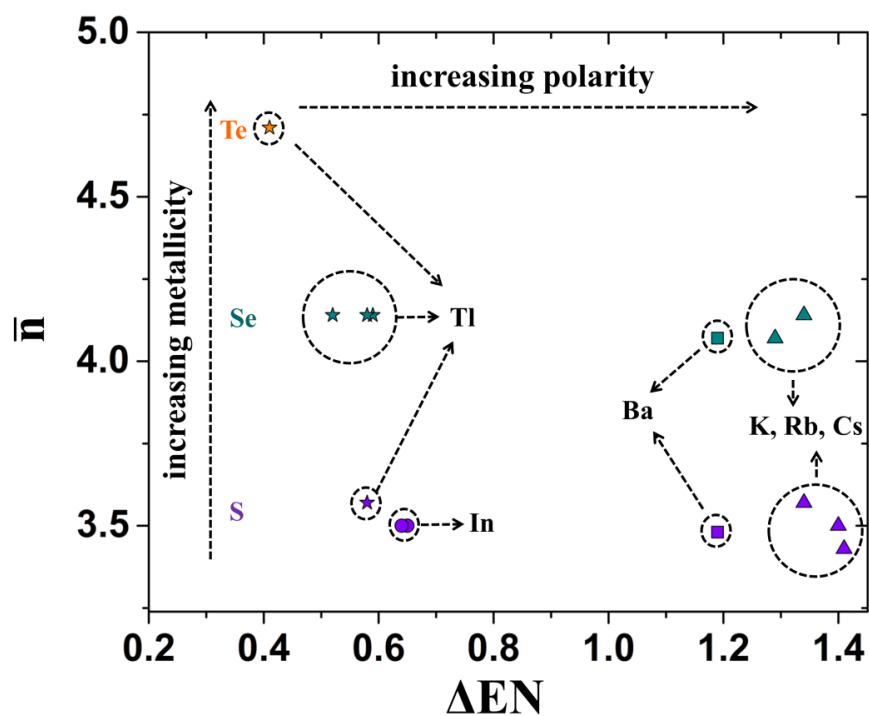


Fig. II.3 Extended Mooser-Pearson plot for ternary and quaternary polar chalcogenides belonging to the 158 (e.g. TlV_5Se_8) family; asterisks: Tl as the cation, circles: In as the cation, squares: Ba as the cation, triangles: K, Rb and Cs as cations; purple: sulfides, blue: selenides, yellow: tellurides. This plot shows that for the 158 even small changes in the polarity can be resolved when going from Tl to In or when going from Ba to K, Rb and Cs as cations.

Table II.1 Overview over all polar chalcogenides represented in Fig.II.1-3 with the corresponding values for \bar{n} and ΔEN

Compound	\bar{n}	ΔEN	family
Ba _{0.5} CuZrSe ₃	4.36	1.2	1113
BaCuYSe ₃	4.5	1.14	1113
Sr _{0.5} CuZrSe ₃	4.27	1.2	1113
SrCuYSe ₃	4.33	1.14	1113
SrCuLuSe ₃	4.5	1.14	1113
SrCuGdSe ₃	4.5	1.14	1113
SrCuPrSe ₃	4.5	1.12	1113
SrCuCeSe ₃	4.5	1.12	1113
SrCuLaSe ₃	4.5	1.12	1113
Ba ₂ FeSbSe ₅	4.55	1.33	2115
Ba ₂ FeBiSe ₅	4.67	1.33	2115
Ba ₂ FeSbS ₅	4.00	1.4	2115
Ba ₂ FeBiS ₅	4.11	1.4	2115
Ba ₂ GaSbTe ₅	5.11	1.07	2115
Ba ₂ GaBiTe ₅	5.22	1.07	2115
Ba ₂ GaSbSe ₅	4.56	1.29	2115
Ba ₂ GaBiSe ₅	4.67	1.29	2115
Ba ₂ InSbTe ₅	5.22	1.07	2115
Ba _{0.5} Cr ₅ Se ₈	4.07	1.19	158
TlV ₅ Se ₈	4.14	0.52	158
TlCr ₅ Se ₈	4.14	0.59	158
TlTi ₅ Se ₈	4.14	0.59	158
TlV ₅ S ₈	3.57	0.58	158
KCr ₅ S ₈	3.43	1.29	158
RbCr ₅ S ₈	3.5	1.29	158
CsCr ₅ S ₈	3.57	1.34	158
Ba _{0.5} Cr ₅ S ₈	3.48	1.19	158
InTi ₅ S ₈	3.5	0.65	158
InCr ₅ S ₈	3.5	0.65	158
RbCr ₅ Se ₈	4.07	1.29	158
CsCr ₅ Se ₈	4.14	1.34	158
TlCr ₅ Te ₈	4.71	0.41	158

III. Experimental and computational details

1. Mechanical alloying (ball milling)

Mechanical alloying (or ball milling) was used to synthesize polycrystalline materials. The method involves the repeated welding, fracturing and rewelding of powder particles using a high-energy ball mill.^[50] In this case, a planetary micro mill Pulverisette7 (Fritsch, Germany), 20 ml tungsten carbide containers and seven 10 mm tungsten carbide balls were used for all synthesis steps. The tungsten carbide containers are placed on a supporting disc. During the synthesis both, the supporting disc and the containers rotate around their own axis resulting in a centrifugal force (F_c) acting on the reaction mixture in a way illustrated in Fig. III.1

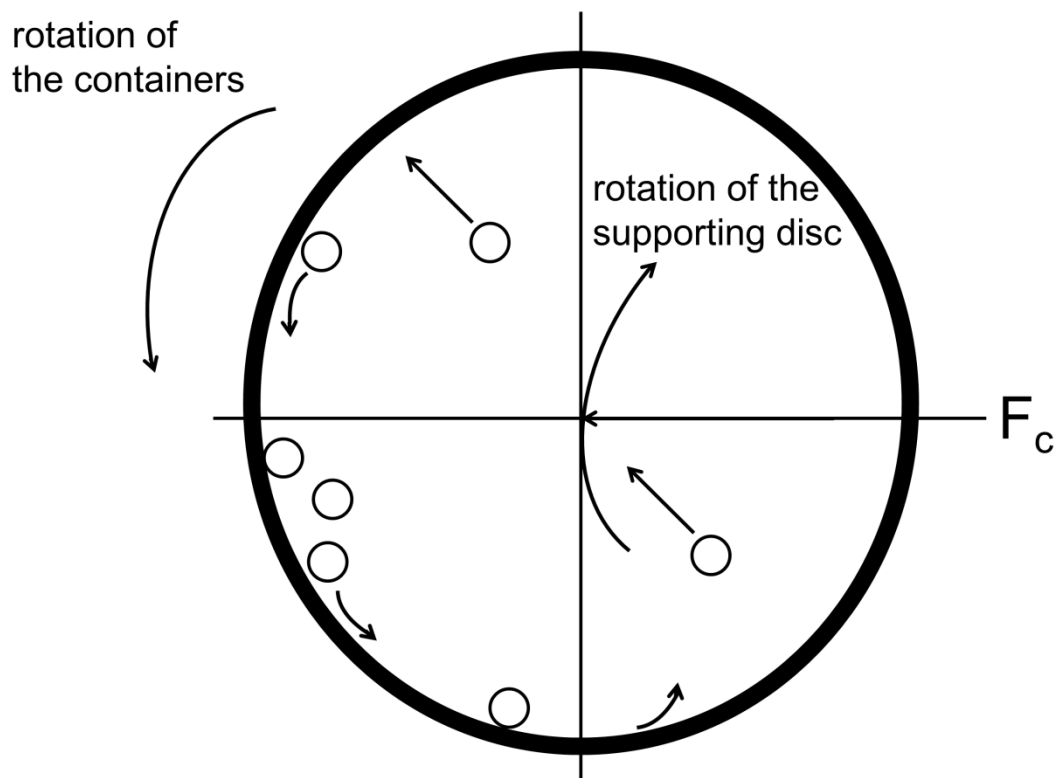


Fig. III.1 Principle of mechanical alloying when using a planetary micro mill

This synthesis method was used to synthesize final products and the precursor BaSe (red/brown powder), which was used for subsequent reactions with other elements in order to increase the reactivity (larger surface area compared to Ba) and to avoid reactions between Ba and fused silica tubes used for high-temperature solid state reactions.

The optimized synthesis conditions for all materials synthesized by mechanical alloying are summarized in Table III.1. Step 1 and 2 refer to subsequent synthesis steps including milling speed (rpm), time and number of milling cycles. The amount of each reaction in a single container was 10 g and 5g in case of $\text{Ba}_4\text{Cu}_8\text{Se}_{13}$. All compounds were synthesized starting from the elements, except for $\text{Ba}_2\text{FePnSe}_5$ (Pn = Sb,Bi), where BaSe was used as a precursor instead of Ba. The starting materials used for all syntheses (mechanical alloying and single crystal growth of precursors and final products) are summarized in Table III.2. All manipulations prior to the milling process were carried out in an argon-filled glove box to ensure an inert atmosphere during reaction.

Table III.1 Optimized synthesis conditions of all polycrystalline samples made by mechanical alloying

	BaSe	Ba₂FeSbSe₅	Ba₂FeBiSe₅	BaBiTe_{3-x}Se_x
step 1				
speed (rpm)	700	700	700	700
time/cycle (min)	2	2	2	2
cycles	15	15	15	15
step 2				
speed (rpm)	-	700	700	-
time (min)	-	30	30	-
cycles	-	16	16	-
break between cycles	-	30	30	-

Table III.2 Starting materials for all syntheses including mechanical alloying and single crystal growth

element	form	purity	source
Ba	pieces / rod	99+%	Alfa Aesar
Se	shot / powder	99.999%	Alfa Aesar
Te	powder	99.999+ %	Alfa Aesar
Cu	shot	99.5 %	Alfa Aesar
Bi	powder	99.99 %	Alfa Aesar
Sb	powder	99.5 %	Alfa Aesar
Fe	powder	99+%	Alfa Aesar
Zr	sponge	99.5 %	Alfa Aesar
Y	chips	99.9 %	Sigmar Aldrich

2. Spark Plasma Sintering

After mechanical alloying all samples were densified by spark plasma sintering. The principle of this sintering method is illustrated in Fig.III.2. Powders synthesized by mechanical alloying were placed in a 15 mm graphite die and in between two graphite punches. All surfaces in contact with the powder were covered with graphite foil. A pulsed DC current and a mechanical pressure were applied during densification. The powder sinters due to the mechanical pressure and Joule heating, which allows reaching densities close to the theoretical limit. In this case a HP D 25/1 spark plasma sintering furnace (FCT, Germany) and high density graphite dies (Carbon-Lorraine, France) were used to densify the samples. Cylindrical samples with a diameter and thickness of 15 mm and 5 mm were obtained after sintering.

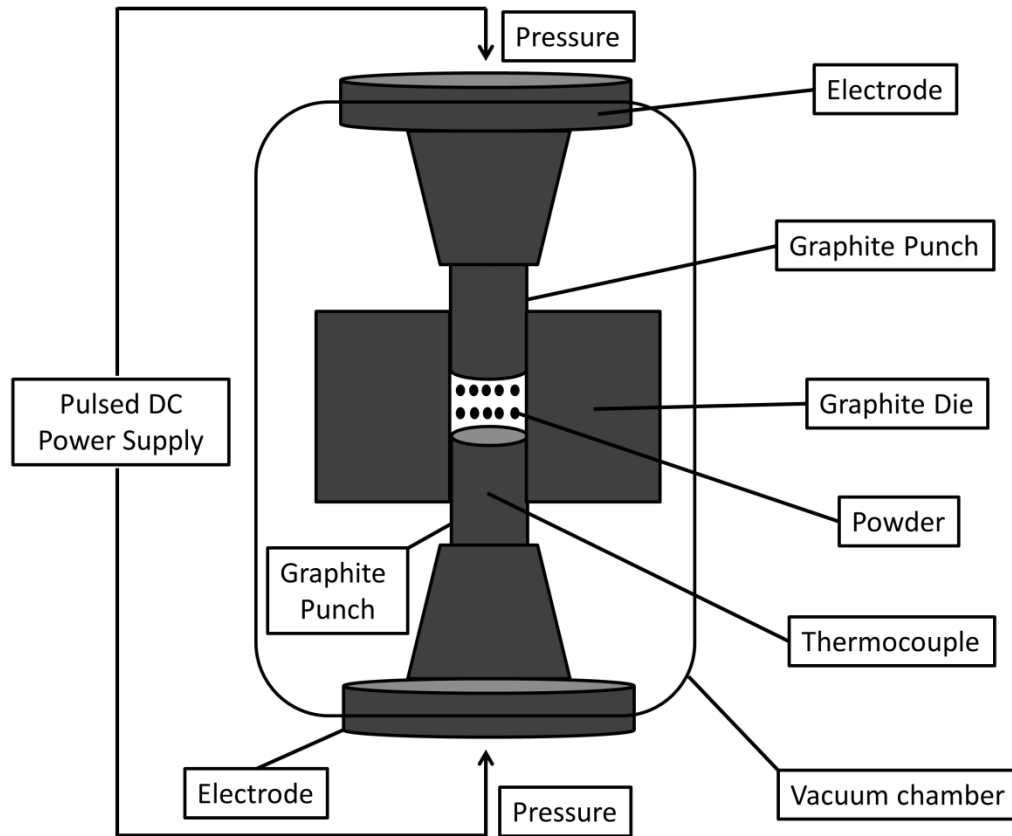


Fig. III.2 Schematic principle of the spark plasma sintering method

The densification of $\text{Ba}_2\text{FePnSe}_5$ ($\text{Pn} = \text{Sb}, \text{Bi}$) was conducted for 60 min at $500\text{ }^\circ\text{C}$ with a heating rate of $23\text{ }^\circ\text{Cmin}^{-1}$ up to $250\text{ }^\circ\text{C}$ and $6\text{ }^\circ\text{Cmin}^{-1}$ between $250\text{ }^\circ\text{C}$ and $500\text{ }^\circ\text{C}$, a cooling rate of $8\text{ }^\circ\text{Cmin}^{-1}$ and an applied mechanical pressure of 51 MPa. The same sintering profile was used for $\text{BaBiTe}_{3-x}\text{Se}_x$ ($x = 0, 0.05, 0.1$ and 3), but with a cooling rate of $16\text{ }^\circ\text{Cmin}^{-1}$. A slower cooling rate was required for $\text{Ba}_2\text{FePnSe}_5$ ($\text{Pn} = \text{Sb}, \text{Bi}$) to avoid cracks in the samples. For $\text{Ba}_4\text{Cu}_8\text{Se}_{13}$ the densification was conducted for 30 min at $400\text{ }^\circ\text{C}$ with a heating rate of $23\text{ }^\circ\text{Cmin}^{-1}$ up to $250\text{ }^\circ\text{C}$ and $3\text{ }^\circ\text{Cmin}^{-1}$ between $250\text{ }^\circ\text{C}$ and $400\text{ }^\circ\text{C}$, a cooling rate of $13\text{ }^\circ\text{Cmin}^{-1}$ and an applied mechanical pressure of 51 MPa. The maximum sintering temperature was decreased since the melting point of $\text{Ba}_4\text{Cu}_8\text{Se}_{13}$ is $523\text{ }^\circ\text{C}$. Experimental (ρ_{exp}) and theoretical densities (ρ_{theo}) as well as all $\rho_{\text{exp}}/\rho_{\text{theo}}$ values are summarized in Table III.3.

Table III.3 Experimental and theoretical densities of all samples

	$\rho_{\text{exp}} \text{ (g/cm}^3\text{)}$	$\rho_{\text{theo}} \text{ (g/cm}^3\text{)}$	$\rho_{\text{exp}} / \rho_{\text{theo}}$
Ba ₂ FeSbSe ₅	4.81	5.31	0.91
Ba ₂ FeBiSe ₅	5.61	5.83	0.96
Ba ₄ Cu ₈ Se ₁₃	5.77	6.04	0.96
BaBiTe ₃	6.44	6.73	0.96
BaBiTe _{2.95} Se _{0.05}	6.14	6.75	0.91
BaBiTe _{2.9} Se _{0.1}	5.6	6.70	0.84
BaBiSe ₃	6.37	6.43	0.995

3. Single crystal growth

Single crystals were grown from conventional high-temperature solid state reactions. All starting materials were loaded in silica ampoules, which were subsequently fused under dynamic vacuum. For reactions with pure alkaline-earth elements as precursors the ampoules were coated with a thin film of carbon by evaporating either acetone or ethanol in order to avoid a reaction of Ba with the ampoules. All starting elements used for the reactions are listed in Table III.2. All manipulations were carried out in an argon-filled glove box to ensure an inert atmosphere during reaction.

Growth of $A_{0.5}\text{CuZrSe}_3$ and ACuYSe_3 ($A = \text{Sr, Ba}$), $\text{Ba}_2\text{FePnSe}_5$ ($\text{Pn} = \text{Sb, Bi}$) and $\text{Ba}_4\text{Cu}_8\text{Se}_{13}$ single crystals

Ba_{0.5}CuZrSe₃ was synthesized from BaSe, Cu, Zr and Se precursors, SrCuYSe₃ from Cu₂Se, Sr, Y, Se and all other compounds were obtained from reactions of stoichiometric amounts of the elements. Cu₂Se was prepared by heating a stoichiometric mixture of the elements up to 600 °C, where it was kept for 24 h and subsequently cooled down to room temperature in 24 h. The target compounds were synthesized by heating stoichiometric amounts of the reactants up to 500 °C within 7 h. The reaction temperature was kept constant for 24 h and subsequently raised to 800 °C and kept constant for another 48 h before cooling the samples to 200 °C within 96 h.

The same temperature profile was used to grow $\text{Ba}_2\text{FePnSe}_5$ (Pn = Sb, Bi) and $\text{Ba}_4\text{Cu}_8\text{Se}_{13}$ single crystals starting from a stoichiometric mixture of the elements. Black needles with metallic luster were obtained in the case of $\text{A}_{0.5}\text{CuZrSe}_3$ (A = Sr, Ba), yellow needles in the case of ACuYSe_3 (A = Sr, Ba) and black platelets with metallic luster in the case of $\text{Ba}_2\text{FePnSe}_5$ (Pn = Sb, Bi) and $\text{Ba}_4\text{Cu}_8\text{Se}_{13}$.

4. Single crystal structure determination

All compounds are air-stable and therefore single crystals were picked in air under a thin film of oil. Intensity data of $\text{Ba}_{0.5}\text{CuZrSe}_3$ and SrCuYSe_3 was collected on a Bruker AXS SMART diffractometer (University of Delaware). For $\text{Ba}_{0.5}\text{CuZrSe}_3$ and SrCuYSe_3 data was collected at 200 K under a constant stream of nitrogen cooled to the target temperature. All other data collections were performed at 293 K using a Bruker Nonius four-circle diffractometer (CRISMAT). Both diffractometers are equipped with a SMART APEX II CCD area detector and a Mo- $K\alpha$ radiation source ($\lambda = 0.71073 \text{ \AA}$). The reason for using two different temperatures and diffractometers is that $\text{Ba}_{0.5}\text{CuZrSe}_3$ and SrCuYSe_3 were discovered in the laboratory of Prof. Svilen Bobev at the University of Delaware, while all other compounds were discovered at the CRISMAT laboratory. For $\text{Ba}_4\text{Cu}_8\text{Se}_{13}$, a full data collection was performed at room temperature and 100 K (reasons for these two temperatures are discussed in chapter V) and the diffraction frames were analyzed using the Apex II suite, CrysAlisPro and Jana2006.^[51] Data acquisition and processing were performed using the software SMART^[52] and APEX II, while data reduction and integration were performed using SAINT.^[53] Semiempirical absorption corrections were applied using SADABS.^[54]

Structure solution and refinement of $\text{Ba}_4\text{Cu}_8\text{Se}_{13}$

The structure solution and refinement process of the $\text{Ba}_4\text{Cu}_8\text{Se}_{13}$ crystal structure is further discussed in chapter V since the structure solution was complicated by pronounced real structure effects and diffuse scattering. These points are also discussed in detail in chapter V.

Structure solution and refinement of all other compounds

Structure solution and refinement were carried out using SHELX^[55] and Olex2^[56] was used as a Graphical User Interface for SHELX. The centrosymmetric, orthorhombic space groups $Pnma$ (SrCuYSe_3 , $\text{Ba}_2\text{FePnSe}_5$ (Pn = Sb, Bi) and $Cmcm$ ($\text{A}_{0.5}\text{CuZrSe}_3$ (A = Sr, Ba), BaCuYSe_3) were established from the Laue symmetry (mmm for both cases), systematic

absences (*cf.* Table III.4) and E-value statistics using the program XPREP. E-value statistics is a term referring to the statistical analysis of structure factor amplitudes^[57], where E corresponds to normalized structure factors:

$$|E_{hkl}| = \frac{|F_{hkl}|}{\sqrt{\langle |F|^2 \rangle}} \quad (\text{III.1})$$

$|E_{hkl}^2 - 1|$ can be expected to be 0.986 for centrosymmetric and 0.786 for non-centrosymmetric space groups, which allows distinguishing between them. Normalizing the structure factors is necessary to overcome the problem of F_{hkl} being dependent on the atomic form factors (f_i), which in turn depend on the diffraction angle (θ). Hence intensity changes with respect to θ due to changes in f_i are accounted for. Initial atomic positions were located by determining the phase of the structure factors (F_{hkl}) directly from the observed intensities (I_{hkl}) using direct methods and assuming that $I_{hkl} = (F_{hkl})^2$. Finally, the crystal structure data was standardized using the program STRUCTURE TIDY.^[58]

Table III.4 Systematic absences for the space groups *Pnma* and *Cmcm*

symmetry element	set of reflections	reflection condition
<i>P</i> centering	hkl	-
<i>C</i> centering	hkl	$h+k = 2n$
<i>c</i> glide-plane (010)	h0l	$l = 2n$
<i>n</i> glide-plane (100)	0kl	$k+l = 2n$
<i>a</i> glide-plane (001)	hk0	$h = 2n$

5. Powder X-ray diffraction (PXRD)

The average crystal structure of all polycrystalline samples was confirmed using PXRD data collected on a X'Pert Pro MPD diffractometer (PANalitical, Netherlands) equipped with a Cu-K $\alpha_{1/2}$ radiation source ($\lambda_{1/2} = 1.54060/1.54439$ Å). Subsequent Rietveld refinements were carried out using the software FULLPROF.^[59]

The pseudo-Voigt function $pV(x) = \eta L(x) + (1-\eta)G(x)$ was used to describe the peak shape with $L(x)$ and $G(x)$ representing the Lorentzian and Gaussian contributions. Others are the FWHM parameters U , V and W , the scale factor, zero shift, lattice parameters, atomic coordinates, isotropic displacement parameters, the preferred orientation parameter $Pref1$ and the background. For $Ba_4Cu_8Se_{13}$, data was collected on a Bruker D8 Advance Vario1 diffractometer, equipped with a $Cu-K\alpha$ radiation source ($\lambda = 1.54060 \text{ \AA}$) and a Johansson monochromator. A LeBail refinement was carried out using Jana2006 and the average structural model obtained by single crystal X-ray diffraction. Instrument parameters were refined using the fundamental parameter approach and the peak-shape was modeled using a Pseudo-Voigt function and Legendre polynomials were used to fit the background. High-temperature PXRD patterns up to $500 \text{ }^\circ\text{C}$ were recorded on a two circle BRUKER D8 Advance Vario1 diffractometer equipped with a Ge-111 monochromator and a high-temperature chamber operating under dynamic primary vacuum.

6. Electron microscopy and energy dispersive X-ray spectroscopy

Microstructure and homogeneity of sintered, polycrystalline $Ba_2FePnSe_5$ ($Pn = Sb, Bi$) samples were analyzed by transmission and scanning electron microscopy (TEM, SEM) as well as energy dispersive spectroscopy (EDS) using a Supra 55 scanning electron microscope (Zeiss, Germany) equipped with an EDAX EDS detector (Ametek, USA). Selected Area Electron Diffraction (SAED) patterns were recorded using a 2010 JEOL transmission electron microscope (possible tilt angles between $\pm 60^\circ$) and HRTEM images were taken using a TECNAI G²UT30 working at 200 kV and with $C_s = 0.7$. Both transmission electron microscopes are equipped with EDS detectors. In the case of $Ba_4Cu_8Se_{13}$, a JEM-ARM200F microscope from JEOL was used for all the analyses and HAADF images were simulated using the software JEMS. To analyze microstructure and chemical composition of $BaBiTe_{3-x}Se_x$ a Hitachi S-3400N-II scanning electron microscope with variable-pressure tungsten filament and an Oxford INCAx-act SDD EDS system was used.

7. Thermoelectric characterization

Low-temperature characterization

The TTO option in a Physical Properties Measurements System (Quantum Design, US) was used to measure simultaneously low-temperature Seebeck coefficient, electrical resistivity and thermal conductivity on bar-shaped, densified bulk sample.^[60] Silver epoxy paste was used for making contacts between sample holder and samples. Low-temperature electrical resistivities of $\text{Ba}_2\text{FePnSe}_5$ (Pn = Sb, Bi) and $\text{Ba}_4\text{Cu}_8\text{Se}_{13}$ were measured on a Physical Properties Measurements System (Quantum Design, US) using the four-probe method. Cu wires were connected via In contacts to the surface of bar-shaped, densified and polycrystalline samples with cross sections of 2.13 mm x 2.16 mm for Pn = Sb, 1.93 mm x 2.18 mm for Pn = Bi and 2.78 mm x 2.61 mm for $\text{Ba}_4\text{Cu}_8\text{Se}_{13}$. The measurements were performed at contact distances of 2.80 mm for $\text{Ba}_2\text{FeSbSe}_5$, 1.36 mm for $\text{Ba}_2\text{FeBiSe}_5$ and 6.21 mm for $\text{Ba}_4\text{Cu}_8\text{Se}_{13}$.

High-temperature characterization

High-temperature thermal conductivities were calculated from the density, heat capacity (c_p), and the thermal diffusivity (D_{th}), measured on graphite coated 6 mm x 6 mm x 1 mm bulk samples using a LFA457 MicroFlash (Netzsch, Germany) laser flash system. The heat capacity was estimated using the Dulong-Petit approximation with $c_p = 3k_B/\text{atom}$. The Nd laser source ($\lambda = 1064$ nm) in the laser flash system was used to change between an amorphous and a crystalline phase of $\text{Ba}_2\text{FePnSe}_5$ (Pn = Sb, Bi) while measuring the thermal diffusivity. Electrical resistivity (ρ), hall carrier concentration (n) and mobility (μ) were measured using a home-built measurement system^[60], the van der Pauw method and pressure-assisted Mo contacts. A magnetic field of 2T was applied during the hall measurements. Positive and negative fields were applied to verify the accuracy of the data. The Seebeck coefficient was measured using a home-built measurement system^[61] and Chromel-Nb thermocouples.

8. Magnetic measurements

Bar-shaped samples with a mass of 116.1 mg for $\text{Ba}_2\text{FeSbSe}_5$ and $m = 143$ mg for $\text{Ba}_2\text{FeBiSe}_5$ were prepared from the corresponding SPS pellets. The magnetization (M) was measured as a function of temperature and magnetic field using a MPMS 5S Superconducting Quantum Interference Device (SQUID, Quantum Design, USA). Zero-field-cooled (ZFC) and field-cooled (FC) susceptibilities were measured subsequently in settle mode, applying a constant magnetic field of 0.1 T. Measurements were performed between 2 K – 300 K for $\text{Ba}_2\text{FeSbSe}_5$ and 2 K – 400 K for $\text{Ba}_2\text{FeBiSe}_5$. The magnetic susceptibility (χ) was calculated as follows:

$$\chi = \frac{\mu M}{m H} \quad (\text{III.2})$$

where μ , M , m and H correspond to the measured magnetic moment, molar mass, sample mass and magnetic field, respectively.

9. Dielectric measurements

All dielectric measurements of $\text{Ba}_2\text{FeSbSe}_5$ were carried out using a Quantum Design PPMS equipped with a home-built sample holder connected to a Agilent 4284A LCR meter. Thin plates with a square cross-section of 2 mm x 2 mm and a thickness of 0.5 mm were prepared and electrodes of silver paste were deposited prior to the measurements. The dielectric permittivity (ϵ) of a material can be extracted from the capacity of an ideal capacitor (C), which is defined as:

$$C = \frac{\epsilon_0 \epsilon S}{d} \quad (\text{III.3})$$

S and d correspond to the plate area of the capacitor and the distance between the plates, while ϵ_0 is the vacuum permittivity. The capacity can be related to the charge accumulated at the capacitor plates (Q) and the voltage (V) between the plates:

$$Q = CV = C A \sin(\omega t) = \int I dt \quad (\text{III.4})$$

A and I correspond to the amplitude of the applied AC voltage and the current associated to the applied voltage, while ω corresponds to the frequency of the applied voltage. Hence, the capacity can be obtained by applying an AC voltage and measuring the current.

The reason, why an AC voltage is chosen is that the resistance (R) then becomes an impedance (Z), which has both a magnitude (real part) and a phase (imaginary part), which relate to the resistance and the capacitance as follows:

$$\frac{1}{Z} = \frac{1}{R} + C\omega j \quad (\text{III.5})$$

A purely imaginary impedance is a measure for the electrostatic storage of charge induced by voltages between two conductors (i.e. the charge accumulated at the capacitor plates). Hence, materials with a large resistance and dielectric losses ($\tan\delta$) close to 0 are needed to ensure the measurement of a purely imaginary impedance.

$$\tan\delta = \frac{1}{CR\omega} \quad (\text{III.6})$$

In a first step, suitable frequencies were selected for which the impedance (Z) is purely imaginary (i.e. a purely capacitive response is measured and $\tan\delta \sim 0$) and where extrinsic effects can be excluded (i.e. frequencies larger than 10^4 Hz are needed). The selected frequencies in this case are 30 kHz, 40 kHz, 50 kHz and 60 kHz. Subsequently the impedance was measured as a function of temperature and magnetic field and the capacitance and dielectric permittivity were calculated according to (III.5) and (III.3).

10. X-ray Pair Distribution Function (XPDF) analysis

2D scattering data over a wide range of momentum transfer ($Q_{\max} = 36 \text{ \AA}^{-1}$) were recorded at the I15-1 XPDF beamline at the Diamond Light Source (Didcot, UK) using a focused X-ray beam (20 μm in size) with a wavelength of 0.16 \AA . Densely packed 0.7 mm borosilicate capillaries were prepared prior to data collection. The capillaries were placed horizontally on a 10 Hz capillary spinner and all samples were constantly rotated during data collection. The beamline is equipped with a Bent-Laue monochromator (700 μm horizontal focusing), a multi-layer mirror (20 μm vertical focusing) and a Perkin Elmer XRD1611 CP3

area detector with an active area of $409.6 \times 409.6 \text{ mm}^2$. Data was collected at room temperature and at 90 K. Low-temperature experiments were performed using a Cryojet operating with liquid nitrogen. The DAWN^[62] software was used for data processing and PDFgetX₃^[63] was used to convert 1D X-ray powder diffraction data to atomic PDFs. PDFfit2^[64] was used to fit the experimental PDFs and PDFgui^[64] was used as a graphical user interface. LaB₆ was used to extract the Q_{damp} and Q_{broad} parameters used for all subsequent refinements. All refinements were performed refining the scale factor, lattice parameters, delta1 (accounts for the correlated motion of atoms at low r , which sharpens the first peak(s) at low r), thermal displacement parameters and atomic positions. The thermal displacement parameters were constrained in a way so that $U_{11} = U_{22} = U_{33}$ and all U of the same atom type were assumed to be identical.

11. Differential scanning calorimetry

A DSC scan with a heating rate of 10 Kmin^{-1} and constant Ar flux was performed on polycrystalline Ba₄Cu₈Se₁₃ using a NETZSCH STA 449 calorimeter and alumina crucibles. An empty alumina crucible was used as an internal standard.

12. Optical absorption measurements

Mid-Infrared ($\sim 0.08 - 0.7 \text{ eV}$) diffuse reflectance (R) spectra of BaBiTe_{3-x}Se_x ($x = 0, 0.05$ and 0.1) were collected under Argon atmosphere in the temperature range $300 - 500 \text{ K}$ with a Nicolet 6700 FTIR Spectrometer equipped with a Praying Mantis attachment and a high-temperature stage from Harric Scientific Instruments. A KBr standard was used as reference. The room temperature diffuse reflectance of BaBiSe₃ was recorded with a Shimadzu UV-3101 PC double-beam, double-monochromator spectrophotometer operating from 200 nm to 2500 nm using BaSO₄ as a non-absorbing reflectance reference. The absorption spectra (a/s) were obtained using the Kubelka-Munk function, which gives a relationship between R and the absorption coefficient (α) and scattering coefficient (s) through

$$\left(\frac{\alpha}{s}\right) = \frac{(1-R)^2}{2R} \quad (\text{III.7})$$

13. Speed of sound measurements

The longitudinal and transversal components of the speed of sound (v_L and v_T) of BaBiTe₃ and BaBiSe₃ were measured applying the pulse-echo method. A piezoelectric transducer coupled to the sample first sends the initial pulse, and then acts as receiver measuring the echoed reflections.^[65] The time delay, t_d , between subsequent reflections was determined by maximizing the cross-correlation of the two reflections as follows. If $\sigma_n(t)$ corresponds to the stress amplitude of reflection (n), then $\sum_t \sigma_n(t)\sigma_{n+1}(t - t_d)$ is maximized by varying t_d . A longitudinal transducer with a principle frequency of 20 MHz (Olympus M116-RM) and a transverse transducer at 5 MHz (Olympus V157-RM) were used with a Panametrics 5072PR pulse-receiver.

A Tektronix TBS 1072B-EDU oscilloscope was used to record the waveforms. The speed of sound (v_s) was calculated from the longitudinal and transversal components v_L and v_T as follows:

$$v_s = \left[\frac{1}{3} \left(\frac{2}{v_T^3} + \frac{1}{v_L^3} \right) \right]^{-1/3} \quad (\text{III.8})$$

From the speed of sound the Debye temperature (θ_D) and Cahill's glass limit of the thermal conductivity^[66] (κ_{glass}) were calculated as follows:

$$\kappa_{\text{glass}} = \frac{1}{2} \left(\frac{\pi}{6} \right)^{\frac{1}{3}} k_B V^{-\frac{2}{3}} (2v_T + v_L) \quad (\text{III.9})$$

$$\theta_D = \frac{\hbar \omega_D}{k_B} \quad (\text{III.10})$$

where ω_D is the Debye frequency:

$$\omega_D = v_s \left(\frac{6\pi^2}{V} \right)^{1/3} \quad (\text{III.11})$$

and where V corresponds to the unit cell volume per atom.

14. Modelling high-temperature thermoelectric transport data

The simplest model for analyzing thermoelectric transport at high temperatures is for the itinerant conduction in a single parabolic band, also called single parabolic band model (SPB). It allows determining, whether or not the carrier concentration of a thermoelectric material is optimized, to extract information about the electronic structure of a material (e.g. the Seebeck effective mass) and it can be an indicator for more complex thermoelectric transport phenomena (e.g. multiband effects or nonparabolicity of the bands).^[67] Seebeck coefficient (S), chemical carrier concentration (n) and zT are given by the following equations:

$$S = \frac{k}{e} \left(\frac{2F_1}{F_0} - \eta \right) \quad (\text{III.12})$$

$$n = 4\pi \left(\frac{2m^*kT}{h^2} \right)^{3/2} F_{1/2} \quad (\text{III.13})$$

$$zT = \frac{S^2}{L + (\psi\beta)^{-1}} \quad (\text{III.14})$$

η , F_j , k , e , h and m^* correspond to the chemical potential, Fermi integrals, Boltzmann constant, elementary charge, Planck constant and ‘‘Seebeck effective mass’’. The Fermi integrals are defined according to (III.15) and the chemical carrier concentration is related to the Hall carrier concentration by $n_H = n/r_H$; where r_H is given by (III.16). The Fermi integrals were obtained by numerical integration using the Simpson method.

$$F_j(\eta) = \int_0^\infty f \epsilon^j d\epsilon = \int_0^\infty \frac{\epsilon^j d\epsilon}{1 + \exp(\epsilon - \eta)} \quad (\text{III.15})$$

$$r_H = \frac{3}{2} F_{1/2} \frac{F_{-1/2}}{2F_0^2} \quad (\text{III.16})$$

The Lorenz number (L), ψ and β were calculated using the following equations:

$$L = \frac{k^2}{e^2} \frac{3F_0F_2 - 4F_1^2}{F_0^2} \quad (\text{III.17})$$

$$\psi = \frac{8\pi e}{3} \left(\frac{2m_e k}{h^2} \right)^{3/2} F_0 \quad (\text{III.18})$$

$$\beta = \frac{\mu_0 (m^*/m_e)^{3/2} T^{5/2}}{\kappa_{ph}} \quad (\text{III.19})$$

κ_{ph} corresponds to the phononic part of the thermal conductivity, which was extracted using the Wiedemann-Franz law (III.20), where σ and T correspond to the electrical conductivity and temperature, respectively.

$$\kappa_{ph} = \kappa - L\sigma T \quad (\text{III.20})$$

In this thesis, the SPB formalism is used to extract the ‘‘Seebeck effective mass’’ (m^*) as a function of temperature and to show that multiple conduction bands contribute to the thermoelectric transport properties of BaBiTe_3 and $\text{BaBiTe}_{2.95}\text{Se}_{0.05}$. This procedure can be viewed as a change of variables, i.e. describing a more complex system (in this case a multiband system) with a simplified model (SPB). This is why the term effective band model instead of SPB model is used. The effective band model is capable of providing useful information concerning the electronic structure and it is sufficient to detect multiband effects in the transport data. However, it is not capable of describing the electronic transport of multiband systems entirely correct, i.e. further research efforts are required to develop a multiband model for BaBiTe_3 .

15. Electronic structure and defect calculations

Ba₂FePnSe₅ (Pn = Sb, Bi)

DFT calculations of Ba₂FePnSe₅ (Pn = Sb, Bi) were carried out in collaboration with Houria Kabbour using the Vienna Ab-initio Package (VASP).^[68] The spin polarized calculations were performed using the Projected Augmented Wave Method (PAW)^[69,70] applying the generalized gradient approximation (GGA). The GGA potential was developed using the Perdew-Burke-Ernzerhof (PBE) functional.^[71] A plane wave energy cutoff of 550 eV, 62 *k* points in the irreducible Brillouin zone and an energy convergence criterion of 10⁻⁶ eV were used. Due to the strongly correlated electrons in the 3*d* open shell of the transition metal cations (Fe³⁺), a Hubbard correction was considered using the Dudarev method.^[72] In this approach the penalty term ($U_{eff} = U - J$), with U representing the on-site coulomb repulsion and J the inter-site interaction, was added to the Kohn-Sham Hamiltonian. While setting $J = 0$ eV, a U value of 2.5 eV was applied and compared with GGA only calculations. The values for J and U are based on previous calculations performed for the isostructural sulfur phases^[73], where reasonable results were obtained with respect to optical absorption data. The calculations on Ba₂FePnSe₅ (Pn = Sb, Bi) were carried out using a supercell of **a**, **2b**, **c** and a similar antiferromagnetic (AFM) configuration to the one used in reference [73].

Details on this configuration can be found in Fig. IV.15. The Electron Localization Function (ELF) of Ba₂FePnSe₅ (Pn = Sb, Bi) was also obtained from these calculations.

BaBiTe_{3-x}Sex

Electronic structure and defect calculations were performed in collaboration with the research group of Geoffroy Hautier using the Vienna ab initio software package (VASP), PAW pseudopotentials, the generalized gradient approximation (GGA) as implemented by Perdew, Burke and Ernzerhoff (PBE) and an energy cutoff of 520 eV. A scissor (operator) shift was applied to the DFT band structure to correct the band gap. This correction is based on the empirical band gap obtained from optical absorption measurements and is consistent with the Goldsmid-Sharp band gap ($E_g = 2eS_{max}T_{max}$). This is further discussed in chapter V. For bulk calculations, the reciprocal space was sampled by a 6x2x2 *k*-point mesh, while for the defect calculations a *k*-point mesh of 2x2x2 and a 3x1x1 supercell were used.

A force convergence criterion of 0.005 eV/Å was adopted for all structure relaxations. The Crystal Orbital Hamilton population (COHP) curves were calculated using the LOBSTER^[74] software. The defect formation energy D in a charge state q was calculated according to III.21^[75]:

$$E_f[D^q] = E[D^q] + E_{corr}[D^q] - E[bulk] - \sum_i n_i \mu_i + q(\varepsilon_{vbm} + \Delta v) + \Delta \varepsilon_F \quad (\text{III.21})$$

$E[D^q]$ and $E[bulk]$ represent the total energy of the supercell with defects D in the charge state q and without any defects. n_i is the number of removed ($n_i < 0$) or added ($n_i > 0$) i -type atoms, and μ_i is the chemical potential. ε_{VBM} is the VBM energy, and $\Delta \varepsilon_F$ is the Fermi energy (chemical potential) of the electrons relative to ε_{VBM} . $E_{corr}[D^q]$ and Δv are correction terms for the spurious image-image interaction and potential alignment.^[76]

The chemical potential of the elements was obtained from a stable region of the Ba-Bi-Te phase diagram supported by all corresponding compounds present in the Materials Project database using the pymatgen package.^[77] The localized defect states with the charge q were corrected using the extended Freysoldt (Kumagai) scheme^[78,79], while for delocalized defects, only a potential alignment between the bulk and neutral state was included.

16. Calculating the optical absorption coefficient

The optical absorption coefficient (α) of BaBiTe₃ was calculated as a function of energy using the PAW-PBE method and a self-consistent field approach.^[69-71,80,81] A scissor (operator) shift was applied to the DFT band structure to correct the band gap. Further details are discussed in chapter V. A very dense k -point mesh of 34x9x9 corresponding to 450 k -points in the irreducible Brillouin zone is utilized to compute α , which is defined as follows:^[82]

$$\alpha(\omega) = \frac{2\omega k(\omega)}{c} \quad (\text{III.22})$$

$k(\omega)$ and c correspond to the extinction coefficient (III.23) and the speed of light, respectively.

$$k(\omega) = \sqrt{\frac{\sqrt{\varepsilon_1^2(\omega) + \varepsilon_2^2(\omega)} - \varepsilon_1(\omega)}{2}} \quad (\text{III.23})$$

$\varepsilon_1(\omega)$ and $\varepsilon_2(\omega)$ represent the average of the three diagonal elements (xx, yy, zz components) of the imaginary and real part of the dielectric tensor. It is worth noting that only vertical (optical) transitions are considered.

*IV. Normal valence Cu-(I)- and Pn-chalcogenides with
Pn = Sb, Bi*

1. Overview

This chapter has its focus on the crystal structure, chemical bonding and physical properties of several normal valence polar chalcogenides. The chemical bonding in all the compounds presented in this chapter can be described by classical $2c-2e$ bonds without violating the octet rule. Hence the electrons can be considered fully localized. The first part of the chapter focuses on the crystal structures of the four new quaternary copper-(I)-selenides $A_{0.5}CuZrSe_3$ and $ACuYSe_3$ ($A = Sr, Ba$) and the influence of the ionic radii on their structure-type and symmetry. All these compounds are charge balanced and a closed shell configuration is reached if a full charge transfer from the cations to selenium is assumed. These compounds can also be considered as being part of the *Zintl* family. The second part of this chapter focuses on $Ba_2FePnSe_5$ ($Pn = Sb, Bi$), two new polar chalcogenides containing stereoactive lone pairs. In these compounds Fe reaches a half-filled d-shell, while all other elements reach a closed shell configuration under the same assumption that the charge transfer between the cations and Se is complete. In this case the Zintl electron counting concept can be applied, but the compounds are not part of the *Zintl* family since Fe does not reach a closed shell, i.e. they are antiferromagnetic at low temperatures. The crystal structures of $Ba_2FePnSe_5$ ($Pn = Sb, Bi$) are discussed with special focus on structural distortions caused by the Sb and Bi lone pairs. It follows a discussion of the electronic structure, electrical resistivity and thermal conductivity of both compounds. It was discovered that both compounds undergo rapid, radiation-induced phase changes from the crystalline to an amorphous phase. These results and the possible origin of these phase changes in resonant bonding will also be discussed in the second part of this chapter, which concludes with a discussion of anomalies in thermal conductivity and dielectric permittivity, which occur at the Néel temperature.

2. Polar chalcogenides with classical two-center two-electron ($2c-2e$) bonds

2.1 $A_{0.5}CuZrSe_3$ and $ACuYSe_3$ ($A = Sr, Ba$) – four new quaternary copper-(I)-selenides

The motivation behind the synthesis of $A_{0.5}CuZrSe_3$ and $ACuYSe_3$ ($A = Sr, Ba$) was the layered (i.e. anisotropic) crystal structure of $KCuZrSe_3$, which was already known. The K atoms are intercalated between $[CuZrSe_3]^-$ layers. Such a crystal structure is ideal for obtaining materials, which fulfill the phonon-glass electron crystal concept introduced by Slack.^[83] He proposed that such materials are ideal candidates for thermoelectric energy conversion since they contain rigid networks such as the $[CuZrSe_3]^-$ layers, which allow electron conduction (i.e. they behave as electron crystals). At the same time such materials contain parts in their crystal structure, which are less rigid (e.g. rattling atoms) and which effectively scatter phonons resulting in low thermal conductivities (i.e. they behave as a phonon glass). One can imagine that the intercalated K atoms in between the $[CuZrSe_3]^-$ layers can play this role in $KCuZrSe_3$. Replacing K by A ($A = Sr, Ba$) requires a nominal stoichiometry of $A_{0.5}CuZrSe_3$ in order to maintain charge balance and creating vacancies can only enhance phonon scattering and can therefore reduce the thermal conductivity. Unfortunately only a few crystals of $A_{0.5}CuZrSe_3$ and $ACuYSe_3$ ($A = Sr, Ba$) could be synthesized and stable binary side phases prevented a thermoelectric characterization of these compounds.

2.1.1 Introduction

The four new quaternary copper-(I)-selenides $A_{0.5}CuZrSe_3$ and $ACuYSe_3$ ($A = Sr, Ba$)^[84] belong to a group of compounds known as the $AMM'Q_3$ ($A =$ alkali metal or alkaline-earth metal or Tl; $M =$ transition metal or Ba; $M' =$ transition metal or f-block element) or “1113” family. There are more than 160 compounds and seven different known structure types within this family.^[85] which demonstrates its incredible structural flexibility towards ion exchange. Five of these structure types ($KCuZrS_3$ ^[86], Eu_2CuS_3 ^[87], Ba_2MnS_3 ^[88], $NaCuTiS_3$ ^[89] and $TiCuTiS_3$ ^[90]) form two dimensional, layered structures, while two of them ($BaAgErS_3$ ^[91] and $BaCuLaS_3$ ^[92]) form channel structures, where the two dimensional layers are connected in the third dimension. All seven structure types are depicted in Fig. IV.1 and IV.2, which group them into layered and channel structures. Structural details such as composition and stacking direction of the layers, channel direction, number and type of crystallographically unique positions and the A, M and M' coordination are summarized in Table IV.1 and IV.2. All layered structure types consist of MQ_4 tetrahedra and $M'Q_6$ octahedra forming layers, which are separated by the A atoms. In $KCuZrSe_3$, Eu_2CuS_3 (a slightly distorted variant of $KCuZrSe_3$ where the A coordination changes from bicapped trigonal prismatic to monocapped trigonal prismatic) and Ba_2MnS_3 the layers are stacked along [010] and [001] and they consist of alternating chains of edge-sharing $M'Q_6$ octahedra and corner sharing MQ_4 tetrahedra. In the case of the Ba_2MnS_3 structure type the layers are highly puckered and Ba occupies both, the A and M' position. This is similar to the situation in Eu_2CuS_3 , where Eu occupies also these two positions. In $NaCuTiS_3$ and $TiCuTiTe_3$ the layers are composed of alternating double chains consisting of edge-sharing MQ_4 tetrahedra and $M'Q_6$ octahedra. The difference between these two structure types is that the MQ_4 and $M'Q_6$ polyhedra point in the same direction in $TiCuTiTe_3$ when comparing different layers, while in $NaCuTiS_3$ the polyhedra point in alternate directions.

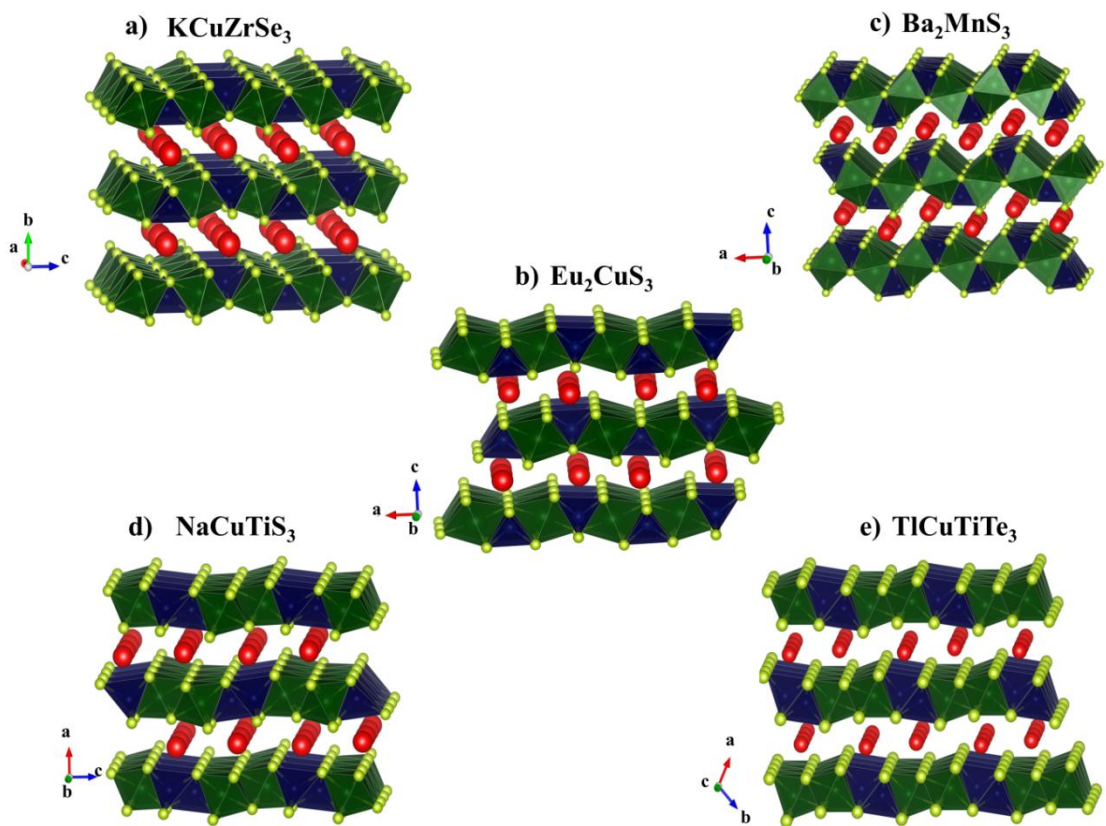


Fig. IV.1 Perspective view of the five $\text{AMM}'\text{Q}_3$ structure types (a) KCuZrSe_3 , b) Eu_2CuS_3 , c) Ba_2MnS_3 , d) NaCuTiS_3 , e) TiCuTiTe_3), which form two dimensional (2D), layered crystal structures (red: A, blue: M, dark green: M', light green: Q).

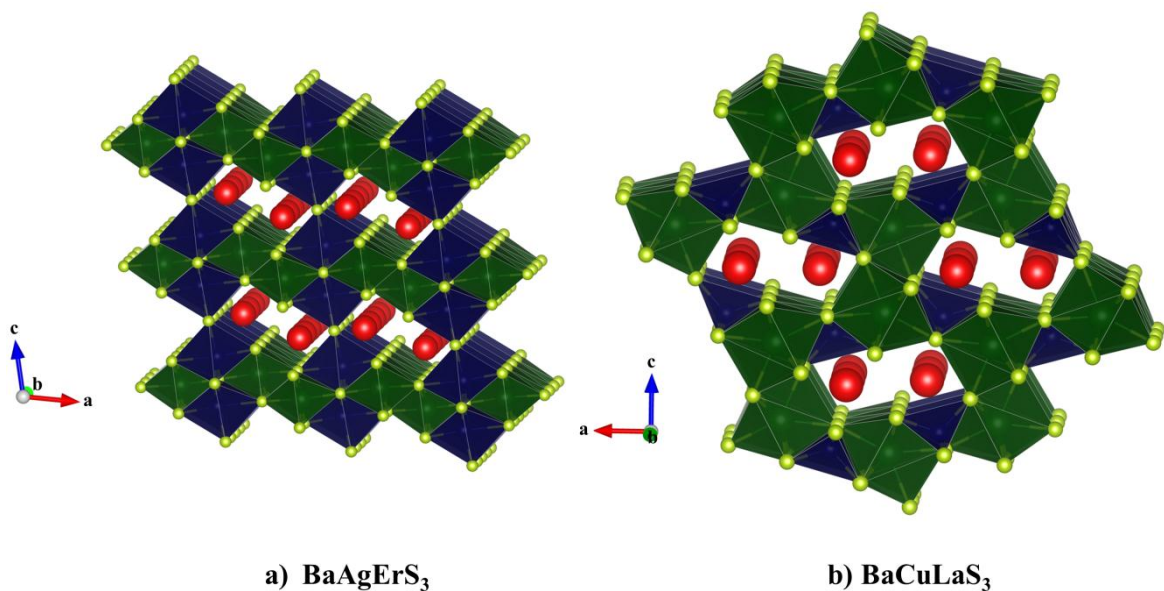


Fig. IV.2 Perspective view of the two $\text{AMM}'\text{Q}_3$ structure types (a) BaAgErS_3 and b) BaCuLaS_3), which form channel structures (red: A, blue: M, dark green: M', light green: Q).

The M and M' coordination is the same comparing the layered structure types, which is not the case for the channel structures. In BaAgErS₃ the M atoms are coordinated by five Q atoms forming trigonal bipyramids, while the M' atoms are coordinated octahedrally. The octahedra form double chains through edge-sharing and these double chains are connected through corners resulting in two dimensional layers. These layers are connected through the trigonal bipyramids, which share edges within the layers and corners across the layers and the A atoms are located in the channels. The channels in BaCuLa₃ on the other hand are built up by chains of vertex sharing MQ₄ tetrahedra and double chains of face sharing M'Q₇ monocapped, trigonal prisms. These double chains are connected to each other via corners and the MQ₄ tetrahedra are connected to these double chains via corners and edges and the A atoms are located in the channels.

Up to now the 1113 family was divided into two subgroups: A⁺¹M⁺¹M'⁺⁴(Q²⁻)₃ and A⁺²M⁺¹M'⁺³(Q²⁻)₃. The first subgroup only contains compounds crystallizing in the KCuZrS₃, NaCuTiS₃ and TiCuTiTe₃ structure types, while the second subgroup contains compounds crystallizing in the KCuZrS₃, Eu₂CuS₃, Ba₂MnS₃, BaAgErS₃ and BaCuLaS₃. So far, compounds with M = Cu were only obtained by combining di- (A²⁺) and trivalent (M'³⁺) or mono- (A⁺) and tetravalent (M'⁴⁺) cations with a [CuSe₃]⁵⁻ network without considering the possibility of vacancies on the A site. Examples are combinations of alkaline earth and rare-earth metals (e.g. BaCuM'Se₃ with M' = La^[92], Ce^[93], Gd^[94] and SrCuM'Se₃^[95-97] with M' = La-Pr, Nd, Sm, Gd-Lu) or alkali and group 4 transition metals.

For the SrCuM'Se₃ (M' = La, Gd, Lu) series the crystal structure changes between three orthorhombic structures with different coordination environments for Sr²⁺ and M'³⁺ depending on the ionic radii of the lanthanides. For La³⁺ the Ba₂MnS₃ structure type is obtained, while changing M' to the smaller Gd³⁺ results in the Eu₂CuS₃ structure type. When going towards the even smaller Lu³⁺ the KCuZrS₃ structure type is obtained. The crystal structures of SrCuM'Se₃ are higher symmetric (*Cmcm*) for the smaller and heavier lanthanides (M' = Lu-Ho), while the symmetry is reduced for M' = Dy-Gd, Sm, Nd-La resulting in the space group *Pnma*.^[96] Another example, where the M'³⁺ cation radius changes the crystal structure is the study of SrCuCeSe₃^[97] and SrCuPrSe₃.^[97] The recent discovery of BaAgTbS₃^[98], BaCuGdTe₃^[98], BaCuTbTe₃^[98], BaAgTbTe₃^[98] and CsAgUTe₃^[98] as new members of the 1113 family underlines again the remarkable flexibility of the KCuZrS₃ structure type towards ion exchange and it shows that even with more than 160 compounds in this family there is still more to discover.

Table IV.1 Structural details of the $AMM'Q_3$ structure types forming two dimensional, layered crystal structures

structure type	$KCuZrS_3$	Eu_2CuS_3	Ba_2MnS_3	$NaCuTiS_3$	$TiCuTiTe_3$
space group	<i>Cmcm</i>	<i>Pnma</i>	<i>Pnma</i>	<i>Pnma</i>	<i>P2₁/m</i>
layer composition	$\frac{2}{\infty}[MM'Q_3]^-$	$\frac{2}{\infty}[MM'Q_3]^-$	$\frac{2}{\infty}[M(A1)Q_3]^{2-}$	$\frac{2}{\infty}[MM'Q_3]^-$	$\frac{2}{\infty}[MM'Q_3]^-$
stacking direction	[010]	[001]	[001]	[100]	[101]
unique crystallographic positions	5	6	6	6	6
type of unique crystallographic positions	A, M, M', Q1, Q2	A, M, M', Q1, Q2, Q3	A1, A2, M, Q1, Q2, Q3	A, M, M', Q1, Q2, Q3	A, M, M', Q1, Q2, Q3
A coordination	AQ ₈ bicapped trigonal prisms	AQ ₇ monocapped trigonal prisms			
M coordination	MQ ₄ tetrahedra	MQ ₄ tetrahedra	MQ ₄ tetrahedra	MQ ₄ tetrahedra	MQ ₄ tetrahedra
M' coordination	M'Q ₆ octahedra	M'Q ₆ octahedra	-	M'Q ₆ octahedra	M'Q ₆ octahedra

Table IV.2 Structural details of the BaAgErS₃ and BaCuLaS₃ structure types forming channel structures.

structure type	BaAgErS ₃	BaCuLaS ₃
space group	<i>C2/m</i>	<i>Pnma</i>
layer composition	$\frac{2}{\infty}[M^{3+}Q_3]^{4+}$	$\frac{2}{\infty}[MM'Q_3]^{-}$
channel direction	[010]	[010]
unique crystallographic positions	7	6
type of unique crystallographic positions	A, M, M', Q1, Q2, Q3, Q4	A, M, M', Q1, Q2, Q3
A coordination	AQ ₇ monocapped trigonal prisms	AQ ₇ monocapped trigonal prisms
M coordination	1x Q1, 1x Q2, 1x Q3, 2x Q4	2x Q1, 1x Q2, 1x Q3
M' coordination	3x Q1, 2x Q2, 1x Q4	2x Q1, 3x Q2, 2x Q3

During this chapter it is demonstrated that there is a third subgroup ($A_{0.5}^{+2}M^{+1}M'^{+4}(Q^{2-})_3$) in the 1113 family, where half of the A site is vacant. This discovery might give access to an entirely new group of compounds within the 1113 family with $A_{0.5}CuZrSe_3$ (A = Sr, Ba) as its first members. It will be shown, that not only the $M^{3+/4+}$ (M = Zr, Y) or A^{2+} (A = Ba, Sr) ionic radii determine structure type and symmetry of $A_{0.5}CuZrSe_3$ and $ACuYSe_3$ (A = Sr, Ba), but their ratio $r(A^{2+})/r(M^{3+/4+})$. This conclusion also holds for the analogous $SrCuM'Se_3$ (M' = La, Ce, Pr, Gd, Lu) compounds, where $SrCuLuSe_3$ crystallizes in the space group *Cmcm*, while the other compounds crystallize in the space group *Pnma*. Hence, the $r(A^{2+})/r(M^{3+/4+})$ ratio is a powerful parameter for predicting the symmetry of new compounds belonging to the 1113 family and for understanding the reoccurring observation of the *Cmcm-Pnma* group-subgroup relationship in this family of compounds.

2.1.2 Results and Discussion

2.1.2.1 Crystal structures obtained by single crystal X-ray diffraction

In this part of the chapter the crystal structures of $A_{0.5}\text{CuZrSe}_3$ ($A = \text{Sr}, \text{Ba}$) and ACuYSe_3 ($A = \text{Sr}, \text{Ba}$) obtained by single crystal X-ray diffraction are discussed. The results of the structure solution and refinement of $A_{0.5}\text{CuZrSe}_3$ ($A = \text{Sr}, \text{Ba}$) and ACuYSe_3 ($A = \text{Sr}, \text{Ba}$) are summarized in Table IV.3-5. Table IV.3 contains all important crystallographic information concerning each crystal structure solution and refinement. All final equivalent isotropic displacement parameters and atomic coordinates are summarized in Table IV.4, while Table IV.5 gives an overview over selected interatomic distances. $\text{Ba}_{0.5}\text{CuZrSe}_3$ and $\text{Sr}_{0.5}\text{CuZrSe}_3$ crystallize in the layered KCuZrS_3 structure type with the orthorhombic space group $Cmcm$ ($a = 3.8386(7) \text{ \AA}$, $b = 14.197(2) \text{ \AA}$, $c = 10.1577(17) \text{ \AA}$ and $a = 3.8386(7) \text{ \AA}$, $b = 14.196(2) \text{ \AA}$, $c = 10.1577(17) \text{ \AA}$, respectively). The crystal structure (*cf.* Fig. IV.3) consists of $\frac{2}{\infty}[\text{CuZrSe}_3]^-$ layers (*cf.* Fig. IV.4) parallel to the ac plane and stacked along $[010]$ and A^{2+} cations and vacancies, which are separating the anionic layers.

Table IV.3 General crystallographic information obtained from single crystal structure solutions and refinements.

	Ba_{0.5}CuZrSe₃	Sr_{0.5}CuZrSe₃	BaCuYSe₃	SrCuYSe₃
Formula weight (amu)	460.31	435.46	526.67	477.95
Space group	<i>Cmcm</i> (No. 63)	<i>Cmcm</i> (No. 63)	<i>Cmcm</i> (No. 63)	<i>Pnma</i> (No. 62)
<i>a</i> (Å)	3.8386(7)	3.8386(7)	4.1800(7)	10.620(2)
<i>b</i> (Å)	14.196(2)	14.197(2)	13.940(2)	4.1000(8)
<i>c</i> (Å)	10.1577(17)	10.1577(17)	10.6200(17)	13.540(3)
<i>V</i> (Å ³)	553.54(17)	553.54(17)	618.82(18)	589.6(2)
<i>Z</i>	4	4	4	4
F(000)	796	746	904	816
ρ_{calcd} (g cm ⁻³)	5.523	5.2499	5.653	5.373
<i>T</i> (K)	200(2)	293(2)	293(2)	200(2)
Crystal dimensions (mm)	0.270×0.043×0.033	0.323×0.060×0.071	0.151×0.097×0.087	0.192×0.073×0.049
Radiation	Mo <i>K</i> α , $\lambda = 0.71073$ Å			
μ (Mo <i>K</i> α) (mm ⁻¹)	28.764	30.272	36.495	40.823
2 θ limits	5.74 - 61.38	5.74 - 55.08	5.74 - 68.37	4.88 - 60.08
Data collected	-5≤ <i>h</i> ≤ 5, -20≤ <i>k</i> ≤ 20, -14≤ <i>l</i> ≤ 14	-4≤ <i>h</i> ≤ 4, -17≤ <i>k</i> ≤ 17, -13≤ <i>l</i> ≤ 12	-6≤ <i>h</i> ≤ 3, -17≤ <i>k</i> ≤ 22, -12≤ <i>l</i> ≤ 16	-13≤ <i>h</i> ≤ 14, -5≤ <i>k</i> ≤ 5, -19≤ <i>l</i> ≤ 18
No. of measured reflections	4403	2807	2277	5048/
No. of unique reflections with <i>I</i> > 2 σ (<i>I</i>)	512	363	636	972
No. of parameters	23	22	23	36
<i>R</i> (<i>F</i>) for $F_o^2 > 2\sigma(F_o^2)$ ^a	0.0257	0.0237	0.0281	0.0331
<i>R</i> _w (F_o^2) ^b / <i>R</i> _{int}	0.0675/0.0271	0.0610/0.0324	0.0674/0.0478	0.0761/0.0536
Goodness of fit	1.185	1.025	1.274	0.982
($\Delta\rho$) _{max} , ($\Delta\rho$) _{min} (e Å ⁻³)	1.373, -1.074	1.3973, -0.6595	2.046, -2.891	1.7234, -1.9452

Table IV.4 Equivalent isotropic displacement factors (\AA^2) and positional parameters.

Atom	Wyckoff position	s.o.f.	x	Y	z	U_{eq} (\AA^2)
Ba_{0.5}CuZrSe₃						
Ba1	4c	0.5	0	0.74576(6)	0.25	0.0133(2)
Zr1	4a	1	0	0	0	0.01254(19)
Cu1	4c	1	0	0.46230(8)	0.25	0.0179(2)
Se1	8f	1	0	0.37049(4)	0.05046(5)	0.01142(16)
Se2	4c	1	0	0.06851(6)	0.25	0.01275(19)
Sr_{0.5}CuZrSe₃						
Sr1	4c	0.5	0	0.74890(12)	0.25	0.0145(4)
Zr1	4a	1	0	0	0	0.0122(2)
Cu1	4c	1	0	0.46467(9)	0.25	0.0185(3)
Se1	8f	1	0	0.36517(4)	0.05322(6)	0.0112(2)
Se2	4c	1	0	0.07555(6)	0.25	0.0119(2)
BaCuYSe₃						
Ba1	4c	1	0	0.74671(4)	0.2500	0.0112(2)
Y1	4a	1	0	0	0	0.0077(3)
Cu1	4c	1	0	0.46711(10)	0.25	0.0142(4)
Se1	8f	1	0	0.36482(5)	0.05983(6)	0.0082(2)
Se2	4c	1	0	0.06907(7)	0.25	0.0075(3)
SrCuYSe₃						
Sr1	4c	1	0.26253(7)	0.25	0.00078(6)	0.01287(19)
Y1	4c	1	0.00916(6)	0.25	0.24641(5)	0.00862(19)
Cu1	4c	1	0.24284(8)	0.25	0.72144(8)	0.0135(2)
Se1	4c	1	0.055497	0.25	0.61281(5)	0.00953(19)
Se2	4c	1	0.25741(6)	0.25	0.32879(6)	0.00871(19)
Se3	4c	1	0.42449(7)	0.25	0.60816(5)	0.00964(19)

Table IV.5 Selected interatomic distances

Atom pairs	Distances (Å)	Atom pairs	Distances (Å)
Ba_{0.5}CuZrSe₃			
Ba1•••Ba1	3.8386(7)	Zr1•••Se1 (4x)	2.7068(5)
Se1 (4x)	3.3057(7)	Se2 (2x)	2.7193(5)
Se1 (2x)	3.4696(9)	Cu1•••Se1 (2x)	2.4098(9)
Se2 (2x)	3.1647(11)	Se2 (2x)	2.4407(9)
Zr1•••Cu1 (4x)	3.2278(4)		
Sr_{0.5}CuZrSe₃			
Sr1•••Sr1	3.8386(7)	Zr1•••Se1 (4x)	2.7640(5)
Se1 (4x)	3.2254(10)	Se2 (2x)	2.7566(5)
Se1 (2x)	3.4798(11)	Cu1•••Se1 (2x)	2.4476(10)
Se2 (2x)	3.1210(16)	Se2 (2x)	2.4823(10)
Zr1•••Cu1 (4x)	3.2224(4)		
BaCuYSe₃			
Ba1•••Ba1	4.1800(7)	Y1•••Se1 (4x)	2.8849(6)
Se1 (4x)	3.3404(7)	Se2 (2x)	2.8242(5)
Se1 (2x)	3.6392(9)	Cu1•••Se1 (2x)	2.4723(11)
Se2 (2x)	3.2404(10)	Se2 (2x)	2.5275(10)
Y1•••Cu1 (4x)	3.4099(4)		
SrCuYSe₃			
Sr1•••Sr1	4.1000(8)	Y1•••Se1 (2x)	2.8641(8)
Se1 (2x)	3.2033(9)	Se2 (2x)	2.8628(10)
Se2 (2x)	3.1096(9)	Se3 (2x)	2.8822(8)
Se3	3.4705(12)	Cu1•••Se1 (2x)	2.4646(12)
Se3 (2x)	3.1998(9)	Se2	2.5130(8)
		Se3	2.4742(12)

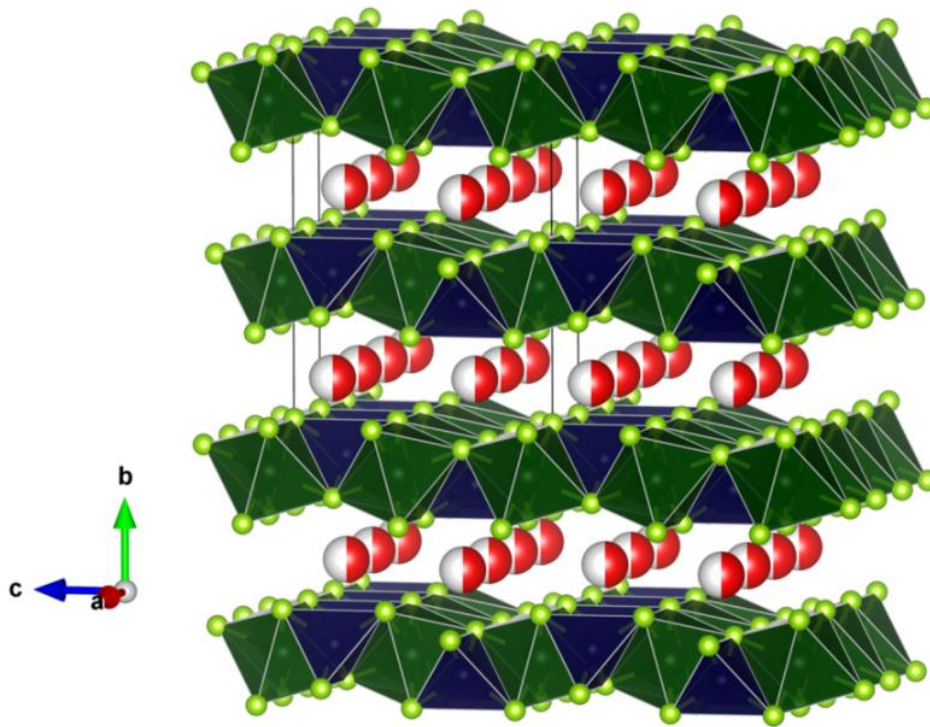


Fig. IV.3 Crystal structure of $A_{0.5}CuZrSe_3$ ($A = Sr, Ba$). ${}^2_{\infty}[CuZrSe_3]^-$ layers in the ac -plane are separated by A^{2+} cations and stacked along b . red: A; white: vacancies, blue: Cu, dark green: Zr, light green: Se.

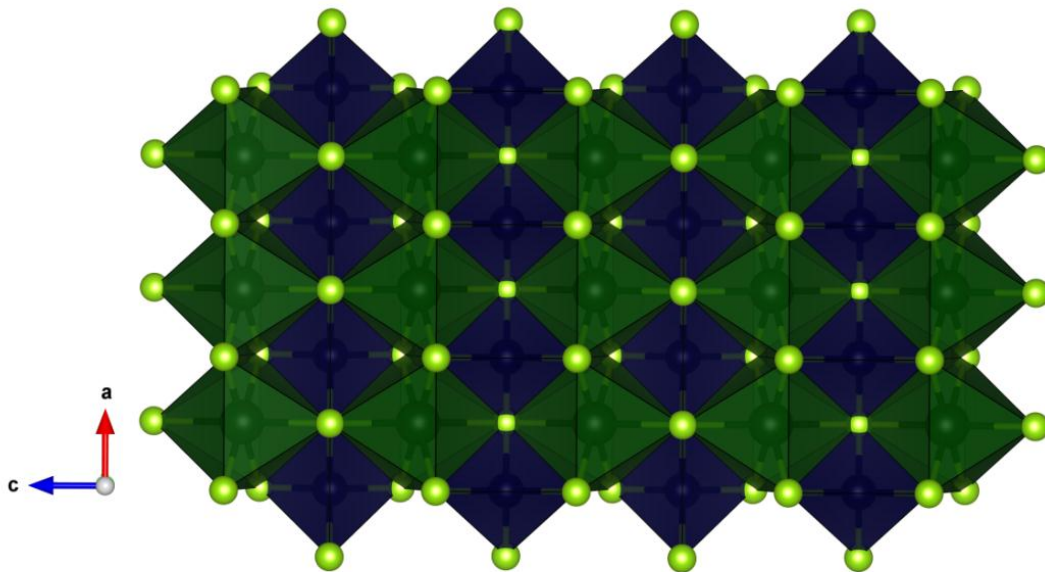


Fig. IV.4 The ${}^2_{\infty}[CuZrSe_3]^-$ layer, which is built up by one dimensional chains of corner-sharing $CuSe_4$ tetrahedra running along a and the two dimensional network of $ZrSe_6$ octahedra sharing edges along a and corners along c . Two separated ${}^1_{\infty}[CuSe_{2.1}Se_{2.2}]^{5-}$ chains are rotated by 180° .

The characteristic building blocks of the ${}^2_{\infty}[\text{CuZrSe}_3]^-$ layers are infinite ${}^1_{\infty}[\text{CuSe}_{2/1}\text{Se}_{2/2}]^{5-}$ chains containing vertex-sharing CuSe_4 tetrahedra (cf. Fig. IV.5a) and ZrSe_6 octahedra, which share edges along [100] and vertices along [001] forming an infinite ${}^2_{\infty}[\text{ZrSe}_{2/2}\text{Se}_{4/2}]^{2-}$ network (cf. Fig. IV.5b). Two parallel ${}^1_{\infty}[\text{CuSe}_{2/1}\text{Se}_{2/2}]^{5-}$ chains are rotated by 180° towards each other and the A^{2+} cations between the ${}^2_{\infty}[\text{CuZrSe}_3]^-$ layers are coordinated by 8 Se atoms forming a $A\text{Se}_8$ bicapped trigonal prism (cf. Fig. IV.5c), where A is either occupied by Sr/Ba or vacant. The lattice parameters of BaCuYSe_3 are already known.^[99] However, no complete structure solution and refinement was performed. BaCuYSe_3 ($a = 4.1800(7) \text{ \AA}$, $b = 13.940(2) \text{ \AA}$, $c = 10.6200(17) \text{ \AA}$) is isostructural to KCuZrS_3 , while SrCuYSe_3 ($a = 10.620(2) \text{ \AA}$, $b = 4.1000(8) \text{ \AA}$, $c = 13.540(3) \text{ \AA}$) crystallizes in the Eu_2CuS_3 structure type (cf. Fig. IV.6). The change in symmetry observed for SrCuYSe_3 does neither affect the building blocks in the ${}^2_{\infty}[\text{CuM}'\text{Se}_3]$ layers described for the Zr compounds, nor their connectivity. However, Sr in SrCuYSe_3 is only coordinated by 7 Se atoms resulting in SrSe_7 monocapped trigonal prisms. For SrCuYSe_3 the stacking direction of the layers changes from [010] to [001] and the ${}^1_{\infty}[\text{CuSe}_{2/1}\text{Se}_{2/2}]^{5-}$ chains run along [010] instead of [100]. Replacing tetravalent Zr by trivalent Y causes an increase in the negative charge of the ${}^2_{\infty}[\text{CuMSe}_3]$ layers from -1 to -2 and the cation position becomes fully occupied by Ba or Sr.

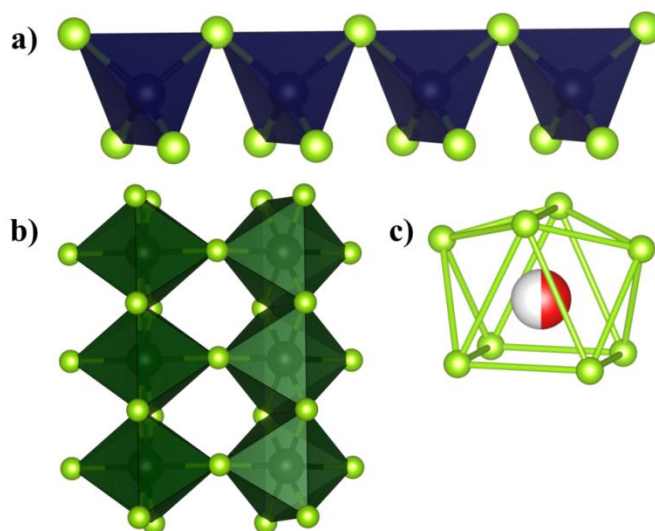


Fig. IV.5 a) linear ${}^1_{\infty}[\text{CuSe}_{2/1}\text{Se}_{2/2}]^{5-}$ chains built up by corner sharing CuSe_4 tetrahedra; b) edge- and corner sharing ZrSe_6 octahedra forming an infinite two dimensional Zr-Se network. The same building blocks and connectivity can be found in the ${}^2_{\infty}[\text{CuYSe}_3]^{2-}$ layers with YSe_6 octahedra; c) $A_{0.5}\text{Se}_8$ bicapped trigonal prism in $A_{0.5}\text{CuZrSe}_3$ ($A = \text{Sr}, \text{Ba}$).

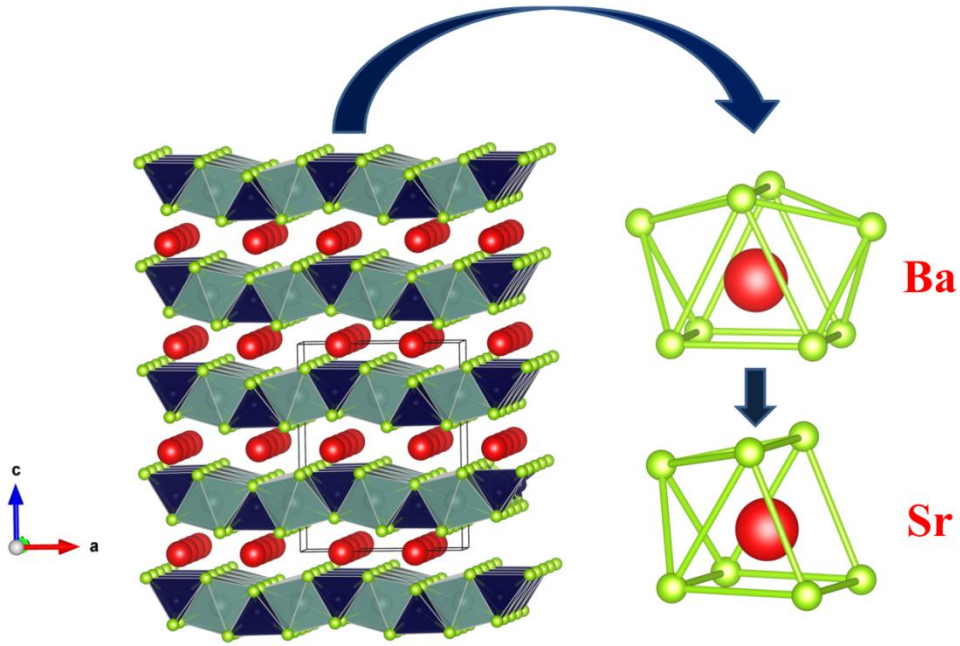


Fig. IV.6 Perspective view of the SrCuYSe₃ crystal structure and an illustration of the different coordination environments of Ba and Sr in the ACuYSe₃ structures; red: Sr, light blue: Y, dark blue: Cu, green: Se.

Ba_{0.5}CuZrSe₃ and BaCuYSe₃ have the same symmetry despite the different ionic radii of Zr⁴⁺ and Y³⁺ of 0.72 Å^[100] and 0.90 Å^[100]. Replacing tetravalent Zr by trivalent Y also leads to an increase in unit cell volume (*cf.* Fig. IV.7) from 553 Å³ to 619 Å³ going from Ba_{0.5}CuZrSe₃ to BaCuYSe₃ due to a larger ionic radius of Y³⁺ (0.90 Å) compared to Zr⁴⁺ (0.72 Å). The larger cell volume is a net result of a simultaneous increase in all intralayer transition metal distances and a decrease in the interlayer distances (*cf.* Fig. IV.8-9) causing **a** and **c** to enlarge and **b** to contract. Replacing the larger Ba²⁺ (ionic radius: 1.42 Å for CN = 8)^[100] by the smaller Sr²⁺ (ionic radii: 1.26 Å for CN = 8 and 1.21 Å for CN = 7)^[100] in ACuYSe₃ has the inverse effect on the unit cell volume. Its decrease from 619 Å³ for BaCuYSe₃ to 590 Å³ for SrCuYSe₃ is mainly caused by shorter Sr²⁺ ••• Sr²⁺ distances compared to Ba²⁺ ••• Ba²⁺ resulting in shorter interlayer distances.

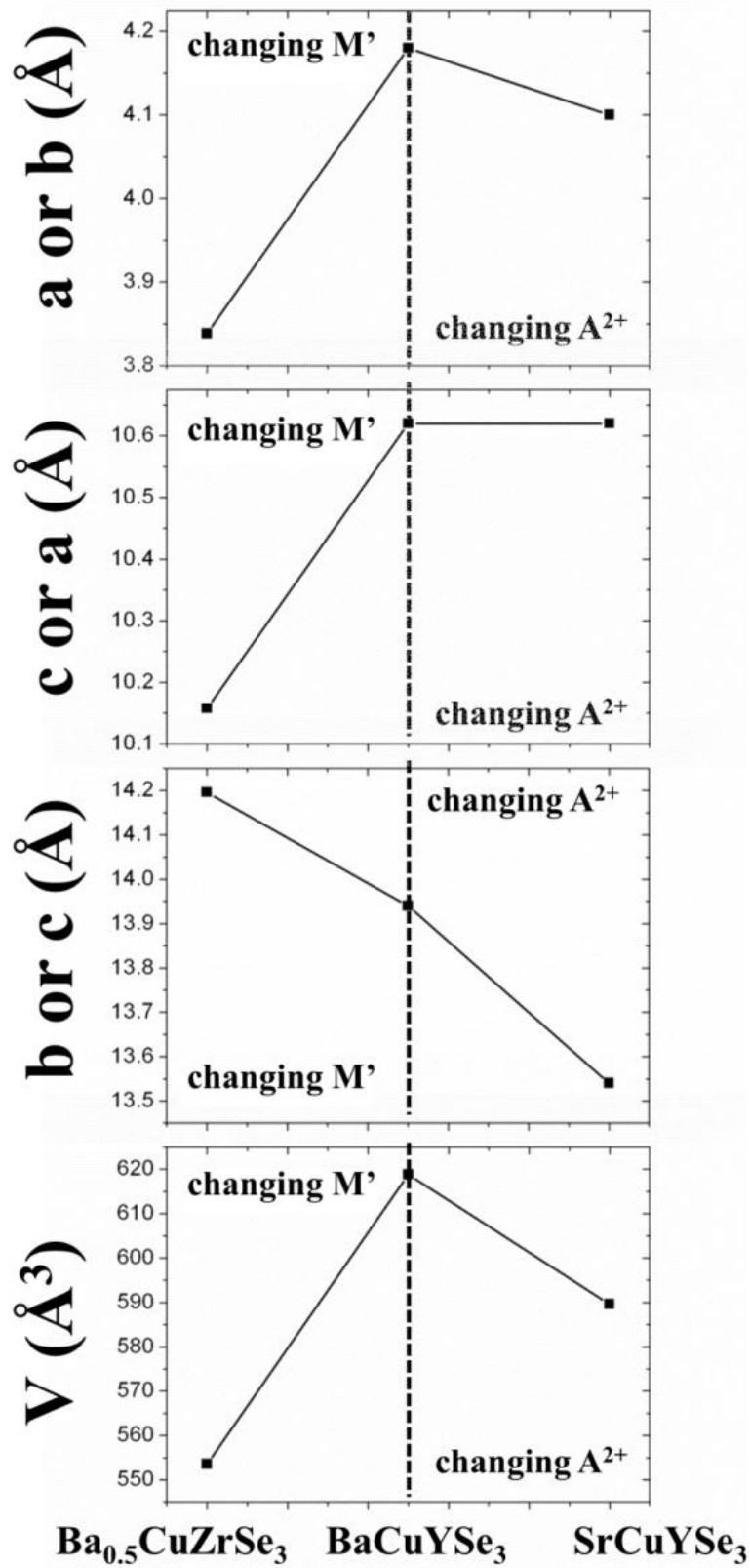


Fig. IV.7 Changes in the lattice parameters and unit cell volume depending on the transition metal and the cation in the structure. The first letters on the y axis correspond to the lattice parameters and unit cell volume of the compounds crystallizing in the higher symmetric $Cmcm$ space group ($Ba_{0.5}CuZrSe_3$ and $BaCuYSe_3$), while the second ones correspond to $SrCuYSe_3$ crystallizing in the lower symmetric space group $Pnma$.

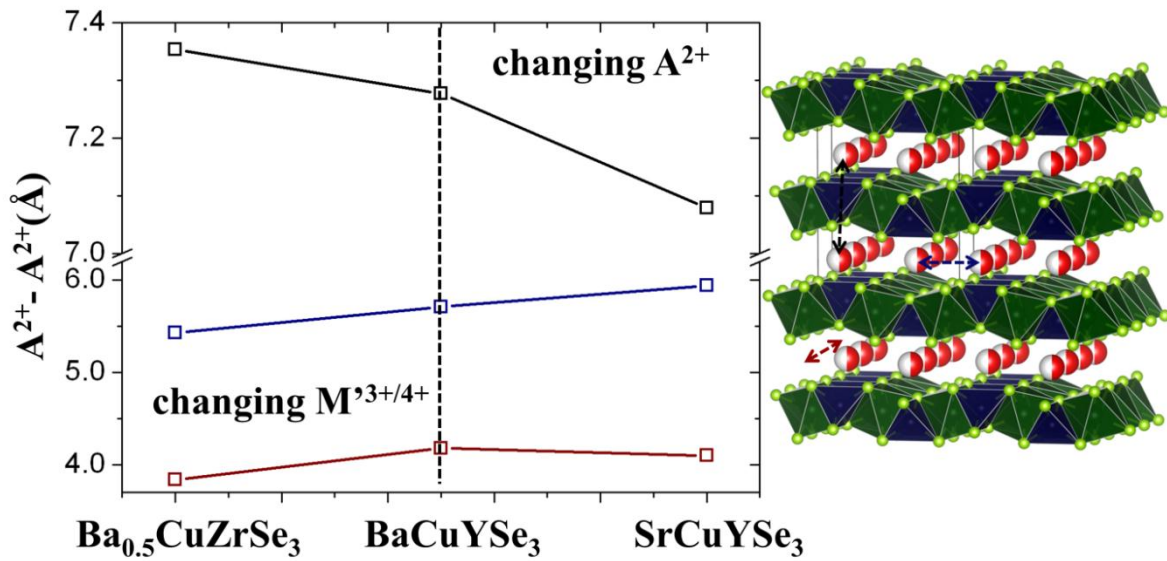


Fig. IV.8 Differences in the $A^{2+}\cdots A^{2+}$ interatomic distances between $Ba_{0.5}CuZrSe_3$, $BaCuYSe_3$ and $SrCuYSe_3$. Black, blue and red arrows mark the corresponding distances in the structure (red: Ba, Sr; white: vacancies in the case of $Ba_{0.5}CuZrSe_3$; light green: Se, dark green: Zr/Y, blue: Cu).

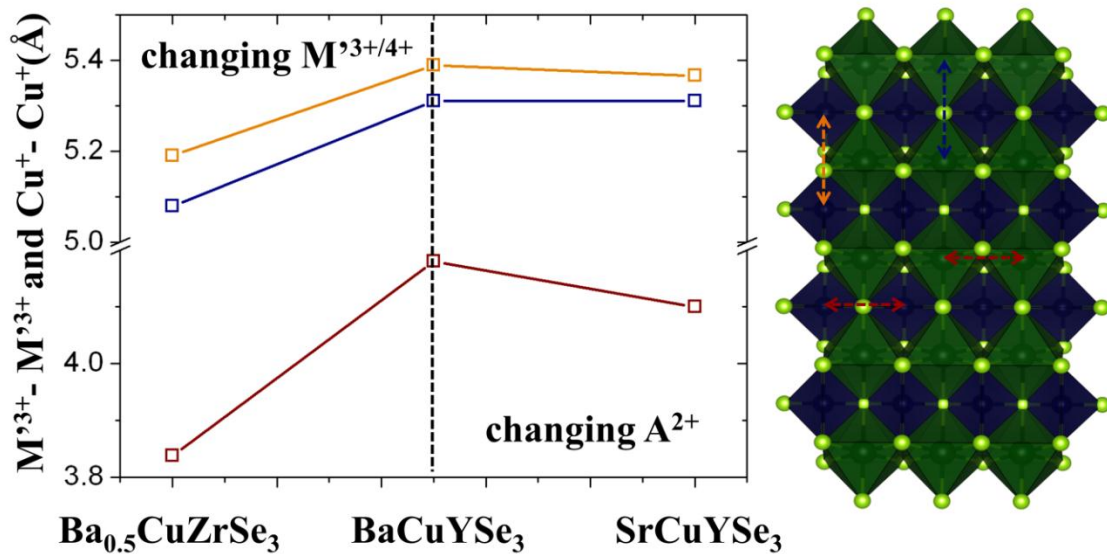


Fig. IV.9 Differences in the intralayer transition metal distances between $Ba_{0.5}CuZrSe_3$, $BaCuYSe_3$ and $SrCuYSe_3$. Orange, blue and red arrows mark the corresponding distances in the ${}^2_{\infty}[CuZrSe_3]^-$ and ${}^2_{\infty}[CuYSe_3]^{2-}$ layers (light green: Se, dark green: Zr/Y, blue: Cu).

2.1.2.2 Influence of the $r(A^{2+})/r(M'^{3+/4+})$ ratio on the structure type and symmetry

In this part of the chapter the influence of the $r(A^{2+})/r(M'^{3+/4+})$ ratio of the A and M' ionic radii on the structure type and symmetry is discussed. Within the four new copper-(I)-selenides $A_{0.5}CuZrSe_3$ and $ACuYSe_3$ (A = Sr, Ba) there is only one compound, $SrCuYSe_3$, crystallizing in the lower symmetric space group $Pnma$, a direct subgroup of the higher symmetric space group $Cmcm$, in which the other three compounds crystallize. This gain or reduction in symmetry is also observed for the $SrCuM'Se_3$ compounds, which are higher symmetric ($Cmcm$) for the smaller and heavier lanthanides ($M' = Lu-Ho$), while the symmetry is reduced for $M' = Dy-Gd, Sm, Nd-La$. The same phenomenon was found for the $EuCuM'S_3$ compounds, which crystallize in the higher symmetric $KCuZrS_3$ structure type for $M' = Lu, Yb, Tm$ and in the lower symmetric Eu_2CuSe_3 structure type for $M' = Y, Dy, Tb, Gd$ and Eu . This part of the chapter aims at explaining this reoccurring change in structure type and symmetry. Previous studies led to the understanding that replacing sulfur by selenium does not change the structure type, while the size of M' has a significant influence on the structure type and symmetry.^[85] Suggestions were made, that the size of the A atom somewhat influences structure type and symmetry as well, but no clear trend could be derived.^[85]

Going from $Ba_{0.5}CuZrSe_3$ to $BaCuYSe_3$ changes neither symmetry nor structure type despite the different ionic radii of Zr^{4+} and Y^{3+} of 0.72 Å and 0.90 Å, while the symmetry is reduced from $Cmcm$ to $Pnma$ when going from $BaCuYSe_3$ and $Sr_{0.5}CuZrSe_3$ to $SrCuYSe_3$. These results clearly show, that changes in the size of M' or A alone cannot explain this gain or reduction in symmetry. Therefore, the influence of the ratio of the A^{2+} and $M'^{3+/4+}$ ionic radii on the symmetry and structure type of $A_{0.5}CuZrSe_3$ and $ACuYSe_3$ (A = Sr, Ba) was investigated and the study was extended towards the $SrCuM'Se_3$ $M' = Lu, Gd, Pr, Ce, La$) compounds (*cf.* Fig. IV.10).

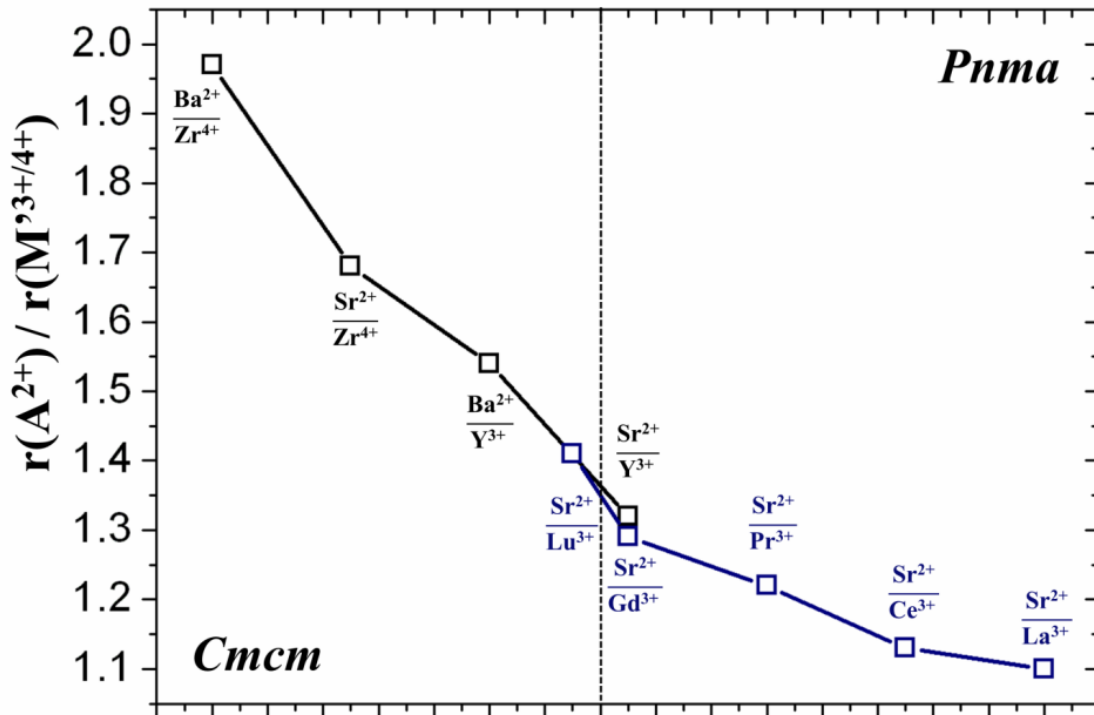


Fig. IV.10 Ratio between the cation and transition metal/lanthanum ionic radii $r(A^{2+})/r(M^{3+/4+})$. Black squares: the four title compounds containing transition metals; blue squares: $SrMCuSe_3$ compounds with $M' = Lu, Gd, Pr, Ce, La$. The image shows the symmetry dependence on the $r(A^{2+})/r(M^{3+/4+})$ ratio with a change from the higher symmetric space group *Cmcm* to the lower symmetric space group *Pnma* between $1.41 < r(A^{2+})/r(M^{3+/4+}) < 1.32$. All ionic radii were taken from Ref [100].

Comparing the ratio between the cation and transition metal/lanthanum ionic radii $r(A^{2+})/r(M^{3+/4+})$ shows, that the higher symmetric $KCuZrS_3$ structure type (*Cmcm*) is stabilized for $r(A^{2+})/r(M^{3+/4+}) > 1.32$, while the lower symmetric space group *Pnma* is favored for $r(A^{2+})/r(M^{3+/4+}) < 1.41$ (cf. Fig. IV.10). Hence, the threshold for a change from the higher symmetric space group *Cmcm* to the lower symmetric subgroup *Pnma* lies in between these two values. The difference in symmetry observed for $SrCuYSe_3$, which is accompanied by a change in the local coordination environment of the A^{2+} cation from a bicapped trigonal $BaSe_8$ prism to a monocapped trigonal $SrSe_7$ prism can therefore be explained by its $r(Sr^{2+})/r(Y^{3+})$ ratio of 1.32 – the lowest for the four new compounds $A_{0.5}CuZrSe_3$ and $ACuYSe_3$ ($A = Sr, Ba$). Hence, Yttrium represents the frontier between transition metal and lanthanide chemistry in the “1113 family”.

The maximum cation-selenium distances increase with a decreasing $r(A^{2+})/r(M^{3+/4+})$ ratio (cf. Fig. IV.10-11) and the distortion around the $CuSe_4$ and $M'Se_6$ polyhedra is largest for $BaCuYSe_3$ with a $r(A^{2+})/r(M^{3+/4+})$ ratio closest to the critical one before the $Cmcm-Pnma$ transition. Hence, it is probable that too long cation-selenium distances in combination with a certain degree of structural distortion around the $CuSe_4$ and $M'Se_6$ polyhedra triggers the change in A^{2+} coordination number and symmetry, which is accompanied by a reduction in structure distortion and maximum cation-selenium distances (cf. Fig. IV.11).

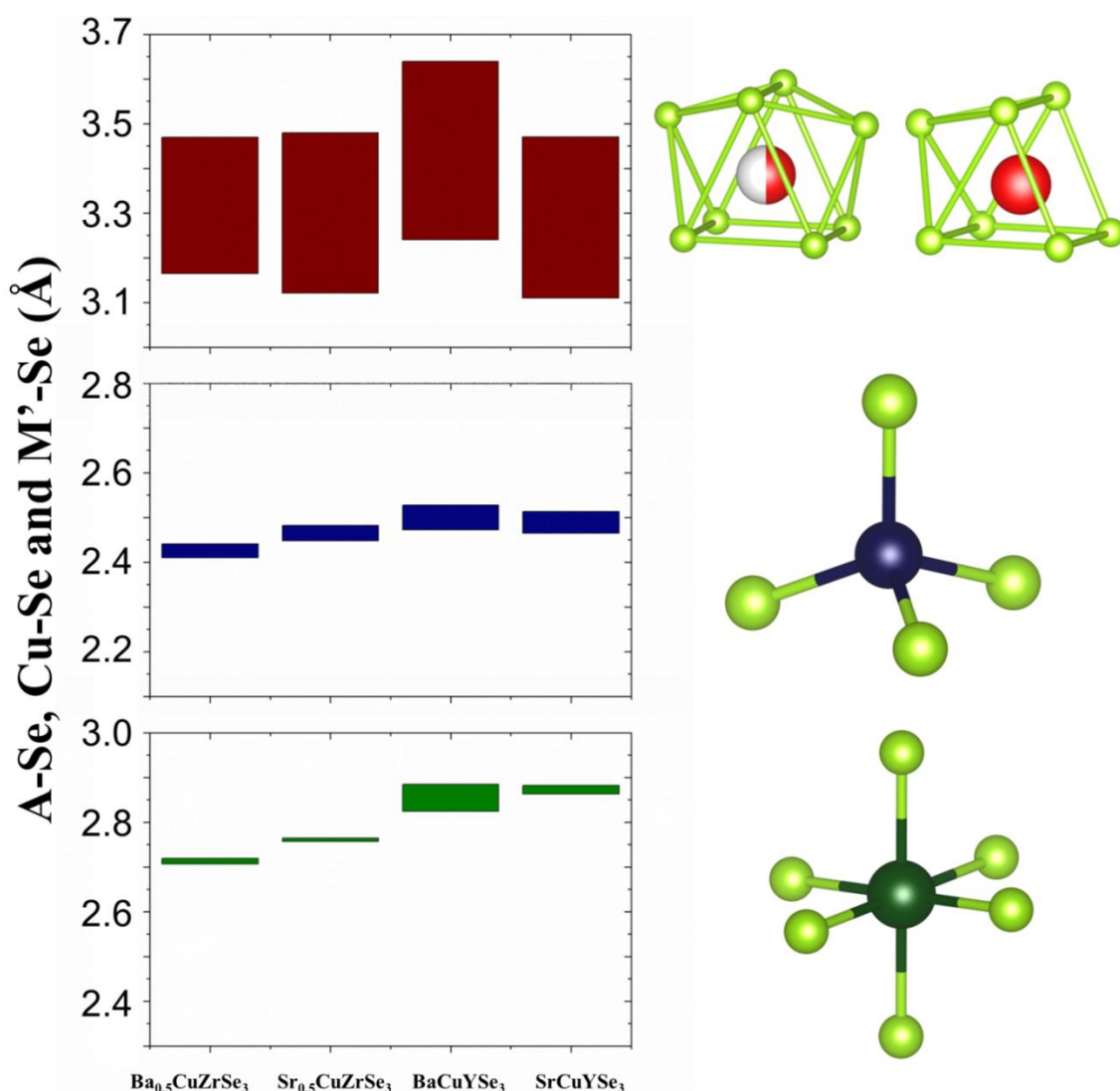


Fig. IV.11 Red: $A\cdots Se$ ($A = Sr, Ba$), blue: $Cu\cdots Se$ and green: $M'\cdots Se$ ($M = Zr, Y$) distance ranges in the four title compounds. The largest distortion in the $CuSe_4$ tetrahedra and $M'Se_6$ octahedra is present for $BaCuYSe_3$ with a $r(A^{2+})/r(M^{3+/4+})$ ratio closest to the critical one and an increase in the maximum cation-selenium distances with a decreasing $r(A^{2+})/r(M^{3+/4+})$ ratio was found for the three higher symmetric title compounds.

2.1.3 Conclusion

The four new quaternary copper(I) selenides, $\text{Sr}_{0.5}\text{CuZrSe}_3$, $\text{Ba}_{0.5}\text{CuZrSe}_3$, SrCuYSe_3 and BaCuYSe_3 were synthesized by high-temperature solid state reactions and their crystal structures were determined using single-crystal X-ray diffraction. The discovery of $\text{Sr}_{0.5}\text{CuZrSe}_3$ and $\text{Ba}_{0.5}\text{CuZrSe}_3$ shows that there is a third subgroup, $\text{A}_{0.5}^{+2}\text{M}^{+1}\text{M}'^{+4}(\text{Q}^{2-})_3$, within the 1113 family, where half of the A site is vacant. These findings might give access to an entirely new group of compounds within the 1113 family with $\text{A}_{0.5}\text{CuZrSe}_3$ (A = Sr, Ba) as its first members. A combination of the alkaline-earth metals Ba and Sr with the group 4 transition metal Zr leads to a stabilization of the KCuZrS_3 structure type accompanied by the formation of cation vacancies. Replacing tetravalent Zr by trivalent Y causes an increase in the negative charge of the $\text{}^2_{\infty}[\text{CuM}'\text{Se}_3]$ layers from -1 to -2 and the cation position is fully occupied by Ba or Sr. $\text{Ba}_{0.5}\text{CuZrSe}_3$, $\text{Sr}_{0.5}\text{CuZrSe}_3$ and BaCuYSe_3 crystallize in the higher symmetric KCuZrS_3 structure type (*Cmcm*), while SrCuYSe_3 is isostructural to Eu_2CuS_3 crystallizing in the orthorhombic space group *Pnma* - a direct subgroup of *Cmcm*. The cation coordination environment in BaCuYSe_3 and SrCuYSe_3 changes from a bicapped trigonal BaSe_8 prism towards a monocapped trigonal SrSe_7 prism, the $\text{}^2_{\infty}[\text{CuMSe}_3]$ layers are stacked along [001] instead of [010] and the $\text{}^1_{\infty}[\text{CuSe}_{2/1}\text{Se}_{2/2}]^{5-}$ chains run along [010] instead of [100]. The ratio between the cation and transition metal (or lanthanide) ionic radii $r(\text{A}^{2+})/r(\text{M}'^{3+/4+})$ determines symmetry and structure type, which does not only apply to the four title compounds, but also to the previously reported SrCuMSe_3 ($\text{M} = \text{La, Ce, Pr, Gd, Lu}$) family. Compounds with $r(\text{A}^{2+})/r(\text{M}'^{3+/4+}) > 1.32$ crystallize in the higher symmetric KCuZrS_3 structure (*Cmcm*), while the lower symmetric Eu_2CuS_3 structure type (*Pnma*) are favored for $r(\text{A}^{2+})/r(\text{M}'^{3+/4+}) < 1.41$. A transition from the higher to the lower symmetric space group occurs between these two values, which explains the lower symmetry observed for $\text{SrCuM}'\text{Se}_3$ ($\text{M}' = \text{Gd, Pr, Ce, La}$) and SrCuYSe_3 . The $r(\text{A}^{2+})/r(\text{M}'^{3+/4+})$ ratio can therefore be used as a very intuitive and powerful parameter to explain and predict structure type and symmetry for compounds belonging to the 1113 family.

3. Polar chalcogenides with stereoactive lone pairs and potential resonant bonding

Chemical bonding in the 1113 family can be entirely described by $2c-2e$ bonds, which is also the case for $\text{Ba}_2\text{FePnSe}_5$ (Pn = Sb, Bi), which are the subject of this part of the chapter. These compounds were synthesized not only with the intention of making new compounds with complex crystal structures in order to obtain low thermal conductivities, but also to synthesize compounds with potentially interesting magnetic properties. Synthesizing $\text{Ba}_2\text{FePnSe}_5$ (Pn = Sb, Bi) was a choice based on the fact that Fe-based compounds can be superconducting at low temperatures and that the $\text{Ba}_2\text{FePnS}_5$ (Pn = Sb, Bi) phases were already known. Another factor leading to the study of $\text{Ba}_2\text{FePnSe}_5$ (Pn = Sb, Bi) was the stereoactive lone pairs of Sb and Bi, which can lead to structural distortions. These can enhance structural complexity and result in a distortion of neighbouring Fe centered coordination polyhedra, which can be accompanied by interesting magnetic properties and the breaking of centrosymmetry.

3.1 $\text{Ba}_2\text{FePnSe}_5$ (Pn = Sb, Bi)

3.1.1 Introduction

Iron selenides, which contain FeSe_4 tetrahedra receive increasing attention since the discovery of superconductivity in FeSe with $T_c \sim 30$ K and related intercalation compounds such as $\text{K}_x\text{Fe}_2\text{Se}_2$ and others.^[101-107] Combining these Fe-Se building blocks with strong cations such as Ba led to a variety of compounds with complex crystal structures and mixed-valent Fe, where a charge transfer from the cation to the Fe-Se network occurs.^[108-110] By using elements with stereoactive lone-pairs (e.g. Sb and Bi) asymmetric or distorted coordination environments and hence increasingly complex crystal structures with inherently low thermal conductivities can be obtained. The two isostructural compounds $\text{Ba}_2\text{FePnSe}_5$ (Pn = Sb, Bi) were simultaneously and independently discovered by Wang et al.^[111] and their crystal structure is isomorphic to the high-pressure phase of Ba_3FeS_5 .^[112] Also reported are the related compounds $\text{Ba}_2\text{FePnS}_5$ (Pn = Sb, Bi)^[113], $\text{Ba}_2\text{GaPnQ}_5$ (Pn = Sb, Bi, Q = Se, Te)^[114], $\text{Ba}_2\text{BiGaS}_5$ ^[115], $\text{Ba}_2\text{InSbQ}_5$ (Q = Se, Te).^[114]

All these compounds are centrosymmetric except $\text{Ba}_2\text{InSbSe}_5$, which is isostructural to $\text{Ba}_2\text{BiInS}_5$ ^[115] and crystallizes in the noncentrosymmetric space group $Cmc2_1$. $\text{Ba}_2\text{FePnSe}_5$ (Pn = Sb, Bi) melt congruently and recrystallize at T_m/T_c 1055 K/1001 K ($\text{Ba}_2\text{FeSbSe}_5$) and 1105 K/1049 K ($\text{Ba}_2\text{FeBiSe}_5$) and they order antiferromagnetically below $T_N = 58$ K ($\text{Ba}_2\text{FeSbSe}_5$) and $T_N = 79$ K ($\text{Ba}_2\text{FeBiSe}_5$).^[111] At this stage, a short introduction into the field of chalcogenide-based phase change materials and their applications^[116] is given since $\text{Ba}_2\text{FePnSe}_5$ (Pn = Sb, Bi) undergo rapid, irradiation induced phase changes between a crystalline and amorphous phase (*cf.* section *Irradiation induced phase changes between crystalline and amorphous $\text{Ba}_2\text{FePnSe}_5$ (Pn = Sb, Bi)*). Stanford Ovshinsky can be considered as the founding father of phase-change materials, which exhibit an intriguing combination of physical properties. By applying electrical or laser pulses a rapid change (usually within nanoseconds) between a crystalline and an amorphous phase can be achieved. Both phases significantly differ in resistivity and optical properties due to the changes in the local atomic arrangement.^[117,118] Optical data storage, random access memory, neuromorphic computing, thermal energy storage and thermoelectric energy conversion are only a few examples where phase-change materials are of interest.^[36,119-122] It is believed, that the origin of the phase-change properties lies in a transition from classical covalent bonding in the amorphous phase to resonant bonding in the crystalline phase as it occurs in IV-VI, V_2 -VI₃ and V materials such as Sb. This type of bonding is also considered as one origin of low lattice thermal conductivities in IV-VI compounds crystallizing in the rocksalt-type structure.^[25,26] In general elements with small electronegativity differences are required for phase-change applications since a high ionicity reduces resonant bonding due to a localization of charges at the ion cores.^[123] The Pn-Se (Pn = Sb, Bi) network in the $[\text{FePnSe}_5]^{4-}$ anionic framework is built up by elements with similar electronegativities and the PnSe_6 octahedra are highly distorted in both compounds, which is ideal for resonant bonding, effective phonon scattering processes and to achieve low thermal conductivities. The latter usually change upon crystallization due to a change of bonding accompanied by a simultaneous increase in the sound velocity and a softening of the optical phonon modes.^[124] Therefore, the thermal conductivity can be used as an indicator for the transition from an amorphous to a crystalline state and vice versa. A previous study also shows that $\text{Ba}_2\text{FeBiSe}_5$ has promising photoelectric properties interesting for solar light absorbers and photosensitive switching^[125], which makes $\text{Ba}_2\text{FeSbSe}_5$ and $\text{Ba}_2\text{FeBiSe}_5$ highly interesting semiconductors.

3.1.2 Results and Discussion

3.1.2.1 Crystal structure

The results of the structure solution and refinement of $\text{Ba}_2\text{FePnSe}_5$ (Pn = Sb, Bi) are summarized in Table IV.6-7. Important crystallographic data is summarized in Table IV.6, while equivalent isotropic displacement factors and positional parameters can be found in Table IV.7. The crystal structures of $\text{Ba}_2\text{FePnSe}_5$ (Pn = Sb, Bi) contains a $[\text{FePnSe}_5]^{4-}$ channel-like network with “channels” running along **b** (*cf.* Fig. IV.12). The Ba atoms are located within the “channels” and they are coordinated by 8 Se atoms forming a distorted bicapped trigonal prism (*cf.* Fig. IV.13). The $[\text{FePnSe}_5]^{4-}$ network is built up by distorted FeSe_4 tetrahedra and PnSe_6 octahedra. The former are connected either via corners and edges, only corners or only edges to the PnSe_6 octahedra (*cf.* Fig. IV.12a-c), while the PnSe_6 octahedra are either not connected to each other or they share edges.

Table IV.6 Crystallographic data for Ba₂FePnSe₅ (Pn = Sb, Bi).

	Ba₂FeSbSe₅	Ba₂FeBiSe₅
Formula weight (amu)	847.08	934.31
Space group	<i>Pnma</i> (No. 62)	<i>Pnma</i> (No. 62)
<i>a</i> (Å)	12.650(3)	12.620(3)
<i>b</i> (Å)	9.1400(18)	9.1200(18)
<i>c</i> (Å)	9.1700(18)	9.1700(18)
<i>V</i> (Å ³)	1060.2(4)	1055.4(4)
<i>Z</i>	4	4
F(000)	1436	1564
ρ_{calcd} (g cm ⁻³)	5.307	5.880
<i>T</i> (K)	293(2)	293(2)
Crystal dimensions (mm)	0.118x0.130x0.142	0.218x0.294x0.317
Radiation	Mo <i>K</i> α , $\lambda = 0.71073$ Å	
μ (Mo <i>K</i> α) (mm ⁻¹)	28.28	42.501
2θ limits	4.74–72.77 °	4.74–83.79
Data collected	-21 $\leq h \leq$ 0, -14 $\leq k \leq$ 0, -15 $\leq l \leq$ 0	-22 $\leq h \leq$ 23, -17 $\leq k \leq$ 14, -15 $\leq l \leq$ 17
No. of reflections	2822	43023
No. of unique reflections	2613	3793
No. of parameters	49	49
$R(F)$ for $F_o^2 > 2\sigma(F_o^2)$ ^a	0.031	0.0595
R_{int}	0.045	0.0795
Goodness of fit	1.19	1.11
$(\Delta\rho)_{\text{max}}, (\Delta\rho)_{\text{min}}$ (e Å ⁻³)	2.25, -2.03	4.77, -9.05

Table IV.7 Thermal displacement parameters (\AA^2) and positional parameters for $\text{Ba}_2\text{FePnSe}_5$ (Pn = Sb, Bi).

Atom	Wyckoff position	s.o.f.	x	y	z	U_{11} (\AA^2)	U_{22} (\AA^2)	U_{33} (\AA^2)	U_{eq} (\AA^2)
$\text{Ba}_2\text{FeSbSe}_5$									
Ba1	8d	1	-0.00762(4)	0.37692(4)	0.01273(11)	0.01311(18)	0.0106(2)	0.01448(17)	0.01273(11)
Sb1	4c	1	0.02806(5)	0.2500	0.01240(6)	0.0119(3)	0.0135(3)	0.0145(2)	0.01331(14)
Se1	8d	1	-0.05782(5)	-0.03987(8)	0.18326(7)	0.0148(3)	0.0103(3)	0.0146(3)	0.01325(14)
Se2	4c	1	0.00716(7)	-0.2500	0.54270(9)	0.0111(4)	0.0154(5)	0.0129(3)	0.01313(18)
Se3	4c	1	0.21724(7)	0.2500	0.11656(9)	0.0123(4)	0.0127(5)	0.0138(3)	0.01292(18)
Se4	4c	1	0.27926(7)	0.2500	0.60793(9)	0.0097(3)	0.0144(5)	0.0147(3)	0.01293(18)
Fe1	4c	1	0.09763(10)	0.2500	0.66698(13)	0.0107(5)	0.0101(6)	0.0114(5)	0.0107(2)
$\text{Ba}_2\text{FeBiSe}_5$									
Ba1	8d	1	0.32377(3)	0.00864(4)	0.61818(4)	0.01190(16)	0.01430(17)	0.01867(15)	0.01439(10)
Bi1	4c	1	0.02334(3)	0.2500	0.47631(4)	0.01351(19)	0.01190(18)	0.01776(17)	0.01495(9)
Se1	8d	1	0.05846(5)	0.03809(7)	0.68701(7)	0.0150(3)	0.0112(3)	0.0182(3)	0.01480(13)
Se2	4c	1	0.22077(8)	0.2500	0.37426(9)	0.0125(4)	0.0151(4)	0.0169(3)	0.01486(16)
Se3	4c	1	0.27978(8)	0.2500	0.88874(9)	0.0103(4)	0.0156(4)	0.0180(4)	0.01464(16)
Se4	4c	1	0.49424(8)	0.2500	0.45738(10)	0.0110(4)	0.0158(4)	0.0172(3)	0.01466(16)
Fe1	4c	1	0.40296(10)	-0.2500	0.33155(13)	0.0102(5)	0.0110(5)	0.0143(4)	0.0119(2)

Particularly interesting is the distortion of the PnSe_6 polyhedra around Sb and Bi (*cf.* Fig. IV.13). This distortion originates in a displacement of the Pn atoms from the center of the PnSe_6 polyhedra resulting in three shorter (stronger) and three longer (weaker) bonds per octahedron, which can be described as a 3+3 coordination. The different bond lengths are caused by the presence of stereoactive $5s^2$ and $6s^2$ Sb and Bi lone pairs, which are not significantly contributing to the bonding (*cf.* section *Electronic structure and electrical resistivity*). Calculating the electron localization function (ELF) allows the visualization of the nodal structure of the molecular orbitals, including lone pair electrons.^[126] Fig. IV.13 a) and b) contain the 3D isosurfaces for an ELF value of 0.82 for which the lone pairs appear lobe-shaped.

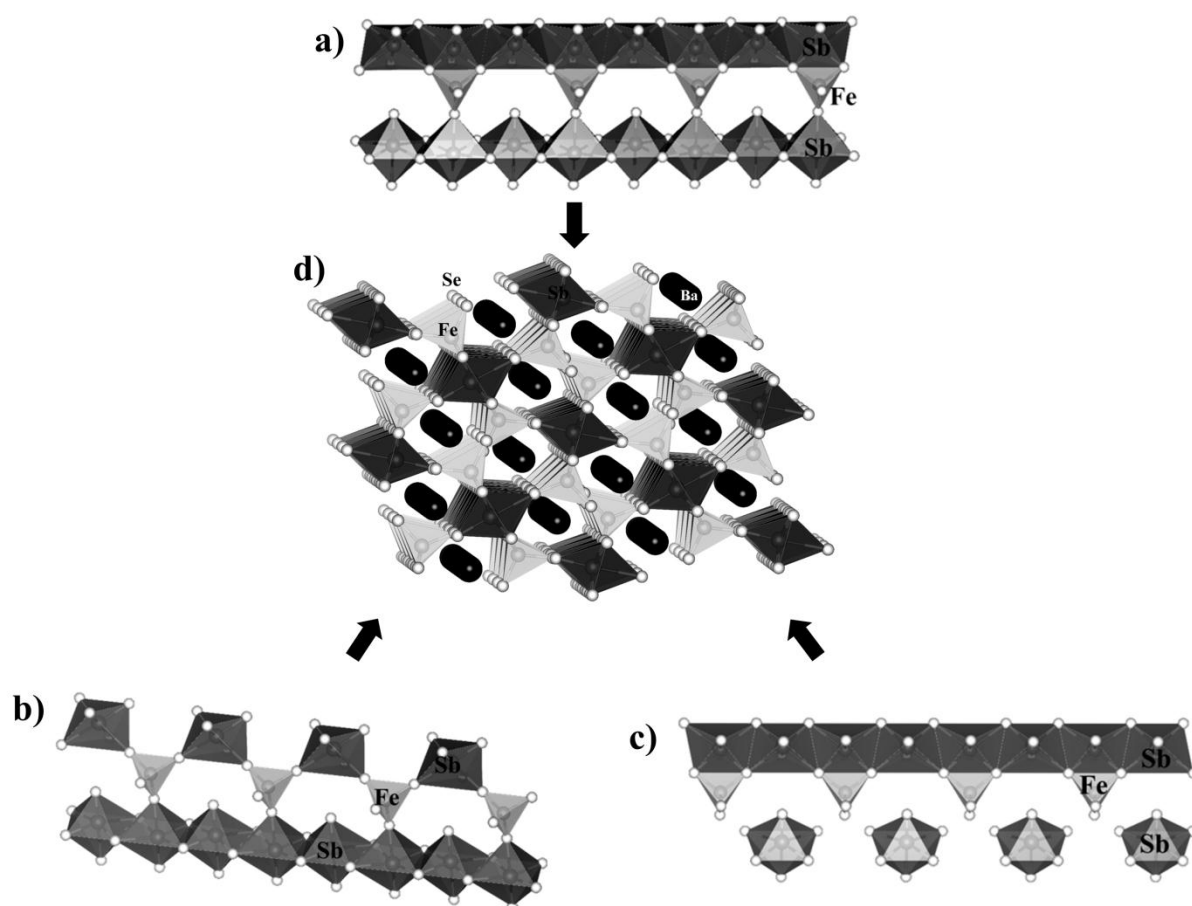


Fig. IV.12 Crystal structure of $\text{Ba}_2\text{FeSbSe}_5$; a) –c) show how the FeSe_4 tetrahedra are connected to the SbSe_6 octahedra; in a) the FeSe_4 tetrahedra are connected to the SbSe_6 octahedra via corners and edges, while in b) and c) they are connected only via corners and edges, respectively; d) shows the complete crystal structure (black: Ba, light grey: Fe, dark grey: Sb, white: Se); replacing Sb by Bi results in the $\text{Ba}_2\text{FeBiSe}_5$ structure.

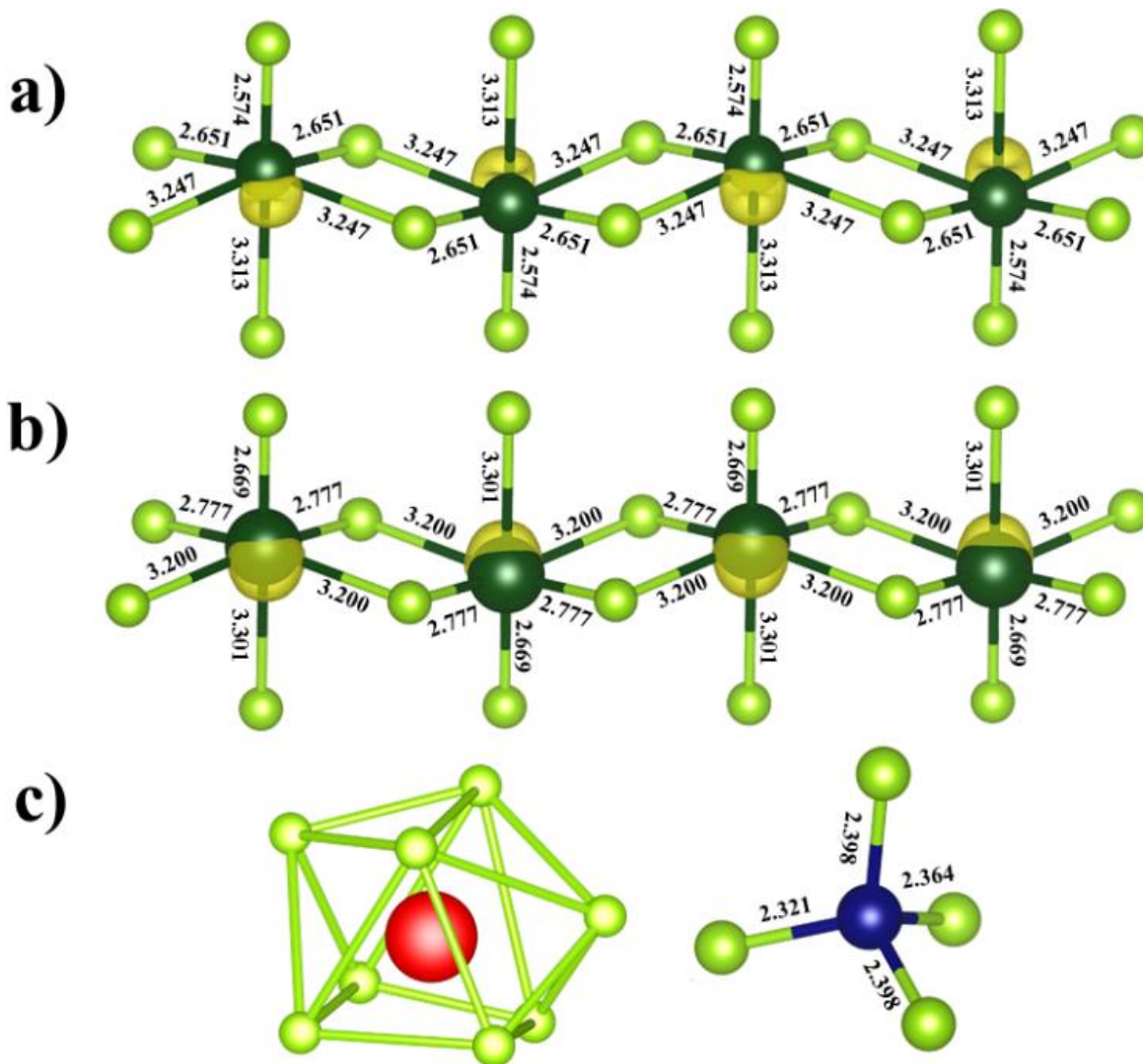


Fig. IV.13 a) and b) show the coordination environment of Pn = Sb and Bi and their displacement from the center of the PnSe₆ octahedra caused by the stereoactive 5s² and 6s² Sb and Bi lone pairs. These are interpreted from DFT calculated Electron Localization Functions (ELF): the 3D isosurfaces (shown in yellow) are represented for ELF= 0.82 for both compounds. The distorted coordination environments of Ba (bicapped, trigonal prismatic) and Fe (tetrahedral) in Ba₂FeBiSe₅ are depicted in c). Ba: red, Bi: dark green, Se: light green, Fe: blue.

5g of polycrystalline Ba₂FePnSe₅ with experimental densities between 91 % and 96 % of the theoretical values were obtained by ball milling and subsequent Spark Plasma Sintering. The corresponding Rietveld refinement results are shown in Fig. IV.14 and Table IV.8. The structural model obtained by Wang et al.^[111] was used to perform the corresponding refinements.

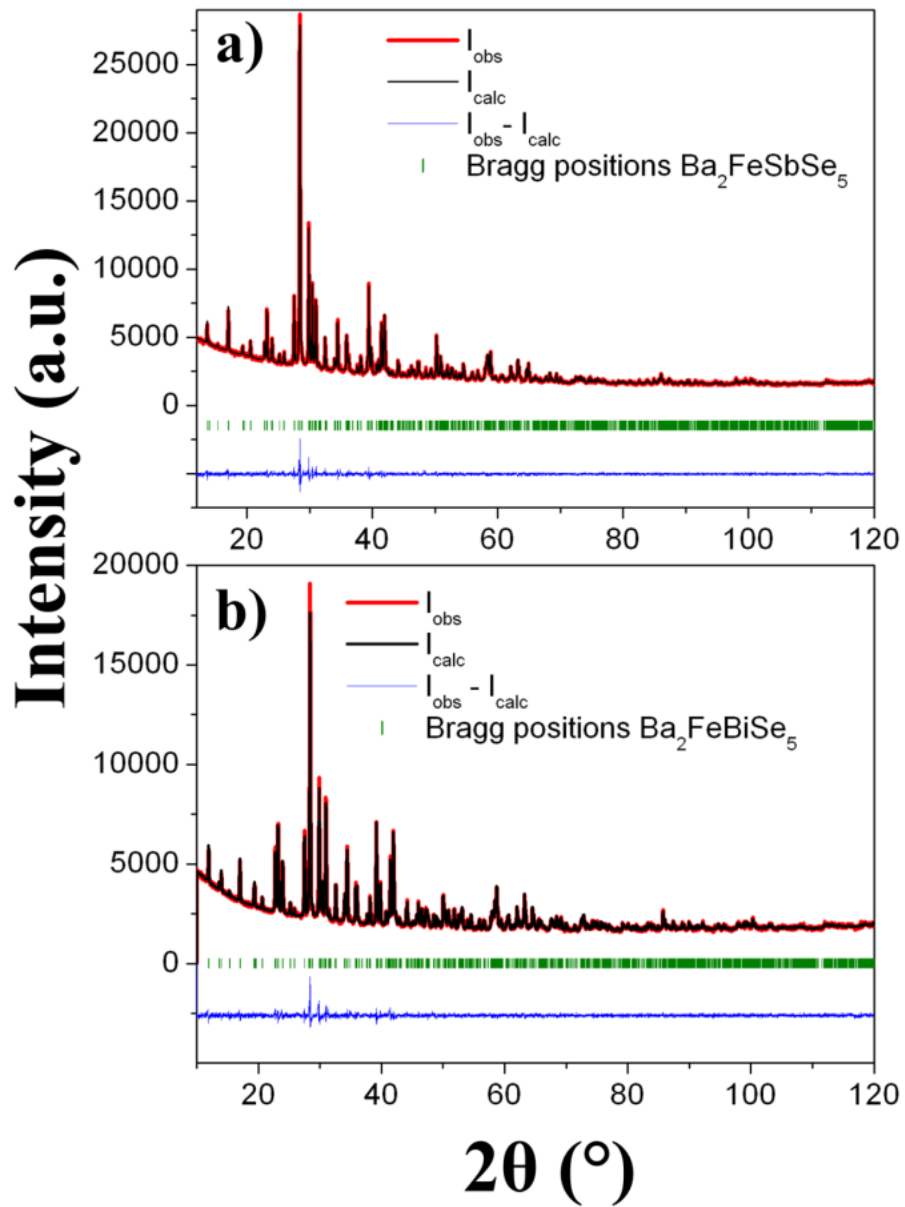


Fig. IV.14 Rietveld refinements of experimental diffraction patterns (red): a) $\text{Ba}_2\text{FeSbSe}_5$ and b) $\text{Ba}_2\text{FeBiSe}_5$. Calculated diffraction patterns, difference plots and reflection positions are depicted in black, blue and green respectively.

Table IV.8Rietveld refinement results for Ba₂FePnSe₅ (Pn = Sb, Bi).

Nominal composition	Ba₂FeSbSe₅	Ba₂FeBiSe₅
Space group	<i>Pnma</i> (No. 62)	<i>Pnma</i> (No. 62)
Z	4	4
<i>a</i> (Å)	12.64916(19)	12.65032(15)
<i>b</i> (Å)	9.13368(13)	9.15193(13)
<i>c</i> (Å)	9.18267(15)	9.19415(11)
<i>V</i> (Å ³)	1060.906(28)	1064.452(24)
ρ_{calc} (gcm ⁻³)	5.304	5.830
Radiation	Cu-K $\alpha_{1/2}$, $\lambda_{1/2} = 1.54060/1.54439$ Å	
2θ limits (°)	5.01-119.99	5.01-119.99
Constraints	0	0
No. of reflections	1771	1781
Refined parameters	114	86
R_f	0.0371	0.0383
R_{bragg}	0.0406	0.0421
χ^2	1.88	1.83

3.1.2.2 Electronic structure and electrical resistivity

In this part of the chapter the electronic ground state of $\text{Ba}_2\text{FePnSe}_5$ ($\text{Pn} = \text{Sb, Bi}$) is determined based on band structure calculations and electrical resistivity measurements. First-principle electronic structure calculations were carried out for $\text{Ba}_2\text{FeSbSe}_5$ and $\text{Ba}_2\text{FeBiSe}_5$ using GGA and GGA+ U ($U_{\text{eff}} = 2.5$ eV) calculations with the antiferromagnetic configuration represented in Fig. IV.15. The reason for including a Hubbard term of $U_{\text{eff}} = 2.5$ eV is discussed at a later stage, when the theoretical band gaps are compared to those found experimentally. GGA calculations without Hubbard correction result in band structures and total density of states (DOS) represented in Fig. IV.16.

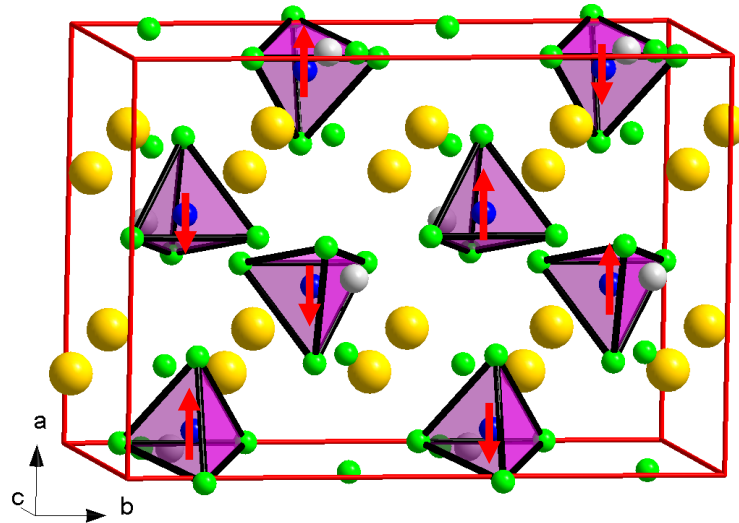


Fig. IV.15 Antiferromagnetic configuration used for all spin-polarized calculations in the supercell $a, 2b, c$. FeSe_4 tetrahedra are represented in purple; red arrows are indicating spin up or down for each Fe atom (blue) of the supercell. Ba, Se and Sb/Bi are represented in yellow, green and grey, respectively.

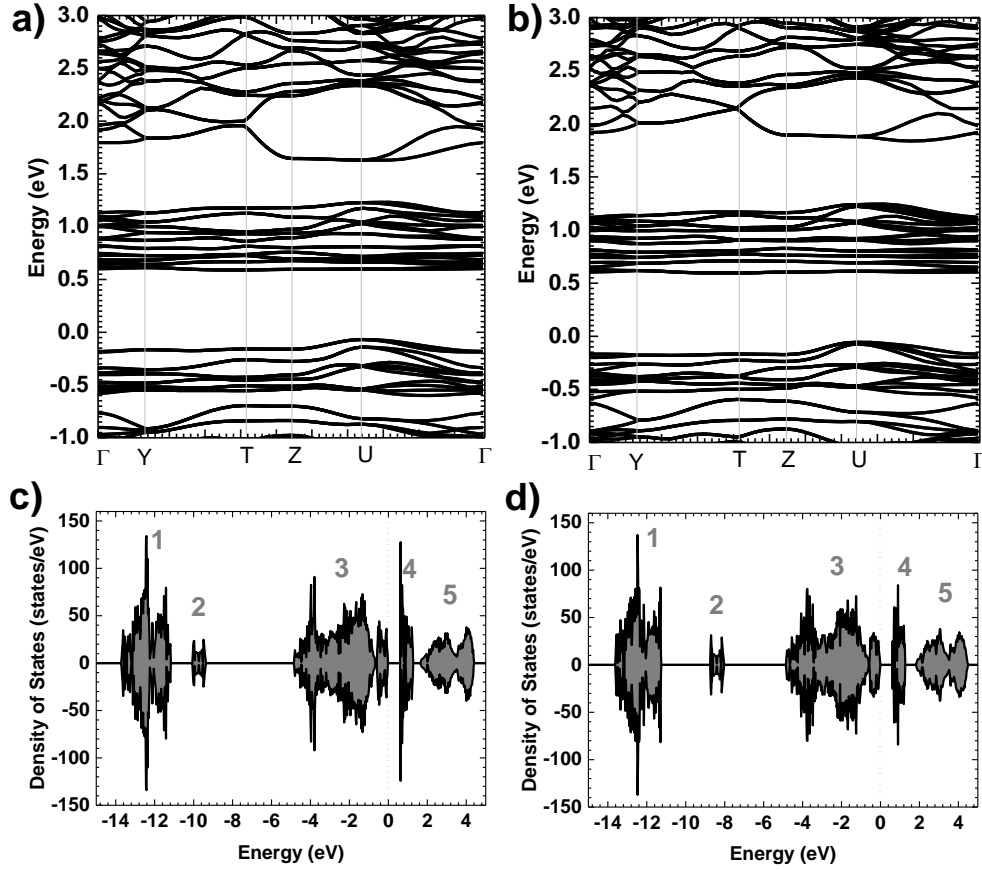


Fig. IV.16 Band structures (obtained from GGA calculations) along high symmetry k points of the Brillouin zone for a) $Pn = \text{Bi}$ and b) $Pn = \text{Sb}$; the total DOS is represented in c) for $Pn = \text{Bi}$ and d) $Pn = \text{Sb}$. The Fermi level is set to 0.

Without including a Hubbard term in the calculations very similar band gaps of ~ 0.60 eV and ~ 0.62 eV were obtained for $Pn = \text{Sb}$ and $Pn = \text{Bi}$ respectively, which suggests that the region of the band gap is only weakly affected by the substitution of Sb by Bi. Including a Hubbard term of $U_{\text{eff}} = 2.5$ eV increases the band gap to 0.94 eV for both compounds (Fig. IV.17), i.e. correct band gaps are difficult to determine without comparing them to experimental results, which will be done after discussing the electronic structure (obtained by GGA+U calculations) of $\text{Ba}_2\text{FeSbSe}_5$ and $\text{Ba}_2\text{FeBiSe}_5$ in detail.

The band structure of both compounds show a maximum of the valence band (VB) located at the U point of the Brillouin Zone (BZ). The minimum of the conduction band (CB) is not as straightforward due to a rather flat band for which the minimum energy extends along several segments of the BZ. For $\text{Ba}_2\text{FeSbSe}_5$, local minima can be identified along the Γ -Y line and at the T point such that the gap can be interpreted as indirect. If the conduction band minimum is considered at the U point, the band gap can be considered direct, i.e. I cannot conclude, whether the band gap is direct or indirect, only by looking at the electronic structure.

The Density of States (DOS) of both phases can be divided into three blocks (block 1, 2 and 3) in the valence band (VB) and two blocks (blocks 4 and 5) in the conduction band (CB). The general features of the DOS are quite similar for both compounds, except for the second block, which is shifted between block 1 and block 3 from one phase to the other. According to the projected density of states or PDOS (Fig. IV.18-19), the region 1 in the VB extends from -13.6 eV to -10.9 eV for both compounds. It is dominated by Ba(*p*) states together with a contribution of Se (*s*) states. Higher in the VB, region 2 extends from -10.0 eV to -9.2 eV for $Pn = \text{Bi}$ and from -8.6 eV to -7.8 eV for $Pn = \text{Sb}$. The major orbital contribution in this region comes from the Sb(*s*) or Bi(*s*) states, i.e. the stereoactive $5s^2$ and $6s^2$ lone pairs do not contribute to the electronic transport since they are localized at the Sb/Bi atoms (*cf.* Fig. 2) and they can be considered as not contributing significantly to any type of chemical bonding. Block 3 is located at the top of the VB near the Fermi level and extends from \sim -5.2 eV to 0 eV for both compounds. The Fe (*3d*) states are found mixed with the Se (*4p*) states, which represents Fe-Se bonding interactions. The Se (*4p*) states also mix with Bi/Sb (*p*) states, i.e. the Pn-Se bonds are formed mainly through *p*-bonding, while the stereoactive $5s^2$ and $6s^2$ lone pairs do not contribute significantly to the Pn-Se bonds. The segment of the DOS around -5 eV exhibits a peak-shaped area due to the localized Fe (*3d*) states. Above E_F , another narrow-shaped contribution is found around 1.4 eV due to the Fe *3d* empty states mixed with Se (*4p*) states with a small contribution of the Bi/Sb(*p*) states in the same region. Slightly higher in the CB, a segment (from 1.8 eV to 4.6 eV for $Pn = \text{Bi}$ and from 1.9 eV to 4.7 eV for $Pn = \text{Sb}$) composed of *Pn* (*p*) states, Se (*4p*) states and Ba (*d*) states is found. Concerning the PDOS related to Fe, the general features show spin *up* (\uparrow) states being occupied while spin *down* (\downarrow) are empty. This picture is consistent with Fe *d* orbitals being in the d^5 high-spin (HS) configuration, i.e. Fe^{3+} -HS. In addition the calculated magnetic moment was found to be 3.58/3.60 μ_B for $Pn = \text{Bi}/Pn = \text{Sb}$.

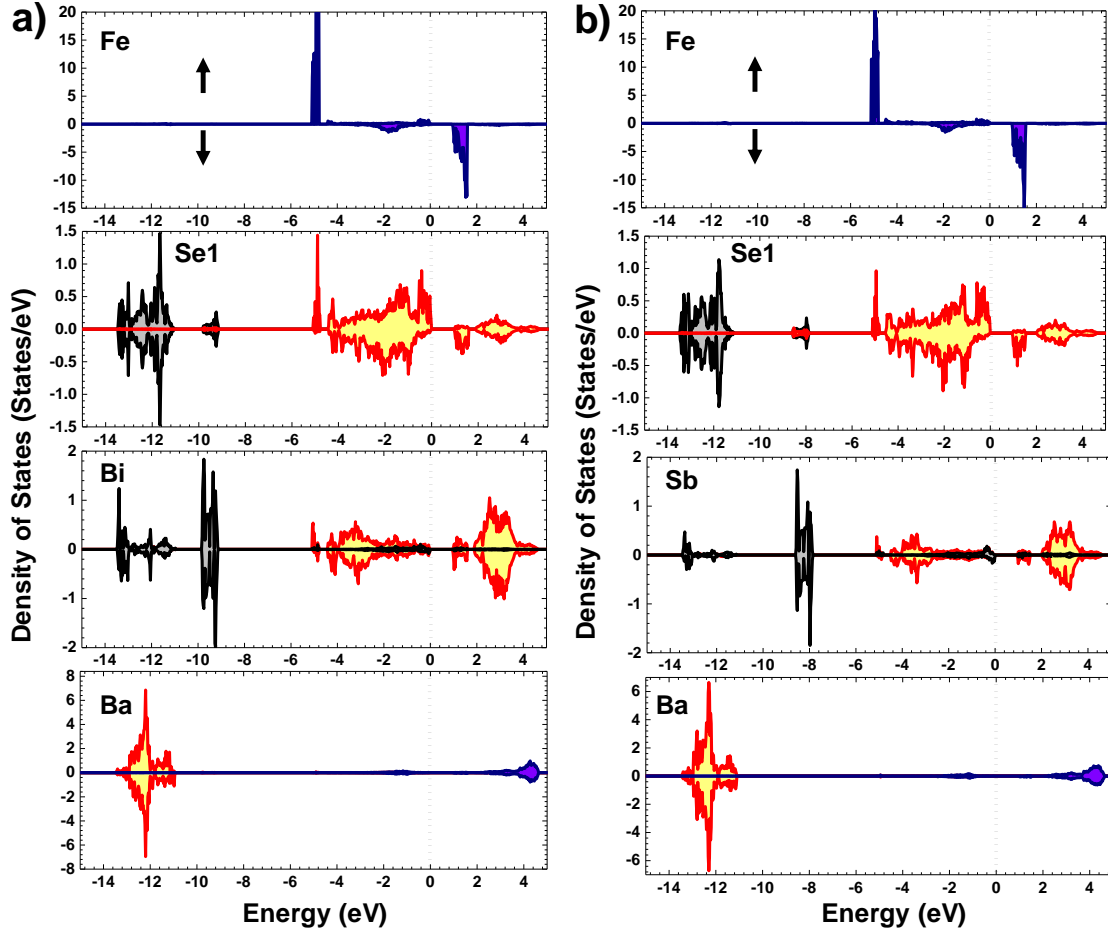


Fig. IV.18 PDOS of a) $\text{Ba}_2\text{FeBiSe}_5$ and b) $\text{Ba}_2\text{FeSbSe}_5$ obtained from GGA+U calculations. s , p and d states are represented by black, red and blue lines, respectively. The Fermi level is set to 0. The arrows indicate spin up (\uparrow) and down (\downarrow) populations. For Se atoms, Se1 is represented while Se2, Se3 and Se4 are reported in the SI. The projected DOS are issued from single sites in the supercell because of the AFM configuration. The sum of all contributions (including the Se contributions in Fig. 7) results in the total DOS represented in Figure 5, which corresponds to an AFM state.

This value is lower compared to what can be expected for a d^5 (HS) configuration with a spin-only contribution ($S = 5/2$, $L = 0$, $\mu(\text{Fe}^{3+}) = (4S(S+1))^{1/2} = 5.92 \mu_B$). This can be explained by the severe approximations included in the calculation method and a magnetic dilution towards the ligand atoms (Se) due to covalence effects, *i.e.* covalent interactions between a closed shell anion orbital and unpaired spins leading to a redistribution of the spins.^[128] Small magnetic moments are found on the four Se atoms surrounding iron, *i.e.* Se4 (0.19/0.18 μ_B), Se3 (0.14/0.15 μ_B) and Se1(0.11/0.11 μ_B) ($\times 2$), for $Pn = \text{Bi}/Pn = \text{Sb}$). At the top of the VB, they show similar features except Se2 which is exclusively bonded to Sb. The small spin polarization observed for Se1, Se3 and Se4 is not found for Se2.

The later exhibits also a smaller contribution to the total DOS than other Se atoms just below the Fermi level. Considering the nature of the states close to the Fermi level (below and above), charge transfer most probably occurs from occupied Se $4p$ states to unoccupied Fe $3d$ states.

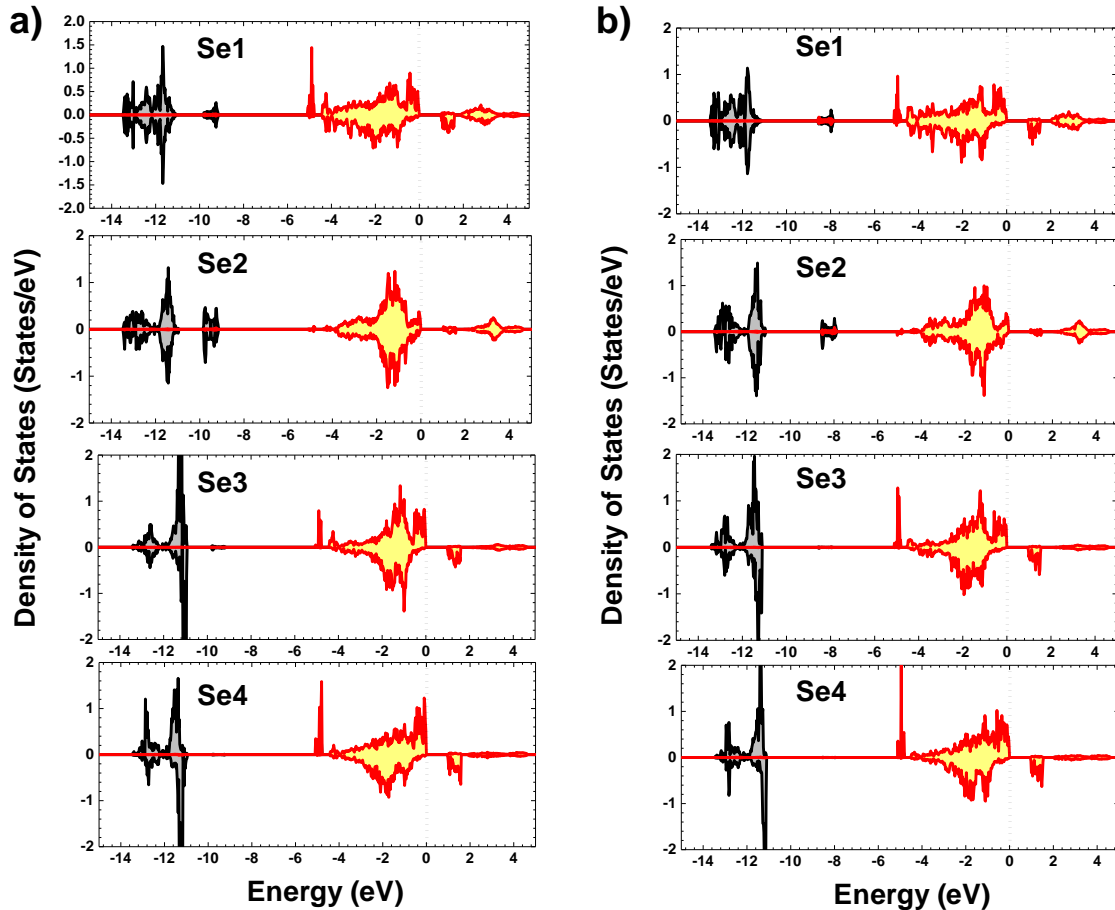


Fig. IV.19 PDOS for the compound a) $\text{Ba}_2\text{FeBiSe}_5$ and b) $\text{Ba}_2\text{FeSbSe}_5$ using spin polarized GGA+U ($U=2.5\text{eV}$) and for each type of Se atoms. The s and p states are respectively represented in black and red. The Fermi level is set to 0.

The semiconducting character of both $\text{Ba}_2\text{FeSbSe}_5$ and $\text{Ba}_2\text{FeBiSe}_5$ found by GGA and GGA+U calculations can be confirmed by electrical resistivity measurements (*cf.* Fig. IV.20). Experimental band gaps of $E_g = 1.14\text{ eV}$ and $E_g = 1.04\text{ eV}$ were found for $\text{Ba}_2\text{FeSbSe}_5$ and $\text{Ba}_2\text{FeBiSe}_5$, respectively. These gaps, agree well with the GGA+U calculations, i.e. GGA calculations without a Hubbard term underestimate the experimental band gaps of $\text{Ba}_2\text{FeSbSe}_5$ and $\text{Ba}_2\text{FeBiSe}_5$ by ca. 47 % and 40 %, respectively. This underestimation is due to an inaccurate description of the strong Coulomb repulsion between the $3d$ electrons of Fe, which results in an inaccurate description of the electronic ground state of $\text{Ba}_2\text{FeSbSe}_5$ and

$\text{Ba}_2\text{FeBiSe}_5$. This problem can be overcome by including the previously discussed Hubbard term, which accounts for on-site Coulomb repulsions between the $3d$ electrons of Fe.

The experimental band gaps were obtained from a linear fit to the corresponding $1000T^{-1}$ vs. $\ln\rho$ plots (*cf.* inset figures in Fig. IV.20) using the following expression for the resistivity: $\rho = \rho_0 \exp(E_g/2k_B T)$ (*cf.* inset figures b) and c) in Fig. 4). A substitution of Sb by Bi logically leads to a decrease in the band gap due to the higher metallicity of Bi compared to Sb. These findings are in opposition to what was found for the corresponding sulfides, where optical band gaps of 0.95 eV and 1.28 eV are reported for $\text{Ba}_2\text{FeSbS}_5$ and $\text{Ba}_2\text{FeBiS}_5$, respectively.^[73]

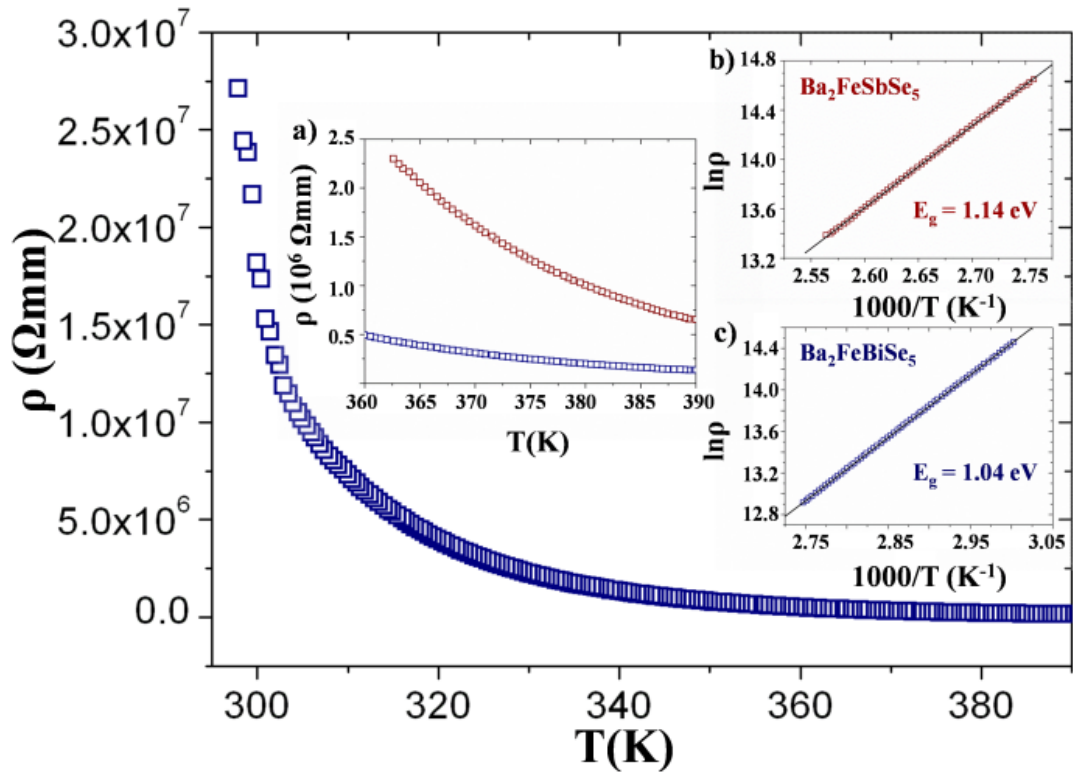


Fig. IV.20 Electrical resistivities of $\text{Ba}_2\text{FeSbSe}_5$ (red) and $\text{Ba}_2\text{FeBiSe}_5$ (blue). The corresponding $\ln\rho$ vs. $1000/T$ plots and the experimental band gaps are depicted in the insets b) and c), respectively. Inset figure a) shows a comparison between the resistivity of $\text{Ba}_2\text{FeSbSe}_5$ (red) and $\text{Ba}_2\text{FeBiSe}_5$ (blue).

3.1.2.3 Thermal conductivity

The low- and high-temperature thermal conductivities of $\text{Ba}_2\text{FeBiSe}_5$ and $\text{Ba}_2\text{FeSbSe}_5$ were measured in order to evaluate, whether or not these compounds can be considered for thermal management applications such as thermal barrier coatings or thermoelectric application, which require materials with low thermal conductivities. The high-temperature thermal conductivities (*cf.* Fig. IV.21) of $\text{Ba}_2\text{FeSbSe}_5$ and $\text{Ba}_2\text{FeBiSe}_5$ range from 0.9 to $0.4 \text{ Wm}^{-1}\text{K}^{-1}$ and from 0.8 to $0.4 \text{ Wm}^{-1}\text{K}^{-1}$ between room temperature and $500 \text{ }^\circ\text{C}$.

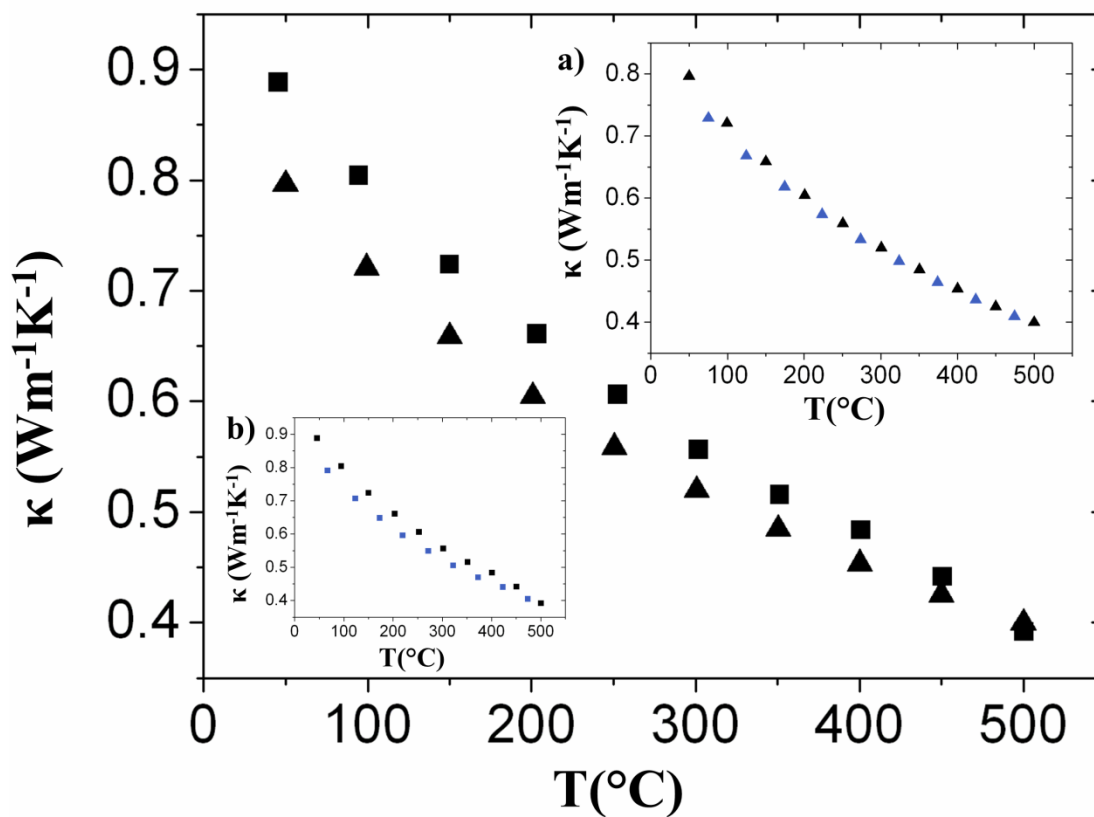


Fig. IV.21 High-temperature thermal conductivities of $\text{Ba}_2\text{FeSbSe}_5$ (squares) and $\text{Ba}_2\text{FeBiSe}_5$ (triangles), black: heating, blue: cooling.

These values are indeed remarkably low and significantly lower compared to ordinary covalent semiconductors with heavy elements and rather simple crystal structures such as Ge (60 W/mK)^[129], GaAs (45 W/mK)^[130], GaSb (60 W/mK)^[131] and InSb (20 W/mK)^[131]. Therefore, unique lattice properties can be expected for $\text{Ba}_2\text{FeSbSe}_5$ and $\text{Ba}_2\text{FeBiSe}_5$.

Structural complexity of $\text{Ba}_2\text{FeSbSe}_5$ and $\text{Ba}_2\text{FeBiSe}_5$ and significant structural distortions (especially in the $[\text{FePnSe}_5]^{4-}$ network) can be considered the main reasons for these remarkably low thermal conductivities. Other possible explanations for such low κ values are the presence of the stereoactive $5s^2$ and $6s^2$ lone pairs of Sb and Bi and the possibility of resonant bonding within the $\text{Ba}_2\text{FePnSe}_5$ ($\text{Pn} = \text{Sb, Bi}$) crystal structure (*cf.* section *Potential resonant bonding in $\text{Ba}_2\text{FePnSe}_5$ ($\text{Pn} = \text{Sb, Bi}$)*) since resonant bonding can result in low lattice thermal conductivities as reported for PbS, PbSe, PbTe.^[26] The thermal conductivity is slightly lower for $\text{Ba}_2\text{FeBiSe}_5$, which can be explained by the larger mass of Bi compared to Sb resulting in a higher mass contrast in the anionic framework. The low-temperature thermal conductivities of both title compounds (*cf.* Fig. IV.22-23) show a kink at the Néel temperatures and a significant increase below T_N resulting in a maximum thermal conductivity of $2.6 \text{ Wm}^{-1}\text{K}^{-1}$ and $2.8 \text{ Wm}^{-1}\text{K}^{-1}$ at 30 K for $\text{Ba}_2\text{FeBiSe}_5$ and $\text{Ba}_2\text{FeSbSe}_5$, respectively. Hence, the antiferromagnetic ordering influences the thermal conductivity of both compounds. The increase in κ below T_N indicates an increase in the phonon mean free path due to the antiferromagnetic ordering. Between 5 K and 30 K, where boundary scattering processes are usually dominant, the thermal conductivity of both compounds strongly increases with temperature until it reaches maximum. Above 30 K, the thermal conductivity of both compounds decreases, probably because other scattering mechanisms such as Umklapp scattering become dominant.

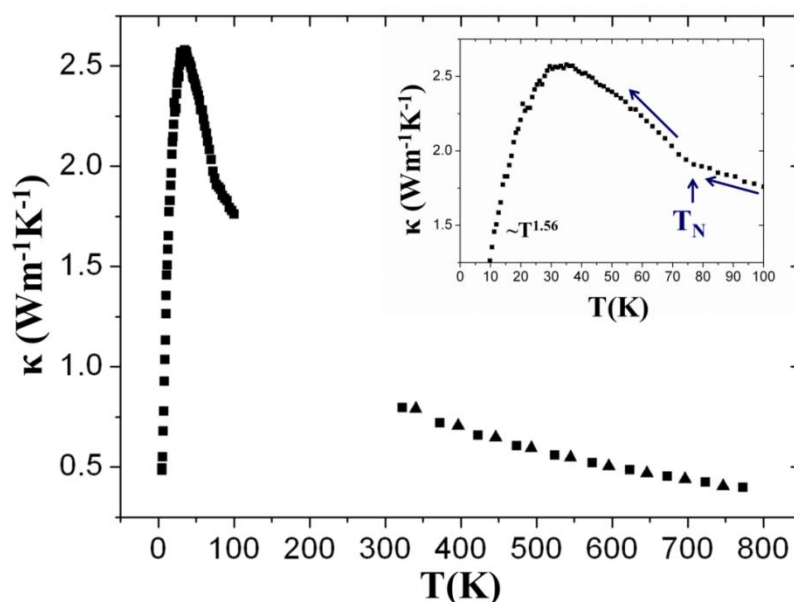


Fig. IV.22 Low- and high-temperature thermal conductivities of $\text{Ba}_2\text{FeBiSe}_5$. The inset shows the influence of the antiferromagnetic ordering on κ ; for high-temperature measurements: squares: heating, triangles: cooling.

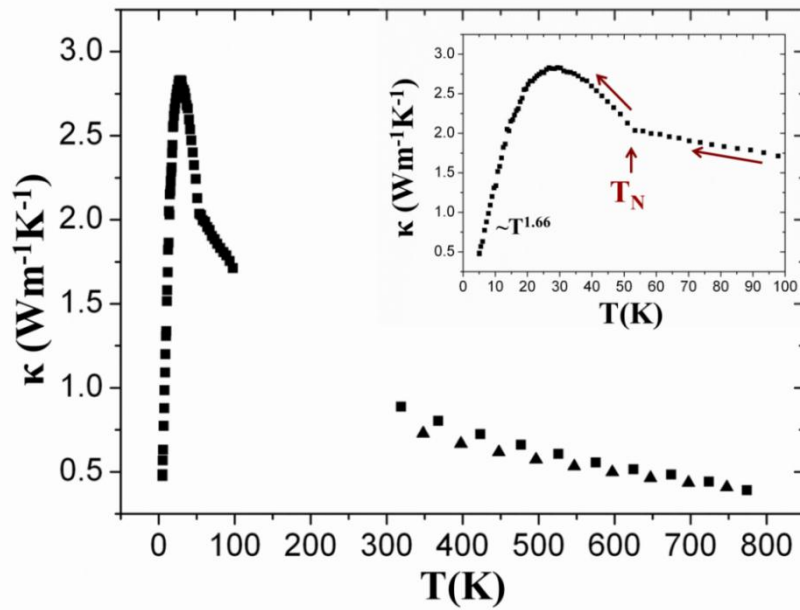


Fig. IV.23 Low- and high-temperature thermal conductivities of $\text{Ba}_2\text{FeSbSe}_5$. The inset shows the influence of the antiferromagnetic ordering on κ ; for high-temperature measurements: squares: heating, triangles: cooling.

3.1.2.4 Irradiation induced phase changes between crystalline and amorphous $\text{Ba}_2\text{FePnSe}_5$ (Pn = Sb, Bi)

After measuring the high-temperature thermal conductivity, an optical change of the surface of both compounds was observed (*cf.* Fig. IV.24d). Therefore, X-ray diffraction patterns were recorded from the surface before and after measuring the high-temperature thermal conductivity and compared to the corresponding PXRD patterns. The results shown in Fig. IV.25 are for $\text{Ba}_2\text{FeSbSe}_5$.

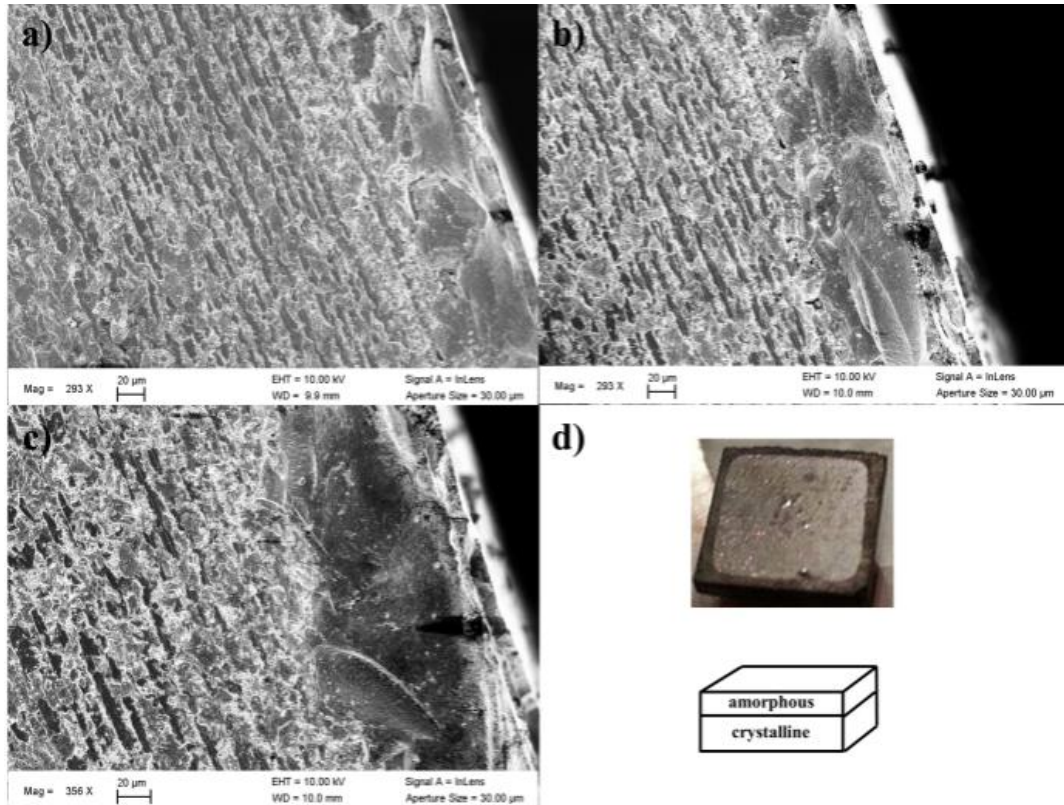


Fig. IV.24 a) – c) SEM images of the cross section of polycrystalline $\text{Ba}_2\text{FeBiSe}_5$ showing the textured crystalline bulk material and the amorphous layer on the surface of the sample after measuring the thermal conductivity. d) sample with an amorphous layer obtained after measuring the thermal conductivity. A clear optical difference between the amorphous and crystalline phase is visible, which is a strong indication for their different optical properties.

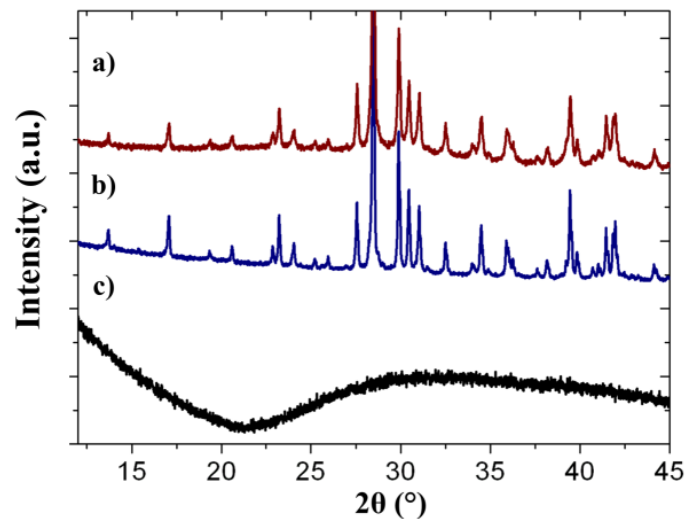


Fig. IV.25 Room temperature PXRD patterns of $\text{Ba}_2\text{FeSbSe}_5$. a) and b) correspond to the surface and powder of the sample without any laser treatment, while c) corresponds to the surface after measuring the thermal conductivity showing a fully amorphous surface.

The pattern from the crystalline surface before measuring κ shows no difference compared to a powdered sample, while the surface after the high-temperature thermal conductivity measurement is amorphous. In order to conclude, whether the amorphization is thermally or irradiation-induced, high-temperature PXRD patterns (*cf.* Fig. IV.26) were recorded from a fresh powdered sample. The results strongly suggest an irradiation-induced amorphization since no broadening of the reflections or structural changes are visible up to 500 °C.

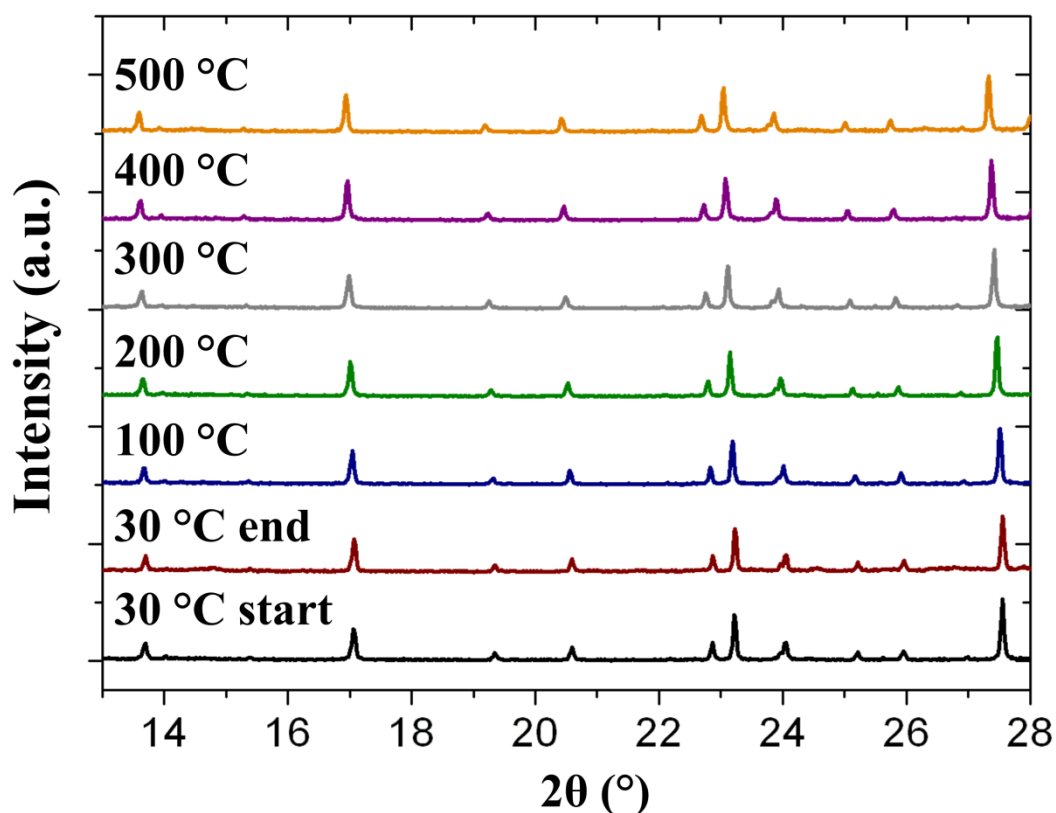


Fig. IV.26 High-temperature PXRD patterns for Ba₂FeSbSe₅. No changes in the structure are detected up to 500 °C, i.e. the laser pulse is responsible for the amorphization of the surface.

This hypothesis is supported by the amorphization of both compounds after exposing them to an electron beam with $\lambda = 0.00196$ nm. This effect was observed in situ during TEM analysis. Fig. IV.27 shows a HRTEM image of a Ba₂FeSbSe₅ crystallite recorded ca. 15 min after exposure to the electron beam ($\lambda = 0.00196$ nm).

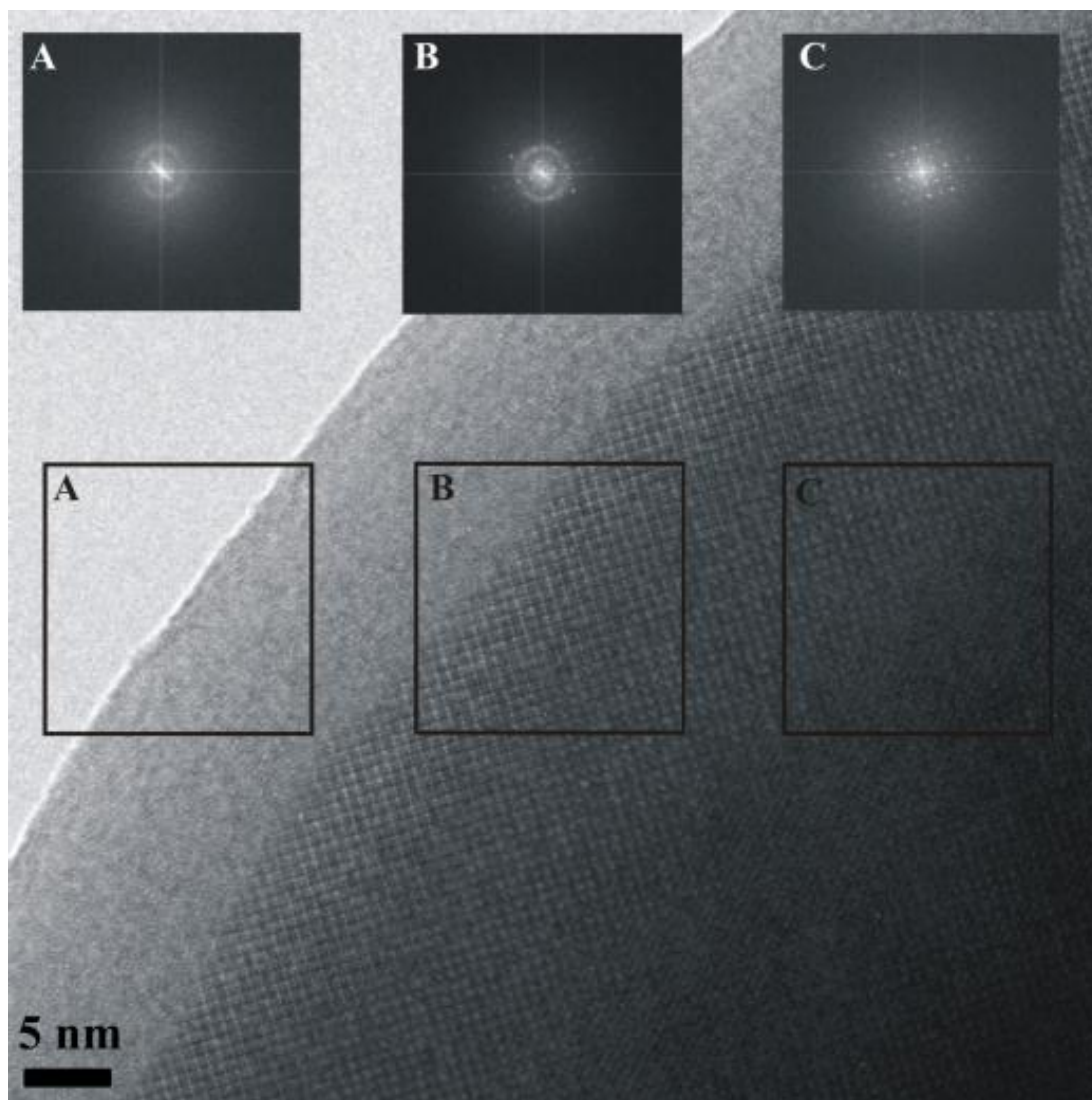


Fig. IV.27 HRTEM image of a Ba₂FeSbSe₅ crystallite after approximately 15 min of the TEM analysis. The image shows an amorphous (left) and a crystalline (right) region and the interface between the two. The corresponding Fourier Transforms are depicted in the insets A-C and they correspond to A: the purely amorphous part, B: the interface between amorphous and crystalline part and C: crystalline Ba₂FeSbSe₅. The areas from which the Fourier transforms were calculated are highlighted by grey squares.

An amorphous zone with ca. 10-15 nm thickness can be seen from Fig. IV.27. Calculating the Fourier transform of different parts of the image allows the differentiation between an amorphous and a crystalline area. The lack of long range order results in diffuse rings in the Fourier transform (*cf.* Fig. IV.27A), while the appearance of sharp reflections is visible for long-range ordered, crystalline areas (*cf.* Fig. IV.27C). At the amorphous/crystalline interface both, diffuse rings and sharp reflections can be observed (*cf.* Fig. IV.27B). Hence, Ba₂FeSbSe₅ and Ba₂FeBiSe₅ are highly sensitive towards irradiation of very different energies.

The in situ amorphization is depicted in Fig. IV.28, which shows HRTEM images taken in the [100] and [110] zone axes and the corresponding SAED patterns. The amorphous region increases with time (compare Fig. IV.28 b) and c) as well as d) and e) and the amorphization starts at the border of the crystallite, where the thickness is the lowest. The interface between amorphous and crystalline $\text{Ba}_2\text{FeBiSe}_5$ can also be seen in Fig. IV.24a-c, which correspond to SEM images of the cross section of polycrystalline $\text{Ba}_2\text{FeBiSe}_5$ taken after measuring κ . A textured, crystalline bulk material and an amorphous layer with a thickness of ca. $67\ \mu\text{m} - 84\ \mu\text{m}$ is visible.

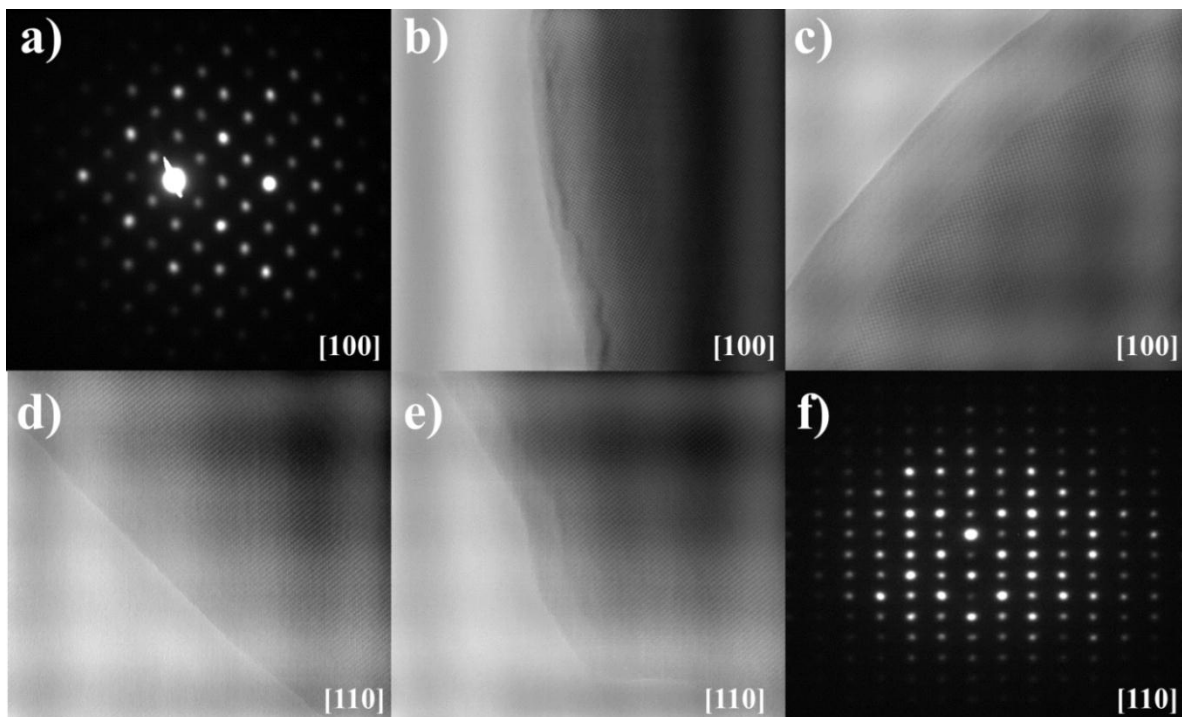


Fig. IV.28 HRTEM images and SAED patterns of a $\text{Ba}_2\text{FeSbSe}_5$ crystallite; a)-c) were recorded in the zone axes [100] and d)-f) in the zone axis [110]; b) and c) as well as d) and e) show a time-dependent in situ amorphization starting from the border of the crystallite.

Both, a single pulse and a series of laser pulses ($\lambda = 1064\ \text{nm}$) with a sufficient amount of time in between the pulses, e.g. while measuring the thermal diffusivity at high temperatures, lead to an amorphous surface. A series of laser pulses at room temperature with $\lambda = 1064\ \text{nm}$ was applied to a crystalline surface of $\text{Ba}_2\text{FeBiSe}_5$, while the thermal conductivity was measured as a function of the number of laser pulses (*cf.* Fig. IV.29). The sample surface was analyzed by X-ray diffraction after 0, 1, 24 and 170 laser pulses (*cf.* Fig. IV.30).

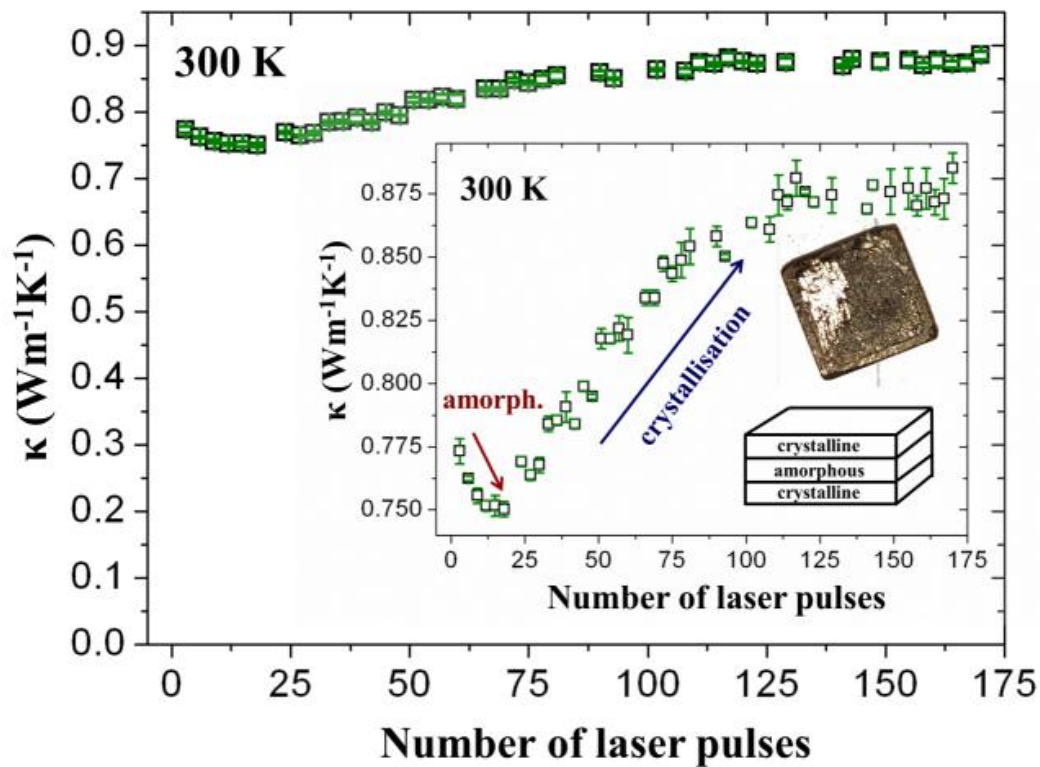


Fig. IV.29 Thermal conductivity of $\text{Ba}_2\text{FeBiSe}_5$ at room temperature as a function of number of laser pulses. A decrease/increase in thermal conductivity corresponds to the amorphization/crystallisation of the surface. Once the crystallization is completed a plateau is reached in the thermal conductivity. The sample after 170 laser pulses is shown in the inset figure with the surface of the sample removed from its top left corner. The sample surface is recrystallized and no significant optical contrast is visible between the initial and final crystalline phase. Below the crystalline surface parts of the sample are still amorphous with clear optical contrast to both crystalline phases.

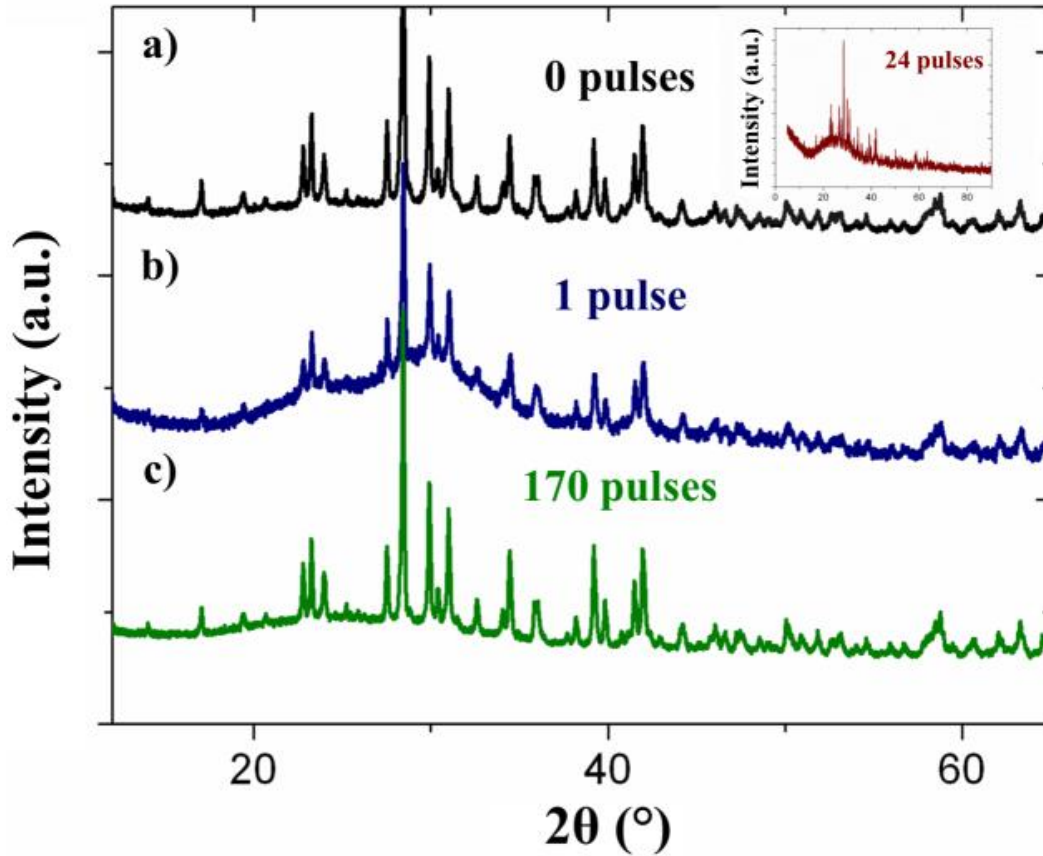


Fig. IV.30 Room temperature PXRD patterns of $\text{Ba}_2\text{FeBiSe}_5$. a) corresponds to the surface of the sample without any irradiation treatment, b) and c) correspond to the surface after one and 170 laser pulses ($\lambda = 1064 \text{ nm}$) of 0.3 ms at room temperature; inset: surface after 24 laser pulses, where the minimum in κ was measured. The image shows that one laser pulse is sufficient to obtain an amorphous surface, while a sufficiently long series of laser pulses at room temperature leads to a recrystallization of surface.

The penetration depths of X-rays is larger than $\sim 50 \mu\text{m}$ ^[132] and therefore parts of the crystalline bulk is visible in the X-ray patterns. The surface is amorphous after 1 and 24 pulses and crystalline after 170 pulses, which indicates an amorphization up to 24 pulses and a subsequent recrystallization. Removing parts of the surface revealed an amorphous layer below the recrystallized surface and above the crystalline bulk material. (*cf.* inset in Fig. IV.29) A change in thermal conductivity upon crystallization due to a change of bonding accompanied by a simultaneous increase in the sound velocity and a softening of the optical phonon modes is known from other phase-change materials.^[124] κ can therefore be used as an indicator for changes between amorphous and crystalline $\text{Ba}_2\text{FePnSe}_5$ (Pn = Sb, Bi).

The thermal conductivity of $\text{Ba}_2\text{FeBiSe}_5$ at room temperature increases from the amorphous to the recrystallized state by ca. $0.13 \text{ Wm}^{-1}\text{K}^{-1}$, which is significant compared to the standard deviations (green error bars in Fig. IV.29) of the measurement. A decrease in κ can be observed up to 24 laser pulses, which is consistent with an initial amorphization, which is followed by a recrystallization. Only semiconductors with unsaturated p-bonds are suitable phase-change materials, which excludes all sp^3 -bonded materials. A mixing between Sb/Bi and Se p states (*cf.* Fig. IV.18) as well as Pn-Se angles of 95° - 98° in $\text{Ba}_2\text{FeBiSe}_5$ and 93° - 97° in $\text{Ba}_2\text{FeSbSe}_5$ allow the conclusion of p-bonding between Pn and Se. Crucial for phase-change applications is also the average number of valence electrons per atom (N_{sp}).^[133] The N_{sp} of compounds, which can be used as phase-change materials was found to be always larger than 4 and range usually between 4.3 and 5. In the case of $\text{Ba}_2\text{FePnSe}_5$ (Pn = Sb, Bi) $N_{\text{sp}} = (4+8+5+30)/9 = 5.22$, which is close to the ideal range and which makes the two title compounds promising candidates for potential phase-change applications.

3.1.2.5 Potential resonant bonding in $\text{Ba}_2\text{FePnSe}_5$ (Pn = Sb, Bi)

This part of the chapter proposes resonant bonding as the possible origin of the observed phase changes between crystalline and amorphous $\text{Ba}_2\text{FePnSe}_5$ (Pn = Sb, Bi). I showed, that the crystal structure of $\text{Ba}_2\text{FePnSe}_5$ (Pn = Sb, Bi) contains a system of three shorter (stronger) and three longer (weaker) Pn-Se bonds per PnSe_6 octahedron and that this bond elongation is caused by the stereoactive $5s^2$ and $6s^2$ lone pairs of Sb and Bi, which are not significantly contributing to the Pn-Se bonding. A similar bonding situation with three stronger and three weaker covalent bonds is described for Sb in $\text{Ba}_2\text{Sb}_2\text{Se}_4\text{F}_2$ ^[134] and for Ge/Sb in cubic $\text{Ge}_2\text{Sb}_2\text{Te}_5$.^[135] The so-called umbrella-flip transformation described for $\text{Ge}_2\text{Sb}_2\text{Te}_5$ was proposed as the mechanism transforming the crystalline into an amorphous phase and vice versa, while Ge is considered to change from an octahedral to a tetrahedral coordination environment and back without breaking the stronger covalent bonds. This mechanism is possible due to three longer and shorter bonds per octahedron, which result from a shift of Ge and Sb away from their f.c.c. sites. This shift is considered to be the reason for the good cycleability of $\text{Ge}_2\text{Sb}_2\text{Te}_5$. The stereoactive $5s^2$ and $6s^2$ lone pairs of Sb and Bi cause a similar displacement of Sb and Bi away from the center of the PnSe_6 octahedra in the $\text{Ba}_2\text{FePnSe}_5$ (Pn = Sb, Bi) structure. Moving Sb or Bi along the red arrows depicted in Fig. IV.31 results in two different bonding situations where the Fe and Se atoms keep their atomic positions.

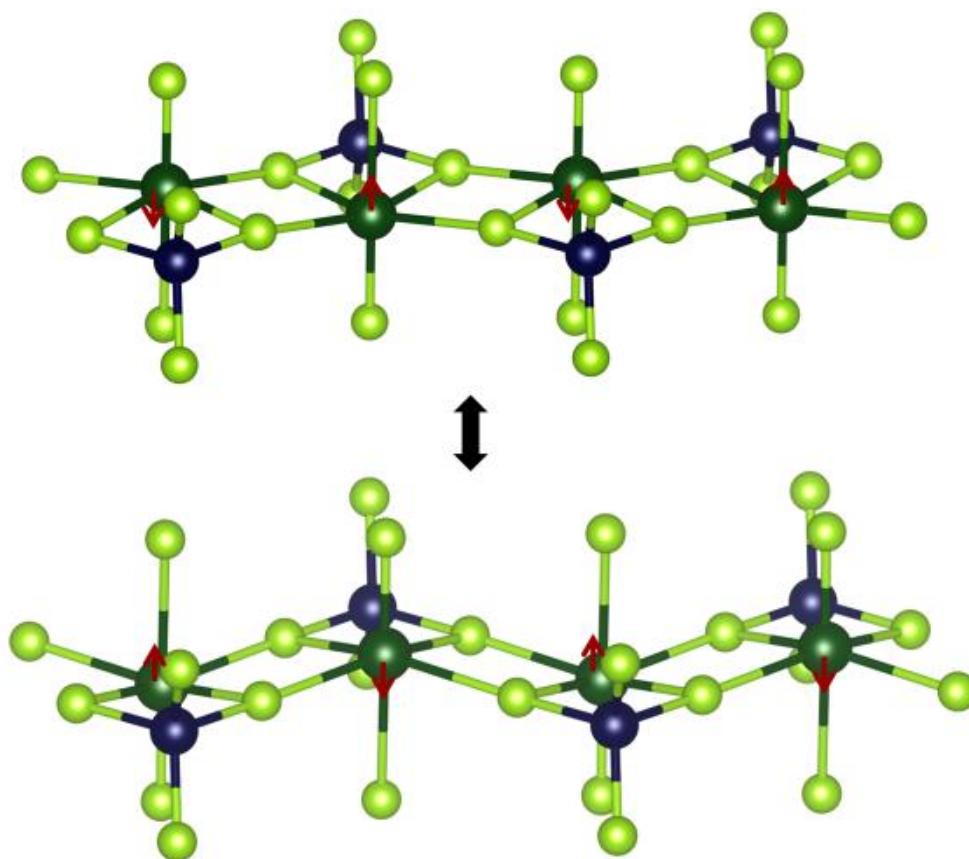


Fig. IV.31 Two possible bonding situations (i.e. one possible resonant bonding situation) for the Sb-Fe-Se network are shown. They depend on the position of Sb and can be converted into each other by displacing Sb along the red arrows without breaking any bonds and without distorting the FeSe_4 tetrahedra. The same bonding situation can be drawn for $\text{Ba}_2\text{FeBiSe}_5$ and the effect most probably originates from the stereoactive $5s^2$ and $6s^2$ lone pairs of Sb and Bi. Sb: dark green, Se: light green. Different types of resonant bonding situations are possible in the three different, one dimensional chains.

This form of resonant bonding is probably responsible for the observed phase-change properties of $\text{Ba}_2\text{FePnSe}_5$ ($\text{Pn} = \text{Sb}, \text{Bi}$) and in partly for the remarkably low thermal conductivities of both compounds. Future efforts will be dedicated to studying the local crystal structure of crystalline and amorphous $\text{Ba}_2\text{FeSbSe}_5$ by means of PDF in order to understand the underlying atomistic mechanism responsible for the observed phase-change properties with special focus on the role of the stereoactive $5s^2$ and $6s^2$ lone pairs of Sb and Bi. The reason for focusing on the lone pairs is that Ovshinsky, who based his research on polymeric lone-pair chain structures, already understood that lone pairs can easily be excited by optical and electrical fields.^[120] If the excitation energy cannot be accommodated by the amorphous phase, a change towards a crystalline phase occurs.

Hence, it is possible that the observed phase changes in $\text{Ba}_2\text{FePnSe}_5$ ($\text{Pn} = \text{Sb}, \text{Bi}$) are driven by a reorientation of the $5s^2$ and $6s^2$ lone pairs of Sb and Bi leading to different bonding situations, which are separated by a potential barrier (in analogy to the inversion barrier in NH_3 ^[136]), which can be overcome by an external excitation by an optical or electrical field.

3.1.2.6 $\text{Ba}_2\text{FeSbSe}_5$: striction driven changes in the dielectric permittivity?

I started studying the dielectric properties of $\text{Ba}_2\text{FeSbSe}_5$ because of its large resistivity, the antiferromagnetic ordering of the spins below 58 K, the anomalies in the thermal conductivity at the Néel temperature (T_N) and the distortion of the SbSe_6 octahedra, which is driven by the $5s^2$ lone pairs of Sb. The objective was to explore the possibility of a coupling between ferroelectric/antiferroelectric and magnetic order parameters, which can lead to the magnetoelectric effect (i.e. the induction of magnetization by an electric field or of polarization by a magnetic field) or simply to a coupling between spins and electric dipoles, which does not result in a macroscopic polarization or magnetization. While the magnetoelectric effect is strongly restricted by symmetry (i.e. noncentrosymmetry is required), magnetodielectric coupling can occur regardless of the symmetry of the crystal or magnetic structure.^[137] Previous studies suggested that the $6s^2$ lone pairs of Bi in BiMnO_3 can lead to a weak coupling of the ferroelectric and magnetic orders.^[138] This is one more reason why $\text{Ba}_2\text{FeSbSe}_5$ seemed to be a promising candidate for exploring the possibility of finding the magnetoelectric effect or magnetodielectric coupling.

The coupling of magnetic and dielectric properties is of considerable interest not only from a fundamental point of view, but also in terms of technological applications such as magnetic sensors and spin-charge transducers. Research on magnetoelectric materials flourished within the past decades^[139] partly due to the discovery of the colossal magnetodielectric effect in several oxides such as TbMn_2O_5 , DyMn_2O_5 , HoMnO_3 and YMnO_3 .^[140,141] Current challenges are understanding the origin of both effects and finding new materials, where the coupling between magnetic spins and electric dipoles occurs close to room temperature and is strong enough to be considered for technological applications. Recent studies revealed that complex spin structures^[142], magnetostructural^[143] and magnetoelastic^[144] coupling can cause magnetodielectric coupling. Another possible origin is the interaction of spins and phonons.

Since the dielectric permittivity is largely determined by optical phonons it is considered that spin-lattice coupling shifts the optical phonon frequencies and in turn leads to changes in ϵ .^[137] Magnetodielectric coupling is a well-known phenomenon in oxides^[145-149], but has not been studied extensively in higher chalcogenides such as selenides or tellurides since most of them possess much lower electrical resistivities compared to oxides, which results in large dielectric losses. However, polar selenides or tellurides containing elements with a large difference in electronegativity (ΔEN) are often insulators with relatively large band gaps.

Changes in the dielectric permittivity at the Néel temperature were observed, when measuring ϵ as a function of temperature. These findings are illustrated in Fig. 21, which also contains the magnetic susceptibility and low-temperature thermal conductivity (κ), in order to emphasize that there are anomalies in both, the dielectric permittivity and κ at the Néel temperature. These anomalies strongly indicate the coupling between phonons, spins, and electric dipoles at the Néel temperature. Since the capacitance can also change due to charge effects at the interface between the sample surface and the electrodes it is important to measure $\epsilon(T)$ for several different frequencies. If such interfacial charge effects occur, the $\epsilon(T)$ curve strongly depends on the frequency. Here, the $\epsilon(T)$ curve is independent of the frequency (*cf.* Fig. IV.32), which shows that the changes in ϵ at the Néel temperature are intrinsic. Fig. 22 also shows the dielectric losses ($\tan\delta$), which are close to 0 over the whole temperature range and for all frequencies, i.e. a purely imaginary impedance is measured and no leakage current occurs over the whole temperature range. These are ideal measurement conditions since $\text{Ba}_2\text{FeSbSe}_5$ is a good insulator, which is also reflected in its large resistivity (*cf.* inset figure in Fig.IV.32).

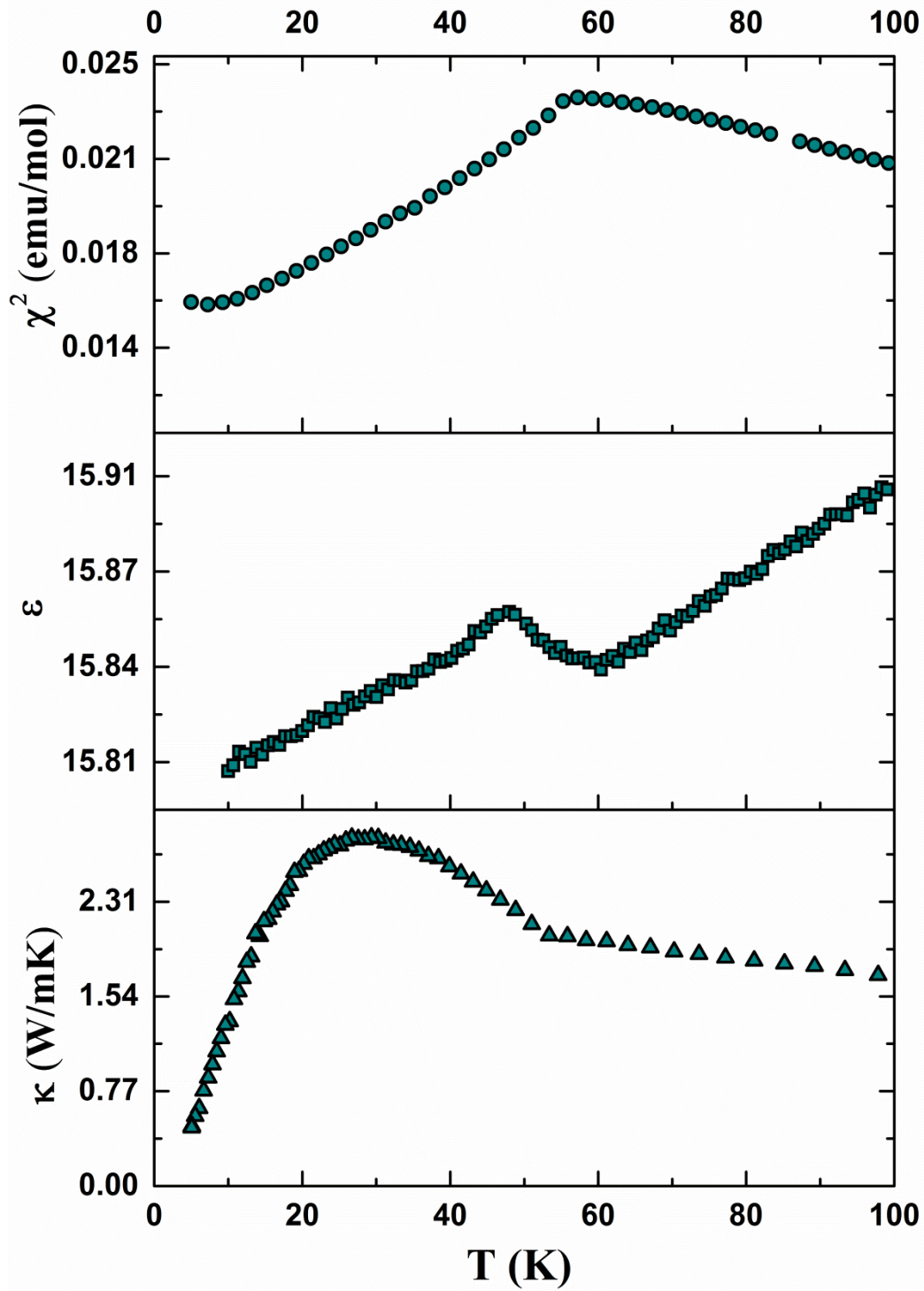


Fig. IV.32 top: magnetic susceptibility, middle: dielectric permittivity and bottom: thermal conductivity of $\text{Ba}_2\text{FeSbSe}_5$ as a function of temperature; the image illustrates the coupling of magnetic spins, electric charges and phonons at the Néel temperature.

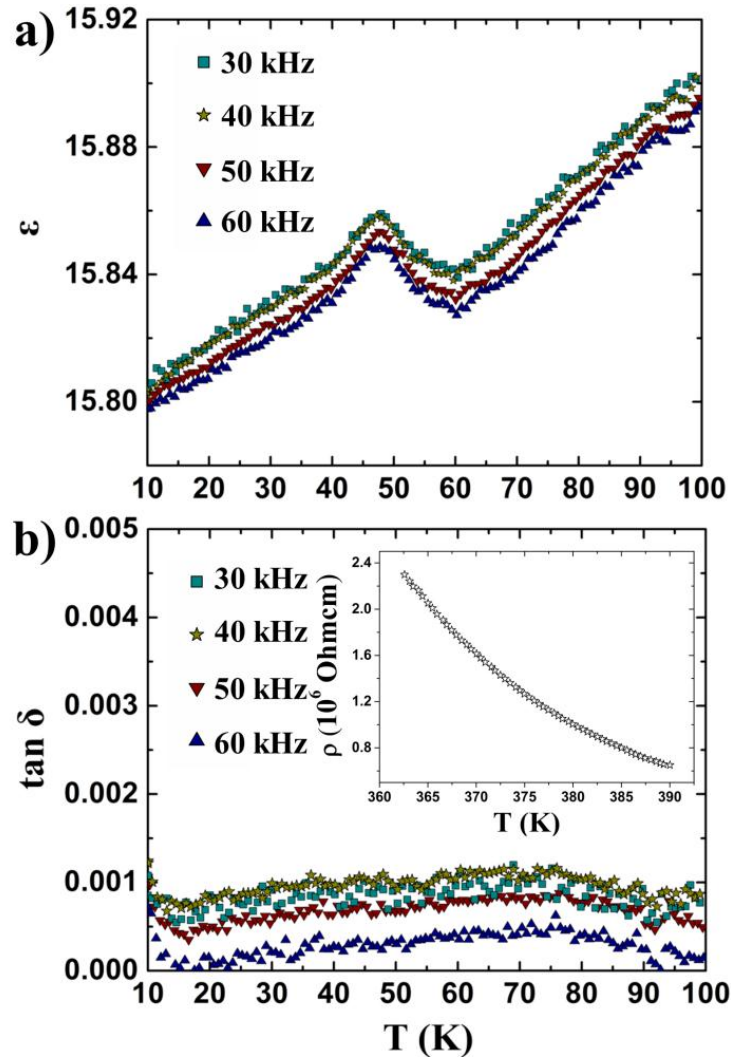


Fig. IV.33 a) dielectric permittivity as a function of temperature measured at different frequencies between 30 kHz and 60 kHz; b) dielectric losses for all measurements shown in a) and the resistivity (inset) of $\text{Ba}_2\text{FeSbSe}_5$; ϵ does not depend on the frequency, i.e. the changes in ϵ are intrinsic.

The results presented in Fig. IV.32 and Fig. IV.33 point towards magnetodielectric coupling in $\text{Ba}_2\text{FeSbSe}_5$. However, the capacitance (and hence the dielectric permittivity) shows no dependence on the magnetic field (*cf.* Fig. IV.34) when going through the magnetic transition, i.e. the observed anomalies in the $\epsilon(T)$ curves do not result from magnetodielectric coupling. Based on the anomalies in thermal conductivity and dielectric permittivity at the Néel temperature it seems probable that these effects rather arise from a coupling of magnetic order parameters and changes in the crystal structure, which in turn causes magnetostrictive strains and fluctuations in the dielectric permittivity (i.e. the changes in ϵ are striction driven). However, in order to understand the origin of the observed anomalies in κ and ϵ at T_N , further information concerning the low-temperature crystal structure is required.

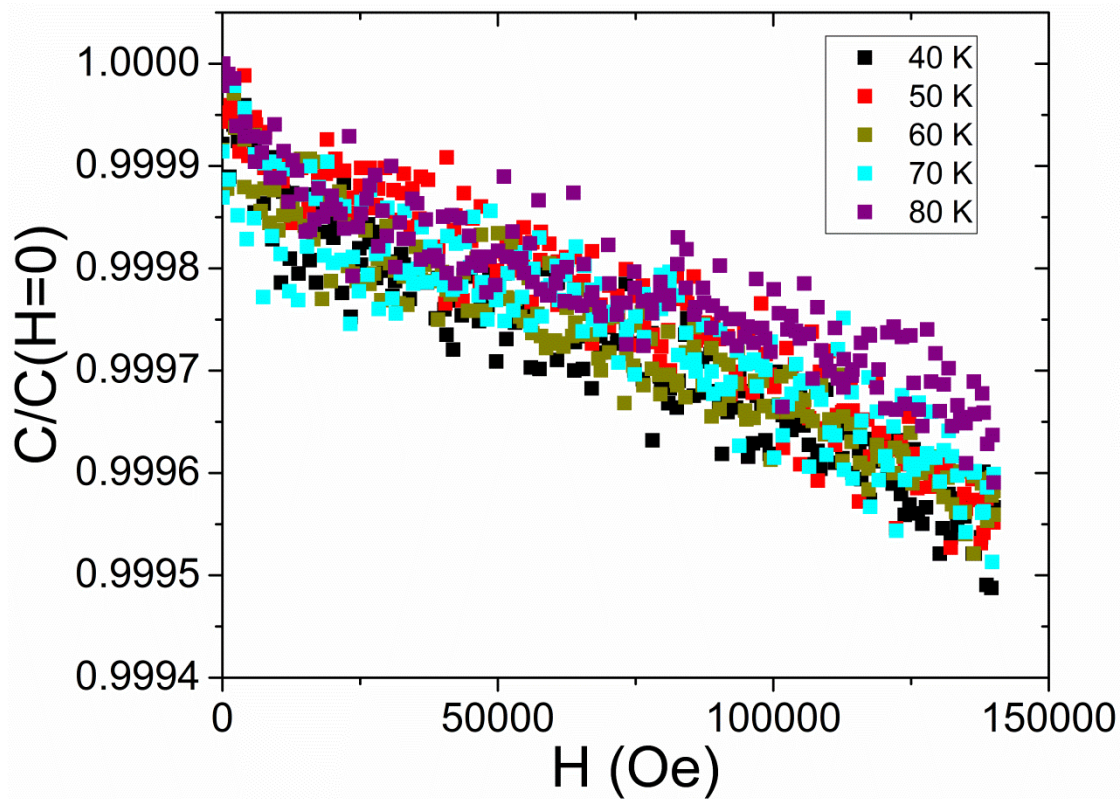


Fig. IV.34 Capacitance normalized by $C(H=0)$ as a function of magnetic field.

3.1.3 Conclusion

The two quaternary polar chalcogenides $Ba_2FePnSe_5$ ($Pn = Sb, Bi$) were discovered and their crystal structure was solved by means of single crystal X-ray diffraction simultaneously and independently of Wang et al.^[111] I also developed a new synthesis route of $Ba_2FePnSe_5$ ($Pn = Sb, Bi$), which involves ball milling and subsequent spark plasma sintering allowing the synthesis of large amounts (~ 10 g) of polycrystalline material. Crystal structure and phase homogeneity of polycrystalline $Ba_2FePnSe_5$ ($Pn = Sb, Bi$) were confirmed by PXRD experiments and subsequent Rietveld refinements as well as transmission and scanning electron microscopy. $Ba_2FePnSe_5$ ($Pn = Sb, Bi$) are both semiconducting with band gaps of 1.14 eV and 1.04 eV with a decrease of the gap going from Sb to Bi in contrary to the sulfides, where the gap increases from Ba_2FeSbS_5 to Ba_2FeBiS_5 . Both, $Ba_2FeSbSe_5$ and $Ba_2FeBiSe_5$ possess remarkably low thermal conductivities ranging from 0.9 to 0.4 $Wm^{-1}K^{-1}$ and from 0.8 to 0.4 $Wm^{-1}K^{-1}$ between room temperature and 500 °C.

Such low thermal conductivities can be explained by the structural complexity of $\text{Ba}_2\text{FeSbSe}_5$ and $\text{Ba}_2\text{FeBiSe}_5$. Other possible origins for such low thermal conductivities are the presence of the stereoactive $5s^2$ and $6s^2$ lone pairs of Sb and Bi and the possibility of resonant bonding within the $\text{Ba}_2\text{FePnSe}_5$ (Pn = Sb, Bi) crystal structure. It was discovered that both compounds undergo a rapid phase transition between an amorphous and a crystalline phase, which is most probably irradiation-induced. An amorphous layer can be obtained after one laser pulse of 0.3 ms with $\lambda = 1064$ nm and after measuring the thermal conductivity up to 773 K. A loss of long-range order upon irradiation with an electron beam of $\lambda = 0.00196$ nm was observed, which underlines the high sensitivity of both compounds towards external irradiation. A series of laser pulses with $\lambda = 1064$ nm at room temperature enables the amorphization and recrystallization of the surface of $\text{Ba}_2\text{FeBiSe}_5$ and the thermal conductivity can be used to follow the phase transitions. These phase changes probably arise from resonant bonding – a key requirement for phase-change materials and one origin of low thermal conductivities. Most of the established phase-change materials exclusively contain elements with similar electronegativities as a high ionicity leads to localized charges at the ion cores prohibiting resonant bonding. In $\text{Ba}_2\text{FePnSe}_5$ the stereoactive $5s^2$ and $6s^2$ lone pairs of Sb and Bi cause an elongation of three of the Pn-Se bonds in the PnSe_6 octahedra. Hence, resonant bonding is possible within the distorted octahedral Pn-Se network, where p-bonding is dominant, three longer (weaker) and three shorter (stronger) Pn-Se bonds per octahedron are present and where the difference in electronegativity between the elements is small. The average number of valence electrons per single atom of 5.22 is close to the ideal range of other compounds used as phase-change materials (4.3-5), which makes the two title compounds promising candidates for phase-change applications. Anomalies of the dielectric permittivity and the thermal conductivity at the Néel temperature were discovered as well. An additional contribution to the low-temperature thermal conductivities was observed below T_N , which has its origin in the antiferromagnetic ordering of the Fe spins below T_N . These effects cannot be entirely explained up to now. However, one probable origin of these anomalies is a coupling of magnetic order parameters and changes in the crystal structure (i.e. magnetoelastic effects), which in turn causes magnetostrictive strains and fluctuations in the dielectric permittivity.

***V. Hypervalent Cu-(I)- and Pn-chalcogenides with Pn = Sb,
Bi – from fully localised to partially delocalised electrons***

1. Overview

This chapter focuses on polychalcogenides (*cf.* chapter I), where classical bonding concepts such as the two-center two-electron bond and the octet rule, are not sufficient to rationalize their crystal structure and where hypervalent bond models and the concept of resonance are required to accurately describe the bonding situation in these compounds. The first part of the chapter focuses on $\text{Ba}_4\text{Cu}_8\text{Se}_{13}$, a new copper-(I)-selenide and the first hypervalent compound in the ternary system Ba/Cu/Se. This compound reaches a closed shell configuration by forming classical and hypervalent Se-Se bonds and through a charge transfer from the cations to Se. The *Zintl* electron counting concept can be applied to rationalize its crystal structure and apart from the hypervalent Se-Se bonds, $\text{Ba}_4\text{Cu}_8\text{Se}_{13}$ fulfills Nesper's criteria of a *Zintl* phase (*cf.* chapter I). The structure solution process as well as the crystal structure and chemical bonding in $\text{Ba}_4\text{Cu}_8\text{Se}_{13}$ is discussed with special focus on Se-Se and Cu-Cu bonding and the question of whether $\text{Ba}_4\text{Cu}_8\text{Se}_{13}$ is a cluster compound or not. It follows a discussion concerning nanotwinning, structural modulation and real structure effects, which complicated the structure solution of $\text{Ba}_4\text{Cu}_8\text{Se}_{13}$. The average crystal structure of $\text{Ba}_4\text{Cu}_8\text{Se}_{13}$ is then confirmed by transmission electron microscopy and compared to the local crystal structure. The first part of this chapter closes by discussing the low-temperature transport properties of $\text{Ba}_4\text{Cu}_8\text{Se}_{13}$. The second part of this chapter then focuses on $\text{BaBiTe}_{3-x}\text{Se}_x$ ($x = 0, 0.05, 0.1$ and 3). In BaBiTe_3 no clear oxidation state can be assigned to Te due to an extended, hypervalent Te-Te network. Hence, it is debatable of whether or not BaBiTe_3 is a *Zintl* phase. The bonding situation in this compound is reexamined in this chapter by means of *ab initio* calculations based on the density functional theory (DFT). Then, the electronic structure is discussed, including all orbital contributions to the band edges. The electronic structure of BaBiTe_3 is then related to its optical properties and to those of Se substituted variants of BaBiTe_3 . It follows a detailed discussion of the thermoelectric transport properties of $\text{BaBiTe}_{3-x}\text{Se}_x$ ($x = 0, 0.05$ and 0.1) with special focus on the question how native defects and the complex electronic structure of these compounds affects the thermoelectric transport properties.

2. Polar chalcogenides with hypervalent three-center four-electron (3c-4e) bonds

2.1 Ba₄Cu₈Se₁₃ – a new ternary copper-(I)-selenide

Copper selenides such as Cu_{2-x}Se are promising thermoelectric materials and the high mobility of Cu can result in many interesting physical properties (e.g. fast ion conduction, glass-like thermal conductivities). The growing interest of the thermoelectric community in copper selenides was the main motivation for studying the ternary system Ba-Cu-Se. What made this system also attractive is the fact that there is only one compound (BaCu₂Se₂), which is reported so far. With Ba₄Cu₈Se₁₃, this thesis now turns from normal valent to a hypervalent compound with “molecular-like” hypervalent units. In these units the electrons are not fully localized anymore, but partially delocalized, which requires the description of chemical bonding using the concept of resonance (*cf.* chapter I).

2.1.1 Introduction

It was already outlined in the introduction that polychalcogenides exhibit a rich structural chemistry including a variety of complex anionic frameworks with homonuclear bonds between negatively charged chalcogen atoms (Q).^[27,150] In chalcogen-rich tellurides, selenides and sulfides helical Q_n²⁻ (n = 1-13) chains are typically found.^[29,151] More uncommon motifs such as linear chains^[152] and square-planar nets (both distorted and undistorted variants)^[153,154] especially occur in polytellurides. The size of the anionic fragment depends on the number of electrons transferred to the chalcogen atom. Quasi-molecular units and homonuclear Q-Q bonds can form if the anionic framework is highly electron-rich.^[155] By using a charge transfer from a strong cation such as Ba²⁺ towards a Cu-Se network, crystal structures with Se₂²⁻ or linear, hypervalent Se₃⁴⁻ units become accessible. The existence of linear Se₃⁴⁻ units was first discovered in Ba₂Ag_{4-x}Cu_xSe₅^[151], which is the only example up to now where the Se-Se angle in the Se₃⁴⁻ fragment is 180°, while an almost linear Se₃⁴⁻ fragment (Se-Se angle of 164°) is reported for Rb₁₂Nb₆Se₃₅.^[156] A variety of other copper chalcogenides such as ACu₄Q₃ (A = K, Rb, Cs, Tl and Q = S, Se)^[157-161], Na₃Cu₄S₄^[162,163], NaCu₆Se₄^[164], TlCu₂Q₂ (Q = S and Se)^[165] have a single negative charge on the chalcogen atom without the presence of chalcogen-chalcogen bonds, which underlines the rich structural chemistry of polar ternary copper chalcogenides.

Originally these compounds with its latest example NaCu_4Se_3 ^[166] were separated in two categories – those which contain only Cu^+ and Q^{2-} ^[167-169] and those with mixed-valent $\text{Cu}^{1+/2+}$ and Q-Q bonds. BaCu_2Se_2 ^[167], which belongs to the first category, is the only known compound in the ternary system Ba/Cu/Se, which received considerable attention for its promising thermoelectric properties.^[170,171] Here, the crystal structure and transport properties of the second member of this system - $\text{Ba}_4\text{Cu}_8\text{Se}_{13}$ are presented. $\text{Ba}_4\text{Cu}_8\text{Se}_{13}$ is the first compound with Cu_4Se_9 building blocks containing planar Cu rectangles and an anionic framework with coexisting Se_2^{2-} and linear, hypervalent Se_3^{4-} units.

2.1.2 Results and Discussion

2.1.2.1 Average crystal structure obtained by single crystal X-ray diffraction

Single crystal structure determination

The structure solution of $\text{Ba}_4\text{Cu}_8\text{Se}_{13}$ was complicated by the presence of overlapping Bragg reflections, diffuse intensities and the absence of clear periodicities along a specific direction of the reciprocal space. Due to these “real structure effects” not all observed reflections can be indexed in a straightforward fashion. Several crystals exhibit the same features, which seem to be typical for crystals obtained by the previously described synthesis route. This led to the conclusion that these effects are related to intrinsic real structure effects in the crystal structure. The **a** and **b** cell parameters could be determined without problems, while the periodicity along the **c*** direction could not be obtained in a straightforward fashion (*cf.* Fig. V.1a) since a quasi-continuum of intensities can be observed for some reciprocal rows of reflections running along **c*** (see profile (green) of the $[311]^*$ row in Fig. V.1a).

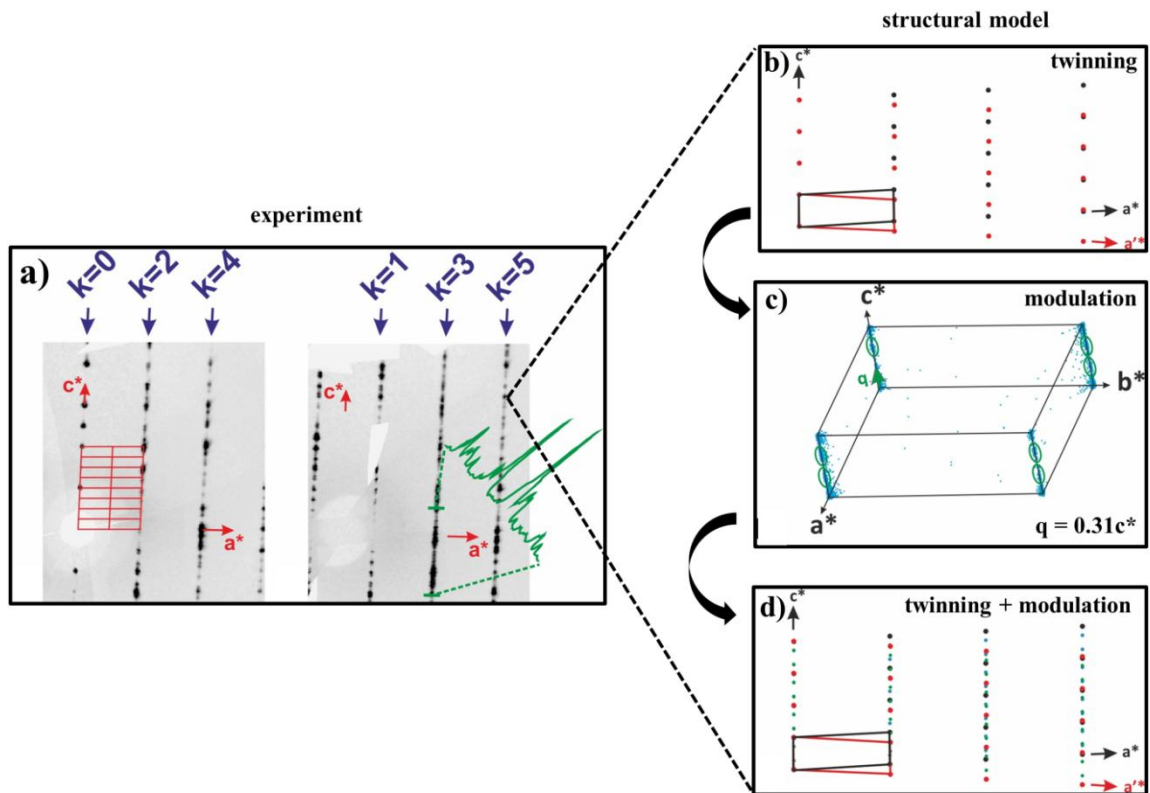


Fig. V.1: a) left: $(h0l)^*$ and right: $(h1l)^*$ planes obtained from experimental X-ray diffraction frames collected on a $\text{Ba}_4\text{Cu}_8\text{Se}_{13}$ single crystal. The unit cell (red) corresponds to $a = 9.171(8) \text{ \AA}$, $b = 9.146(8) \text{ \AA}$, $c = 27.35(3) \text{ \AA}$, $\beta = 93.21(3)^\circ$; the profile of a segment of the $[13l]^*$ row is depicted in green and it shows a quasi-continuum along c^* ; b) schematic drawing of the $(h0l)^*$ diffraction plane when only two twin domains associated to a twofold axis parallel to c^* (one twin domain in black, the second one in red) are considered in the structural model; c) all observed reflections extracted from the experimental frames of the single crystal X-ray diffraction experiment projected into the average unit cell; a weak enhancement of the reflection density at $0.31c^*$ allows the definition of the wave vector $q = 0.31c^*$ (green color); d) schematic drawing showing the $(h0l)^*$ diffraction plane expected for the cell $a = 9.171(8) \text{ \AA}$, $b = 9.146(8) \text{ \AA}$, $c = 27.35(3) \text{ \AA}$, $\beta = 93.21(3)^\circ$ when a modulation vector of $q = 0.31c^*$ and twinning according to b) is considered in the structural model.

However, on the basis of the strongest reflections, an average periodicity was chosen leading to the following cell parameters: $a = 9.171(8) \text{ \AA}$, $b = 9.146(8) \text{ \AA}$, $c = 27.35(3) \text{ \AA}$ and $\beta = 93.21(3)^\circ$. Analyzing the oriented diffraction planes assembled from the experimental frames (cf. Fig. V.1a) revealed that the limiting diffraction condition $hkl: h + k = 2n$ is fulfilled, which is consistent with a C centering of the lattice. In the $(h0l)^*$ planes the $l = 2n$ condition seems to be fulfilled, which is characteristic for the existence of a c glide plane perpendicular to the \mathbf{b} direction.

Hence, $C2/c$ was chosen as the space group to proceed with since the analysis of the reciprocal space is consistent with the space group determined by CellNow.^[55] At this step, a new data collection was performed at 100 K in order to verify whether or not the observed real structure effects along c^* has its origin in temperature induced disorder in the structure and to obtain diffraction patterns with reduced diffusion along c^* to simplify the structure solution. The diffraction patterns show no difference from those collected at room temperature, i.e. the real structure effects causing the overlapping Bragg reflections, diffusion and the absence of clear periodicities along c^* are also present at 100 K. We now discuss the problem of coexistence of periodicities along the c^* direction. Pseudo-merohedral twinning was included, where a twofold axis parallel to a was considered as the twin element. Including this type of twinning allowed a description of one part of the unindexed reflections (*cf.* Fig. V.1b). The integration of the dataset collected at room temperature was performed considering the cell parameters $a = 9.171(8) \text{ \AA}$, $b = 9.146(8) \text{ \AA}$, $c = 27.35(3) \text{ \AA}$, $\beta = 93.21(3)^\circ$ and twinning. Anisotropic atomic displacement parameters were introduced for all the atoms and refining the site occupancies resulted in a full occupancy of all atomic positions. The final refinement led to a relatively high value for the reliability factor ($R_F = 12.5 \%$) and the presence of a fairly large residual electron density mainly in the vicinity of the Ba atoms. These features will be discussed in the section “*Nanotwinning, structural modulations and real structure effects along c^** ”. However, we obtained a first, chemically reasonable structural model of the average crystal structure by single crystal X-ray diffraction, which is discussed in the section “*Description of the average crystal structure*”. Detailed information on the data collection and refinement are summarized in Table V.1. Equivalent isotropic displacement factors and positional parameters can be found in Table V.2 and selected interatomic distances and bond angles are summarized in Table V.3.

Table V.1 General crystallographic information obtained from single crystal structure solution and refinement

Formula weight (g/mol)	2084.21
Space group	C2/c (No. 15)
<i>a</i> (Å)	9.171(8)
<i>b</i> (Å)	9.146(8)
<i>c</i> (Å)	27.35(3)
β (°)	93.21(3)
<i>V</i> (Å ³)	2290.791
<i>Z</i>	4
F(000)	3592
ρ_{calcd} (g cm ⁻³)	6.0432
<i>T</i> (K)	293
Crystal dimensions (mm)	0.096x0.101x0.249
Radiation	Mo-K α
μ (Mo K α) (mm ⁻¹)	34.655
2 θ limits	2.98 – 67.28
Data collected	-9 $\leq h \leq$ 14, -14 $\leq k \leq$ 9, -35 $\leq l \leq$ 41
No. of measured reflections	14316
No. of unique reflections	3991
No. of unique reflections with $I > 3\sigma(I)$	3152
No. of parameters	136
$R(F)$ for $F_o^2 > 2\sigma(F_o^2)$	0.1250
$R_w(F_o^2)/R_{\text{int}}$	0.2087/0.0468
Goodness of fit	1.74
$(\Delta\rho)_{\text{max}}, (\Delta\rho)_{\text{min}}$ (e Å ⁻³)	11.07, -5.75

Table V.2 Equivalent isotropic displacement factors (\AA^2) and positional parameters

Atom	Wyckoff position	s.o.f.	x	y	z	$U_{\text{eq}}(\text{\AA}^2)$	$U_{11}(\text{\AA}^2)$	$U_{22}(\text{\AA}^2)$	$U_{33}(\text{\AA}^2)$
Ba1	8f	1	0.7432(5)	0.4604(5)	0.20451(16)	0.0175(5)	0.0155(7)	0.0170(8)	0.0206(8)
Ba2	8f	1	0.4842(6)	0.2291(6)	0.02357(17)	0.0243(6)	0.0259(11)	0.0274(12)	0.0194(9)
Se1	4e	1	0.5	0.2088(5)	0.25	0.0189(10)	0.0124(15)	0.0146(17)	0.030(2)
Se2	8f	1	0.0834(3)	0.3026(3)	0.18960(10)	0.0147(7)	0.0143(11)	0.0183(13)	0.0120(12)
Se3	8f	1	-0.0178(3)	0.7078(3)	0.15085(10)	0.0127(6)	0.0118(10)	0.0136(11)	0.0136(11)
Se4	8f	1	0.2205(3)	0.4617(3)	0.05486(9)	0.0131(6)	0.0134(10)	0.0142(11)	0.0120(11)
Se5	8f	1	-0.1886(3)	0.3647(3)	0.07325(10)	0.0157(7)	0.0158(11)	0.0133(12)	0.0185(13)
Se6	8f	1	0.3963(3)	0.6163(3)	0.19024(10)	0.0140(7)	0.0165(11)	0.0140(12)	0.0121(11)
Se7	8f	1	0.1270(3)	0.0511(3)	0.07358(11)	0.0150(7)	0.0155(11)	0.0131(12)	0.0171(13)
Cu1	8f	1	0.2294(4)	0.6605(4)	0.12051(13)	0.0167(9)	0.0159(14)	0.0162(16)	0.0180(16)
Cu2	8f	1	0.4298(4)	0.4606(4)	0.12040(14)	0.0190(10)	0.0192(16)	0.0202(17)	0.0180(17)
Cu3	8f	1	0.0262(4)	0.4574(4)	0.11824(15)	0.0202(10)	0.0164(15)	0.0206(18)	0.0244(19)
Cu4	8f	1	0.2268(4)	0.2569(4)	0.11780(15)	0.0229(11)	0.0202(16)	0.0182(17)	0.031(2)

Table V.3 Selected interatomic distances and angles

Atom pairs	Distances (Å)	Atom pairs	Distances (Å)
Se1•••Se3	2.708(3)	Cu4•••Se4	2.543(5)
Se2•••Se6	2.418(4)	Cu1•••Se5	2.416(5)
Se5•••Se7	2.401(4)	Cu3•••Se5	2.417(5)
Cu1•••Cu2	2.593(5)	Cu1•••Se6	2.412(4)
Cu1•••Cu3	2.629(5)	Cu2•••Se6	2.416(5)
Cu2•••Cu4	2.632(5)	Cu2•••Se7	2.420(5)
Cu3•••Cu4	2.598(5)	Cu4•••Se7	2.391(5)
Ba1•••Cu2	3.579(6)	Cu3•••Se2	2.444(5)
Ba1•••Cu3	3.605(6)	Cu4•••Se2	2.460(5)
Ba1•••Cu4	3.600(6)	Cu1•••Se3	2.495(4)
Ba2•••Cu4	3.600(7)	Cu2•••Se3	2.495(5)
Ba2•••Cu3	3.594(6)	Ba1•••Se1	3.483(5)
Cu3•••Se3	2.499(5)	Ba1•••Se2	3.483(5)
Cu4•••Se3	2.503(5)	Ba1•••Se3	3.527(5)
Cu1•••Se4	2.553(4)	Ba2•••Se7	3.441(6)
Cu2•••Se4	2.552(4)	Ba2•••Se5	3.454(6)
Cu3•••Se4	2.555(5)	Ba2•••Se3	3.488(5)
angles:			
Se3-Se1-Se3	179.61°	Se5-Cu3-Se4	104.21°
Se4-Cu1-Se5	100.80°	Se3-Cu3-Se4	111.57°
Se6-Cu1-Se5	110.30°	Se3-Cu3-Se5	110.92°
Se6-Cu1-Se4	115.57°	Se2-Cu3-Se4	115.16°
Se3-Cu1-Se6	107.80°	Se2-Cu3-Se5	109.13°
Se4-Cu1-Se3	111.21°	Se2-Cu3-Se	105.90°
Se3-Cu1-Se5	111.09°	Se2-Cu4-Se4	115.27°
Se4-Cu2-Se3	111.25°	Se7-Cu4-Se4	104.04°
Se6-Cu2-Se7	110.38°	Se7-Cu4-Se3	110.87°
Se4-Cu2-Se7	100.60°	Se7-Cu4-Se2	109.30°
Se6-Cu2-Se3	108.31°	Se4-Cu4-Se3	111.46°
Se6-Cu2-Se4	115.10°	Se2-Cu4-Se3	105.97°
Se7-Cu2-Se3	111.07°		

However, the combination of the chosen unit cell and of 2 twin domains is not sufficient to describe the reflection sequences observed along the reciprocal rows of reflections along \mathbf{c}^* . For further investigations, the position of all reflections was gathered from the experimental frames excluding any information concerning cell parameters. This list of reflections was then introduced into the indexing procedure of Jana2006. Once the previously determined unit cell was introduced, all reflections were projected into the origin of the reciprocal cell (*cf.* Fig. V.1c). They show, as expected for a regular crystal, a large density of reflections located at the corners of the parallelepiped. In addition, we observe lines of reflections along the \mathbf{c}^* direction. An accurate analysis of these lines shows a slight enhancement in reflection density at the positions $\pm 0.31\mathbf{c}^*$ (*cf.* Fig. V.1c). Hence, including these reflections and describing $\text{Ba}_4\text{Cu}_8\text{Se}_{13}$ as a modulated structure is necessary in order to obtain a better description of the observed real structure effects along \mathbf{c}^* (compare Fig. V.1 a) and d). A detailed interpretation of these findings can be found in the section “*Nanotwinning, structural modulation and real structure effects*”.

Description of the average crystal structure

The crystal structure of $\text{Ba}_4\text{Cu}_8\text{Se}_{13}$ (*cf.* Fig. V.2) is built up by unprecedented Cu_4Se_9 fragments containing four slightly distorted, edge-sharing CuSe_4 tetrahedra (*cf.* Fig. V.3a). In the \mathbf{ab} -plane the Cu_4Se_9 fragments are connected by selenium bridges formed by homonuclear Se-Se bonds resulting in two dimensional layers (*cf.* Fig. V.3b). Two of these layers are connected along \mathbf{c} via linear, hypervalent Se_3^{4-} groups resulting in “sandwich-like”, layered building blocks stacked along \mathbf{c} . In terms of charge balance $\text{Ba}_4\text{Cu}_8\text{Se}_{13}$ can be rationalized using the Zintl formalism as $(\text{Ba}^{2+})_4(\text{Cu}^{1+})_8(\text{Se}^{2-})_2(\text{Se}_2^{2-})_4(\text{Se}_3^{4-})$ assuming a complete charge transfer from the barium atoms to the anionic framework. This notation takes into account the Se_2^{2-} groups formed between Se5-Se7 and Se2-Se6 and the linear, hypervalent Se_3^{4-} groups, which are formed by Se1 and Se3 (*cf.* Fig. V.3c). In Fig. V.3d it is illustrated how four electrons are delocalized over three selenium atoms, which is typical for hypervalent $3c-4e$ bonds resulting in a formal charge of -4 on the Se_3 units. Se_3^{4-} is isoelectronic to the well-known I_3^- anion and the Sb_3^{7-} unit found in $\text{Yb}_{14}\text{MnSb}_{11}$.^[172]

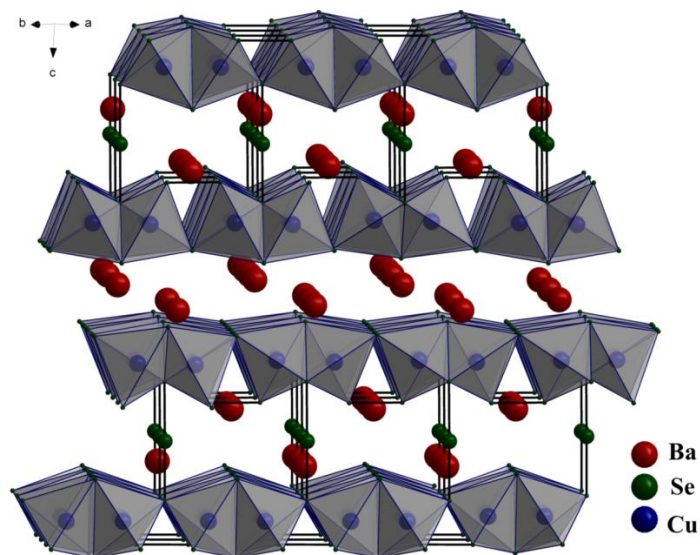


Fig. V.2: Average crystal structure of $\text{Ba}_4\text{Cu}_8\text{Se}_{13}$ obtained from single crystal X-ray diffraction and viewed along $[110]$: The basic Cu_4Se_9 building blocks consisting of four edge-sharing CuSe_4 tetrahedra (grey) are connected in two dimensions via Se atoms and Se-Se bonds (black) resulting in two dimensional Cu-Se layers. Two of these layers are connected by hypervalent Se_3^{4-} units resulting in covalently bonded, “sandwich-like” building blocks, which are stacked along c and the Ba atoms are intercalated between each Cu-Se layer. Ba: red, Se: green, Cu: blue.

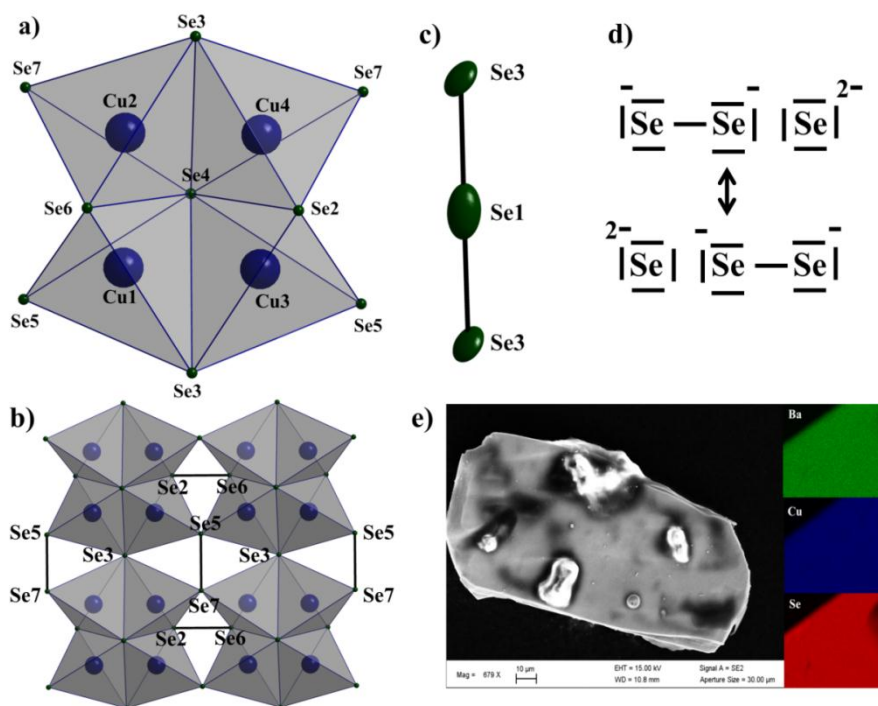


Fig. V.3: a) one Cu_4Se_9 unit in polyhedral representation; b) thermal ellipsoids of the linear, hypervalent Se_3^{4-} unit, which is slightly elongated along the bond axis; c) schematic representation of the hypervalent bonding in Se_3^{4-} which explains the slight elongation of the thermal ellipsoids along the bond axis; d) two dimensional connection of the Cu_4Se_9 building blocks via Se3, Se2-Se6 and Se5-Se7 bonds e) SEM image of a $\text{Ba}_4\text{Cu}_8\text{Se}_{13}$ single crystal and the corresponding compositional maps.

The interatomic Se-Se distances of 2.708(3) Å (*cf.* Table V.3) in the linear, hypervalent Se₃⁴⁻ units are comparable to those found in Ba₂Ag_{4-x}Cu_xSe₅ (2.7706(9) Å – 2.783(1) Å)^[151] and Rb₁₂Nb₆Se₃₅ (2.68 Å).^[156] The thermal ellipsoid of Se1 in Ba₄Cu₈Se₁₃ is slightly elongated along the bond axis (*cf.* Fig. V.3c and Table V.2), which suggests that Se1 is slightly disordered along this direction and the disorder can be rationalized using the resonant bonding picture illustrated in Fig. V.3d. The interatomic distances in the Se₂²⁻ units (2.401(4) Å and 2.418(4) Å) are slightly longer, but comparable to those found in elemental selenium (2.34 Å in α-Se and 2.37 Å in trigonal Se)^[173,174] and other chalcogenides such as USe₃ (2.36 Å).^[175] The Cu-Cu distances range from 2.593(5) Å – 2.632(5) Å and they are comparable to those found in elemental copper (2.5527(35) Å).^[176] Comparable values are also reported for other copper selenides such as Rb₃Cu₈Se₆ (2.49 Å), Cs₃Cu₈Se₆ (2.46 Å) and K₃Cu₈Se₆ (2.50 Å).^[177,178] These short Cu-Cu distances in Ba₄Cu₈Se₁₃ raise the question of whether Cu(I)-Cu(I) bonding interactions have to be considered. In this case Ba₄Cu₈Se₁₃ is better described as a cluster compound containing Cu₄Se₉ clusters with direct Cu-Cu bonds (*cf.* Fig. V.4).

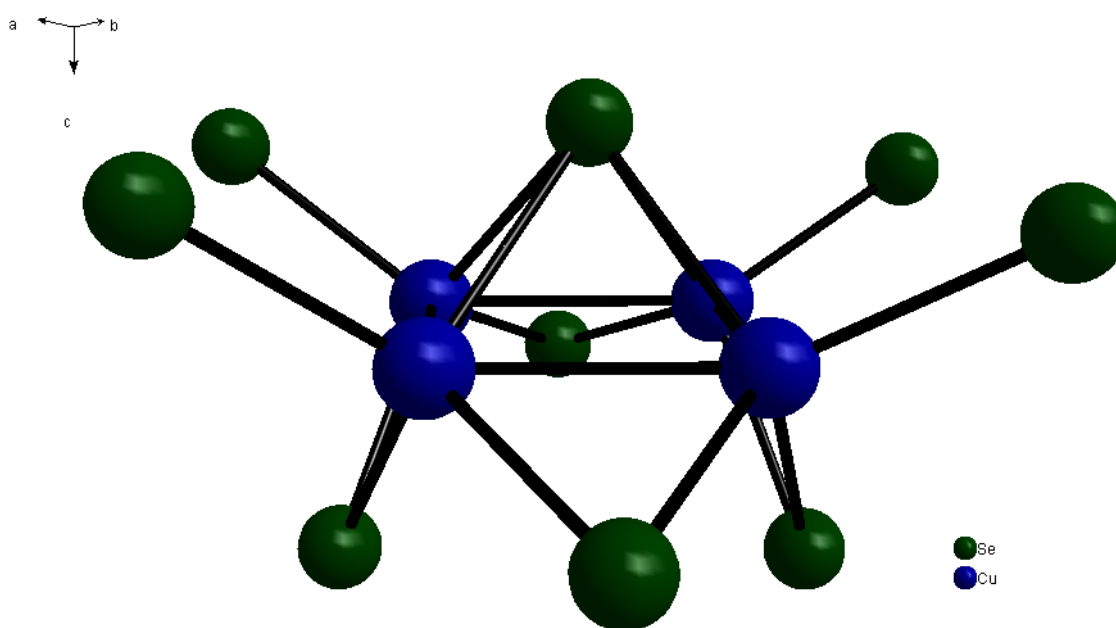


Fig. V.4: Cu₄Se₉ cluster with a slightly distorted D_{4d} symmetry and where Cu(I)-Cu(I) bonding interactions are considered.

Mehrotra et al. studied such potential Cu(I)-Cu(I) bonding interactions in organocopper(I) compounds including clusters with Cu_4^{4+} squares and Cu-Cu distances of 2.42 Å.^[179] The authors computed binding energies and overlap populations in these Cu_4^{4+} units as a function of the Cu-Cu distance including considerations of steric effects of the ligands. For a Cu-Cu distance of 2.57 Å in Cu_4^{4+} squares with an ideal D_{4h} symmetry, which comes closest to the situation in $\text{Ba}_4\text{Cu}_8\text{Se}_{13}$, a binding energy of -0.984 eV and an overlap population of 0.080 was found. The authors concluded that both, direct Cu(I)-Cu(I) bonding interactions and ligand stereochemistry, are responsible for the short Cu-Cu distances when considering a mixing of the 3d, 4s and 4p orbitals of Cu. Considering these findings, a description of $\text{Ba}_4\text{Cu}_8\text{Se}_{13}$ as a cluster compound, which contains Cu_4Se_9 clusters with Cu(I)-Cu(I) bonding interactions seems also reasonable. The dihedral angle between the Cu2-Cu1-Cu3 and Cu4-Cu3-Cu1 planes is 179.75°, i.e. the copper atoms in the Cu_4Se_9 clusters can be considered as being in plane resulting in an almost ideal D_{4d} symmetry, however broken by the slightly unequal Cu-Cu distances. It is known, that isolated, square planar transition metal clusters are difficult to stabilize, if only d-orbitals are considered since orbital symmetry restrictions allow no more than two in-plane metal-metal bonds.^[180] This has been demonstrated for the $\text{Os}_4(\text{CO})_{16}$ cluster, which shows a strong distortion away from an ideal D_{4h} geometry. It is intriguing, that the Cu_4Se_9 “clusters” in $\text{Ba}_4\text{Cu}_8\text{Se}_{13}$ come very close to an ideal D_{4d} symmetry. Possible explanations are s- and p-orbital contributions allowing four in plane Cu-Cu bonds and steric effects coming from the ligands and the neighboring Cu_4Se_9 building blocks. In Fig. V.3d a SEM image of a $\text{Ba}_4\text{Cu}_8\text{Se}_{13}$ single crystal and the corresponding compositional mapping are depicted and the latter shows a homogenous distribution of all three elements within the crystal.

2.1.2.2 Nanotwinning, structural modulation and real structure effects

The relatively high reliability factor and residual electron density peaks mainly observed 0.78 Å away from Ba2 at the final stage of the refinement can be considered as directly related to the previously described real structure effects. In this part of the chapter the origin of these effects is discussed. The previously described structural model represents an average model describing the main characteristics of the sample including twinning.

In order to obtain additional information concerning the real structure and local order in $\text{Ba}_4\text{Cu}_8\text{Se}_{13}$, a detailed transmission electron microscopy analysis was performed on polycrystalline $\text{Ba}_4\text{Cu}_8\text{Se}_{13}$. The HAADF image shown in Fig. V.5a corresponds to a part of a crystallite of polycrystalline $\text{Ba}_4\text{Cu}_8\text{Se}_{13}$ synthesized under the same conditions as the single crystals.

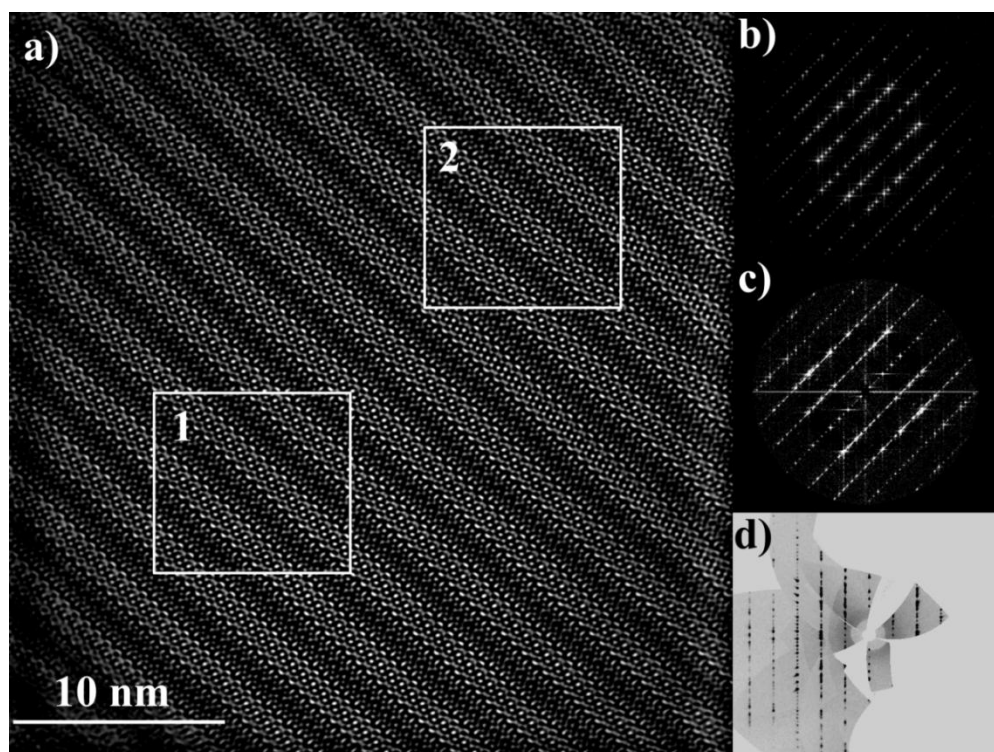


Fig. V.5: a) HAADF image taken of a polycrystalline sample in the zone axis $[110]$ and b) the corresponding Fourier Transform of area 1 showing no real structure effects; c) the corresponding Fourier Transform of area 2 showing real structure effects along the c^* -axis; d) $(0kl)$ diffraction pattern obtained from single crystal X-ray diffraction, i.e. real structure effects can be observed in both single crystalline and polycrystalline $\text{Ba}_4\text{Cu}_8\text{Se}_{13}$.

This analysis revealed areas without (*cf.* Fig. V.5b) and with real structure effects (*cf.* Fig. V.5c) analogical to those observed by single crystal X-ray diffraction (*cf.* Fig. V.5d). Analyzing area 2 of the HAADF image reveals the presence of nanotwins confirming our findings from single crystal X-ray diffraction. Some of the building blocks are rotated by 180° around **c**. Fig. V.6 represents an enlargement of parts of the HAADF image shown in Fig. V.5a including area 2.

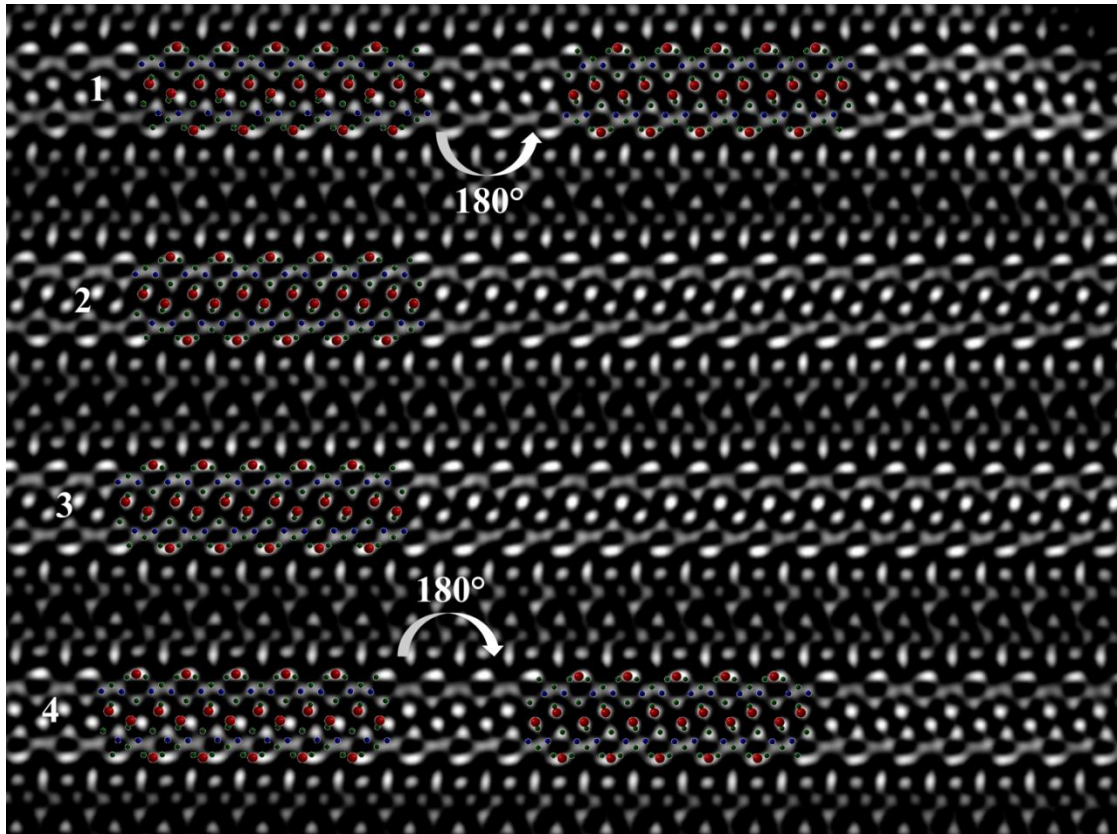


Fig.V.6: Enlargement of a part of the HAADF image shown in Fig.V.5, which contains real structure effects. Four, “sandwich-like” building blocks of the crystal structure and four layers (labeled 1-4) of the HAADF image are superimposed by simple translation of the building block resulting in a misfit of the atoms in layer 1 and 4. The building blocks with the misfit are rotated 180° around c (right part of the image). The rotation leads to a perfect overlap of the atoms. This type of nanotwinning found in layer 1 and layer 4 can explain some of the additional reflections along c^* ; red: Ba, blue: Cu, green: Se.

Four parts of the image are superimposed by the average structural model obtained by single crystal X-ray diffraction and these parts are labeled 1-4. A simple translation of parts of the structural model from layer 2 to layer 3 leads to a perfect overlap of the average structural model with the HAADF image. The same translation with respect to layer 1 and layer 4 on the other hand results in a misfit of some of the atoms. This misfit is illustrated in Fig. V.7a, which corresponds to an enlargement of part 1 with parts of the average structural model translated from part 2 and superimposed on part 1. If the whole building block is rotated by 180° around c the atoms overlap perfectly with the HAADF image again (*cf.* Fig. V.7b).

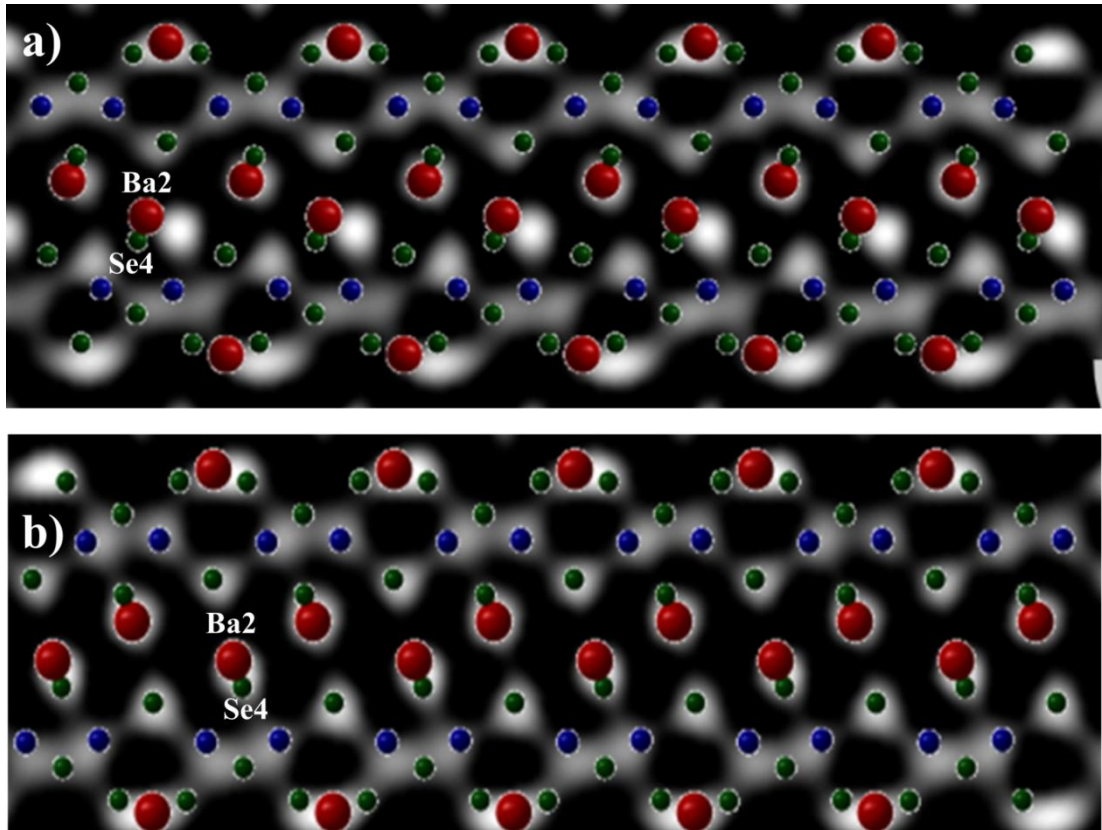


Fig. V.7: Enlargement of layer 1 shown in Fig.V.6; a) shows the misfit of the atoms after translating the building block from layer 2 to layer 1 without a rotation of the building block; b) shows a perfect overlap of the atoms after rotating the building block 180° around c; red: Ba, blue: Cu, green: Se; the nanotwins are especially visible by looking at Ba2 and Se4.

Hence area 2 of the HAADF image clearly contains nanotwins corresponding to a 180° rotation of some of the covalently bonded, “sandwich-like” building blocks around the c-axis, which is consistent with the twin domains introduced in our single crystal structural model describing the average crystal structure of $\text{Ba}_4\text{Cu}_8\text{Se}_{13}$. These nanotwins are especially visible by looking at the Ba2 and Se4 atoms as it is illustrated in Fig. V.8.

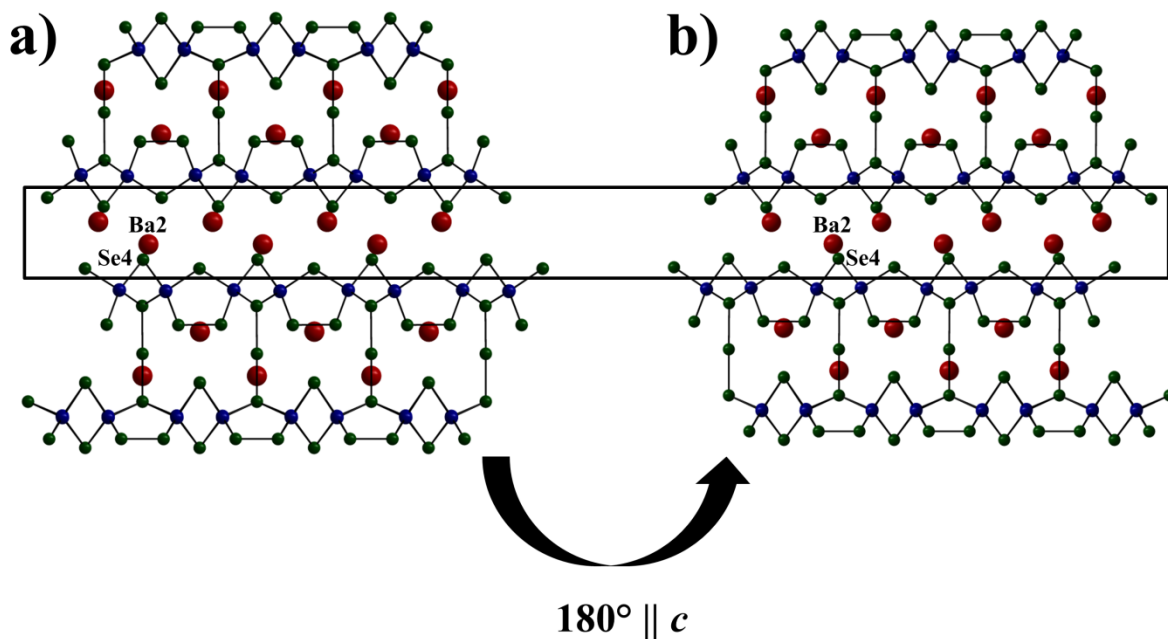


Fig. V.8: Illustration of the nanotwins with special focus on the interface of two “sandwich-like” building blocks and on the Ba2 and Se4 atoms; a) shows a [110] projection of the structural model, while b) corresponds to a 180° rotation of the [110] projection around the c -axis. This illustration shows that a rotation of entire building blocks is possible without breaking any covalent bonds within the two covalently bonded, “sandwich-like” building blocks.

The image shows that a 180° rotation of the covalently bonded, “sandwich-like” building blocks around c is possible without breaking any covalent bonds since these building blocks are only separated by Ba atoms. These nanotwins lead to a slight shift of the atoms in the ab -plane, which alters the periodicity along c and they can explain some of the additional reflections along c^* . However, they cannot explain the entire reflection sequences observed along this direction. This is why the previously discussed $0.31c^*$ periodicity was included (*cf.* section “*Single crystal structure determination*”) in our structural model since these additional reflections contain information about structural modulations, i.e. deviations of the atomic positions from their equilibrium positions. To account for these additional reflections a superspace formalism developed for the description of aperiodic crystal structures was used^[181] and a modulation wave vector of $\mathbf{q} = 0.31 \mathbf{c}^*$ was thus introduced.

A schematic representation of the $(h0l)^*$ plane, including twinning and satellite reflections, is provided in Fig V.1d, which is meant to be compared to Fig. V.1a. The data, collected at room temperature, was integrated using the unit cell $a = 9.171(8) \text{ \AA}$, $b = 9.146(8) \text{ \AA}$, $c = 27.35(3) \text{ \AA}$, $\beta = 93.21(3)^\circ$ and the \mathbf{q} vector. Starting from the average structural model and the superspace group $C2/c (\sigma_1\theta\sigma_3)0s$, harmonic waves were developed up to the first order and introduced for all atoms in order to describe possible atomic displacements. The final model led to a reasonable reliability factor for the satellite reflections (ca. 19 %) considering the partial overlap of the reflections (cf. Fig. V.1a and d). The modulation can be understood as a cooperative atomic displacement observed within a single layer. As a consequence each motif keeps its general characteristics described in the section “*Description of the average crystal structure*”. Thus, the Cu_4Se_9 units inside the layers are globally identical in each of the “sandwich-like”, layered building blocks. However, considering the stacking direction, each of the different motifs within an individual building block can exhibit small shifts along \mathbf{a} and \mathbf{b} . These shifts are one possible explanation for the diffuse intensities along \mathbf{c}^* . The modulation of the Ba1 atoms is more pronounced compared to the Ba2 atoms, which could have its origin in the different Cu-Se environments (cf. Fig. V.9).

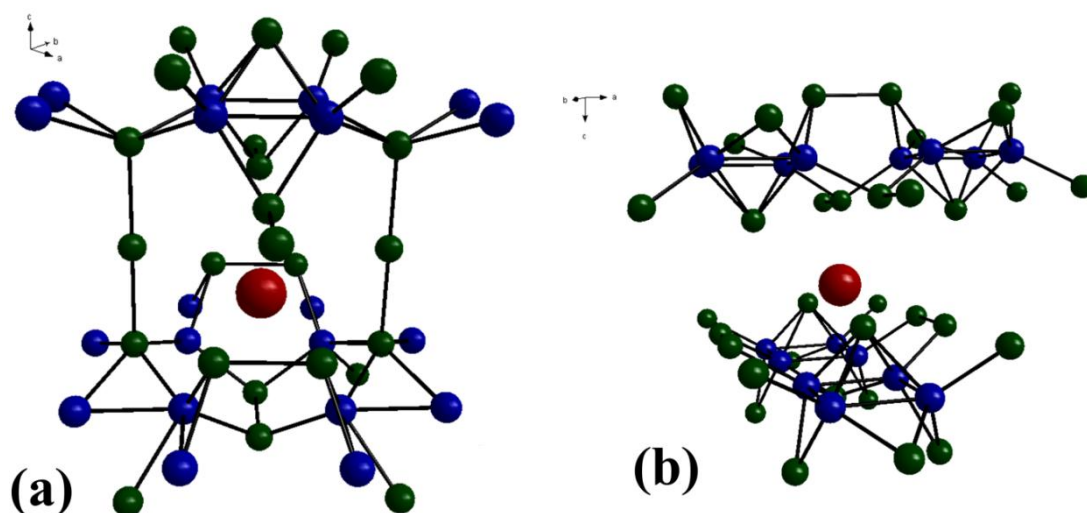


Fig V.9: a) Ba1 and b) Ba2 environments in the $\text{Ba}_4\text{Cu}_8\text{Se}_{13}$ crystal structure. The Ba1 atoms are located within the sandwich-like building blocks containing Se_3^4 units, while the Ba2 atoms are separating these building blocks and they have no Se_3^4 units in their environment.

The Ba1 atoms are located between Cu-Se layers, which are connected through Se_3^{4-} groups, which are missing in the environment of the Ba2 atoms. The Se_3^{4-} groups seem to restrict the movement of the Ba1 atoms in the **ab** plane, which might result in a large displacement along **c**. Studying the real structure effects in $\text{Ba}_4\text{Cu}_8\text{Se}_{13}$ provides a basic understanding of the origin of the diffuse intensities and absence of a clear periodicity along \mathbf{c}^* and it explains, why a relatively large reliability factor and residual electron density were obtained after solving and refining the average crystal structure of $\text{Ba}_4\text{Cu}_8\text{Se}_{13}$.

2.1.2.3 Confirmation of the structural model by transmission electron microscopy

The average structural model obtained by single crystal X-ray diffraction can be confirmed by our TEM analyses of polycrystalline $\text{Ba}_4\text{Cu}_8\text{Se}_{13}$ synthesized under the same conditions as the single crystals. This is illustrated in Fig. V.10, which shows that the structural model ([110] projection) obtained by single-crystal X-ray diffraction overlaps perfectly with the HAADF image of polycrystalline $\text{Ba}_4\text{Cu}_8\text{Se}_{13}$ taken in the [110] zone axis. This is also the case for the corresponding simulation (*cf.* Fig. V.10b). The HAADF image also clearly shows the presence of the Cu_4Se_9 and Se_3^{4-} units.

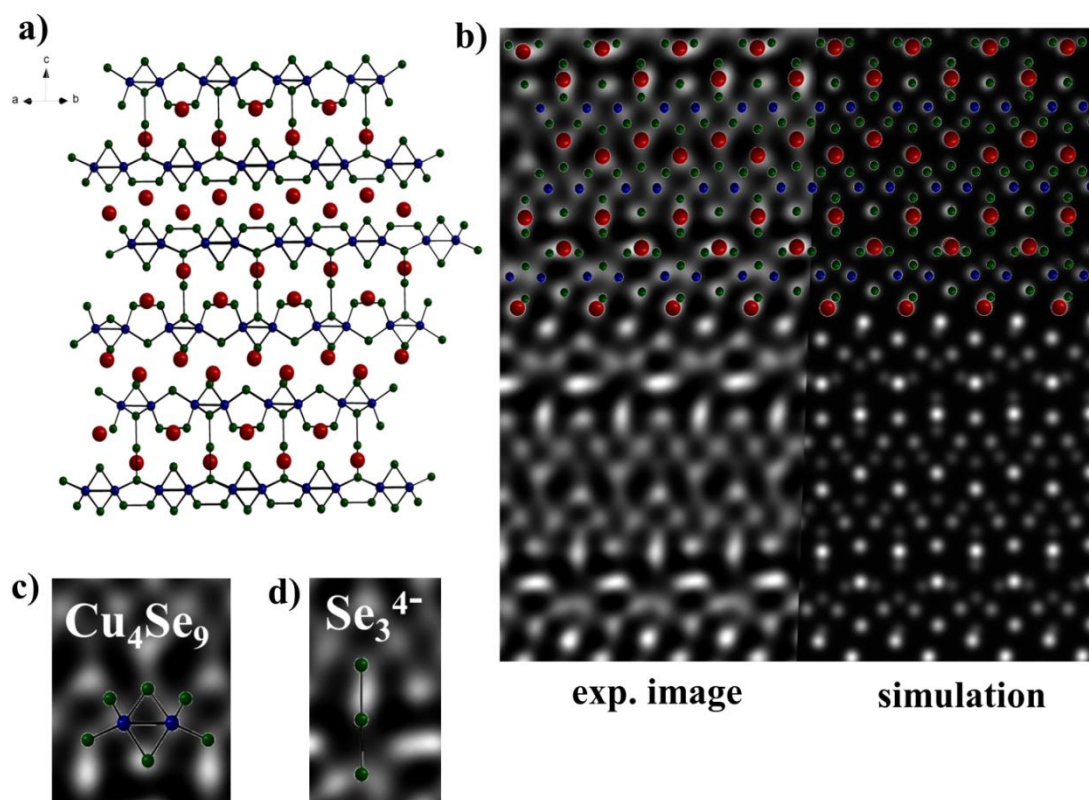


Fig. V.10: a) Projection of the $\text{Ba}_4\text{Cu}_8\text{Se}_{13}$ structure in the $[110]$ zone axis without coordination polyhedra b) HAADF image (left) taken from a polycrystalline sample in the $[110]$ zone axis and the corresponding simulation (right), both superimposed by the structural model shown in a); the Cu_4Se_9 building blocks (c) and Se_3^{4-} units (d) are clearly visible; red: Ba, blue: Cu, green: Se.

2.1.2.4 Local crystal structure

The diffuse intensities observed in both, single crystal X-ray diffraction and selected area electron diffraction patterns motivated the study of the local crystal structure of $\text{Ba}_4\text{Cu}_8\text{Se}_{13}$. The X-ray pair distribution function (XPDF) method is a total scattering technique. Hence it also accounts for diffuse scattering and it allows judging whether or not diffuse scattering is caused by disorder or changes in the local crystal structure (i.e. the first few coordination spheres) compared to the average crystal structure obtained by single crystal X-ray diffraction. In the case of $\text{Ba}_4\text{Cu}_8\text{Se}_{13}$ a XPDF analysis allows to specifically answer the question of whether or not the observed nanotwins (cf. section *Nanotwinning, structural modulation and real structure effects*) can fully explain the diffuse scattering or if there is additional disorder in the local crystal structure causing the observed real structure effects.

Fig. V.11 shows the experimental (blue) and calculated (red) atomic pair distribution function ($G(r)$). The average structural model obtained by single crystal X-ray diffraction was used as a starting model. Table V.4 summarizes the refined thermal displacement parameters and the differences in atomic positions comparing local and average crystal structure.

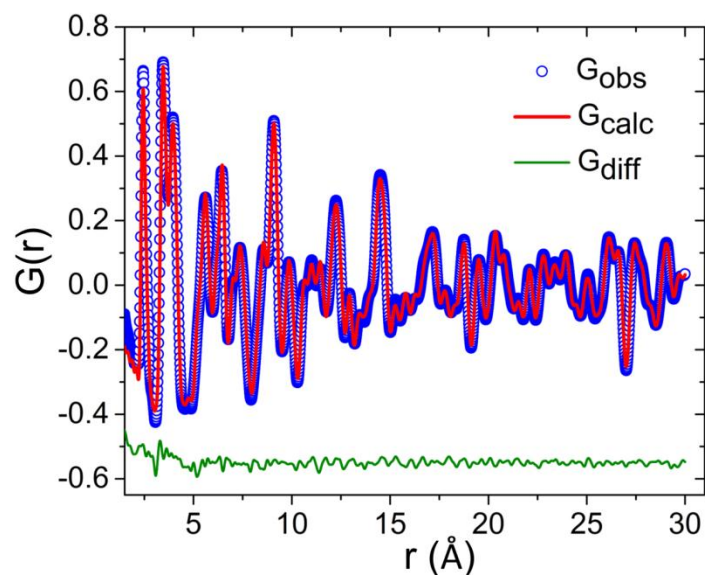


Fig.V.11: Atomic pair distribution function of $\text{Ba}_4\text{Cu}_8\text{Se}_{13}$; blue: experimental data, red: calculated PDF using the average structural model obtained from single crystal X-ray diffraction.

Table V.4 Refined thermal displacement parameters and differences in atomic positions between the local and average crystal structure

Atom	Wyckoff position	Δx	Δy	Δz	$U_{11=22=33} (\text{\AA}^2)$
Ba1	8f	0.0028	0.0021	0.00041	0.0155
Ba2	8f	0.0043	0.0078	0.00003	0.0155
Se1	4e	0.0000	0.0004	0.00000	0.0129
Se2	8f	0.0024	0.0053	0.00051	0.0129
Se3	8f	0.0025	0.0029	0.00098	0.0129
Se4	8f	0.0007	0.0017	0.00017	0.0129
Se5	8f	0.0003	0.0008	0.00045	0.0129
Se6	8f	0.0004	0.0054	0.00084	0.0129
Se7	8f	0.0003	0.0022	0.00001	0.0129
Cu1	8f	0.0000	0.0026	0.00120	0.0161
Cu2	8f	0.0019	0.0037	0.00110	0.0161
Cu3	8f	0.0029	0.0064	0.00170	0.0161
Cu4	8f	0.0056	0.0024	0.00101	0.0161

The results show that the structural model of the average crystal structure compares well to the local structural model. This is not only reflected in the good fit of G_{obs} and G_{calc} , but also in the small differences in atomic positions (*cf.* Table V.4) and lattice parameters ($\Delta a = 0.02 \text{ \AA}$, $\Delta b = 0.01 \text{ \AA}$ and $\Delta c = 0.00 \text{ \AA}$). Hence, the diffuse intensities observed in single crystal X-ray diffraction and selected area electron diffraction patterns do not originate in disorder within the first few coordination spheres (up to 30 \AA) and is best explained by disorder on a larger scale (domain disorder) such as the previously discussed nanotwins. The XPDF analysis also removes any doubt about the correctness of the average structural model of $\text{Ba}_4\text{Cu}_8\text{Se}_{13}$ one might have by looking at the large reliability factor and residual electron density obtained from the single crystal structure solution. Hence, the PDF method is also useful to confirm structural models in cases where intrinsic disorder such as nanotwinning (or stacking faults) complicates single crystal structure solutions.

2.1.2.5 Transport properties

The crystal structure of $\text{Ba}_4\text{Cu}_8\text{Se}_{13}$ is highly complex, the Ba atoms in $\text{Ba}_4\text{Cu}_8\text{Se}_{13}$ can act as phonon scattering centers and the more rigid Cu-Se network facilitates electron conduction. This is ideal for thermoelectric applications according to the phonon-glass electron-crystal (PGEC) concept introduced by Slack as being a key concept towards materials with inherently low thermal conductivities and high thermoelectric performance.^[83] Since $\text{Ba}_4\text{Cu}_8\text{Se}_{13}$ appears to fulfill this concept, the low-temperature transport properties were measured on a densified bulk sample synthesized by ball milling and subsequent spark plasma sintering. In order to confirm the crystal structure and to ensure phase purity of the sample a LeBail refinement was performed on an experimental PXRD pattern recorded after spark plasma sintering (*cf.* Fig. V.12). Detailed information on the refinement is summarized in Table V.5.

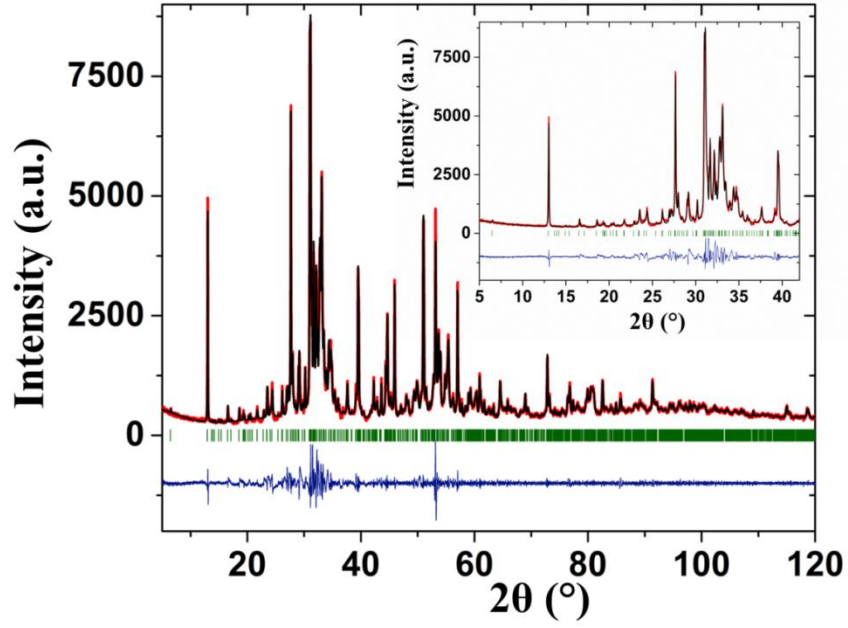


Fig. V.12: LeBail refinement of an experimental PXRD pattern recorded after spark plasma sintering; red: experimental intensities (I_{obs}), black: calculated intensities (I_{calc}), blue: $I_{\text{obs}} - I_{\text{calc}}$, green: reflection positions of $\text{Ba}_4\text{Cu}_8\text{Se}_{13}$.

Table V.5 Le Bail refinement results

Nominal composition	$\text{Ba}_4\text{Cu}_8\text{Se}_{13}$
Space group	$C2/c$ (No. 15)
Z	16
a (Å)	9.14556(15)
b (Å)	9.14137(15)
c (Å)	27.356(7)
β (°)	93.14
F(000)	3592
2θ limits (°)	5.01-119.99
Radiation	Cu-K α
Constraints	0
Refined parameters	27
R_f/R_{wp}	0.0496/0.0735
goof	1.89

$\text{Ba}_4\text{Cu}_8\text{Se}_{13}$ has a melting point of 796 K (*cf.* Fig. V.13a) and is an intrinsic p-type semiconductor (*cf.* Fig. V.13b), which is indicated by the positive Seebeck coefficient. The semiconducting behavior of the electrical resistivity is consistent with the bonding analysis, which results in the charge balanced description of the title compound as $(\text{Ba}^{2+})_4(\text{Cu}^{1+})_8(\text{Se}^{2-})_2(\text{Se}_2^{2-})_4(\text{Se}_3^{4-})$. This is in contrast to mixed-valence copper chalcogenides such as NaCu_4Se_3 , which are metallic.^[166] $\text{Ba}_4\text{Cu}_8\text{Se}_{13}$ possesses a very low thermal conductivity κ (*cf.* Fig. V.13c) even below room temperature (e.g. $0.77 \text{ Wm}^{-1}\text{K}^{-1}$ at 200 K) and a large Seebeck coefficient (*cf.* Fig. V.13d) over a broad temperature range between 100 K and 200 K reaching a value of $380 \mu\text{VK}^{-1}$ at 200 K. The electronic contribution to the thermal conductivity is negligible and the temperature dependence of κ is therefore governed by the phononic thermal conductivity (κ_{ph}). The shape of the thermal conductivity is typical for crystalline materials, where grain boundary and point defect scattering are dominant at low temperatures, while Umklapp scattering processes dominate at intermediate and high temperatures.^[182] The Seebeck coefficient shows two anomalies at ~ 50 K and ~ 125 K. Below ~ 125 K charges become increasingly localized, which is reflected in the increase in resistivity. The Seebeck coefficient on the other hand decreases sharply below ~ 125 K and shows a change in slope at ~ 50 K as does the resistivity. The drop in S is rather typical for a transition from a semiconductor to a metal, which stands in contradiction to the increase in resistivity. One possible explanation for these anomalies is a change in the electronic structure associated with order-disorder transitions as proposed for $\text{KCu}_{7-x}\text{S}_4$.^[183] However, providing a detailed explanation of the origin of these transitions requires further studies.

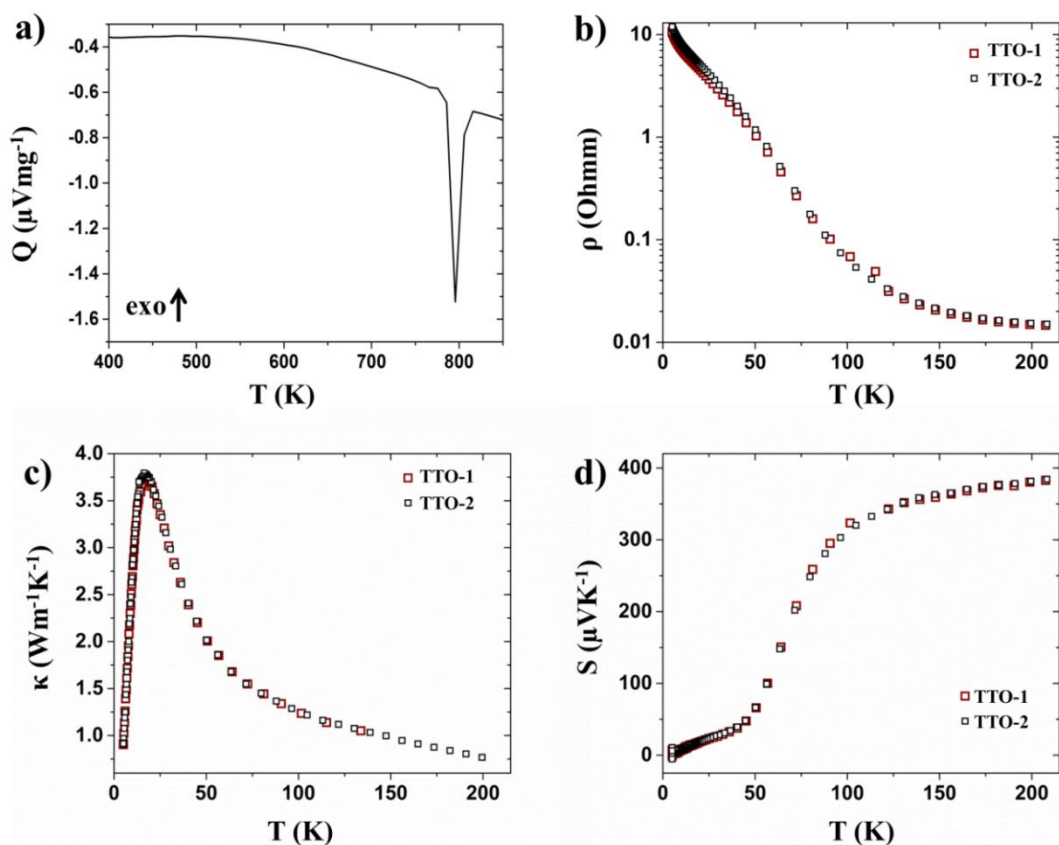


Fig. V.13: a) DSC scan showing the melting point of $\text{Ba}_4\text{Cu}_8\text{Se}_{13}$, b) electrical resistivity, c) thermal conductivity and d) Seebeck coefficient of polycrystalline $\text{Ba}_4\text{Cu}_8\text{Se}_{13}$; the abbreviations TTO-1 and TTO-2 refer to data obtained from two subsequent measurements on the same polycrystalline sample.

2.1.3 Conclusion

The new copper(I)-selenide $\text{Ba}_4\text{Cu}_8\text{Se}_{13}$ was discovered and its average crystal structure was determined by single crystal X-ray diffraction and confirmed by transmission electron microscopy. The compound crystallizes in a new structure type and it is the first example, which simultaneously contains Se_2^{2-} and linear, hypervalent Se_3^{4-} units as well as unprecedented Cu_4Se_9 building blocks with hitherto unknown planar Cu rectangles. Taking into account homonuclear bonds between selenium atoms, the compound can be rationalized as $(\text{Ba}^{2+})_4(\text{Cu}^{1+})_8(\text{Se}_2^{2-})_2(\text{Se}_2^{2-})_4(\text{Se}_3^{4-})$, i.e. it is charge balanced, which is consistent with the semiconducting behavior of the electrical resistivity. HAADF images clearly reveal the presence of the Se_3^{4-} and Cu_4Se_9 building blocks as well as nanotwins, introduced by a 180° rotation of some of the covalently bonded, “sandwich-like” building blocks, which are built up by Se_2^{2-} , Se_3^{4-} and Cu_4Se_9 fragments.

These nanotwins and a structural modulation with a modulation wave vector of $\mathbf{q} = 0.31\mathbf{c}^*$ provide a basic understanding of the real structure effects observed along \mathbf{c}^* , which made the structure solution unusually complex. Comparing average and local crystal structure revealed that the diffuse intensities, which complicated the structure solution, do not come from disorder in the first few coordination spheres. Hence, the diffraction can be entirely explained by domain disorder such as the nanotwins. $\text{Ba}_4\text{Cu}_8\text{Se}_{13}$ possesses a very low thermal conductivity (e.g. $0.77 \text{ Wm}^{-1}\text{K}^{-1}$ at 200 K) and a large Seebeck coefficient ($380 \mu\text{VK}^{-1}$ at 200 K) over a wide temperature range. Hence, $\text{Ba}_4\text{Cu}_8\text{Se}_{13}$ fulfills two requirements for efficient thermoelectric materials. The Seebeck coefficient shows anomalies at $\sim 50 \text{ K}$ and $\sim 125 \text{ K}$, where also the resistivity changes its slope. Further studies are required in order to reach an understanding of the origin of these anomalies.

3. Polar chalcogenides with an extended hypervalent network

3.1 BaBiTe_{3-x}Se_x (x = 0, 0.05, 0.1 and 3)

After Ba₄Cu₈Se₁₃ – a compound with hypervalent, molecular-like units – this thesis now turns to BaBiTe₃, a compound with a more extended hypervalent network where the electrons are even more delocalised than in Ba₄Cu₈Se₁₃. The unique and complex crystal structure of BaBiTe₃, hypervalent Te···Te bonds in the structure and its narrow band gap motivated the systematic study of the thermoelectric transport properties of BaBiTe_{3-x}Se_x (x = 0, 0.05 and 0.1) presented here. From the beginning the thermoelectric properties of BaBiTe₃ seemed to be fairly promising, which is why it was of interest to reach a deeper understanding of its thermoelectric transport properties. This study gives insight in the unusually complex chemical bonding and thermoelectric transport properties of BaBiTe₃.

3.1.1 Introduction

It was already outlined in chapter *I* and in the introduction of the Ba₄Cu₈Se₁₃ part of this chapter, that polychalcogenides exhibit a strikingly diverse crystal chemistry due to the formation of homonuclear and often hypervalent bonds between negatively charged chalcogen atoms (Q). This highly diverse anion chemistry led to the discovery of a vast amount of new compounds with interesting physical properties over the past decades.^[27,29,145,184-186] Within the family of polychalcogenides there are several examples with promising thermoelectric properties such as HfTe₅^[187], Ba₃Cu_{14-δ}Te₁₂^[188] and BaCu_{5.7}Se_{0.6}Te_{6.4}^[189] and A₂BaCu₈Te₁₀ (A = K, Rb, Cs).^[190] Many of them possess low thermal conductivities, which can be well explained by their complex crystal structures, while their overall electronic transport properties are often poorly understood. Since it was discovered that multi-valley bands^[191,192] and band convergence^[193,194] of multiple valence or conduction bands can result in high thermoelectric efficiencies, it is of interest to look deeper into the thermoelectric transport properties of polychalcogenides with complex crystal structures since many of them possess complex electronic structures and inherently low thermal conductivities. The polytelluride BaBiTe₃ is isostructural to BaBiSe₃^[195] and BaSbTe₃^[195] and it was first discovered by Chung et al.^[196] and its thermoelectric transport properties were measured on single crystals.

The unique part of the structure of BaBiTe₃ is the parallel stripes of weak hypervalent Te···Te bonding - the nature of which is still little understood. BaBiTe₃ is an ideal candidate for fulfilling the requirements of a phonon glass and an electron crystal, which according to Slack results in a low thermal and a high electrical conductivity.^[83] The rigid one dimensional [Bi₄Te₁₀]_∞ rods allow electron conduction, while the heavy Ba atoms and weak Te···Te bonding result in a low thermal conductivity similar to previously studied compounds containing Ba or Tl.^[13,197-200] In addition the electrostatic repulsion between the s² lone pairs of Bi and the neighboring Te atoms can lead to a strong anharmonicity in the lattice vibrations and hence low phononic thermal conductivities (κ_{ph}) close to the amorphous limit.^[201-204] Low-temperature thermoelectric measurements of both p- and n-type single crystalline BaBiTe₃^[196], electronic band structure calculations^[205], a pressure dependent study of the thermoelectric properties of p-type BaBiTe₃ single crystals^[206] and a recent study of K and La substituted variants of BaBiTe₃^[207] gave a first impression of its promising thermoelectric properties.

The focus of this part of the chapter lies on the nature of the Te···Te bonding in BaBiTe₃, the origin of the two, previously observed optical transitions as well as the defect chemistry and thermoelectric transport properties of BaBiTe_{3-x}Se_x (x = 0, 0.05 and 0.1) with special focus on multiband effects in the transport data. Understanding the chemical bonding is crucial since the type of bonding (metallic, covalent, ionic or hypervalent) can significantly affect the physical properties due to a different degree of electron delocalization. The electrons are for example more delocalized in hypervalent bonds than they are in classical two-center two-electron bonds. The main objectives for alloying BaBiTe₃ with Se were to reduce its thermal conductivity, determine the minimum thermal conductivity, optimize its carrier concentration and to understand the effect of the Se substitution on the thermoelectric properties of BaBiTe₃. During this study it became clear that the electronic structure, optical properties and defect chemistry of BaBiTe₃ are crucial for understanding its transport properties.

3.1.2 Results and Discussion

3.1.2.1 Crystal structure and hypervalent Te-Te bonding

The crystal structure of BaBiTe₃ (*cf.* Fig. V.14) was first determined by Chung et al.^[196] and the authors discussed two alternative Te···Te bonding situations, which can both describe the chemical bonding in the crystal structure. Their discussion is based on unusual Te···Te contacts (Te2-Te6: 3.098(2) Å and Te2···Te2: 3.170(2) Å) found between the rod-shaped columnar [Bi₄Te₁₀]_∞ segments, which are built up by edge-sharing BiTe₆ octahedra. These Te···Te distances are larger compared to those found for normal covalent Te···Te single bonds (2.69-2.80 Å)^[50], but well below typical Van der Waals interactions (4.0 Å - 4.2 Å)^[51] so that Te2-Te2 and Te2-Te6 bonding interactions have to be taken into account.

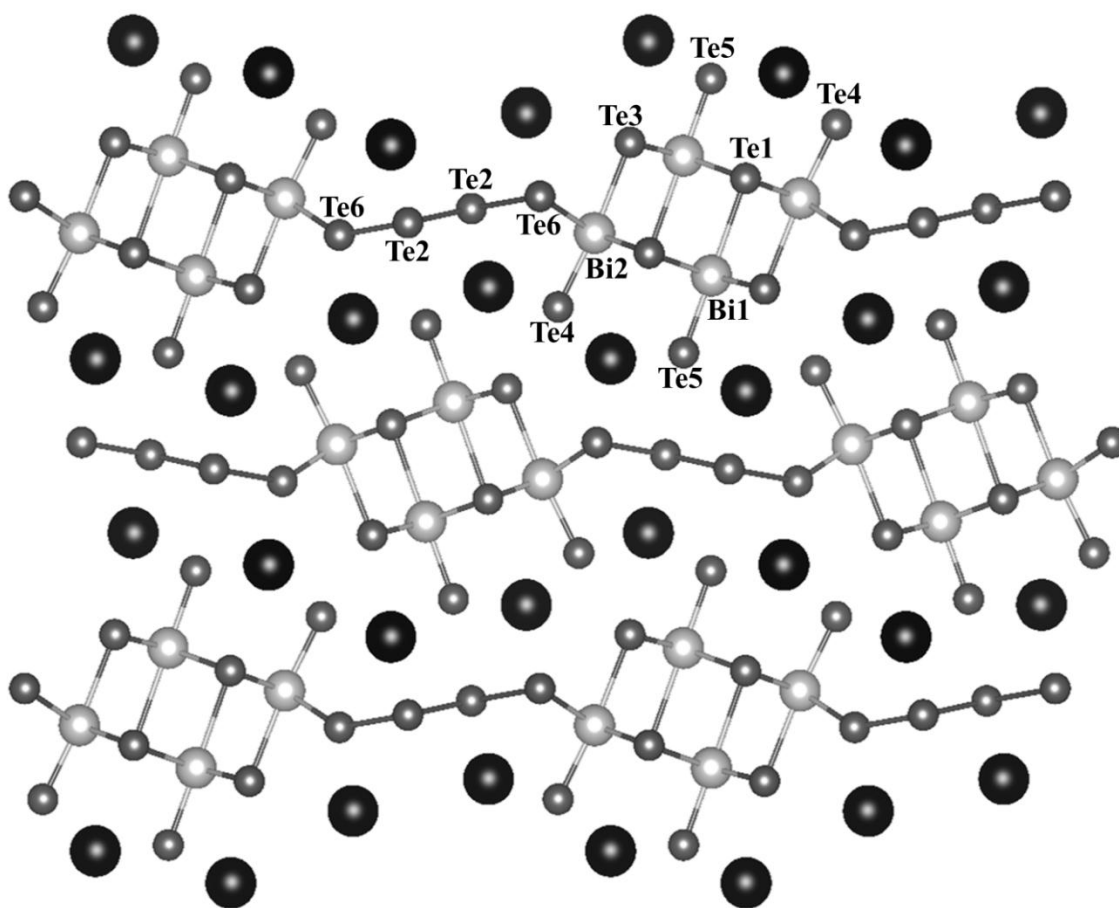


Fig. V.14 Crystal structure of BaBiTe₃ (black: Ba, light grey: Bi, dark grey: Te)

The first description rationalizes the structure as columnar $[\text{Bi}_4\text{Te}_{10}]_\infty$ segments alternating with infinite Te_n chains with $\text{Te}\cdots\text{Te}$ bonds only between the Te2 atoms, i.e. the Te_n chains are separated from the $[\text{Bi}_4\text{Te}_{10}]_\infty$ segments (*cf.* Fig. V.15a). The second description rationalizes the structure as $[\text{Bi}_4\text{Te}_{10}(\text{Te}_2)]_n^{8n-}$ “herring-bone” shaped segments with interdigitating $(\text{Te}^{-1})_2$ side groups (*cf.* Fig. V.15b). According to this description there are no bonds between the Te2 atoms and hence no infinite Te_n chains in the structure.

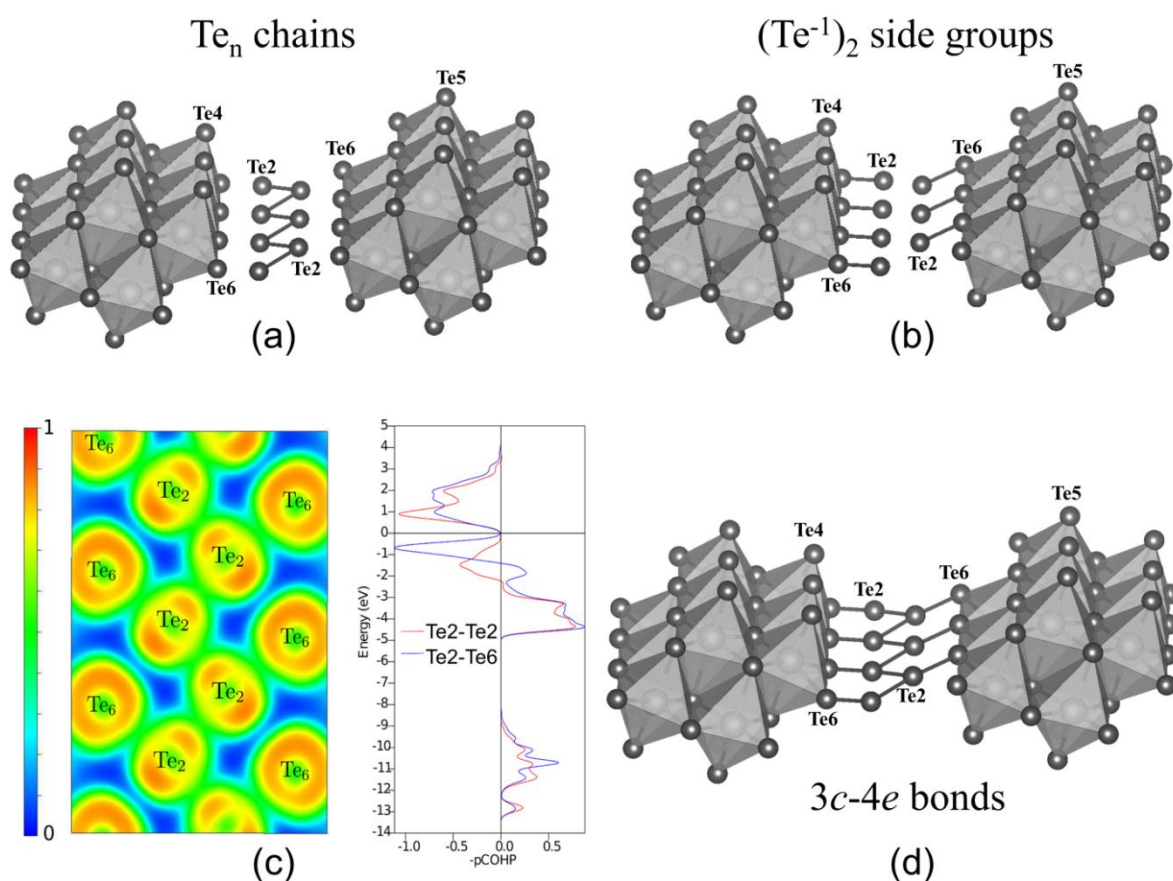


Fig. V.15 Previously described $\text{Te}\cdots\text{Te}$ bonding situations: a) Te_n chains and b) interdigitating $(\text{Te}^{-1})_2$ side groups; c) electron localization function of Te2 and Te6 (left) and $-\text{pCOHP}$ curves of the Te2-Te2 and Te2-Te6 pairs (right) showing bonding interactions between Te2-Te2 and Te2-Te6; d) hypervalent $\text{Te}\cdots\text{Te}$ bonding, which can be understood as a linear combination between a) and b) and which involves three-center-four-electron ($3c-4e$) bonds; the bonding situation in d) is based on results from $-\text{pCOHP}$ and ELF calculations shown in c); this new $\text{Te}\cdots\text{Te}$ bonding situation represents an electron delocalization over the Te2 and Te6 atoms, which reduces electrostatic repulsion between the Te2 and the Te6 atoms by minimizing their negative charge.

Chung et al. found negative overlap populations from their extended Hückel calculations and concluded, based on these findings, that the crystal structure is better described as $[\text{Bi}_4\text{Te}_{10}(\text{Te}_2)]_n^{8n-}$ rods with $(\text{Te}^{1-})_2$ side groups and that there are no Te_n chains in the BaBiTe_3 crystal structure. The bonding analysis presented here (*cf.* Fig. V.15c) focuses on the bonding between Te2 and Te6 and is based on the computation of the Electron Localization Function (ELF) and the Crystal Orbital Hamilton Population (COHP). Our analysis unambiguously shows Te2-Te2 and Te2-Te6 bonding interactions consistent with the similar interatomic Te2-Te2 and Te2-Te6 distances. This new bonding situation is shown in Fig. V.15d and can be rationalized as a linear combination of the two previous descriptions of the crystal structure given by Chung et al. in 1997 and it can be understood as a delocalization of electrons over the Te2 and Te6 atoms through the formation of three-center-four-electron (3c-4e) bonds. Such kind of hypervalent bonding can also explain the slightly longer bond lengths compared to classical $\text{Te}\cdots\text{Te}$ single bonds. The amount of occupied antibonding $\text{Te}\cdots\text{Te}$ p-states is slightly larger for the $\text{Te2}\cdots\text{Te6}$ interactions compared to those between the Te2 atoms. Hence, the former are slightly weaker and the part of the BaBiTe_3 crystal structure that is dominated by $\text{Te}\cdots\text{Te}$ bonding is significantly strained due to the population of antibonding Te p-states.

3.1.2.2 Preferential site substitution of Se on the Te_4 and Te_5 sites

The crystal structure of polycrystalline $\text{BaBiTe}_{3-x}\text{Se}_x$ ($x = 0, 0.05$ and 0.1) was confirmed by PXRD and subsequent Rietveld refinements (*cf.* Fig. V.16) based on the structural model obtained from a previous single crystal structure analysis of BaBiTe_3 .^[196] The site occupancy factors (s.o.f.) were refined for the Se substituted variants and we find that for $x = 0.05$ Se substitutes Te on the Te5 site (s.o.f. on Te5: 0.96/0.04 Te/Se), while Se substitutes Te on the Te4 and Te5 sites for $x = 0.1$ with a slight preference towards Te5 (s.o.f. on Te4: 0.9/0.1 Te/Se and s.o.f. on Te5: 0.78/0.22 Te/Se) and all other sites are fully occupied. The corresponding results of the refinements are summarized in Table V.6 and the refined site occupancy factors are visualized exemplary for $x = 0.1$ in Fig. V.17. The clear changes in the lattice parameters (*cf.* Table V.6) provide proof for a successful substitution of Te by Se, which can be confirmed by complementary EDS analyses (*cf.* Fig. V.18).

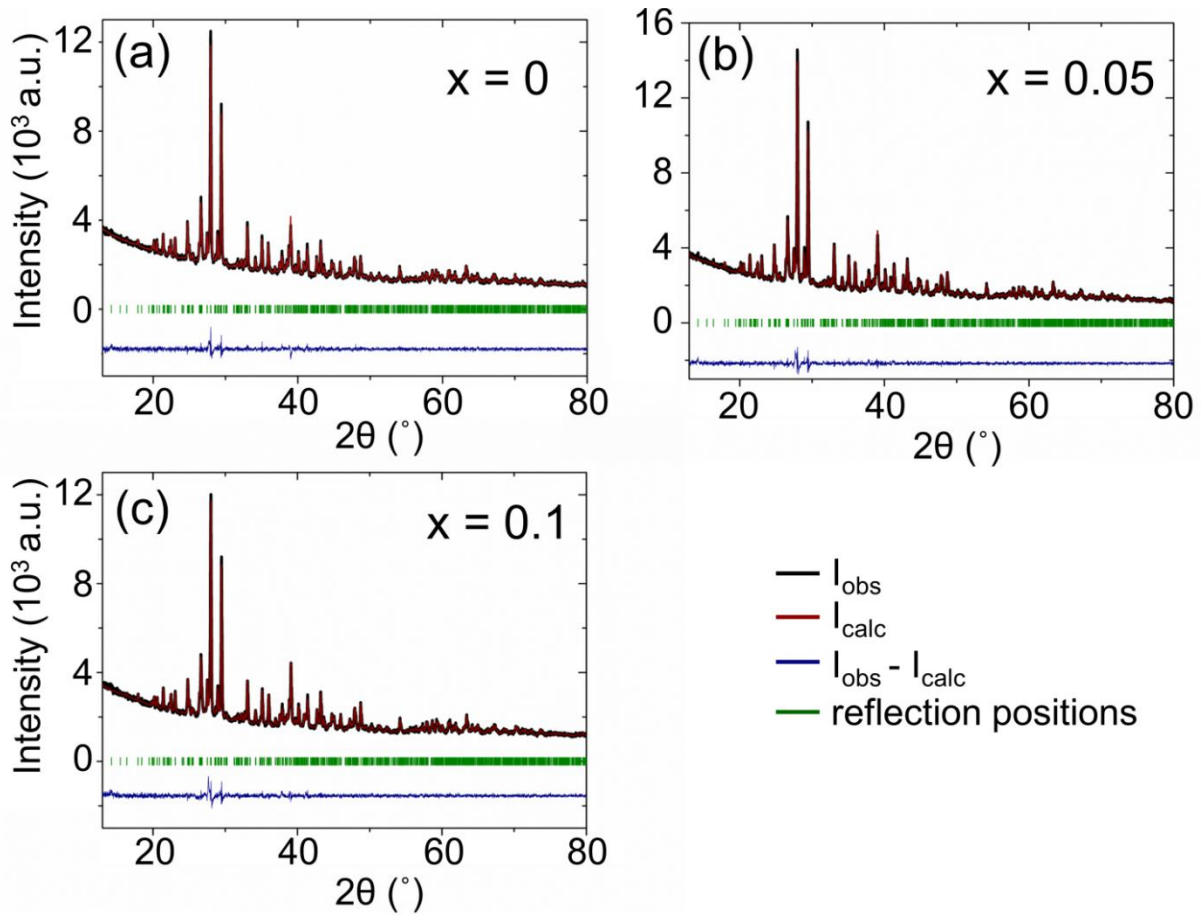


Fig. V.16 Rietveld refinements of experimental diffraction patterns (black) of a) BaBiTe_3 , b) $\text{BaBiTe}_{2.95}\text{Se}_{0.05}$ and c) $\text{BaBiTe}_{2.9}\text{Se}_{0.1}$ recorded after spark plasma sintering. Calculated diffraction patterns, difference plots and reflection positions are depicted in red, blue and green, respectively; all experimental diffraction patterns were recorded after spark plasma sintering.

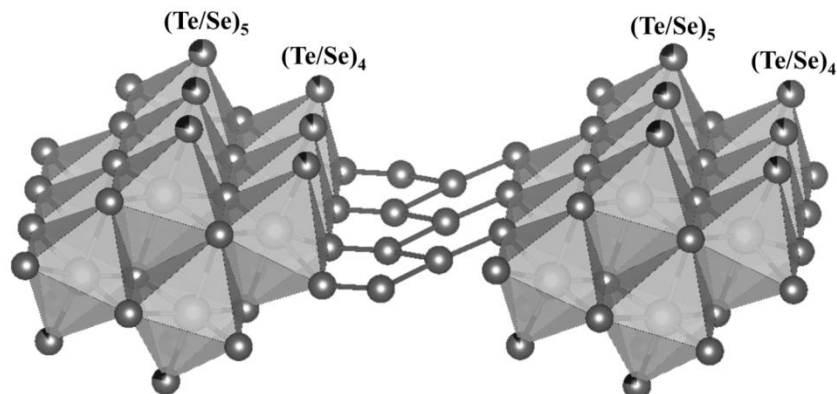
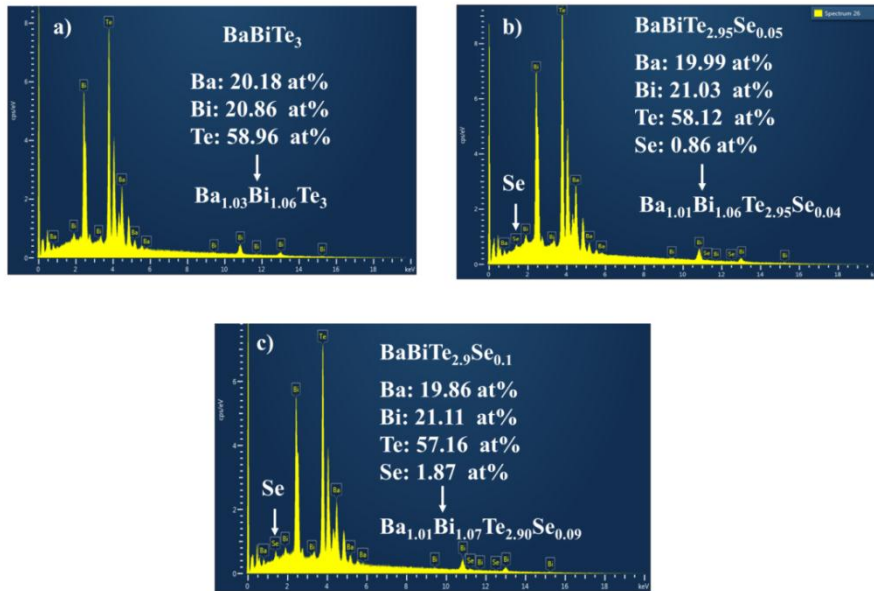


Fig. V.17: Parts of the $\text{BaBiTe}_{2.9}\text{Se}_{0.1}$ crystal structure with refined site occupancy factors (black: Se; grey: Te) illustrating the preferential site substitution of Te4 and Te5.

Table V.6 Rietveld X-ray refinement results for BaBiTe_{3-x}Se_x (x = 0, 0.05, 0.1)

Nominal composition	BaBiTe ₃	BaBiTe _{2.95} Se _{0.05}	BaBiTe _{2.9} Se _{0.1}
Space group	P2 ₁ 2 ₁ 2 ₁ (No. 19)	P2 ₁ 2 ₁ 2 ₁ (No. 19)	P2 ₁ 2 ₁ 2 ₁ (No. 19)
Z	8	8	8
a (Å)	4.6147(1)	4.6103(1)	4.6056(1)
b (Å)	17.0365(4)	17.0287(4)	17.0171(5)
c (Å)	18.2990(4)	18.2785(4)	18.2503(5)
V (Å ³)	1439	1435	1430
ρ_{calc} (gcm ⁻³)	6.733	6.746	6.702
Radiation	Cu-K $\alpha_{1/2}$, $\lambda_{1/2} = 1.54060/1.54439$ Å		
2 θ limits (°)	5.01-119.99	5.01-119.99	5.01-119.99
R _f	0.041	0.030	0.0401
R _{bragg}	0.048	0.036	0.0464
χ^2	1.48	1.62	1.64

**Fig. V.18** Experimental EDS spectra of all characterized samples with the corresponding nominal and experimental compositions.

The experimental compositions extracted from EDS analyses are provided in Table V.7 and agree well with the nominal composition. Since there is a preferential site substitution on the Te sites that are not involved in Te···Te bonding it can be concluded that a Se substitution of Te2 and/or Te6 atoms would destabilize the crystal structure and is therefore energetically not favorable. This is in good agreement with the extrinsic defect calculations (*cf.* section *Defect chemistry of BaBiTe₃*).

Table V.7 Experimental compositions obtained from EDS analyses after thermoelectric characterization.

nominal composition	Ba (at. %)	Bi (at. %)	Te (at. %)	Se (at. %)	exp. composition
BaBiTe ₃	20.18	20.86	58.96	-	Ba _{1.03} Bi _{1.06} Te ₃
BaBiTe _{2.95} Se _{0.05}	19.99	21.03	58.12	0.86	Ba _{1.01} Bi _{1.06} Te _{2.95} Se _{0.04}
BaBiTe _{2.90} Se _{0.10}	19.86	21.11	57.16	1.87	Ba _{1.01} Bi _{1.07} Te _{2.90} Se _{0.09}

3.1.2.3 Optical properties, electronic structure and its orbital contributions

Electronic structure

The electronic structure of BaBiTe₃ was calculated and described previously.^[196,205] Both studies could not entirely clarify the nature of the two transitions at ~0.28 eV (transition 1) and ~0.42 eV (transition 2) observed by diffuse reflectance (DR) measurements, which inspired the recalculation of the electronic structure in order to better understand the thermoelectric transport properties of BaBiTe₃ and the unusual shape of its experimental optical absorption spectrum, which is discussed in the section *Band convergence and an explanation for the two optical transitions*. It is important to note that spin-orbit coupling (SOC) does not significantly affect the overall band structure of BaBiTe₃.^[205] It does, however significantly decrease the band gap. For narrow band gap materials it is difficult to obtain accurate band gaps from DFT-PBE calculations, which is why a scissor (operator) shift was applied to correct the band gap to the empirical value of 0.26 eV based on the optical band gap (experimental). This value is also consistent with calculations including SOC (0.26 eV)^[205] and the Goldsmid-Sharp band gap (ca. 0.23 eV), which is discussed in the section *Thermoelectric properties*.

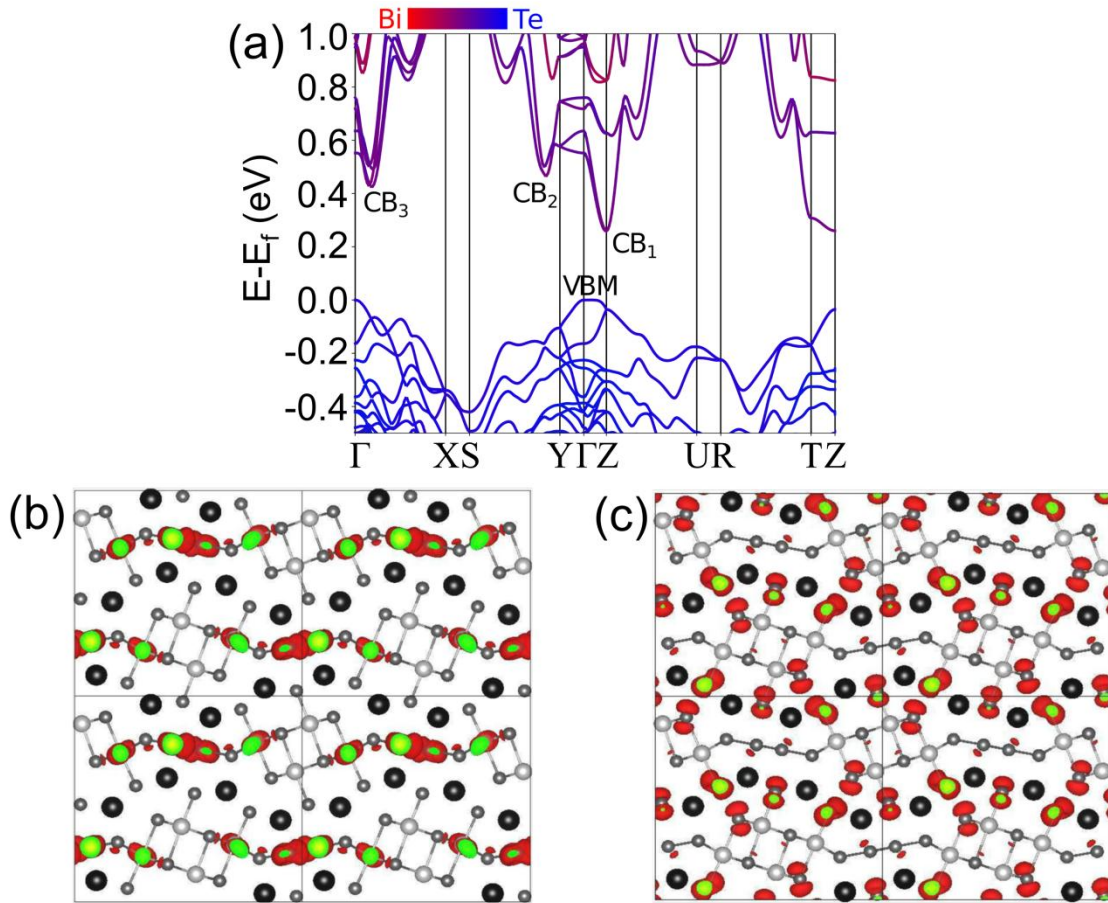


Fig. V.19 a) Electronic structure of BaBiTe₃ with three electron pockets (CB₁, CB₂ and CB₃) and the atomic contributions to the conduction band minimum (CBM) and valence band maximum (the Fermi level is set to 0 eV); b) and c) correspond to the charge density distribution of the CBM and the valence band maximum (VBM) showing the strongest atomic contributions to the CBM and VBM

The results show three electron pockets (CB₁, CB₂ and CB₃) that lie close in energy in a range of only 100 meV and which are also present in Se substituted variants of BaBiTe₃. CB₁ and CB₃ are located along the ΓZ and ΓX directions, allowing nearly direct transitions from the VBM, while CB₂ is located along the SY direction allowing indirect transitions from the VBM. The three electron pockets signify a material system with multiple valleys, which is an important feature since complex band structures with multi-valley bands (i.e. a large valley degeneracy N_v) and contributions of multiple conduction and/or valence bands can lead to high-efficiency thermoelectric materials as it was demonstrated for CoSb₃ and PbTe_{1-x}Se_x.^[208,193]

Orbital contributions to the band edges

Knowing the orbital contributions to the band edges is important in order to understand which part of the crystal structure governs the electronic transport, especially in compounds where ionic and covalent bonding coexist and where it is often assumed that the covalent part of the structure dominates the electronic transport. In the case of BaBiTe₃ the band edges are dominated by the Bi and Te states (*cf.* Fig. V.19a). The strongest contribution to the valence band edge of BaBiTe₃ comes from the Bi6*p*-Te5*p* and Te5*p*-Te5*p* bonding states, while their corresponding antibonding states are the main contributors to the conduction band edge (*cf.* Fig. V.20).

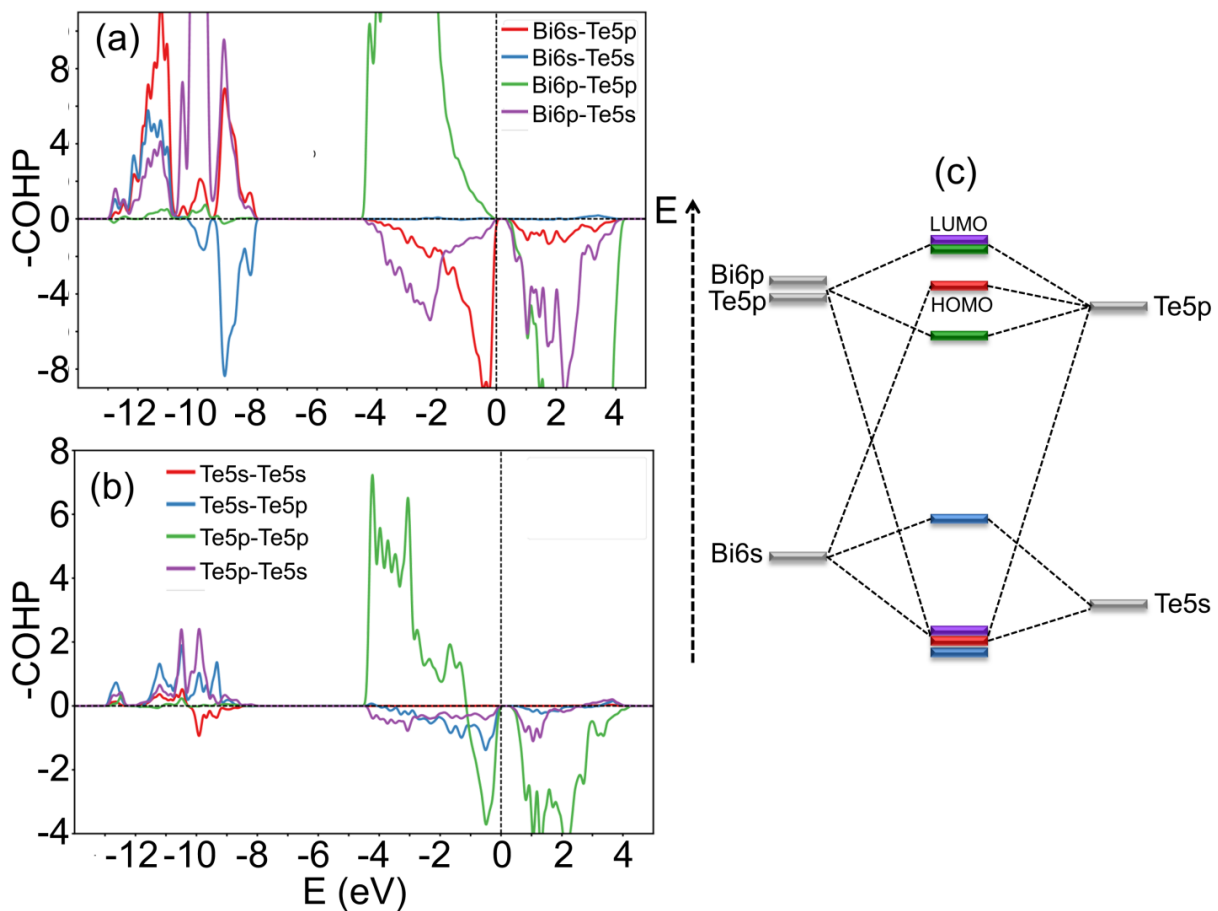


Fig. V.20 COHP curves of BaBiTe₃ containing a) Bi-Te interactions and b) Te-Te interactions; c) shows a MO diagram with 5 hybrid orbitals, reflecting the COHP analysis.

These $\text{Bi}6p\text{-Te}5p$ and $\text{Te}5p\text{-Te}5p$ contributions are also visualized in Fig. V.19 (other contributions are not shown for clarity reasons). Fig. V.19b) and c) show the charge density distribution of the conduction band minimum (CBM) and the valence band maximum (VBM) containing only the $\text{Bi}6p\text{-Te}5p$ and $\text{Te}5p\text{-Te}5p$ contributions. This representation allows visualizing the orbital contribution of each atom to the CBM and VBM and hence a more detailed description of the band edges. The main $\text{Bi}6p$ and $\text{Te}5p$ contributions to the CBM come from the Te2 and Bi2 atoms and those contributing to the VBM come from the Te3, Te4 and Te5 atoms. However, not only the Bi and Te p -states are of importance, but also the $\text{Bi}6s$ and $\text{Te}5s$ states (*cf.* Fig. V.20). The former mix with the $\text{Te}5p$ states leading to significant contributions of $\text{Bi}6s\text{-Te}5p$ antibonding states to the valence band edge. The conduction band edge also shows significant contributions of antibonding $\text{Bi}6p\text{-Te}5s$ states. This COHP analysis and the corresponding MO diagram (*cf.* Fig. V.20) provide a comprehensive picture of all covalent bonding interactions in BaBiTe_3 and these analyses show to which extent the different parts of the crystal structure contribute to the electronic transport. Fig. V.20 entirely neglects the ionic part of the crystal structure, which is not shown for clarity reasons. A detailed COHP analysis of the ionic part of the crystal structure (*cf.* Fig. V.21) shows significant contributions of the $\text{Ba}6s\text{-Te}5p$ bonding states and $\text{Ba}5p\text{-Te}5p$ antibonding states to the valence band edge. Hence, a complete COHP analysis reveals that both the covalent and the ionic part of the crystal structure can be expected to play an important role in the electronic transport of BaBiTe_3 including the Bi lone pairs.

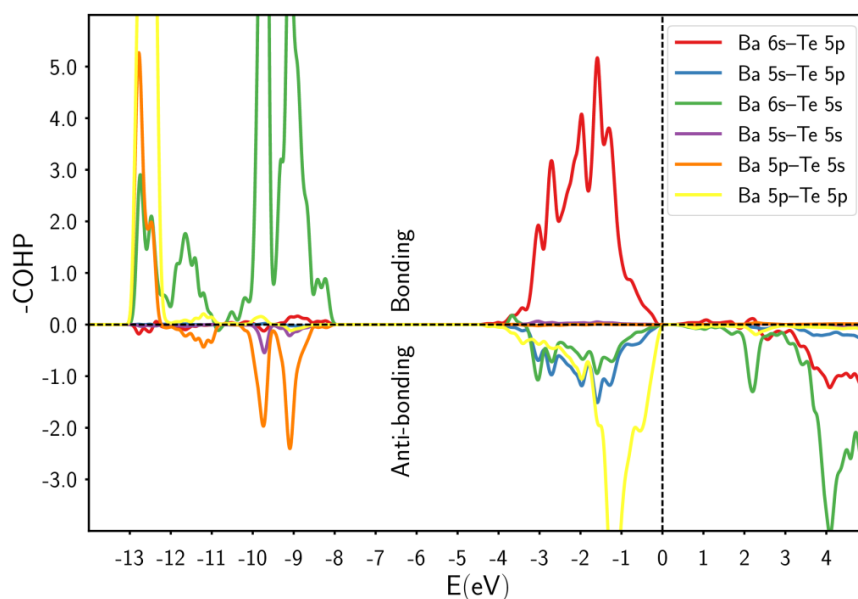


Fig. V.21 COHP curves showing all Ba-Te interactions. This graph shows significant contributions of Ba6s-Te5p bonding and Ba5p-Te5p antibonding states to the valence band edge, i.e. the ionic part of the crystal structure of BaBiTe₃ can be expected to play a significant role to the electronic transport in BaBiTe₃.

Optical properties

Optical absorption measurements of polycrystalline BaBiTe₃ (*cf.* Fig. V.22a) confirm the results obtained for single crystalline BaBiTe₃ in 1997, which made it possible to use this compound as a standard for further optical absorption measurements of BaBiTe_{2.95}Te_{0.05}, BaBiTe_{2.9}Se_{0.1} and BaBiSe₃ (*cf.* Fig. V.22a). These show that the optical band gap does not change significantly for compositions up to $x = 0.1$, while BaBiSe₃ has only one transition at ~ 0.90 eV (*cf.* Fig. V.22a), which corresponds to an optical band gap significantly larger compared to those of BaBiTe_{3-x}Se_x ($x = 0, 0.05$ and 0.1). The two optical transitions observed for BaBiTe₃ are also found for the Se substituted variants with $x = 0.05$ and 0.1 as it is illustrated in Fig. V.22b for $x = 0.05$ and the energies of the two transitions are shown as a function of Se content in Fig. V.22c.

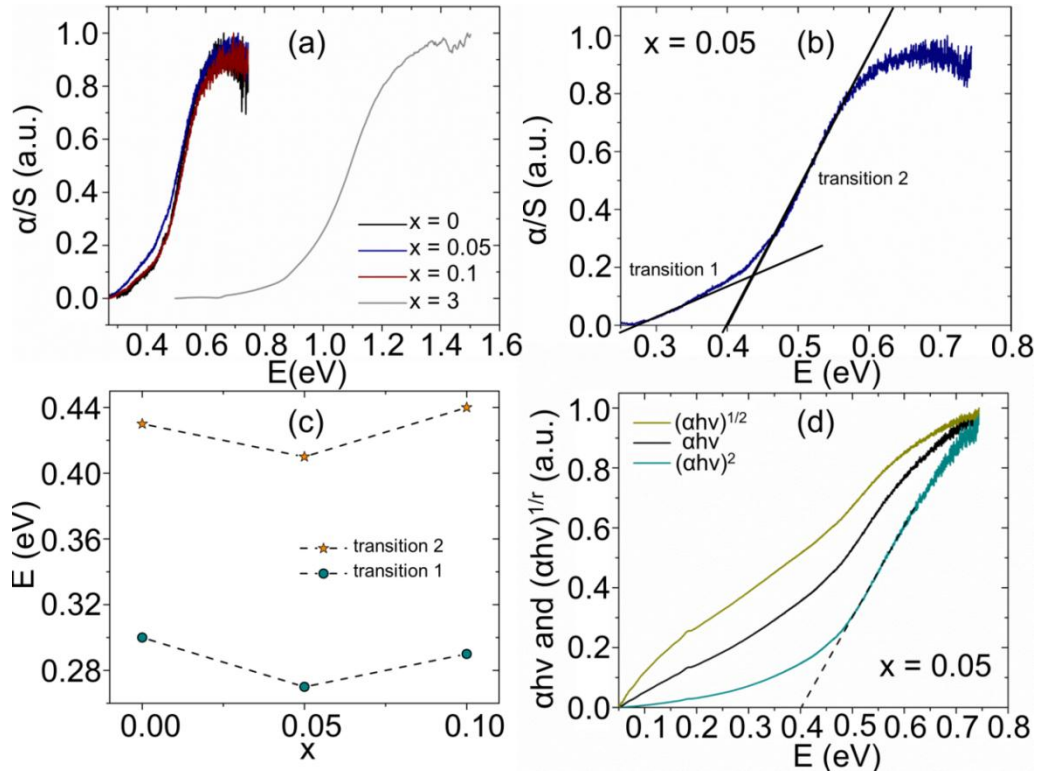


Fig. V.22 a) experimental band gaps of BaBiTe_{3-x}Se_x (x = 0, 0.05, 0.1 and 3) determined by diffuse reflectance measurements; b) enlargement of the optical absorption of BaBiTe_{2.95}Se_{0.05} emphasizing the two transitions corresponding to transitions from the VBM to CB₁ and from CB₁ to CB₂; c) energy of the two transitions as a function of the Se content; d) tauc plots for x = 0.05 showing that transition 2 can be considered direct.

3.1.2.4 Band convergence and an explanation for the two optical transitions

After providing a comprehensive picture of the bonding interactions in BaBiTe₃, its electronic structure including orbital contributions and after showing that BaBiTe_{3-x}Se_x (x = 0, 0.05 and 0.1) are multiband systems I now relate the experimentally observed optical transitions to the electronic structure in order to explain the two optical transitions observed experimentally. I then use these results to demonstrate that band convergence occurs in BaBiTe_{2.95}Se_{0.05}. Analyzing transition 2 of BaBiTe_{2.95}Se_{0.05} by the Tauc method (*cf.* Fig. V.22d) revealed that this transition is direct, which excludes the possibility of indirect VBM-CB₂ and VBM-CB₃ transitions being associated to transition 2.

Fig. V.23a shows the electronic structure and density of states (DOS) of BaBiTe₃ including two transitions, which can qualitatively explain the shape of the experimental absorption spectra shown in Fig. V.22a and b. This is also quantitatively validated in Fig. V.23b and c, which show the joint density of states and calculated optical absorption spectrum of BaBiTe₃, respectively.

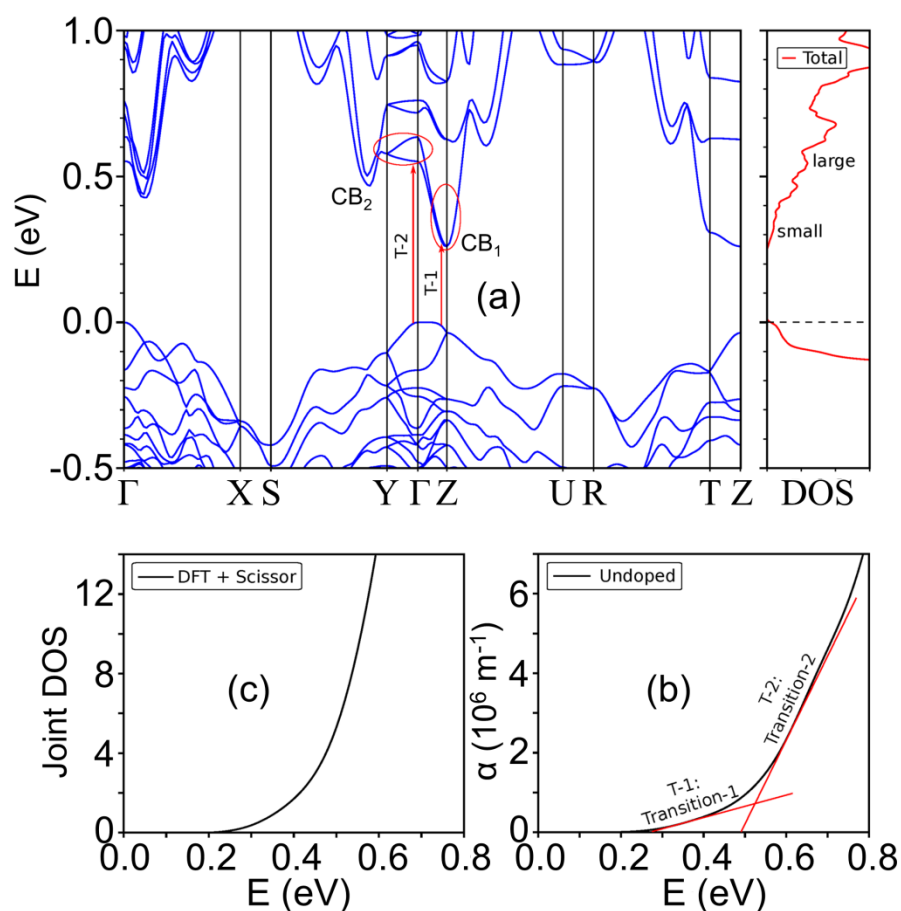


Fig. V.23 a) Electronic band structure and density of states (DOS) of BaBiTe₃ showing the two optical transitions taken into account for calculating the optical absorption spectrum; b) calculated joint density of states (joint DOS) and c) optical absorption coefficient as a function of energy. The abbreviations T-1 and T-2 refer to transition 1 and transition 2.

These calculations were performed assuming that BaBiTe₃ is undoped (or has a very low carrier concentration). From these calculations it is possible to conclude that transition 1 and 2 correspond to transitions from the valence band maximum (VBM) to CB₁ and to bands higher in the conduction band next to CB₂. These bands are located along the ΓY direction between CB₁ and CB₂ (*cf.* Fig. V.23a).

Transition 2 is direct, which is consistent with the Tauc analysis shown in Fig. V.22d. This transition is significantly stronger than transition 1 in terms of intensity. This can be explained by the lower dispersion of the bands higher in the conduction band compared to those at CB_1 . A lower dispersion (i.e. when the bands are more flat) results in a larger density of states (*cf.* Fig. V.23a). This is why the number of optical transitions at 0.26 eV (transition 1) is smaller than at 0.5 eV (transition 2). This is reflected in the joint density of states (*cf.* Fig. V.23b), which are a measure for the amount of states in the valence and conduction band available for a photon of a given energy $h\nu$ to interact with. The larger the available states, the higher is the transition rate and the larger is the intensity of the transition. Transition 2 is more intense than transition 1 since more states are available in the conduction band compared to transition 1. High-temperature optical absorption measurements of $BaBiTe_{2.95}Se_{0.05}$ (*cf.* Fig. V.24a) show that transition 2 moves to lower energies with respect to temperature, while the energy of transition 1 stays constant (*cf.* Fig. V.24b).

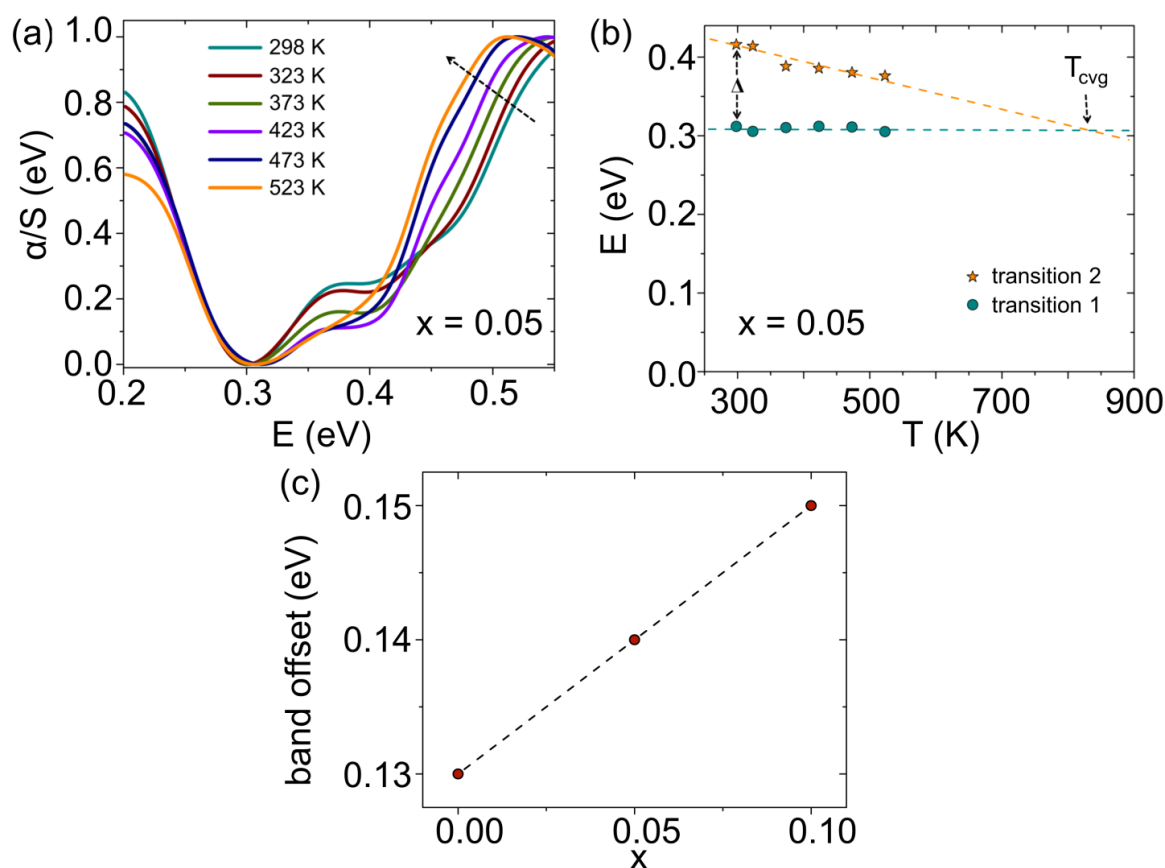


Fig. V.24 a) optical absorption spectra of $BaBiTe_{2.95}Se_{0.05}$ as a function of temperature b) changes in energy of transition 1 and 2 as a function of temperature; CB_1 and CB_3 are converging with temperature; c) band offset as a function of Se content. This image shows that there is band convergence in $BaBiTe_{2.95}Se_{0.05}$ and that the band offset increases with the Se content.

Hence, the bands higher in the conduction band move towards lower energies. At ca. 830 K these bands can be considered as being fully converged with CB_1 . Fig. V.24c shows that the band offset between CB_1 and the bands higher in the conduction band (located along the ΓY direction between CB_1 and CB_2) slightly increases with the Se content. The band offset was extracted from optical absorption measurements.

3.1.2.5 Thermoelectric properties

The thermoelectric properties of polycrystalline $BaBiTe_{3-x}Se_x$ ($x = 0, 0.05$ and 0.1) are summarized in Fig. V.25. Seebeck coefficient and thermal conductivity were measured out of plane, while the electrical resistivity was measured in plane.

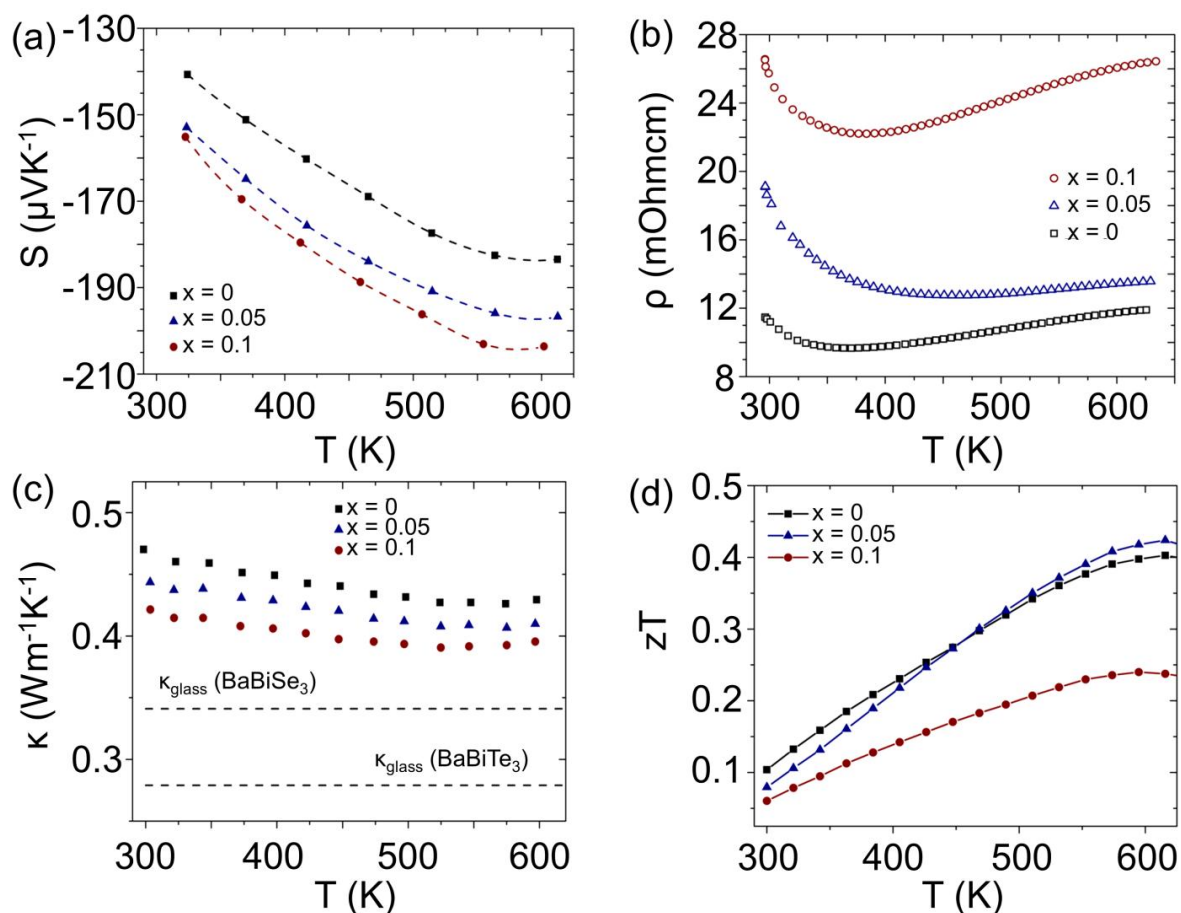


Fig. V.25 Thermoelectric properties of $BaBiTe_{3-x}Se_x$ ($x = 0, 0.05, 0.1$): a) Seebeck coefficient (the dotted lines represent interpolated data), b) electrical resistivity, c) thermal conductivity and minimum thermal conductivity of $BaBiTe_3$ and $BaBiSe_3$ according to Cahill and d) thermoelectric figure of merit (zT).

The Seebeck coefficient (*cf.* Fig. V.25a) of all compounds increases up to ca. 550 K and shows a “roll-over” between 550 K and 600 K due to the activation of minority charge carriers. The maximum of the Seebeck coefficient (S_{\max}) at the temperature T_{\max} is almost independent of the Se content, which is consistent with the optical absorption spectra showing no significant changes in the optical band gap up to $x = 0.1$. The Goldsmid-Sharp band gap ($E_g = 2eS_{\max}T_{\max}$) of all title compounds measures ca. 0.2-0.24 eV, which agrees well with the theoretical band gap (ca. 0.26 eV) obtained from DFT-GGA calculations including spin-orbit coupling. Increasing the Se content leads to higher Seebeck coefficients, which is consistent with the increase in resistivity (*cf.* Fig. V.25b). BaBiTe₃, BaBiTe_{2.95}Se_{0.05} and BaBiTe_{2.9}Se_{0.1} show a small reduction in thermal conductivity (*cf.* Fig. 10c) with an increasing Se content as expected from point defect scattering. This effect could also be due to the slightly different densities of the samples. However, because of the complex low symmetry structure (few acoustic phonons) and large anharmonicity the lattice thermal conductivity is already low (0.41(2) Wm⁻¹K⁻¹ at 600K). All compounds possess remarkably low thermal conductivities close to the glass limit (*cf.* Fig. 10c) of BaBiSe₃ (0.34 Wm⁻¹K⁻¹) and BaBiTe₃ (0.28 Wm⁻¹K⁻¹). The glass limit is slightly higher for BaBiSe₃ since both, the longitudinal and transversal components of the speed of sound are larger for BaBiSe₃ ($v_T = 1535$ m/s, $v_L = 2863$ m/s) compared to BaBiTe₃ ($v_T = 1462$ m/s, $v_L = 2536$ m/s), which can be attributed to the lower mass of Se compared to Te and to softer bonds in BaBiSe₃. Hence, BaBiSe₃ can be expected to be more anharmonic compared to BaBiTe₃. Table V.8 summarizes speed of sound data, Debye temperature and frequency of BaBiTe₃ and BaBiSe₃. Debye temperatures of 147 K and 164 K allow the application of the Dulong-Petit approximation for calculating the thermal conductivity. Fig. V.26 shows the measured Hall mobility (μ) and charge carrier concentration (n) of BaBiTe_{3-x}Se_x ($x = 0, 0.05$ and 0.1).

Table V.8 Speed of sound data, debye temperatures and frequencies of BaBiTe₃ and BaBiSe₃

	BaBiTe ₃	BaBiSe ₃
v_s (m/s)	1820	1977
v_T (m/s)	1462	1535
v_L (m/s)	2536	2863
θ_D (K)	147	164
ω_D (rad/s)	$1.92 \cdot 10^{13}$	$2.15 \cdot 10^{13}$

The electron mobility ranges from $4.8 \text{ cm}^2\text{V}^{-1}\text{s}^{-1}$ to $1.8 \text{ cm}^2\text{V}^{-1}\text{s}^{-1}$ between 350 K and 600 K and it depends only weakly on the temperature. The carrier concentration of BaBiTe₃ is almost constant with temperature up to ca. 370 K and increases significantly between 370 K and 600 K. A similar trend can be observed for BaBiTe_{2.95}Se_{0.05}. However, the increase in carrier concentration is less pronounced and is only significant for temperatures above ca. 500 K. Increasing the Se content further, results in an almost temperature independent carrier concentration for BaBiTe_{2.9}Se_{0.1}. The substitution of Te by Se does not affect the electron mobility in a systematic or significant way, but results in a clear reduction in charge carrier concentration from $1.44 \cdot 10^{20} \text{ cm}^{-3}$ to $0.6 \cdot 10^{20} \text{ cm}^{-3}$ at 310 K and from $3.12 \cdot 10^{20} \text{ cm}^{-3}$ to $0.9 \cdot 10^{20} \text{ cm}^{-3}$ at 600 K. This decrease in carrier concentration can explain the increase in resistivity. Such large carrier concentrations are typical for heavily doped semiconductors. Hence all title compounds can be considered as being unintentionally doped. One possible origin for such large carrier concentrations will be discussed in the section: *Defect chemistry of BaBiTe₃ and its Se substituted variants*. The overall thermoelectric properties of BaBiTe₃ and BaBiTe_{2.95}Se_{0.05} are fairly promising with zT_{max} (cf. Fig. V.25d) of 0.4 and 0.43, respectively.

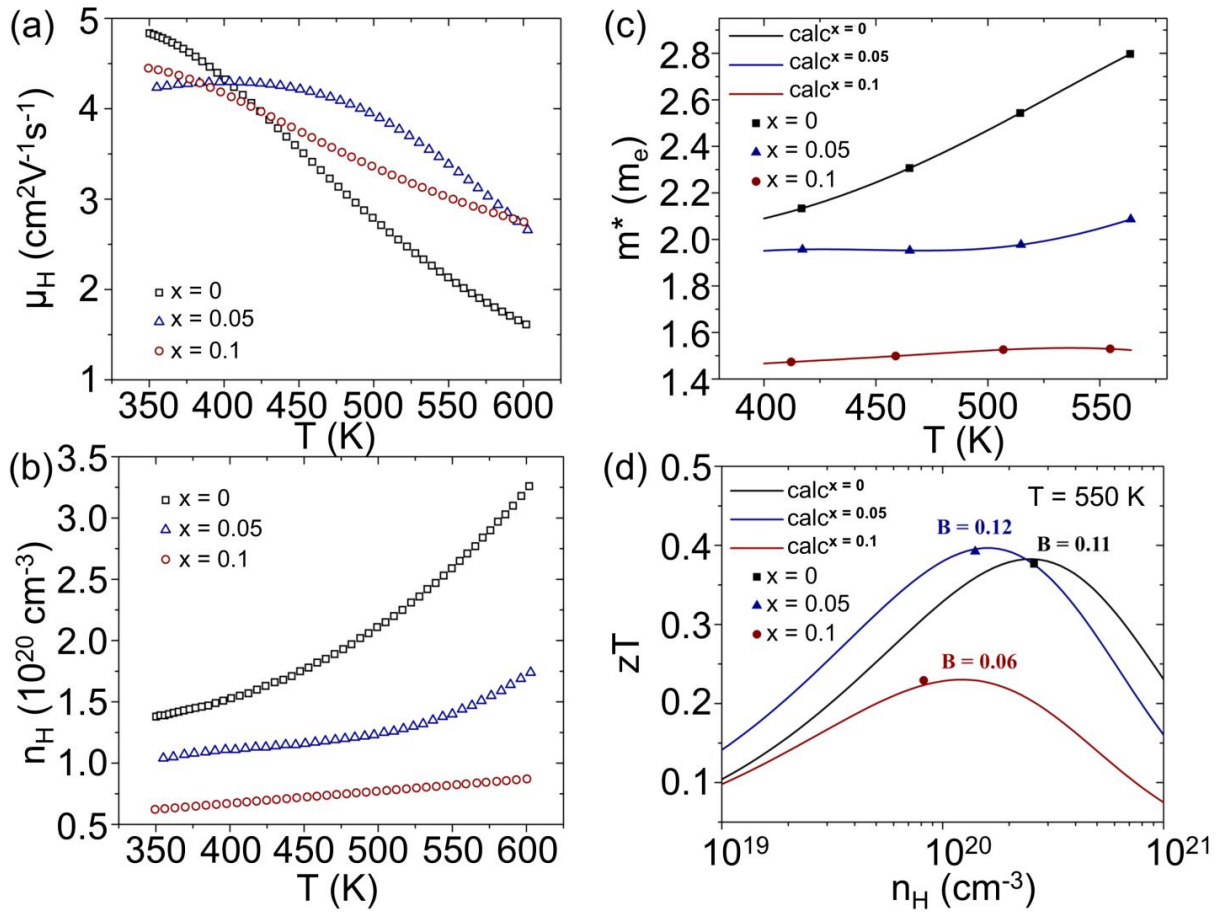


Fig. V.26 a) Hall mobility and b) hall charge carrier concentration of BaBiTe_{3-x}Se_x (x = 0, 0.05, 0.1) as a function of temperature; c) calculated zT as a function of hall carrier concentration: lines and symbols correspond to effective band models and experimental data points, respectively; d) Seebeck effective mass (m^*) as a function of temperature (line and symbols represent calculated m^* obtained from interpolated and experimental Seebeck data, respectively). b)-d) show the contribution of CB₂ for BaBiTe_{3-x}Se_x (x = 0, 0.05) in form of an increase in carrier concentration and m^* with temperature.

3.1.2.6 Multiband effects in the thermoelectric transport properties

Ab initio calculations of the electronic structure and optical absorption coefficient as well as optical absorption measurements clearly point towards a contribution of multiple electron pockets to the thermoelectric transport properties of BaBiTe_{3-x}Se_x, especially at higher temperatures where band convergence effects play a role (*cf.* Fig. V.24). A comparison of this study to those of CoSb₃^[208] and PbSe^[194], where multiband effects also play a role, support this conclusion.

A multiband contribution to the thermoelectric transport data of BaBiTe₃ and BaBiTe_{2.95}Se_{0.05} can indeed be found. It is visible in the increase in carrier concentration (*cf.* Fig. V.26b) and Seebeck effective mass (m^*)^[208] with temperature (*cf.* Fig. V.26c). The effective mass was obtained by fitting an effective band model to the experimental data (*cf.* Fig. V.26d). The modeling was done in the temperature range, where Seebeck coefficient and resistivity show the typical trends of degenerate semiconductors. Details concerning modeling of high-temperature thermoelectric properties can be found in chapter III.^[67] The main signature of multiband effects in the transport data is an increase in effective mass with decreasing Se content (*cf.* Fig. 26c), while the hall mobility remains almost unchanged. Another signature of multiband effects in the thermoelectric transport data is the low effective mass of BaBiTe_{2.95}Se_{0.1} compared to BaBiTe₃ and BaBiTe_{2.95}Se_{0.05}. This suggests that for BaBiTe_{2.95}Se_{0.1} only CB₁ contributes to the thermoelectric transport, while multiple electron pockets (i.e. a larger density of states) contribute in the case of BaBiTe₃ and BaBiTe_{2.95}Se_{0.05} since the Seebeck effective mass is an estimate for the effective density of states. Such a contribution of multiple electron pockets to the thermoelectric transport properties of BaBiTe₃ and BaBiTe_{2.95}Se_{0.05} explains the larger effective mass and carrier concentration and in turn the lower resistivity compared to BaBiTe_{2.95}Se_{0.1}. The previously discussed convergence of bands in the conduction band on the other hand can explain the increase in carrier concentration and effective mass with temperature, which is only observed for $x = 0$ and 0.05 . One possible explanation for not observing any effect of band convergence on the thermoelectric transport properties of BaBiTe_{2.95}Se_{0.1} is the increase in band offset with x , which could also explain the weaker increase in carrier concentration and effective mass for $x=0.05$ compared to $x = 0$. The combined analyses of the electronic structure, optical properties and thermoelectric transport properties strongly suggest that the larger quality factor (B) and zT_{\max} of $x = 0$ and 0.05 compared to BaBiTe_{2.95}Se_{0.1} (*cf.* Fig. 26d) are a result of the previously discussed multiband and band convergence effects. B is a measure for the maximum achievable zT of an optimized thermoelectric material. It was calculated according to (V.1), where m_e and κ_{ph} are the electron mass and phononic contribution to the thermal conductivity.

$$B = 4.3223 * 10^{-6} \mu_0 \left(\frac{m^*}{m_e} \right)^{3/2} \frac{T^{5/2}}{\kappa_{ph}} \quad (\text{V.1})$$

The intrinsic mobility (μ_0) and effective mass (m^*) were obtained from the effective band model described in chapter III. Fitting such a model to the thermoelectric transport data also shows that the carrier concentration of BaBiTe_3 , $\text{BaBiTe}_{2.95}\text{Se}_{0.05}$ and $\text{BaBiTe}_{2.9}\text{Se}_{0.1}$ is close to optimized (*cf.* Fig. V.26d).

3.1.2.7 Defect chemistry

The main reason for studying the defect chemistry of $\text{BaBiTe}_{3-x}\text{Se}_x$ is the large charge carrier concentration of BaBiTe_3 , $\text{BaBiTe}_{2.95}\text{Se}_{0.05}$ and $\text{BaBiTe}_{2.9}\text{Se}_{0.1}$ typical for heavily doped semiconductors, which points towards unintentional doping through native defects. Another reason is that BaBiTe_3 is closely related to Bi_2Te_3 , Bi_2Se_3 and their solid solution including stoichiometric $\text{Bi}_2\text{Te}_2\text{Se}$. In these compounds and their solid solution native defects play an important role in their thermoelectric transport properties.^[209-215] Insights in the defect chemistry can help to explain, why BaBiTe_3 and its Se substituted variants are all n-type semiconductors and possibly predict whether intrinsic p-type samples can be obtained. We calculated the formation energies ($E_f[\text{D}^q]$) of intrinsic defects in BaBiTe_3 in three different regions of the Ba-Bi-Te phase diagram (*cf.* Fig. V.27).

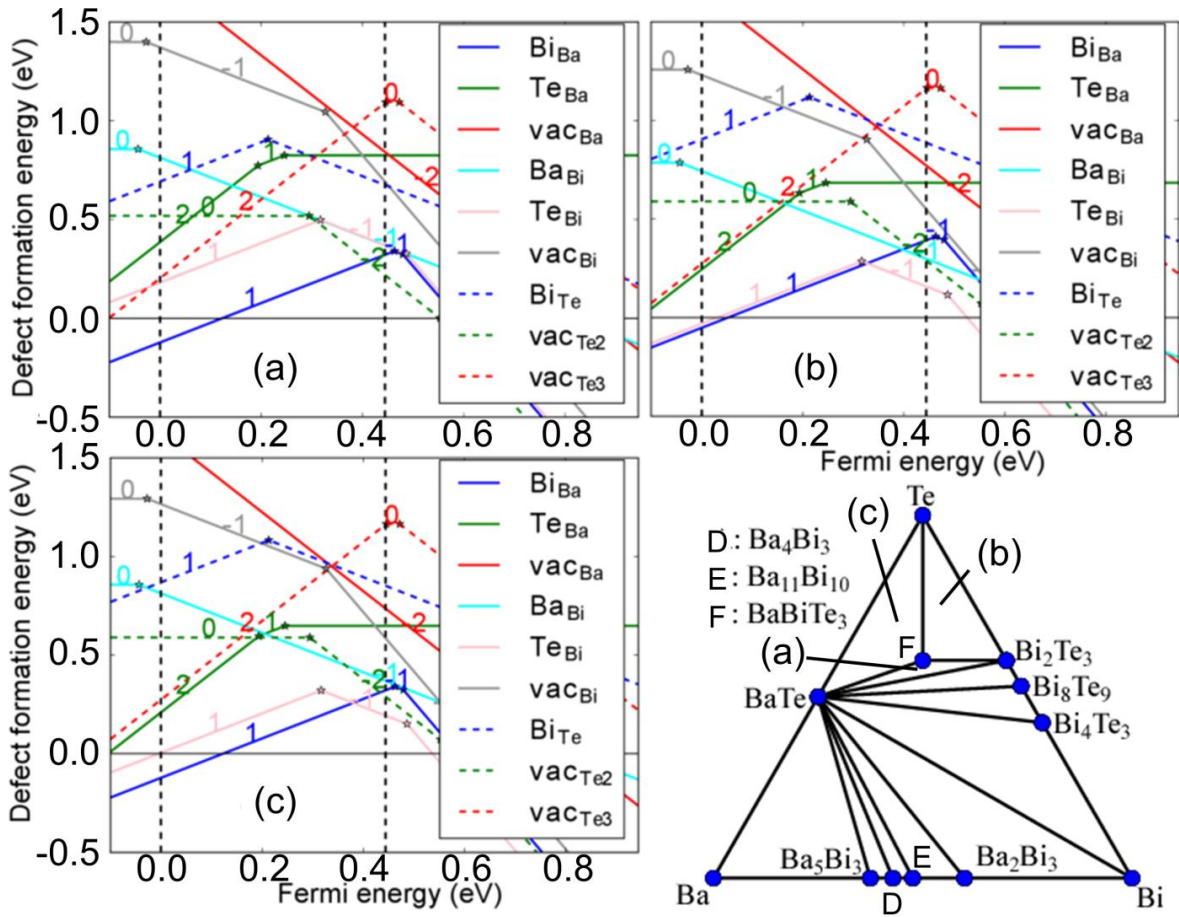


Fig. V.27 Formation energies of intrinsic defects in BaBiTe_3 calculated in three different regions of the Ba-Bi-Te phase diagram: a) region 1: $\text{BaTe-Bi}_2\text{Te}_3\text{-BaBiTe}_3$, b) region 2: BaTe-Te-BaBiTe_3 and c) region 3: $\text{Bi}_2\text{Te}_3\text{-Te-BaBiTe}_3$; the numbers in each graph correspond to the charge q of the each type of defect. These calculations reveal native $\text{Bi}_{\text{Ba}}^{+1}$ defects with negative defect formation energies close to the valence band edge in all three regions of the phase diagram. These defects are competing with native $\text{Te}_{\text{Bi}}^{+1}$ defects in the region 2 (b) of the phase diagram for energies close to the valence band edge; these calculations were performed using the DFT-GGA method without spin-orbit coupling.

The standard methodology for defect computations is grand-canonical and is working with chemical potentials. There is a range of chemical potentials for which BaBiTe_3 is stable. We define here limiting values of chemical potentials and three regions $\text{BaTe-Bi}_2\text{Te}_3\text{-BaBiTe}_3$, BaTe-Te-BaBiTe_3 and $\text{Bi}_2\text{Te}_3\text{-Te-BaBiTe}_3$, which will be referred to as region A, B, and C. These different regions correspond to different thermodynamic conditions in which BaBiTe_3 is stable and are practically related to different synthesis conditions.^[216] Figure V.27 plots the defect formation energy depending on the Fermi level for a series of intrinsic defects in different regions of chemical potential. In all conditions, there are $\text{Bi}_{\text{Ba}}^{+1}$ and $\text{Te}_{\text{Bi}}^{+1}$ defects with negative formation energies close to the valence band maximum.

These defects are electron donors compensating any attempt to dope the material p-type in equilibrium conditions. On the other hand, no negative formation energy defects are present close to the conduction band minimum indicating that the material has no electron traps. We conclude that BaBiTe₃ is thermodynamically favoring n-type conductivity and that any attempt to dope this material p-type will be very challenging. This is in agreement with the n-type nature of the experimentally realized materials. Moreover, our work identifies the potential majority defects, Bi_{Ba}⁺¹, which are the lowest energy electron donors in all regions, probably leading to the observed n-type conduction. In BaBiTe₃ a second cation (Ba²⁺) is present, which is lacking in Bi₂Te₃ and which fundamentally changes the defect chemistry since antisite defects form more easily between two cations than between a cation and an anion. This is evident from the low formation energy of the Bi_{Ba}⁺¹ antisite defects in BaBiTe₃. In n-type Bi₂Te₃ and Bi₂Se₃ Te_{Bi}⁺¹, Se_{Bi}⁺¹ (under Se-rich conditions) and V_{Se}²⁺ (under Bi-rich conditions) defects have the lowest formation energies and are responsible for the observed n-type conduction in these compounds.^[209] The vacancies of Te and Se are also low in energy in Bi₂Te₃, while being much higher in energy than Bi_{Ba}⁺¹ in BaBiTe₃. Interestingly, Bi₂Te₃ can easily be doped p- and n-type, while p-type doping of BaBiTe₃ is challenging due to the low formation energies of the Bi_{Ba}⁺¹ antisite defects. Our defect calculations show that the defect chemistry of BaBiTe₃ differs significantly from the one in Bi₂Te₃ and the reason for the difference is the presence of Ba²⁺ as a second cation. The preferential site substitution of Se on the Te4 and Te5 sites presented above (*cf.* section: *Preferential site substitution of Se on the Te4 and Te5 sites*) motivated the study of the defect chemistry of Se substituted variants of BaBiTe₃ in order to explain this preference from an energetic point of view. Results of our extrinsic defect calculations can be found in Fig. V.28 and they revealed equally low formation energies close to zero for Se_{Te4} and Se_{Te5} defects, which explain the preferential site substitution on the Te4 and Te5 sites.

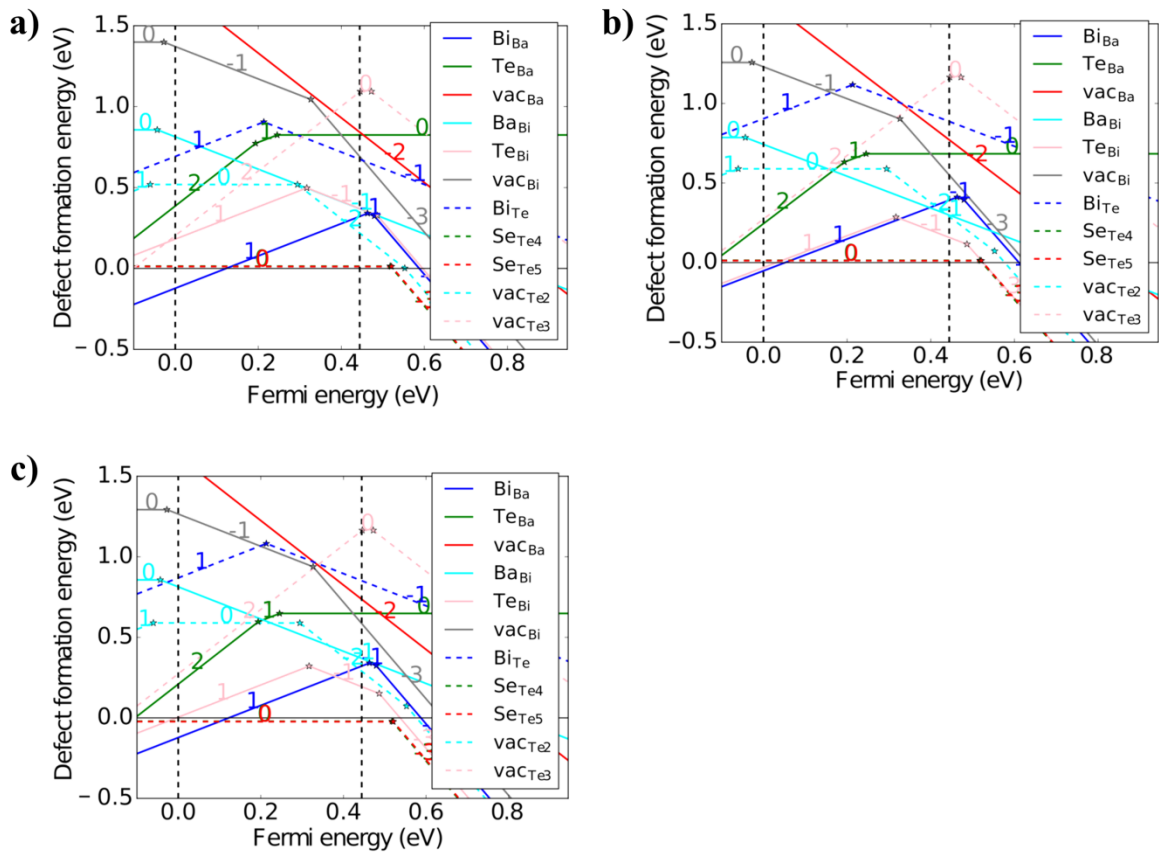


Fig. V.28 Extrinsic defect calculations showing an equally low defect formation energy of 0 for $\text{Se}_{\text{Te}4}$ and $\text{Se}_{\text{Te}5}$ defects. a)-c) correspond to three different regions of the Ba-Bi-Te-Se phase diagram.

3.1.3 Conclusion

The presence of hypervalent $\text{Te}^{\cdots}\text{Te}$ bonds in BaBiTe_3 is best described as a linear combination of interdigitating $(\text{Te}^{1-})_2$ side groups and infinite Te_n chains. Complementary Rietveld refinements and extrinsic defect calculations show that the Se substitution preferentially occurs on the Te4 and Te5 sites, which are not involved in $\text{Te}^{\cdots}\text{Te}$ bonding. Ab initio calculations of the electronic structure, optical absorption measurements and an effective band model analysis of the thermoelectric transport properties of $\text{BaBiTe}_{3-x}\text{Se}_x$ ($x = 0, 0.05$ and 0.1) strongly suggest the presence of multiple conduction bands. Bands higher in the conduction band converge with the conduction band minimum with increasing temperature and contribute to the thermoelectric transport properties of BaBiTe_3 and $\text{BaBiTe}_{2.95}\text{Se}_{0.05}$. This multiband contribution can be considered as the reason for the $\sim 50\%$ higher zT at 617 K compared to $\text{BaBiTe}_{2.9}\text{Se}_{0.1}$, for which no such contribution was found.

The increase in band offset between the CBM and bands higher in the conduction band with respect to the selenium content is one possible explanation for the absence of multiband effects in the thermoelectric transport properties of $\text{BaBiTe}_{2.9}\text{Se}_{0.1}$. A detailed analysis of the defect chemistry of BaBiTe_3 suggests the presence of native $\text{Bi}_{\text{Ba}}^{+1}$ and $\text{Te}_{\text{Bi}}^{+1}$ defects at 0 K and these are probably responsible for the observed n-type conduction. BaBiTe_3 is the first example of a mixed-valent chalcogenide with hypervalent $\text{Te}\cdots\text{Te}$ bonds, where its thermoelectric properties benefit from the contribution of multiple conduction bands. Hence, chalcogenides with hypervalent bonds are promising for continued investigations as new thermoelectric materials.

VI. Conclusion and Outlook

Looking at the number of already known intermetallic phases one might be tempted to think that there is nothing more to discover. Taking the example of the “1113” family demonstrates the opposite. Despite the 160 known compounds, a third subgroup ($A_{0.5}^{+2}M^{+1}M'^{+4}(Q^{2-})_3$) was still unknown up to now (*cf.* chapter IV), which opens a new door for future experiments with different types of elements. Knowing that structure type and symmetry of the 1113 compounds depend on the ratio of the A and M' radii also opens up possibilities for further, systematic experiments. Using the $r(A^{2+})/r(M'^{3+/4+})$ ratio as the only variable could enable to specifically target a certain structure type and symmetry. The *Extended Mooser Pearson plots* presented in chapter II might also help to rationally access polar intermetallics of a certain structure type and even correlate the polarity to their band gaps, which could help to target materials for specific applications based on their polarity. $Ba_2FePnSe_5$ (Pn = Sb, Bi) are two highly interesting semiconductors with respect to their physical properties. The rapid phase changes between a crystalline and amorphous phase by external laser pulses (*cf.* chapter IV) are fascinating. But are they also suitable PCMs? Future research efforts will be dedicated to growing thin films of these compounds and to study their phase change properties in collaboration with the Singapore University of Technology and Design (SUTD). A detailed XPDF study could give insight into changes in the local crystal structure upon amorphization and crystallization, which could help understanding the mechanism behind the phase changes. Another open question is: what is the origin of the anomalies in thermal conductivity and dielectric permittivity at the Néel temperature, which were observed for $Ba_2FeSbSe_5$? The first steps towards answering this question are to solve the crystal and magnetic structures above and below T_N . Probably the most intriguing discovery within this study is $Ba_4Cu_8Se_{13}$ – the first compound with Cu_4Se_9 building blocks as well as coexisting Se_2^{2-} and linear, hypervalent Se_3^{4-} units (*cf.* chapter IV). Are there more compounds containing Cu_4Se_9 units with planar Cu atoms as well as potential Cu-Cu bonds and could this compound be a stepping stone for further understanding the interface between classical solid state chemistry and cluster/molecular chemistry? $BaBiTe_3$ is no less interesting since it contains a unique, hypervalent Te-Te network, which is not trivial to rationalize (*cf.* chapter V). However, theoretical analyses (COHP and ELF) strongly suggest, that this network is best described as a linear combination of interdigitating $(Te^{1-})_2$ side groups and infinite Te_n chains. In $BaBiTe_3$, both native defects and multiband effects seem to play an important role in its thermoelectric transport properties. These findings motivate to look deeper into polar intermetallics with special focus on the thermoelectric properties of compounds with complex band structures.

This study also shows that the concept of resonant bonding in solids is a powerful tool, which helps understanding the chemical bonding in hypervalent polar intermetallics. This is true for both, molecular units such as Se_3^{4-} and extended Q-Q networks like the one in BaBiTe_3 . So far little attention has been paid to the relationship between resonant bonding and the physical properties of polar intermetallics. Taking a closer look at the resonant bonding model for PbS, which was developed by Lucovsky and White, one can find a clear relationship between the resonance energy/integral (K_{12}) and the optical deformation potential D (cf. VI.1), where a , e and ε correspond to the lattice parameter, elemental charge and the real part of the optical frequency dielectric permittivity.

$$D = \frac{8\sqrt{a(\varepsilon-1)}}{3e} K_{12} \quad (\text{VI. 1})$$

K_{12} is a measure for the strength of the resonant bonds, while D represents the degree of coupling between electrons and optical phonons. According to this relationship there should be a direct correlation between resonant bonding and the coupling between electrons and optical phonons in PbS. Since a and ε are measurable quantities and K_{12} can be obtained from the Hückel Method, it is imaginable to obtain D . It is known that low-dimensional systems exhibit new behavior relative to their bulk properties when it comes down to electron-phonon coupling. Very challenging but interesting questions are: How does resonant bonding affect electron-phonon coupling and how does the behavior change when going to low-dimensional materials with resonant bonding and what properties can be expected from these? These questions are also of interest in the light of the studies of Shportko et al. and Lee et al. who suggested that resonant bonding is the underlying phase change mechanism in phase change materials and the origin of the low lattice thermal conductivity of rocksalt-type IV-VI semiconductors, which shows renewed interest in resonant bonding. Probing the physical properties and studying the crystal structure and chemical bonding of both, new and known polar chalcogenides with complex crystal structures resulted in interesting new discoveries, i.e. new compounds and crystal structures as well as unexpected physical properties. The richness of both the chemistry and physical properties of polar chalcogenides is remarkable and it promises many interesting future discoveries.

VII. Bibliography

- [1] F.C. Frank, J. S. Kasper, *Acta Cryst.* **1958**, *11*, 184.
- [2] H. Nowotny, “Crystal Chemistry of Transition Element Defect Silicides and Related Compounds” in “The Chemistry of Extended Defects in Nonmetallic Solids”, Eyring, L., O’Keeffe, M., Eds., North-Holland Publishing Co., Amsterdam and London, **1970**.
- [3] D. C. Fredrickson, S. Lee, R. Hoffmann, J. Lin, *Inorg. Chem.* **2004**, *43*, 6151.
- [4] O. Schwomma, A. Preisinger, H. Nowotny, A. Wittman, *Monatsh. Chem.* **1964**, *95*, 1527.
- [5] Hume-Rothery, W. *J. Inst. Metals* **1926**, *35*, 295.
- [6] W. Hume-Rothery, R. E. Smallman, C. W. Haworth, “The structure of Metals and Alloys”, London: Inst. Metall, **1969**.
- [7] N. F. Mott, H. Jones, “The Theory of the Properties of Metals and Alloys”, New York, **1958**.
- [8] L. Pauling, “The nature of the chemical bond”, Cornell Univ. Press, New York, **1960**.
- [9] H. Schäfer, *Ann. Rev. Mater. Sci.* **1985**, *15*, 1.
- [10] E. Zintl, *Angew. Chem.* **1939**, *52*, 1.
- [11] W. Klemm, E. Busmann, *Z. anorg. allg. Chem.* **1963**, *319*, 297.
- [12] E. Mooser, W. B. Pearson, *Acta Cryst.* **1959**, *12*, 1015.
- [13] R. Lefèvre, D. Berthebaud, O. Perez, D. Pelloquin, S. Hébert, F. Gascoin, *Chem. Mater.* **2015**, *27*, 7110.
- [14] S. M. Kauzlarich, “Chemistry, Structure and Bonding of Zintl phases and Ions“, VCH Publishers, New York, **1996**.
- [15] F. Laves, *Naturwiss.* **1941**, *29*, 244.
- [16] J. I. Musher, *Angew. Chem. Int. Ed.* **1969**, *8*, 54.
- [17] G. N. Lewis, “Valence and the Structure of Atoms and Molecules”, The Chemical Catalog Co, Ch. 8, New York, **1923**.
- [18] I. Langmuir, *Science* **1921**, *54*, 59.
- [19] R. J. Hach, R. E. Rundle, *J. Am. Chem. Soc.* **1951**, *73*, 4321.
- [20] G. C. Pimentel, *J. Chem. Phys.* **1951**, *19*, 446.

- [21] S. Sudgen, "The Parachor and Valency", Knopf, Ch. 6, New York, **1930**.
- [22] G. A. Papoian, R. Hoffmann, *Angew. Chem. Int. Ed.* **2000**, 39, 2408.
- [23] W. Heisenberg, *Z. Physik* **1926**, 39, 499.
- [24] G. Lucovsky, R. M. White, *Phys. Rev. B* **1973**, 8, 660.
- [25] K. Shportko, S. Kremers, M. Woda, D. Lencer, J. Robertson, M. Wuttig, *Nat. Mater.* **2008**, 7, 653
- [26] S. Lee, K. Esfarjani, T. Luo, J. Zhou, Z. Tian, G. Chen, *Nat. Commun.* **2014**, 5, 1.
- [27] W. S. Sheldrick, *Z. Anorg. Allg. Chem.* **2012**, 638, 2401.
- [28] D. M. Smith, J. A. Ibers, *Coord. Chem. Rev.* **2000**, 200-202, 187.
- [29] P. Böttcher, *Angew. Chem. Int. Ed. Engl.* **1988**, 27, 759.
- [30] P. Böttcher, T. Doert, *Phosphorus, Sulfur, Silicon* **1998**, 136-138, 255.
- [31] N.W. Alcock, *Adv. Inorg. Chem. Radiochem.* **1972**, 15, 1.
- [32] G. K. Ahluwalia (Ed.), "Applications of Chalcogenides : S, Se, and Te", Springer, Switzerland, **2017**.
- [33] S. Raoux, M. Wuttig (Eds.), "Phase Change Materials: Science and Applications", Springer, New York, **2009**.
- [34] M. Wuttig, S. Raoux, *Z. Anorg. Allg. Chem.* **2012**, 15, 2455.
- [35] M. Wuttig, N. Yamada, *Nat. Mater.* **2007**, 6, 824.
- [36] M. N. Schneider, T. Rosenthal, C. Stiewe, O. Oeckler, *Z. Kristallogr.* **2010**, 225, 463.
- [37] T. Schröder, T. Rosenthal, N. Giesbrecht, S. Maier, E.-W. Scheidt, W. Scherer, G. J. Snyder, W. Schnick, O. Oeckler, *J. Mater. Chem. A* **2014**, 2, 6384.
- [38] F. Fahrnbauer, D. Sochay, G. Wagner, O. Oeckler, *J. Am. Chem. Soc.* **2015**, 137, 12633.
- [39] H. Scherrer, S. Scherrer, "Bismuth Telluride, Antimony Telluride, and their Solid Solutions" in CRC Handbook of thermoelectrics (Ed. D. M. Rowe), CRC Press, Florida, **1995**.
- [40] V. Fano, "Lead Telluride and Its Alloys" in CRC Handbook of thermoelectrics (Ed. D. M. Rowe), CRC Press, Florida, **1995**.

- [41] Q. H. Zhang, X. Y. Huang, S. Q. Bai, X. Shi, C. Uher, L. D. Chen, *Adv. Eng. Mater.* **2016**, *18*, 194.
- [42] A. D. LaLonde, Y. Pei, H. Wang, G. J. Snyder, *Mater. Today* **2011**, *14*, 526.
- [43] F. Fahrnbauer, S. Maier, M. Grundei, N. Giesbrecht, M. Nentwig, T. Rosenthal, G. Wagner, G. J. Snyder, O. Oeckler, *J. Mater. Chem. C* **2015**, *3*, 10525.
- [44] D.-Y. Chung, T. Hogan, P. Brazis, M. Rocci-Lane, C. Kannewurf, M. Bastea, C. Uher, M. Kanatzidis, *Science* **2000**, *287*, 1024.
- [45] H. Liu, X. Shi, F. Xu, L. Zhang, W. Zhang, L. Chen, Q. Li, C. Uher, T. Day, G. J. Snyder, *Nat. Mater.* **2012**, *11*, 422.
- [46] U. Dehlinger, *Theoretische Metallkunde*, Springer, Berlin, **1955**.
- [47] W. Gordy, W. J. Orville Thomas, *J. Chem. Phys.* **1956**, *24*, 439.
- [48] K. Klepp, H. Boller, *J. Solid State Chem.* **1983**, *48*, 388.
- [49] A. Jain, S. P. Ong, G. Hautier, W. Chen, W. D. Richards, S. Dacek, S. Cholia, D. Gunter, D. Skinner, G. Ceder, K. A. Persson, *APL Mater.* **2013**, *1*, 011002.
- [50] C. Suryanarayana, *Prog. Mater. Sci.* **2001**, *46*, 1.
- [51] V. Petricek, M. Dusek, L. Palatinus, *Z. Kristallogr.* **2014**, *229*, 345.
- [52] SMART, Bruker AXS Inc, Madison, Wisconsin, USA, 2003.
- [53] SAINT, Bruker Bruker AXS Inc, Madison, Wisconsin, USA, 2003.
- [54] SADABS, Bruker AXS Inc, Madison, Wisconsin, USA, 2003.
- [55] G. M. Sheldrick, *Acta Cryst.* **2008**, *A64*, 112.
- [56] O. V. Dolomanov, L. J. Bourhis, R. J. Gildea, J. A. K. Howard, H. Puschmann, *J. Appl. Cryst.* **2009**, *42*, 339.
- [57] C. Giacovazzo, H. L. Monaco, D. Viterbo, F. Scordari, G. Gilli, G. Zanotti, M. Catti, *Fundamentals of Crystallography*, Oxford University press, New York, 1992
- [58] L. M. Gelato, E. Parthé, *J. Appl. Cryst.* **1987**, *20*, 139.
- [59] J. Rodriguez-Carvajal, FULLPROF version July 2011, ILL (unpublished).

- [60] K. A. Borup, J. de Boor, H. Wang, F. Drymiotis, F. Gascoin, X. Shi, L. Chen, M. I. Fedorov, E. Müller, B. B. Iversen, G. J. Snyder, *Energy Environ. Sci.* **2015**, *8*, 423.
- [61] S. Iwanaga, E. S. Toberer, A. LaLonde, G. J. Snyder, *Rev. Sci. Instrum.*, **2011**, *82*, 063905.
- [62] M. Basham, J. Filik, M. T. Wharmby, P. C. Y. Chang, B. El Kassaby, M. Gerring, J. Aishima, K. Levik, B. C. A. Pulford, I. Sikharulidze, et al. *J. Synchrotron Rad.* **2015**, *22*, 853.
- [63] P. Juhás, T. Davis, C. L. Farrow, S. J. L. Billinge, *J. Appl. Cryst.* **2013**, *46*, 560.
- [64] C. L. Farrow, P. Juhás, J. W. Liu, D. Bryndin, E. S. Božin, J. Bloch, T. Proffen, S. J. L. Billinge, *J. Phys. Condens. Matter* **2007**, *19*, 335219.
- [65] R. Truell, C. Elbaum, B. B. Chick, “Ultrasonic Methods in Solid State Physics”, Academic Press Inc., New York, **1969**.
- [66] D. G. Cahill, S. K. Watson, R. O. Pohl, *Phys. Rev. B*, **1992**, *46*, 6131.
- [67] A. F. May, G. J. Snyder “Introduction to Modeling Thermoelectric Transport at High Temperatures” in “Materials, Preparation and Characterization in Thermoelectrics”, Rowe, D. M., Ed, CRC Press, Florida, **2012**.
- [68] G. Kresse, J. Furthmüller, Vienna Ab-initio Simulation Package (VASP); Institut für Materialphysik: Vienna (<http://www.vasp.at/>) **2012**.
- [69] G. Kresse, D. Joubert, *Phys. Rev. B* **1999**, *59*, 1758.
- [70] P.E. Blöchl., *Phys. Rev. B* **1994**, *50*, 17953.
- [71] J. Perdew, K. Burke, M. Ernzerhof, *Phys. Rev. Lett.* **1996**, *77*, 3865.
- [72] S. L. Dudarev, G. A. Botton, S. Y. Savrasov, C. J. Humphreys, A. P. Sutton, *Phys. Rev. B* **1998**, *57*, 1505.
- [73] L. Geng, W.-D.Cheng, H. Zhang, C.-S.Lin, W.-L.Zhang, Y.-Y.Li, Z.-Z. He, *Inorg. Chem.* **2011**, *50*, 2378.
- [74] S. Maintz, V. L. Deringer, A. L. Tchougréeff, R. Dronskowski, *J. Comput. Chem.* **2016**, *37*, 1030.
- [75] C. Freysoldt, B. Grabowski, T. Hickel, J. Neugebauer, G. Kresse, A. Janotti, C. G. Van de Walle, *Rev. Mod. Phys.*, **2014**, *86*, 253.

- [76] S. E. Taylor, F. Bruneval, *Phys. Rev. B*, **2011**, *84*, 075155.
- [77] S. P. Ong, W. D. Richards, A. Jain, G. Hautier, M. Kocher, S. Cholia, D. Gunter, V. L. Chevrier, K. A. Persson, and G. Ceder, *Comput. Mater. Sci.*, **2013**, *68*, 314.
- [78] C. Freysoldt, J. Neugebauer, and C. G. Van de Walle, *Phys. Rev. Lett.*, **2009**, *102*, 016402.
- [79] Y. Kumagai, and F. Oba, *Phys. Rev. B*, **2014**, *89*, 195205.
- [80] M. Gajdoš, K. Hummer, G. Kresse, J. Furthmüller, F. Bechstedt, *Phys. Rev. B* **2006**, *73*, 045112.
- [81] H. Ehrenreich, M.H. Cohen, *Phys. Rev.* **1959**, *115*, 786.
- [82] V.-A. Ha, D. Waroquiers, G.-M. Rignanese, G. Hautier, *Appl. Phys. Lett.* **2016**, *108*, 201902.
- [83] Slack, G. A. “New Materials and Performance Limits for Thermoelectric Cooling” in “CRC Handbook of Thermoelectrics”, Rowe, D. M., Ed., CRC Press, FL, **1995**.
- [84] S. Maier, J. Prakash, D. Berthebaud, O. Perez, S. Bobev, F. Gascoin, *J. Solid State Chem.* **2016**, *242*, 14.
- [85] L. A. Koscielski, J. A. Ibers, *Z. Anorg. Allg. Chem.* **2012**, *638*, 2585.
- [86] M. F. Mansuetto, P. M. Keane, J. A. Ibers, *J. Solid State Chem.* **1992**, *101*, 257.
- [87] P. Lemoine, D. Carré, M. Guittard, *Acta Crystallogr., Sect. C* **1986**, *42*, 390.
- [88] I. E. Grey, H. Steinfink, *Inorg. Chem.* **1971**, *10*, 691.
- [89] M. F. Mansuetto, P. M. Keane, J. A. Ibers, *J. Solid State Chem.* **1993**, *105*, 580.
- [90] M. A. Pell, J. A. Ibers, *J. Alloys Compd.* **1996**, *240*, 37.
- [91] P. Wu, J. A. Ibers, *J. Solid State Chem.* **1994**, *110*, 156.
- [92] A. E. Christuk, P. Wu, J. A. Ibers, *J. Solid State Chem.* **1994**, *110*, 330.
- [93] P. Wu, A. E. Christuk, J. A. Ibers, *J. Solid State Chem.* **1994**, *110*, 337.
- [94] F. Q. Huang, K. Mitchell, J. A. Ibers, *Inorg. Chem.* **2001**, *40*, 5123.
- [95] S. Strobel, Doctoral Thesis, University of Stuttgart, 2004.
- [96] S. Strobel, T. Schleid, *J. Alloys Compd.* **2006**, *418*, 80.

- [97] S. Strobel, Th. Schleid, *Z. Naturforsch.* **2004**, *59b*, 985.
- [98] J. Prakash, A. Mesbah, J. C. Beard, J. A. Ibers, *Z. Anorg. Allg. Chem.* **2015**, *641*, 1253.
- [99] P. Wu, A. E. Christuk, J. A. Ibers, *J. Solid State Chem.* **1994**, *110*, 337.
- [100] R. D. Shannon, *Acta Cryst.* **1976**, *A32*, 751.
- [101] F.-C. Hsu, J.-Y. Luo, K.-W. Yeh, T.-K. Chen, T.-W. Huang, P. M. Wu, Y.-C. Lee, Y.-L. Huang, Y.-Y. Chu, D.-C. Yan, M.-K. Wu, *Proc. Natl. Acad. Sci.* **2008**, *105*, 14262.
- [102] J.-F. Ge, Z.-L. Liu, C. Liu, C.-L. Gao, D. Qian, Q.-K. Xue, Y. Liu, J.-F. Jia, *Nat. Mater.* **2014**, *14*, 285.
- [103] D. Liu, W. Zhang, D. Mou, J. He, Y.-B. Ou, Q.-Y. Wang, Z. Li, L. Wang, L. Zhao, S. He, Y. Peng, X. Liu, C. Chen, L. Yu, G. Liu, X. Dong, J. Zhang, C. Chen, Z. Xu, J. Hu, X. Chen, X. Ma, Q. Xue, X. J. Zhou, *Nature Commun.* **2012**, *3*, 931.
- [104] S. He, J. He, W. Zhang, L. Zhao, D. Liu, X. Liu, D. Mou, Y.-B. Ou, Q.-Y. Wang, Z. Li, L. Wang, Y. Peng, Y. Liu, C. Chen, L. Yu, G. Liu, X. Dong, J. Zhang, C. Chen, Z. Xu, X. Chen, X. Ma, Q. Xue, X. J. Zhou, *Nat. Mater.* **2013**, *12*, 605.
- [105] J. Guo, S. Jin, G. Wang, S. Wang, K. Zhu, T. Zhou, M. He, X. Chen, *Phys. Rev. B.* **2010**, *82*, 180520.
- [106] T. P. Ying, X. L. Chen, G. Wang, S. F. Jin, T. T. Zhou, X. F. Lai, H. Zhang, W. Y. Wang, *Sci. Rep.* **2012**, *2*, 426.
- [107] M. Burrad-Lucas, D. G. Free, S. J. Sedlmaier, J. D. Wright, S. J. Cassidy, Y. Hara, A. J. Corkett, T. Lancaster, P. J. Baker, S. J. Blundell, S. J. Clarke, *Nat. Mater.* **2013**, *12*, 15.
- [108] Y. Hong, H. Steinfink, *J. Solid State Chem.* **1972**, *5*, 93.
- [109] D. Berthebaud, K. R. S. Preethi Meher, D. Pelloquin, A. Maignan, *J. Solid State Chem.* **2014**, *211*, 184.
- [110] D. Driss, E. Janod, B. Corraze, C. Guillot-Deudon, L. Cario, *Inorg. Chem.* **2016**, *55*, 2923.
- [111] J. Wang, J. T. Greenfield, K. Kovnir, *J. Solid State Chem.* **2016**, *242*, 22.
- [112] J. T. Lemley, J. M. Jenks, J. T. Hoggins, Z. Eliezer, H. Steinfink, *J. Solid State Chem.* **1976**, *16*, 117.

- [113] L. Geng, W.-D. Cheng, H. Zhang, C.-S. Lin, W.-L. Zhang, Y.-Y. Li, Z.-Z. He, *Inorg. Chem.* **2011**, *50*, 2378.
- [114] W. Hao, D. Mei, W. Yin, K. Feng, J. Yao, Y. Wu, *J. Solid State Chem.* **2013**, *198*, 81.
- [115] L. Geng, W.-D. Cheng, C.-S. Lin, W.-L. Zhang, H. Zhang, Z.-Z. He, *Inorg. Chem.* **2011**, *50*, 5679.
- [116] S. Raoux, M. Wuttig in “Phase Change Materials: Science and Applications”, Springer, NY, **2009**.
- [117] M. Wuttig, S. Raoux, *Z. Anorg. Allg. Chem.* **2012**, *15*, 2455.
- [118] M. Wuttig, N. Yamada, *Nat. Mater.* **2007**, *6*, 824.
- [119] E. R. Meinders, A. V. Mijritskii, L. van Piersen, M. Wuttig in *Optical Data Storage: Phase Change Media and Recording*, Springer, Berlin, 2006.
- [120] S. R. Ovshinsky, *Phys. Rev. Lett.* **1968**, *21*, 1450.
- [121] S. R. Ovshinsky, B. Pashmakov, *Mater. Res. Soc. Symp. Proc.* **2004**, *803*, 49.
- [122] R. K. Sharma, P. Ganesan, V. V. Tyagi, H. S. C. Metselaar, S. C. Sandaran, *Energy Convers. Manage.* **2015**, *95*, 193.
- [123] D. Lencer, M. Salinga, B. Grabowski, T. Hickel, J. Neugebauer, M. Wuttig, *Nat. Mater.* **2008**, *7*, 972.
- [124] T. Matsunaga, N. Yamada, R. Kojima, S. Shamoto, M. Sato, H. Tanida, T. Uruga, S. Kohara, M. Takata, P. Zalden, G. Bruns, I. Sergueev, H. C. Wille, R. P. Hermann, M. Wuttig, *Adv. Funct. Mater.* **2011**, *21*, 2232.
- [125] X. Li, X. Zhang, G. K. Selvan, S. Arumugam, F. Huang, Y. Wu, J. Yao, *Chem. Asian J.* **2016**, *11*, 3436.
- [126] B. Silvi, A. Savin, *Nature* **1994**, *371*, 683.
- [127] M. I. Aroyo, D. Orobengoa, G. de la Flor, E. S. Tasci, J. M. Perez-Mato, H. Wondratschek, *Acta Cryst.* **2014**, *A70*, 126.
- [128] B. Tofield, *J. Phy. Colloques* **1976**, *37*, 539.
- [129] S. R. Bakhchieva, N. P. Kekelidze, M. G. Kekua, *Phys. Status Solidi A* **1984**, *83*, 139.
- [130] E. F. Steigmeier, I. Kudman, *Phys. Rev.* **1963**, *132*, 508.

- [131] M. G. Holland, *Phys. Rev.* **1964**, *134*, A471.
- [132] K. Tanaka, K. Shimakawa in “Amorphous Chalcogenide Semiconductors and Related Materials”, Springer, New York, **2011**.
- [133] M. Luo, M. Wuttig, *Adv. Mater.* **2004**, *16*, 439.
- [134] H. Kabbour, L. Cario, *Inorg. Chem.* **2006**, *45*, 2713.
- [135] A. V. Kolobov, P. Fons, A. I. Frenkel, A. L. Ankudinov, J. Tominaga, T. Uruga, *Nat. Mater.* **2004**, *3*, 703.
- [136] G. Campoy, A. Palma, L. Sandoval, *Int. J. Quantum Chem.* **1989**, *23*, 355.
- [137] G. Lawes, T. Kimura, C. M. Varma, M. A. Subramanian, N. Rogado, R. J. Cava, A. P. Ramirez, *Prog. Solid State Chem.* **2009**, *37*, 40.
- [138] R. Seshadri, N. A. Hill, *Chem. Mater.* **2001**, *13*, 2892.
- [139] M. Fiebig, *J. Phys. D. Appl. Phys.* **2005**, *38*, R123.
- [140] B. Lorenz, Y. Q. Wang, Y. Y. Sun, C. W. Chu, *Phys. Rev. B* **2004**, *70*, 212412.
- [141] N. Hur, S. Park, P. A. Sharma, S. Guha, S-W. Cheong, *Phys. Rev. Lett.* **2004**, *93*, 107207.
- [142] M. C. Kemei, S. L. Moffitt, L. E. Darago, R. Seshadri, M. R. Suchomel, D. P. Shoemaker, K. Page, J. Siewenie, *Phys. Rev. B* **2014**, *89*, 174410.
- [143] T. D. Sparks, M. C. Kemei, P. T. Barton, R. Seshadri, E.-D. Mun, V. S. Zapf, *Phys. Rev. B* **2014**, *89*, 024405.
- [144] U. Adem, L. Wang, D. Fausti, W. Schottenhamel, P. H. M. van Loosdrecht, A. Vasiliev, L. N. Bezmaternykh, B. Büchner, C. Hess, R. Klingeler, *Phys. Rev. B* **2010**, *82*, 064406.
- [145] J. K. Harada, L. Balhorn, J. Hazi, M. C. Kemei, R. Seshadri, *Phys. Rev. B* **2016**, *93*, 104404.
- [146] K. Singh, A. Maignan, C. Simon, S Kumar, C. Martin, O. Lebedev, S. Turner, G. Van Tendeloo, *J. Phys. Condens. Mat.* **2012**, *24*, 226002.
- [147] K. Singh, A. Maignan, D. Pelloquin, O. Perez, Ch. Simon, *J. Mater. Chem.* **2012**, *22*, 6436.
- [148] N. Bellido, C. Simon, A. Maignan, *J. Magn. Magn. Mater.* **2009**, *321*, 1770.

- [149] N. Imamura, K. Singh, D. Pelloquin, Ch. Simon, T. Sasagawa, M. Karppinen, H. Yamauchi, A. Maignan, *Appl. Phys. Lett.* **2011**, *98*, 072903.
- [150] O. Mayasree, C. R. Sankar, K. M. Kleinke, H. Kleinke, *Coord. Chem. Rev.* **2012**, *256*, 1377.
- [151] A. Assoud, J. Xu, H. Kleinke, *Inorg. Chem.* **2007**, *46*, 9906.
- [152] I. Schewe-Miller, P. Böttcher, *J. Alloys Compd.* **1992**, *183*, 98.
- [153] R. Patschke, M. G. Kanatzidis, *Phys. Chem. Chem. Phys.* **2002**, *4*, 3266.
- [154] C. D. Malliakas, S. J. L. Billinge, H. J. Kim, M. G. Kanatzidis, *J. Am. Chem. Soc.* **2005**, *127*, 6510.
- [155] M. Sturza, F. Han, D. P. Shoemaker, C. D. Malliakas, D. Y. Chung, H. Jin, A. J. Freeman, M. G. Kanatzidis, *Inorg. Chem.* **2013**, *52*, 7210.
- [156] P. Dürichen, M. Bolte, W. Bensch, *J. Solid State Chem.* **1998**, *140*, 97.
- [157] D. B. Brown, J. A. Zubieta, P. A. Vella, J. T. Wroblewski, T. Watt, W. E. Hatfield, P. Day, *Inorg. Chem.* **1980**, *19*, 1945.
- [158] R. Berger, L. E. Tergerius, L. Noren, L. Erisson, *J. Alloys Compd.* **1995**, *224*, 171.
- [159] P. Stoll, C. Näther, I. Jess, W. Bensch, *Acta Crystallogr. C* **1999**, *55*, 286.
- [160] C. Burschka, *Z. Anorg. Allg. Chem.* **1980**, *463*, 65.
- [161] G. V. Vajenine, R. Hoffmann, *Inorg. Chem.* **1996**, *35*, 451.
- [162] C. Burschka, *Z. Naturforsch. B: J. Chem. Sci.* **1979**, *34B*, 396.
- [163] Z. Peplinski, D. B. Brown, T. Watt, W. E. Hatfield, P. Day, *Inorg. Chem.* **1982**, *21*, 1752.
- [164] M. Sturza, C. D. Malliakas, D. E. Bugaris, F. Han, D. Y. Chung, M. G. Kanatzidis, *Inorg. Chem.* **2014**, *53*, 12191.
- [165] R. Berger, C. F. Van Bruggen, *J. Less-Common Met.* **1984**, *99*, 113.
- [166] M. Sturza, D. E. Bugaris, C. D. Malliakas, F. Han, D. Y. Chung, M. G. Kanatzidis, *Inorg. Chem.* **2016**, *55*, 4884.
- [167] J. E. Iglesias, K. E. Pachali, H. Steinfink, *J. Solid State Chem.* **1974**, *9*, 6.

- [168] S. Maier, J. Prakash, D. Berthebaud, O. Perez, S. Bobev, F. Gascoin, *J. Solid State Chem.* **2016**, *242*, 14.
- [169] M. F. Mansuetto, P. M. Keane, J. A. Ibers, *J. Solid State Chem.* **1992**, *101*, 257.
- [170] M. A. McGuire, A. F. May, D. J. Singh, M.-H. Du, G. E. Jellison, *J. Solid State Chem.* **2011**, *184*, 2744.
- [171] J. Li, L.-D. Zhao, J. Sui, D. Berardan, W. Cai, N. Dragoe, *Dalton Trans.* **2015**, *44*, 2285.
- [172] Y. C. Chan, M. M. Olmstead, S. M. Kauzlarich, *Chem. Mater.* **1998**, *10*, 3583.
- [173] R. D. Burbank, *Acta Cryst.* **1951**, *4*, 140.
- [174] P. Cherin, P. Unger, *Inorg. Chem.* **1967**, *6*, 1589.
- [175] A. B. Salem, A. Meerschaut, J. C. R. Rouxel, *Acad. Sci. Sér. 2* **1984**, *299*, 617.
- [176] W. L. Bragg, *Phylos. Mag.* **1914**, *28*, 355.
- [177] H. Shils, W. Bronger, *Z. Anorg. Allg. Chem.* **1979**, *456*, 187.
- [178] C. Näther, D. Röhnert, W. Bensch, *J. Eur. Solid State Inorg. Chem.* **1998**, *35*, 565.
- [179] P. K. Mehrotra, R. Hoffmann, *Inorg. Chem.* **1978**, *17*, 2187.
- [180] J. W. Lauher, *Int. J. Quantum Chem.* **1988**, *22*, 309.
- [181] P.M. De Wolff, T. Jansen, A. Janner, *Acta Crystallogr. A* **1981**, *37*, 625.
- [182] Tritt, T. M. “Thermal Conductivity – Theory, Properties and Applications”, Springer, NY, **2004**.
- [183] Y.-K. Kuo, M. J. Skove, D. T. Verebelyi, H. Li, R. Mackay, S.-J. Hwu, M.-H. Whangbo, J. W. Brill, *Phys. Rev. B* **1998**, *57*, 3315.
- [184] A. Mrotzek, M. G. Kanatzidis, *Acc. Chem. Res.* **2003**, *36*, 111.
- [185] H. Lin, G. J. Tan, J. N. Shen, S. Q. Hao, L. M. Wu, N. Calta, C. Malliakas, S. Wang, C. Uher, C. Wolverton, M. G. Kanatzidis, *Angew. Chem. Int. Ed.* **2016**, *55*, 11431.
- [186] Y. Pei, C. Chang, Z. Wang, M. Yin, M. Wu, G. Tan, H. Wu, Y. Chen, L. Zheng, S. Gong, T. Zhu, X. Zhao, L. Huang, J. He, M. G. Kanatzidis, L.-D. Zhao, *J. Am. Chem. Soc.* **2016**, *138*, 16364.

- [187] N. D. Lowhorn, T. M. Tritt, E. E. Abbott, J. W. Kolis, *Appl. Phys. Lett.*, **2006**, *88*, 022101.
- [188] A. Assoud, S. Thomas, B. Sutherland, H. Zhang, T. M. Tritt, H. Kleinke, *Chem. Mater.* **2006**, *18*, 3866.
- [189] O. Mayasree, C. R. Sankar, Y. Cui, A. Assoud, H. Kleinke, *Eur. J. Inorg. Chem.* **2011**, *26*, 4037.
- [190] R. Patschke, X. Zhang, D. Singh, J. Schindler, C. R. Kannewurf, N. Lowhorn, T. Tritt, G. S. Nolas, M. G. Kanatzidis, *Chem. Mater.* **2001**, *13*, 613.
- [191] G. D. Mahan “Good Thermoelectrics” in “Solid State Physics”, Ehrenreich, H. and Spaepen, F., Eds, Academic Press, Cambridge, **1998**.
- [192] H. J. Goldsmid, “Thermoelectric Refrigeration”, Plenum Press, New York, **1964**.
- [193] Y. Pei, X. Shi, A. LaLonde, H. Wang, L. Chen, G. J. Snyder, *Nature* **2011**, *473*, 66.
- [194] T. C. Chasapis, Y. Lee, E. Hatzikraniotis, K. M. Paraskevopoulos, H. Chi, C. Uher, M. Kanatzidis, *Phys. Rev. B*, **2015**, *91*, 085207.
- [195] K. Volk, G. Cordier, R. Cook, H. Schäfer, *Z. Naturforsch.* **1980**, *35b*, 136.
- [196] D.-Y. Chung, S. Jovic, T. Hogan, C. R. Kannewurf, R. Brec, J. Rouxel, M. G. Kanatzidis, *J. Am. Chem. Soc.* **1997**, *119*, 2505.
- [197] H. Takahashi, N. Raghavendra, F. Gascoin, D. Pelloquin, S. Hébert, E. Guilmeau, *Chem. Mater.* **2013**, *25*, 1809.
- [198] S. Maier, R. Lefèvre, X. Lin, N. Raghavendra, D. Berthebaud, S. Hébert, A. Mar, F. Gascoin, *J. Mater. Chem. C* **2015**, *3*, 10509.
- [199] K. Suekuni, Y. Yakasu, T. Hasegawa, N. Ogita, M. Udagawa, M. A. Avila, T. Takabatake, *Phys. Rev. B* **2010**, *81*, 205207-1.
- [200] M. Christensen, B. B. Iversen, *Chem. Mater.* **2007**, *19*, 4896.
- [201] M. D. Nielsen, V. Ozolins, J. P. Heremans, *Energy Environ. Sci.* **2013**, *6*, 570.
- [202] A. V. Petrov, E. L. Shtrun, *Sov. Phys. Solid State* **1962**, *4*, 1061.
- [203] D. T. Morelli, V. Jovic, J. P. Heremans, *Phys. Rev. Lett.* **2008**, *101*, 035901-1.
- [204] E. J. Skoug, D. T. Morelli, *Phys. Rev. Lett.* **2011**, *107*, 235901-1.

- [205] P. Larson, S. D. Mahanti, M. G. Kanatzidis, *Phys. Rev. B* **2000**, *61*, 8162.
- [206] J. F. Meng, N. V. Chandra Shekar, J. V. Badding, D.-Y. Chung, M. G. Kanatzidis, *J. Appl. Phys.* **2001**, *90*, 2836.
- [207] Y. Zhou, L.-D. Zhao, *J. Solid State Chem.* **2017**, *249*, 131.
- [208] Y. Tang, Z. M. Gibbs, L. A. Agapito, G. Li, H.-S. Kim, M. B. Nardelli, S. Curtarolo, G. J. Snyder, *Nat. Mater.* **2015**, *14*, 1223.
- [209] D. O. Scanlon, P. D. C. King, R. P. Singh, A. de la Torre, S. McKeown Walker, G. Balakrishnan, F. Baumberger, C. R. A. Catlow, *Adv. Mater.* **2012**, *24*, 2154.
- [210] K. K. Wu, B. Ramachandran, Y. K. Kuo, R. Sankar, F. C. Chou, *J. Alloy. Compd.* **2016**, *682*, 225.
- [211] O. N. Bedoya-Martinez, A. Hashibon, C. Elsässer, *Phys. Status Solidi A* **2016**, *3*, 684.
- [212] L.-L. Wang, M. Huang, S. Thimmaiah, A. Alam, S. L. Bud'ko, A. Kaminski, T. A. Lograsso, P. Canfield, D. D. Johnson, *Phys. Rev. B* **2013**, *87*, 125303-1.
- [213] T. Zhu, L. Hu, X. Zhao, J. He, *Adv. Sci.* **2016**, *3*, 1600004-1.
- [214] J. Suh, K. M. Yu, X. Liu, F. Yang, J. Fan, D. J. Smith, Y.-H. Zhang, J. K. Furdyna, C. Dames, W. Walukiewicz, J. Wu, *Adv. Mater.* **2015**, *27*, 3681.
- [215] S. Ohno, U. Aydemir, M. Amsler, J.-H. Pöhls, S. Chanakian, A. Zevalkink, M. A. White, S. K. Bux, C. Wolverton, G. J. Snyder, *Adv. Funct. Mater.* **2017**, *27*, 1606361.

VIII. Publications

Publications based on results presented in this thesis:

[1] “Crystal structures of the four new quaternary copper(I)-selenides $A_{0.5}CuZrSe_3$ and $ACuYSe_3$ (A=Sr,Ba)”

S. Maier, J. Prakash, D. Berthebaud, O. Perez, S. Bobev, F. Gascoin

J. Solid State Chem. **2016**, 242, 14.

[2] “Linear, hypervalent Se_3^{4-} units and unprecedented Cu_4Se_9 building blocks in the copper-(I)-selenide $Ba_4Cu_8Se_{13}$ ”

S. Maier, O. Perez, D. Pelloquin, D. Berthebaud, S. Hébert and Franck Gascoin

Inorg. Chem. **2017**, 56, 9209.

[3] “Synthesis, electronic structure and physical properties of polycrystalline $Ba_2FePnSe_5$ (Pn = Sb, Bi)”

S. Maier, S. Hebert, H. Kabbour, D. Pelloquin, O. Perez, D. Berthebaud, F. Gascoin

Mater. Chem. Phys. published online, DOI: 10.1016/j.matchemphys.2017.09.060.

[4] “Hypervalent bonding, multiband thermoelectric transport and native defects in n-type $BaBiTe_{3-x}Se_x$ (x = 0, 0.05 and 0.1)”

S. Maier, S. Ohno, G. Yu, S. D. Kang, T. C. Chasapis, V.-A. Ha, S. Miller, D. Berthebaud, M. G. Kanatzidis, G.-M. Rignanese, G. Hautier, G. J. Snyder, F. Gascoin

Submitted

Other publications, which resulted from work at the CRISMAT laboratory:

[5] “The solid solution series $Tl(V_{1-x}Cr_x)_5Se_8$: crystal structure, magnetic and thermoelectric properties“

S. Maier, R. Lefèvre, X. Lin, R. Nunna, D. Berthebaud, S. Hèbert, A. Mar, F. Gascoin

J. Mater. Chem. C **2015**, 3, 10509.

Résumé

Ces travaux de thèse portent sur l'étude des propriétés chimiques et physiques de chalcogénures polaires (CPs) à valence normal ou hypervalents. Ces composés appartiennent à la famille des intermétalliques polaires, et s'inscrivent donc dans le champ d'étude de la chimie des intermétalliques. Le but premier de cette étude est la synthèse de nouveaux composés de structure cristalline complexe, afin d'étudier la relation entre la structure cristalline, la nature des liaisons chimiques et les propriétés physiques, déterminées par des mesures expérimentales et des analyses théoriques. Les CPs ont été choisis comme matériaux d'étude car ils se situent à la frontière entre les matériaux métalliques et non-métalliques. Pour ces matériaux (les CPs), les propriétés chimiques sont gouvernées par l'interaction entre les différents types de liaisons – covalente, métallique et ionique – ouvrant la voie à l'étude des liens entre structure cristalline et liaisons chimiques. La recherche de matériaux à structure complexe permet de cibler de potentiels matériaux thermoélectriques prometteurs, puisque la complexité structurale est souvent reliée à une faible conductivité thermique, qui est une propriété clé des thermoélectriques. Les matériaux thermoélectriques transforment la chaleur en électricité, et sont donc au cœur des enjeux économiques et environnementaux actuels. La découverte de thermoélectriques à bon rendement appartenant à la famille des chalcogénures, tels que PbTe, Bi₂Te₃, CsBi₄Te₆ et le composé superionique Cu_{2-x}Se ont orienté les recherches vers l'exploration de composés chalcogénures de type Cu- et Pn- (Pn = Sn, Bi), et ont motivé l'étude de matériaux voisins, comme BaBiTe₃ (chapitre V). Une des possibilités pour induire des structures complexes est d'obtenir un transfert de charge du cation (Ba, Se) vers une structure anionique, créant ainsi des réseaux covalents anioniques complexes sous forme de chaînes ou de couches, qui sont à l'origine de propriétés physiques intéressantes. Une paire d'électrons libres et stéréoactifs peut également augmenter la complexité de la structure, via une distorsion des polyèdres de coordination, ce qui justifie l'étude de matériaux contenant des éléments de type Pn comme Bi ou Sb. L'analyse des propriétés physiques ainsi que l'étude de la structure cristalline et des liaisons chimiques de chalcogénures polaires de structure complexe, certains connus et d'autres découverts au cours de ce travail de thèse, ont résulté en des découvertes prometteuses.

Abstract

This thesis has its focus on the chemistry and physical properties of normal valence and hypervalent polar chalcogenides (PCs). The motivation for this study lies in the synthesis of new compounds with complex crystal structures. It aims at understanding the relationship between crystal structure, chemical bonding and physical properties through experimental and theoretical analyses. PCs are of special interest since they are at the interface between metals and nonmetals. The chemistry at this interface is governed by the interplay between covalent, metallic and ionic bonding, which makes it interesting and challenging to understand the relationship between crystal structure and chemical bonding. The main reason for aiming at structural complexity is to target new materials with low thermal conductivities – a key requirement for efficient thermoelectric materials. Thermoelectrics are capable of converting waste heat into electricity, which is of considerable economic and environmental interest. Previous discoveries of efficient, chalcogenide-based thermoelectrics such as PbTe, Bi₂Te₃, CsBi₄Te₆ and superionic Cu_{2-x}Se motivated the exploratory search for new Cu- and Pn-chalcogenides (Pn = Sb, Bi) and to study related materials such as BaBiTe₃ (*cf.* chapter V). One route towards complex crystal structures is to use a charge transfer from cations such as Sr or Ba to an anionic framework in order to create complex anionic, covalent networks (e.g. channels or layers) which can lead towards interesting physical properties. Stereoactive lone pairs can increase the structural complexity through distortions of the coordination polyhedra, which is one reason for studying systems containing Pn atoms such as Sb and Bi. Probing the physical properties and studying the crystal structure and chemical bonding of both, new and known polar chalcogenides with complex crystal structures resulted in interesting new discoveries, i.e. new compounds and crystal structures as well as unexpected physical properties. The thesis is separated in normal valence compounds, which can be entirely described by classical two-center two-electron (2c-2e) bonds (i.e. where the electrons are fully localized) and those, which contain hypervalent bonds and networks in which the electrons are partially delocalized. It contains four main parts: the study of 1) A_{0.5}CuZrSe₃ et ACuYSe₃ (A = Sr, Ba) belonging to a family of compounds known as the “1113 family”, 2) Ba₂FePnSe₅ (Pn = Sb, Bi), 3) Ba₄Cu₈Se₁₃ and 4) BaBiTe_{3-x}Se_x (x = 0, 0.05, 1 and 3).